MULTIFUNCTIONAL HETEROSTRUCTURES COMPRISED OF CARBON AND METAL NANOSTRUCTURES: GROWTH MECHANISM AND APPLICATIONS

by

JUNCHI WU

NITIN CHOPRA, COMMITTEE CHAIR
MARTIN G. BAKKER
RAMANA G. REDDY
JINHUI SONG
UDAY VAIDYA

A DISSERTATION

Submitted in partial fulfillment of the requirements
for the degree of Doctor of Philosophy
in the Department of Metallurgical and Materials Engineering
in the Graduate School of
The University of Alabama

TUSCALOOSA, ALABAMA

2013

ABSTRACT

Noble metal nanoparticles were synthesized by either nucleation in solution or dewetting from thin metal films, and further oxidized to create a thin surface oxide shell. A detailed analysis of surface oxidation of noble metal nanoparticles is presented in this dissertation. This study allowed for utilizing these nanoparticles with controlled surface oxide to result in the growth of graphene shells around noble metal nanoparticles in a chemical vapor deposition process. Oxidation kinetics of noble metal nanoparticles was studied by combining electron microscopy and x-ray photoelectron spectroscopy techniques. This was further correlated with the growth of graphene shells and thicker oxide shell resulted in larger number of graphene layers. In regard to explore their applications, graphene shells encapsulated nanoparticles were demonstrated as a unique plasmonic substrates and catalytic substrates. Plasmonic modeling was done by discrete dipole approximation, simulated and explored the optical properties of graphene shells encapsulated noble metal nanostructures. This approach of graphene shells growth around noble metal nanoparticles was further exploited to understand the role of catalytic noble metal morphology and thus, detailed investigation of the CVD growth of graphene shells around segmented nanowire system was conducted. It was observed that graphene shells were grown around metal nanowires. However, the melting of the nanowires during the shell growth process must be carefully controlled. This further lead to complex nanowire heterostructures and their incorporation into polymer for bio-applications as demonstrated in this dissertation.

DEDICATION

This dissertation is dedicated to everyone who helped me and guided me through the trials and tribulations of creating this manuscript. In particular, my family and close friends who stood by me throughout the time taken to complete this work.

LIST OF ABBREVIATIONS AND SYMBOLS

a_{eff}	Effective radius
C_n	Flory characteristic ratio
d	Cubic lattice spacing
e	Absolute value of the electron charge
ΔG_{total}	Gibbs free energy of polymer
ΔG_{mixing}	Gibbs free energy from the spontaneous mixing of the fluid molecules with the polymer chains
$\Delta G_{elastic}$	Gibbs free energy due to the elastic retractive forces build within the gel
H	Electron emission depth for the sample in XPS
k_0	Rate-limiting jump rate constant
k_0^o	Rate constant for the case without field
K	Kinetic constant
l	Length of the bond along the polymer backbone
L	Thickness of oxide layer
L_0	Original thickness of oxide layer
$\overline{M_C}$	Molecular weight between two adjacent crosslinks
$\overline{M_n}$	Molecular weight of the polymer chains prepared
M_r	Molecular weight of the repeating units

p	Fraction of metal atoms located in defect sites of the interface
q	Ion charge
qb_0V_0 / L	Field-induced decrease of the jump activation energy
$(\bar{r}_o^{\,2})^{1/2}$	Root-mean-square, unperturbed, end-to-end distance of the polymer
V_1	Molar volume of water
$\bar{v}$	Specific volume of the polymer
χ_1	Polymer-solvent interaction parameter
Ω	Constant quantity related to the built-in potential across the oxide and ionic mobility
μ_1	Chemical potential of the solvent in hydrogel
$\mu_{1,0}$	Chemical potential of the pure solvent.
ξ	Size of the pores

ACKNOWLEDGMENTS

I would like to greatly thank my advisor, Dr. Nitin Chopra for his support and guidance. Dr. Chopra has always looked to challenge me and pushing me beyond what I thought my limits were. He has been my amazing academic mentor, and I truly hope that our interactions will continue for many years. I would also like to thank Dr. Reddy, Dr. Bakker, Dr. Song, and Dr. Vaidya for serving on my committee and fruitful research discussions. I would like to thank all of my group members who helped me at every step of my graduate research, with special thanks to Mr. Wenwu Shi (graduate student), Mr. Lyndon Smith Jr. (graduate student), Mr. Yuan Li (graduate student), Ms. Brandi Freeman (NSF-REU student), Mr. Larry Summerville (NSF-REU student), Ms. Laura Elena Philips (NSF-REU student), Mr. Robert Miller Wright (NSF-REU student), Mr. Paaras Agrawal (NSF-REH), Mr. Andrew Lattner (NSF-REH), Mr. Todd Gilliam (NSR-REH), Mr. John Dykes (NSF-REU student), Mr. Caleb Felker (NSF-REU student), and Ms. Morgan Farrar (NSF-REU).

Thanks to the Central Analytical Facility (CAF) staff including Mr. Rich Martens, Mr. Johnny Goodwin and Mr. Rob Holler for providing training and assistance. I also thank staff from Metallurgical and Materials Engineering (MTE) department and Center for Materials for Information Technology (MINT), Ms. Jan Creitz, Mr. Bob Fanning, Ms. Kim Walker, Ms. Casey McDow, Ms. Jamie Crawford, Dr. Gary Mankey, Dr. Patrick LeClair, Mr. John Hawkins, and Mr. Jason Foster.

I am grateful to Materials Science and Engineering (MSE) program staff including Dr. Garry W. Warren and Dr. Mark L. Weaver for their consistent support through the program. I would like to thank financial support from CAF, MINT, and MSE at the University of Alabama, University of Alabama's Office of Sponsored Programs, Research Grant Committee (RGC) Award, and NSF award (0925445) for my tuition, stipend, instrument time, supplies and infrastructure/resources. Finally, I would like to thank my family and friends with all encouragements and supports.

CONTENTS

LIST OF TABLES

LIST OF FIGURES

CHAPTER 1: INTRODUCTION

1.1 Noble Metal Nanoparticles-Graphene Heterostructure

A particular interest in nanomaterials heterostructure is encapsulating nanoparticles in a thin shell or cage of other components. The purpose of growing shell can be protection of core materials or aim to further functionalization.[1] And the shell materials vary from polymer, metal, to carbon or oxide materials.[1-4] Thin shell is needed for noble metal nanoparticles to prevent nanoparticle aggregation, meanwhile shell should not hinder the core materials to be optically or electronically active. [5] The problem to encapsulate nanoparticles in polymers and oxide shells is attributed to permeability and stability of encapsulating materials, as well as the requirement of precise control over the pH and ionic strength of nanoparticle solution.[6,7] A promising approach is the encapsulation of noble metal nanoparticles in a single crystalline graphene or carbon shells that will uniquely combine properties of both components in one system. Such a graphitic shell can act as a superior surface passivant, and the shell with appropriate thickness may enable the core materials exhibit their unique properties in various applications.

1.1.1 Dewetting of gold film into gold islands

Gold nanoparticles have various applications ranging from cancer cell imaging to low temperature oxidation of CO.[8,9] Size and shape of gold nanoparticles are critical for their applications, therefore the morphology control of gold nanoparticles are of great technological interests. Monolayer of nanoparticles/islands on substrates can be obtained upon annealing of thin metal films, which is referred to as solid state dewetting process and driven by minimization

of surface and strain energy. The optical properties of gold nanoparticles/islands formed by this dewetting process were studied by Rubinstein and his co-workers.[10-12] They prepared gold island films by vapor deposition on transparent substrates (glasses), analyzed the 3D morphology of gold islands by scanning electron microscopy (SEM), cross-sectional transmission electron microscopy (TEM), and atomic force microscopy (AFM) cross-sectional profilometry. One particular interest of Rubinstein's group is studying the localized plasmon properties of gold island film on glass. The variability of size and shape of gold islands, as well as distance between them are provides effective means of tuning the localized surface plasmon resonance (LSPR). Meanwhile the stability of gold islands was increased by partially embedding them in the glass. At the beginning of dewetting, voids forms by various mechanisms such as thermal grooving at grain or twin boundaries, vacancy nucleation at the interface of film/substrate, or due to heterogeneities in the substrate (dust particles or other impurities). As annealing continues, cavity is expected to grow along the area of high stress such as grain boundaries. During the growth of hole, the removal of material from hole-border took place and formed pile-up materials around the hole. Since more materials need to be moved during growth of hole if it remains circular, growth of branched-hole was more often observed, which preferably takes place at the tips of holes. Given enough time and temperature, the metal film will reshape continuously to minimize surface energy.

1.1.2 Methods for synthesizing carbon-graphene encapsulated noble metal nanoparticles

Past research has indicated significant interest in encapsulation of transition-metal nanoparticles with carbon shells using a chemical vapor deposition (CVD) approach.[13] However, it has been observed that in the CVD method, transition-metal nanoparticles not only catalyze growth of a

graphene shell but also of carbon nanotubes (CNTs) and amorphous carbon.[14] On the other hand, noble metal nanoparticles are difficult to be encapsulated in graphitic carbon shells by the CVD approach due to the low carbon solubility in the former.[15] Instead, TEM based electron irradiation of gold nanoparticles (AuNPs) dispersed on carbon grids has been utilized to achieve graphitic carbon shells around AuNPs.[16] However, this process involved high growth temperatures under electron irradiation, and the resulting carbon shells acted like a pressurized chamber with enough surface tension to lead to the ejection of the encapsulated nanoparticle.[16-18] In addition, this approach did not allow for the recovery of hybrid nanoparticles from the TEM grids and severely limits their applications. Polymer coatings on oxidized AuNPs have been converted into carbon shells,[19] but the use of polymer resulted in amorphous carbon and required long processing duration and cleaning of hybrid nanoparticles to eliminate the remaining polymer or impurities.

Carbon nanocapsule and CNT have been produced using palladium nanoparticles (PdNPs) though arc discharge. [20] "Wormlike" palladium-carbon heterostructure has been fabricated by arc treated PdO/graphite mixture. [21] Also, low temperature (~200 ^{o}C) hydrothermal process has been applied to synthesize palladium-carbon core/shell heterostructures.[22] The carbon shells fabricated in above methods are usually thick and disordered. Hollow porous carbon shells with mesopore and micropore have been synthesized and employed to protect palladium nanoparticles as catalyst for aerobic oxidation of alcohols.[23] The hollow core-shell heterostructures were fabricated by removing the intermediate siliceous layer between PdNPs and carbon layers.

Ge and coworkers utilized electron irradiation synthesized fullerene-like carbon shells around platinum nanoparticles (PtNPs).[24] However, this process requires high temperature (1245 ^{o}C) to

form Pt-amorphous carbon specimens, and graphitic shells would only form on small platinum nanoparticles (less than 5 nm) by irradiation. A commonly used method to obtain nanostructured carbons is applying templating procedures using silica-based molds, which involves coverage or filling of the surfaces of the molds with carbon sources followed by carbonization under inert or reductive conditions, and subsequent removal of the molds using chemical etching.[25,26] A more convenient approach for the preparation is to incorporate PtNPs in hollow carbon nanospheres through the photocatalytic reaction of TiO_2 nanoparticles in deaerated aqueous media, where TiO_2 nanoparticles not only act as molds of hollow carbon but also induce simultaneous deposition of PtNPs and phenolic polymers by photocatalytic reduction and oxidation of platinum precursor and phenol, respectively.[27]

Our group previously demonstrated a simple CVD approach to grow carbon shells encapsulated AuNPs.[1,28,29] Since these carbon shells have interlayer spacing consistent with the c-axis spacing of the graphene layers, we also referred to them as graphene shells encapsulating AuNPs (GNPs). The approach utilized commercially bought AuNPs patterned on a silicon (Si) substrate that were plasma oxidized to form surface-oxidized AuNPs. The latter served as the catalyst for the growth of graphene shells in the presence of a hydrocarbon source at temperatures between 600 and 700 °C. The graphene shell thickness was controlled (~1−20 nm) by varying growth times, which indicated the flexibility of our CVD method. Additionally, the rich surface chemistry of the carboxylic-derivatized graphene shells provided an interesting opportunity for bio-analysis and sensing. The most critical step in the formation of GNPs is the pre-CVD plasma oxidation of AuNPs to result in surface gold oxide. It has been observed that such plasma-oxidized AuNPs inhibit the growth of CNTs in a CVD process.[30] It was later demonstrated that

surface-oxidized AuNPs resulted in graphene shells encapsulating the core AuNPs. This makes the approach suitable to grow impurity-free GNPs. However, a detailed understanding of the graphene shells growth mechanism, plasma oxidation kinetics of AuNPs, effect of structural defects in the AuNPs on the graphene shells growth, and large area growth of GNPs remains unexplored and unclear.

1.1.3 Oxidation kinetics of noble metal nanoparticles.

The formation of a surface oxide shell on noble metal nanoparticles is essential for the graphene shells evolution. For this reason, the understanding of the mechanisms and kinetics of oxidation is highly desirable. In general, the growth of oxide layers is controlled by diffusion of ions and electrons under the influence of gradients of their concentrations and self-generated electrical potential (during anodic oxidation, the oxidation can be facilitated and/or driven by external potential).

Cabrera and Mott (CM) proposed a generic model when electric field acts as dominate barrier in diffusion. The CM model states as follows:[31] oxygen molecular or dissociative adsorption at the oxide surface is accompanied by the formation of surface states located (in the absence of the field) above the oxide valence band and below the metal Fermi level, $E_o < E_F$ (where E_o is oxide valence band and E_F is the metal Fermi level). During oxidation, electron tunneling from the metal to vacant surface states, which results in the appearance of charges on the oxide interfaces and accordingly in shift of the energy of these states up to the Fermi level. It generates uniform field in the oxide film as given:

$$\varepsilon = V_0 / L \equiv (E_F - E_o) / eL \qquad (1.1)$$

where L is the thickness of oxide layer, and e is the absolute value of the electron charge. The control step of the oxide growth is assumed to be activated jumps of metal ions located in defect sites on the metal-oxide interface. The electron field is considered to be strong that the jumps are practically irreversible. The rate-limiting jump rate constant is represented as:

$$k_0 = k_0^o \exp(qb_0\varepsilon / k_B T) = k_0^o \exp(qb_0 V_0 / k_B TL) \quad (1.2)$$

In this regard, k_0^o is the rate constant for the case without field, qb_0V_0 / L is the field-induced decrease of the jump activation energy, q is the ion charge, and b_0 is the distance between the positions of the corresponding potential well and barrier. The growth kinetics is given by:

$$dL / dt = a_0 p k_0^o \exp(qb_0 V_0 / k_B TL) \quad (1.3)$$

where a_0 is the distance between nearest-neighbor metal layers, and p is the fraction of metal atoms located in defect sites of the interface. If we set $u = a_0 k_0^o p$ and $A = qb_0V_0 / k_B T$, Equation 1.3 can be rewritten as:

$$dL / dt = u \exp(A / L) \quad (1.4)$$

Usually, the scales of qb_0V_0 and k_BT are 10^{-1} and 10^{-3}, respectively, and the scale of A is about 5-10 nm, thus for thin oxide films, $A/L > 1$. With this condition, integrating Equation 1.4 yields:

$$(L^2 / A)\exp(-A / L) = ut \quad (1.5)$$

Based on these assumptions, the CM model is applicable for describing the formation of relatively thin oxide films (up to about 5-10 nm). To apply CM theory to describe oxidation of nanoscale supported metal particles, we assuming a spherical geometry with the radius R and

oxide shell of thickness L. It implies that the electric field inside a supported particle has a spherical symmetry, assuming the support is inert and the charge transfer between the support and the particle is negligible. Thus The potential in the oxide (at $R-L \le r \le R$, r is the radial coordinate) is

$$U(r) = \frac{B}{r} + C \tag{1.6}$$

where B and C are constants. Since $V_0=U(R-L)-U(R)$, we get:

$$B = \frac{V_0 R(R-L)}{L} \tag{1.7}$$

The electric field near the metal-oxide interface is accordingly given by:

$$\varepsilon = \frac{B}{(R-L)^2} = \frac{V_0 R}{(R-L)L} \equiv \frac{(E_F - E_0)R}{e(R-L)L} \tag{1.8}$$

Submit Equation 1.8 about ε into Equation 1.2 and 1.3, we can rewrite Equation 1.4 as:

$$dL/dt = u\exp\left(\frac{AR}{(R-L)L}\right) \tag{1.9}$$

There are other expressions of CM model. For instance:[32]

$$f(L) = \frac{1}{2}(L^2 - L_0{}^2) - \frac{1}{3R}(L^3 - L_0{}^3) = \Omega t \tag{1.10}$$

where L_0 is the original thickness and Ω is a constant quantity related to the built-in potential across the oxide and ionic mobility. It should be noted that the oxidation in the CM is insensitive to the morphology of oxide layer because the oxidation rate is controlled by the processes

occurring on the interface. However, the CM model is not applicable if the oxidation is accompanied by the formation of cracks in the oxide film.

Considering the fact that oxygen diffusion in the oxide layer is generally the rate-determining step in metal oxidation, and the volume of the oxidation product is usually larger than volume of the metal, Valensi-Carter model is also utilized to describe oxidation kinetics.[33,34] For a spherical particle, the rate of thickening of the oxidation product was assumed inversely proportional to its thickness:

$$dL/dt = k/L \tag{1.11}$$

where k is constant. Integration of Equation 1.11 gave:

$$L^2 = 2kt \tag{1.12}$$

The volume of unreacted material at time t was given as:

$$V = \frac{4}{3}\pi(R-L)^3 = \frac{4}{3}\pi R^3(1-x) \tag{1.13}$$

where x is the fraction of the original sphere which has reacted, or so-called reacted ratio. Thus,

$$L = R[1-(1-x)^{\frac{1}{3}}] \tag{1.14}$$

Substituting Equation 1.14 into 1.12, we obtained

$$[1-(1-x)^{1/3}]^2 = 2kt/R^2 = Kt \tag{1.15}$$

The above analysis needs to be adjusted because of two reasons: First, Equation 1.11 is for the reaction of a plane surface. But the rate of thickening of a spherical shell of the reaction product must depend upon the ratio of the areas of the outer to inner surfaces. Secondly, Equation 1.13 is accurate only when the volume of sphere particle doesn't change after oxidation, but the reality is oxide usually has larger volume than original metal volume. Considering above two reasons, Equation 1.15 can be adjusted to:

$$[1+(z-1)x]^{2/3}+(z-1)(1-x)^{2/3}=z+2(1-z)kt/R_0{}^2 \tag{1.16}$$

Or can be rewritten as:

$$f(x)=[\{1+(z-1)x\}^{2/3}+(z-1)(1-x)^{2/3}-z]/(1-z)=Kt \tag{1.17}$$

where K is a kinetic constant, and z is the volume of oxidation product formed per unit volume of reactant consumed.

1.2 Plasmonic Modeling for Noble Metal Nanoparticles and Core/Shell Heterostructure

1.2.1 Plasmonic background

Surface plasmon resonance (SPR) or dipole plasmon resonance is the collective oscillation of valence electrons in a solid stimulated by incident light (as shown in Figure 1.1). When the frequency of incident light photons matches the natural frequency of surface electrons oscillating against the restoring force of positive nuclei, the resonance condition is established. [35] SPR in nanostructures is known as localized surface plasmon resonance (LSPR), which greatly influence the optical properties of metallic nanostructures.[36] The shape, size and composition of the nanostructure, as well as the optical properties of the surrounding dielectric, are parameters that greatly influence the spectral location of the LSPR. A very interesting phenomenon is that the

induced electromagnetic field associated with the LSPR is greatly enhanced at the metal/dielectric interface, this is the basis for various types of surface enhanced spectroscopy, such as surface enhanced Raman scattering (SERS). Depending on the geometry and size of nanostructure, the near field intensities will be enhanced to different degrees, while the extinction bands will be shifted to different wavelengths.

The scattering and absorption of spherical particles of arbitrary size, or infinite cylinders can be solved by Maxwell's equations.[37] For complicated geometries of nanostructures, approximations need to be made in order to obtain an accurate result. The discrete dipole approximation (DDA) is one such method.

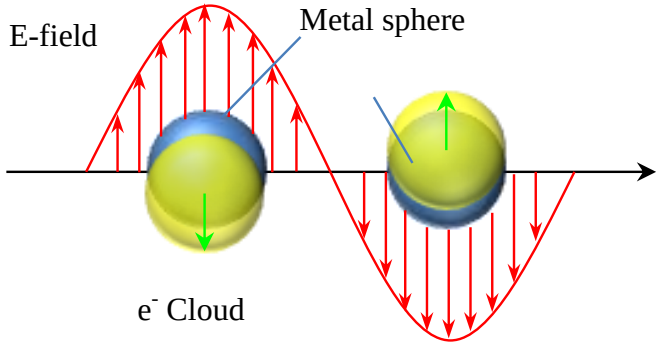

Figure 1.1 Schematic of plasmon oscillation for a sphere, showing the displacement of the conduction electron charge cloud relative to the nuclei.

1.2.2 Discrete dipole approximation and visualization of near field

DDSCAT is an open source software package developed by Draine and Flatau.[38] It is capable of calculating absorption and scattering properties of target through the discrete dipole approximation method. The approach to model a particle's plasmonic resonance is to divide this particle into a finite array of polarizable points (dipoles), calculate scattering and absorbance properties of these separated dipoles, and the interactions between them. The accuracy of this method is dependent on the number of dipoles that represents the target object, which is only limited by the computational power available. Two main criteria the validity of the DDA have to meet:

1. The equation $|m|kd \leq 1$ (where m is the complex refractive index, k is a function of the incident wavelength, and d is the dipole spacing) must be satisfied, which means the lattice spacing d is small enough compared to the wavelength of the incident light striking the target.
2. The target object is accurately depicted, so either d must be small enough or dipole number N is large enough.

An important step of DDA is the calculation of effective radius. If we set V be the actual volume of the target, which is represented by an array of N dipoles, located on a cubic lattice with lattice spacing d, then we get:

$$V = Nd^3 \tag{1.18}$$

Thus the size of the target, so-called the effective radius is given by:

$$a_{eff} \equiv (3V / 4\pi)^{1/3} \tag{1.19}$$

When building irregular geometries or geometries which are consist of multiple shapes or components, it becomes difficult to construct the target and calculate the effective radius. Since DDSCAT allows us to create custom target geometries and arrays which would be difficult or impossible otherwise, we firstly use open source program “Autodesk 3ds Max” to build 3-dimensional target, then convert it into “shape.dat” file through open source programs “MeshLab” and “point-inside-polyhedron”. DDSCAT can identify “shape.dat” file and calculate scattering and absorbance accordingly. Also, the effective radius can be obtained according through the approach we built the target. It should also be noted that, DDSCAT sets the incident light direction is through x-axis, so we can manipulate the orientation of target to simulate the cases when incident light hit the nanostructure from different angles.

It is necessary to check if geometries we built are representing our targets before we process the DDSCAT calculation. Another open source program called “LiteBil” is very useful to visualize our “shape.dat” file to see if it is correct. LiteBil is a software program developed by the Laboratory of Paper Coating and Converting at the Abo Akademi University and is specifically made to be compatible with the DDSCAT package. It can create a three dimensional representation of the shape which can be manipulated in space using the mouse.

To predict the SERS effect of nanostructure, DDSCAT package is capable to calculate the near field of our nanomaterials. And the visualization of near field enhancement can be achieved through an open source program “Python(x,y)”. It is a scientific and engineering development software for numerical computations, data analysis and data visualization based on Python programming language, Qt graphical user interfaces and Spyder interactive development

environment. The three dimensional visualization image obtained from Python(x,y) can be dragged by mouth, in that way the near field enhancement can be presented straightforwardly.

1.3 Nanowires Heterostructures

1.3.1 Synthesis of metal nanowires

The design and fabrication of nanoscale/mesoscale structures have significant impacts on technologies such as chemical sensing and drug delivery.[39-41] Various approaches of one dimensional (1D) nanostructures fabrication have been reported, including chemical vapor deposition, photolithography, and electrodeposition.[42-45] There is an increasing interest on collective behavior of nanostructures, which related to a large ensemble of nanostructures into integrable functional units. The properties of the system as a whole may be fundamentally altered and more complicated than the properties of the elements in isolation, as it involves unique interactions of a group of nano-elements acting together.[46] Arrays of highly ordered and uniform nanostructures are desirable to achieve maximum collective resonance effects. Producing mass-amount of nanostructure arrays is a challenge to the nano-fabrication technique. Top-down approach like electron beam lithography is difficult to achieve that purpose because of its low throughput due to its long exposure time, small field size, and high cost of equipment. On the other hand, the bottom-up approach that using the membrane with aligned channels as a template for nano-fabrication can be applied to synthesize arrays of nanostructures.

Electrodepositing nanowires using porous membrane as template is an effective method to synthesize highly ordered metallic nanowires.[47,48] Template synthesis through electrochemical deposition is a versatile and particularly simple approach. Nanowire arrays can be obtained by filling the porous template that contains a large number of uniform, straight cylindrical holes

with controllable narrow size distribution. This electrochemical approach is also capable to make specific individual segments along the length of the nanowire thus result in so-called "axially heterostructured nanowires",[49] and the combination of different segments nanowires holds promising potential in design of complicated nanostructures with multi-functions.[50-52]

Two types of template are commonly used for nanowires fabrication: polycarbonate (PC) and anodic aluminum oxide (AAO) membranes. The channels inside these membranes are aligned almost parallel to each other, and perpendicular to the surface of the membrane without interconnections between adjacent pores. The pore density of an AAO membrane is about 10^{10}-10^{11} pores/cm^2, whereas for a PC membrane, the pore density is two orders of magnitude lower than that of AAO, about 6×10^8 pores/cm^2.[53] Before electrodeposition, a metallic layer serving as back electrode is evaporated or sputtered onto one side of the membrane. After mounting the membrane into electrodeposition cell, nanowires can be filled using a conventional potentiostat method. After the deposition was done, the PC membrane can be dissolved in 40 ^{o}C dichloromethane (Cl_2CH_2), rinsed in fresh dichloromethane, chloroform, and ethanol,[54] whereas AAO membrane can be dissolved in sodium hydride (NaCl) or potassium hydride (KCl).

1.3.2 Synthesis and applications of nanowire heterostructures

Nanoparticles are usually attached with wires to obtain higher loading amount in practical applications. More importantly, wires can be arranged into two-, or three-dimensional structures as building blocks for nanodevices. Nanowires heterostructure can be classified according to the morphology of different components decorating on the nanowire bone. Hybrid nanowires with axial direction, radial direction multi-segments, branched heterostructures, nanowires decorated

with nanoparticles, and core-shell nanowires have been synthesized, with examples shown in Figure 1.2.[49]

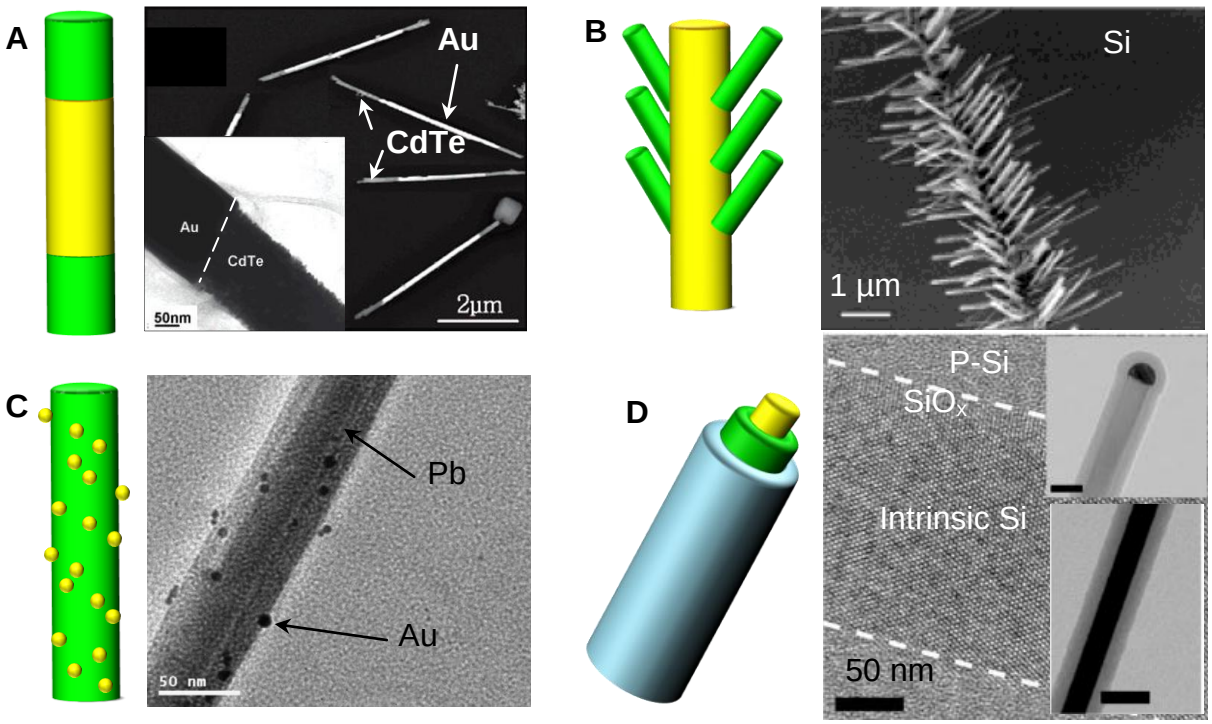

Figure 1.2 Schematic and examples of nanowire-based heterostructures showing (A) Axial-multisegment CdTe-Au-CdTe nanowire sensors for the detection of DNA molecules {Reprinted with permission from (Multisegment nanowire sensors for the detection of DNA molecules). Copyright (2008) American Chemical Society}; (B) Branched silicon nanowires {Reprinted with permission from (Rational Growth of Branched and Hyperbranched Nanowire Structures). Copyright (2004) American Chemical Society}; (C) Au nanoparticles decorated on Pb nanowires {Reprinted from Elsevier, 25, Wang, H.; Wang, X.; Zhang, X.; Qin, X.; Zhao, Z.; Miao, Z.; Huang, N.; Chen, Q., A Novel Glucose Biosensor Based on the Immobilization of Glucose Oxidase onto Gold Nanoparticles-Modified Pb Nanowires. 142-146., Copyright (2009)}; (D) Intrinsic silicon core/SiO_x/p-type silicon shell nanowire, the oxide layer is too thin (<1nm) to be distinguished in the TEM image {Reprinted by permission from Macmillan Publishers Ltd: Nature (Lauhon, L. J.; Gudiksen, M. S.; Wang, C. L.; Lieber, C. M., Epitaxial Core-Shell and Core-Multishell Nanowire Heterostructures. *Nature* **2002,** *420*, 57-61.), copyright (2002)}

For axial heterostructures, multisegment nanowires comprise several different material compositions or phases along the length. Figure 1.2A shows electrochemical deposited nanowires with CdTe-Au-CdTe multisegment in axial direction.[55] After deposition, the gold segment was functionalized with thiol group (-SH) and utilized for binding single strand DNA (ssDNA) fragments. CdTe segments at both ends served to modulate the equilibrium Fermi level of this heterojunction device. Such multisegment nanowires could lead to the fabrication of sophisticated and specific nanosensors by selective functionalization of individual segments.

Figure 1.2B presents branched silicon nanowires.[56] The branched structure was achieved through a multistep nanocluster-catalyzed vapor-liquid-solid (VLS), and the branch diameter and density were controlled by the diameter and density of gold nanocluster. Branched nanowires provide another approach for increasing structural complexity and enabling more functional surface areas.[57] Nanowires can also be utilized as structural material decorated with other composite nanoparticles forming heterostructures.

Figure 1.2C shows gold nanoparticles decorated on lead (Pb) nanowires as glucose sensors.[58] Pb nanowires were fabricated by an L-cyteine-assisted self-assembly route and functioned with thiol group, gold nanoparticles were incorporated onto the nanowire surface through SH-Au bond. The result nanocomposite exhibited an excellent electrocatalytic activity and high sensitivity (135.5 $\mu A\ mM^{-1}\ cm^{-2}$) of glucose with long-term stability. Core-shell nanowires formed by the growth of crystalline overlayers on nanocrystals can enhance emission efficiency.[59]

Figure 1.2D exhibits intrinsic silicon /SiO_x/amorphous p-type silicon multi-shell nanowires.[60] To achieve this core/multi-shell heterostructure, single-crystal intrinsic silicon core-wires were first prepared by gold nanocluster directed axial growth from chemical vapor deposition (CVD),

using silane as the silicon source. The oxide layer was grown at 450 ^{o}C using oxygen and silane. Silicon shells (p-type) were then deposited using silane and 100 ppm diborane helium where the shell thickness was directly proportional to the growth time. The resistivity of these multi-shell nanowires is dominated by the amorphous p-type silicon shell.

1.4 Graphene Encapsulated Nanowire Heterostructure

Graphene is a carbon material consisting of planar monolayer of hexagonal sp^2 hybridized carbons.[61] It attracts tremendous research interests in recent years due to its unique properties such as mechanical flexibility[62] and thermal/chemical stability,[63,64] which make itself an ideal two-dimensional reinforcing component for hybrids or composite materials that possessing an extremely large surface area. Since graphene was unexpected separated from natural graphite by micromechanical drawing,[65] various synthetic methods have been developed for the mass-production of highly functional graphene such as chemical etching,[66] graphene oxide reducing,[67] and CVD growth.[68] Among those methods, oxidative exfoliation of naturally abundant graphite and subsequent reduction offers a highly efficient route to producing chemically functionalized graphene, whereas CVD growth can provide more compact heterostructures between graphene and other components.

Graphene can be wrapped on self-assembled biomolecules to form graphene encapsulated nanowire heterostructure. Han et al. demonstrated a straightforward hybrid assembly of diphenylalanine/graphene core/shell nanowires by single-step solution processing.[69] Diphenylalanine is known as the structural motif for the β-amyloid associated with Alzheimer's disease;[70] it is capable to self-assemble into highly stable nanoscale morphologies such as nanotubes, [70] nanowires,[71] and nanoribbons.[72] They first prepared an aqueous graphene oxide

dispersion following a modified Hummers method, which followed by chemical reduction with hydrazine and formed aqueous dispersion of reduced graphene. The peptide/graphene core/shell nanowires were created immediately, as soon as an organic peptide solution (100 mg/mL diphenylalanine in 1,1,1,3,3,3-hexafluoro-2-propanol (HFP) solution) was diluted in that aqueous graphene dispersion under mild mechanical shaking.[69] They found that the intermolecular interaction governing that marvelous core/shell assembly was varied by the pH of the assembling solution. The core/shell hybrid assembly only occurred in the suitable pH range in (3.7~5.4), and the thickness of graphene shell was tunable with pH variation. Han and co-workers tested the electrical conductivity of an individual core/shell nanowire by I-V measurements, and generated a hollow network of graphene shells by thermal calcinations (400 ^{o}C for 20 min) of peptide cores of highly entangled core/shell nanowires. This graphene shells network could be employed as a supercapacitor electrode with remarkable performance.

Besides self-assembled biomolecules, metal nanowires can also be encapsulated in carbon shells. Synthesis strategies of metal/carbon core/shell nanowire heterostructure can be classified into following ones: Filling CNT core with metal by electrochemical reactions or thermal diffusion;[73,74] surface coating of metal nanowires with carbon shells by hydrothermal synthesis;[75,76] and fabricating metal/carbon core/shell heterostructure through chemical vapor deposition applying metal and carbon sources.[77-79]

In case of filling CNT core with metal through electrochemical reaction, CNTs were prepared firstly and acted as templates for nanowire formation. Copper ions can diffuse into the CNT pores and onto the outer surfaces, and then turn into metallic copper at high temperature in the

presence of the carbon nanomaterials, result in the coverage of copper in parts of the pores and the surfaces of CNT.[73]

Filling CNT core through thermal diffusion is achieved by heating high quality purified CNTs and metal powder under high vacuum and inert environment, thus metals of low sublimation temperatures can vaporize to form thin nanowires within the core of CNTs through capillary action.[74] These nanowires can be completely protected from oxidation and structural decomposition by surrounding walls of CNTs.

The core/shell nanowires formed through hydrothermal reduction/carbonization in the presence of surfactant acting as the structure-directing agent by hydrothermal treatment.[76] In this approach, morphology of metal nanowires can be maintained, but the obtained carbon nanostructures are usually disordered. The chemical vapor deposition approach, on the one hand, can use bottom-up process to grow core/shell heterostructures.[77,78] On the other hand, metal nanowires can act as template for carbon precursor through chemical vapor deposition process.[79] It should be noted that, the product of core/shell nanowire heterostructures synthesized by chemical vapor deposition usually undergoes a significant morphological change (difficult to maintain ordered morphology) due to nanowires' Rayleigh instability under graphene growth conditions.

1.5 Nanowires-CNT Heterostructure Synthesis and Applications

Aligned CNTs can be produced by chemical vapor deposition, in which the outer diameter of CNTs is determined by the diameter of the catalyst particle.[80 81] The arrays of aligned CNTs with uniform diameters and periodic arrangements are generally fabricated using AAO template by chemical vapor deposition.[82] In this case, not only the diameter of CNTs can be controlled, but

also the site density (number of CNTs per unit area) is tunable depending on the density of AAO channels.

Nanowire-CNT heterostructures attract great research attention because of their unique properties. For instance, one dimensional metal/CNT heterojunctions with Ohmic or Schottky current-voltage (I-V) characteristic are building blocks in nanoelectronics, since planar metal/semiconductor heterojunctions are building blocks in microelectronics.[83]

Luo et al. synthesized ordered vertical arrays of Ni/multiwalled CNT (MWCNT)/amorphous CNT (a-CNT) heterojunctions, which consist of a nickel nanowire, a MWCNT, and an a-CNT connected end to end, where the MWCNT is semiconducting and two Schottky contacts exist at the two ends of the MWCNT, respectively.[84] They measured and analyzed the I-V characteristics of the heterojunctions embedded in the arrays by a conductive AFM. It was found that although the long a-CNT segments would bury some electrical signals of the Schottky contacts in heterojunctions, the Schottky contacts in the other heterojunctions played a central role and made the corresponding heterojunctions possess rectifying I-V characteristics.

Carbon nanotubes have also been used as electrodes for supercapacitors because of their excellent electrical properties and high surface areas.[85,86] However, CNT based supercapacitors have their own problems.[87] One of the major issues is the high contact resistance between the electrode and the current collector which limits their performance.[86] The high contact resistance could be lowered by growing CNTs directly on to a conductive substrate, which act as current collector. Ajayan and co-workers fabricated ultra-high power supercapacitors by using multi-segmented CNT/Au nanowire hybrid structures as electrode, where both the CNT electrode and

current collector gold nanowires are integrated into a single nanostructured wire thus resulting in excellent performance of the supercapacitors.[88]

The combination of nanowire and CNT provides broader capabilities and wider functionalities. Ajayan et al. demonstrated that appropriately designed hybrid nanowire/CNT heterostructure can be used to generate structures that can respond to their environment and be manipulated through various external stimuli.[89] Their approach is based on the manipulate composition of hybrid nanowires consisting of multiple segments with hydrophobic carbon nanotubes on one end and hydrophilic metal nanowires on the other. Thus, with the change of hydrophiy of outer environment, the nanowire/CNT hybrid can exhibit different self-assemble behavior. It should be noted that these kind of materials are toxic if been directly implanted into human body, so it is necessary to consider to encapsulate these hybrid materials into bio-friendly materials, for example hydrogels, which is discussed in next section.

1.6 Hydrogel and Nanowires/Nanotubes-Hydrogel Heterostructure

1.6.1 Hydrogel synthesis and properties

Hydrogels are hydrophilic polymers in their crosslinked forms, which can absorb a large amount of water but meanwhile not dissolving due to their network of polymer chains.[90] Hydrogels have demonstrated great potential for biological and medical applications because of their high water content and biocompatibility. Natural hydrogel can be derived from polymers such as collagen, hyaluronic acid (HA), fibrin, alginate, agarose, and chitosan. Collagen, hyaluronic acid, and fibrin can be obtained from various components of the mammalian extracellular matrix. Alternatively, alginate and agarose are derived from marine algae sources, while chitosan is derived from chitin.

Hydrogels can also be fabricated through various chemical methods. Synthesized hydrogels are more appealing to researchers because their networks can be designed and synthesized with molecular-scale control over structure, for instance, crosslinking density, thus obtain tailored properties such as biodegradation, mechanical strength, chemical and biological response to stimuli. Some widely studied neutral synthetic hydrogels can be generated from derivatives of poly(ethylene glycol) (PEG), poly(hydroxyethyl methacrylate) (PHEMA), and poly(vinyl alcohol) (PVA).

PEG hydrogels are nontoxic, non-immunogenic, and widely used for biomedical applications. They can be synthesized by varied methods to covalently crosslink PEG polymers. Among which, photo-polymerization using acrylate-terminated PEG monomers is a particularly appealing approach of crosslinking PEG chains. PEG is inert to most biological molecules such as proteins, so normal PEG hydrogels are passive constituents of the cell environment. However, PEG hydrogels can be modified through numerous methods to make them into versatile templates for many subsequent conjugations. For instance, peptide sequences can be incorporated into PEG hydrogels; or PEG polymers can be chemically modified by formation of copolymers with other materials to induce degradation or modify cell adhesion.

PHEMA hydrogel is well known as a material of making contact lenses and drug delivery. PHEMA has attractive properties include its optical transparency, stability in water, and its mechanical properties. It also can be modified through peptide functionalization and copolymerization to achieve desired properties.

PVA hydrogels are stable, elastic gels that can be formed by both physical and chemical crosslinking methods. Physical method like repeated freezing and thawing process is commonly

used. The physically crosslinked PVA hydrogels are biodegradable and can be used for biomedical applications. Also, PVA can be crosslinked through the use of difunctional crosslinking agents such as glutaraldehyde, acetaldehyde, and formaldehyde. For chemically linked PVA hydrogels, if they are used as biomedical materials, it is critical to remove residual crosslinking agent from the hydrogel, as the release of toxic residue in the body would have undesirable effects. Other methods of chemical crosslinking include utilizing of electron beam or gamma irradiation which would not leave behind toxic agents.

Environmentally responsive hydrogels attract special attention from researchers due to their capability of sensing and responding to changes to external stimulation such as pH, pI, temperature, and specific analytes. These environmental responses are attributed to chemical structure of the polymer network. For pH sensitive hydrogels, their polymer networks contain weakly acidic or basic pendent groups (e.g. -COOH), which can be ionized during water sorption, depending on the solution pH and ionic composition. Common ionic polymers include poly(acrylic acid) (PAA), poly(methacrylic acid) (PMMA), and polyacrylamide (PAAm). These hydrogels can act as semi-permeable membranes for the counter-ions, thereby interact with the external solution through ion exchange, and influence the osmotic balance between them. For example, the equilibrium degree of swelling for ionic hydrogels containing weakly acidic pendent groups increases as increase the pH of the external solution.

Another most widely studied responsive hydrogel systems are temperature-responsive hydrogels. For these hydrogels, reversible volume-phase transition takes place with a change in the temperature of the environmental conditions. Poly(N-isopropylacrylamide) (PNIPAAm) and its derivatives are typical temperature sensitive hydrogels. Their behavior is related to polymer

phase separation as the temperature is raised to a critical value so called lower critical solution temperature (LCST). Above the LCST, polymers tend to shrink or collapse, while hydrogels swell upon lowering the temperature below the LCST. Thermo-sensitive hydrogels are applied in drug delivery and tissue engineering.

1.6.2 Hydrogel encapsulated nanowire/nanotube heterostructures

Devices at nanoscale are promising in the domain of biological engineering. However, their applications are restricted by the requirement of bio-compatibility.[91] Combination of nanomaterials with non/low-toxic polymer is one of approaches to solve this problem. Hydrogel has long chain hydrophilic polymer networks which have the ability to contain a large amount of water. Moreover, its swelling/shrinking process can be sensitive to different stimulations such as temperature, water, change of pH or ion strength. This makes hydrogel into a material which responds to different conditions.[92]

Figure 1.3A shows a temperature sensitive drug releasing system of gold nanorods encapsulated in near-infrared (NIR) light responsive polymer, whose glass transition temperature (T_g) is in the range of body temperature.[93] At normal body temperature ($T<T_g$), the structure is glassy and release is limited, whereas when $T>T_g$, the polymer is rubbery and release is enhanced. The author applied this heating system to trigger release of the chemotherapeutic drug doxorubicin in vitro, multiple cycles of NIR exposure were performed and demonstrated a triggered and stepwise release behavior. As shown in Figure 1.3B, supramolecular single-walled carbon nanotubes (SWNTs) hydrogel was fabricated by π-π interaction between pyrene modified β-cyclodextrin (Py-β-CD) and SWNTs. [94] Due to the high solubility of CD in water, the supramolecular SWNTs hydrogel is water-soluble, which solves the problem of solubilization of

SWNTs. Moreover, cyclodextrin can form host-guest complexes with various kinds of guest molecules which enable to capture guest compounds on the surface of SWNT.[95] Overall, the incorporation of nanomaterials in hydrogel holds great potential for the fabrication of multifunctional, bio-compatible nanodevices in the fields of tissue engineering and medicine.

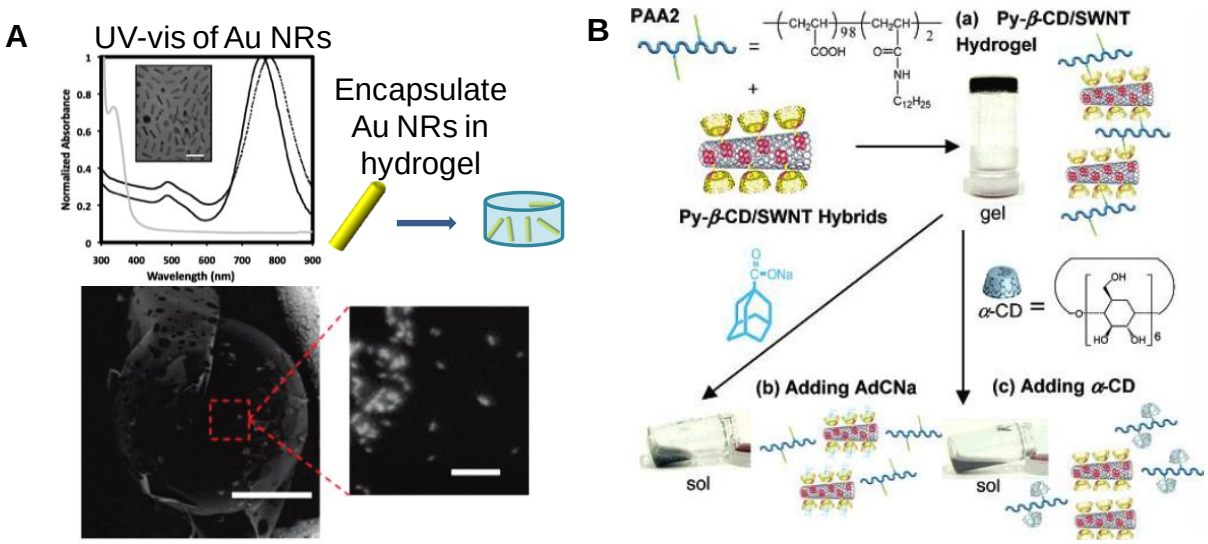

Figure 1.3 Schematics of nanomaterials-hydrogel hybrids showing (A) Gold nanorods-hydrogel for temperature sensitive drug releasing {Reprinted with permission from (Hribar, K. C.; Lee, M. H.; Lee, D.; Burdick, J. A., Enhanced Release of Small Molecules from Near-Infrared Light Responsive Polymer-Nanorod Composites. *Acs Nano* **2011,** *5*, 2948-2956.), Copyright (2011) American Chemical Society}; (B) Functionalized single wall carbon nanotube-hydrogel for gel to sol transition {Reprinted with permission from (Ogoshi, T.; Takashima, Y.; Yamaguchi, H.; Harada, A., Chemically-Responsive Sol-Gel Transition of Supramolecular Single-Walled Carbon Nanotubes (SWNTs) Hydrogel Made by Hybrids of SWNTs and Cyclodextrins. *Journal of the American Chemical Society* **2007,** *129*, 4878-4879.). Copyright (2007) American Chemical Society}

1.6.3 Hydrogel modeling

The network structure of hydrogels determines their performance in a particular application. The most important parameters for structure characterization include the polymer volume fraction in a swollen state ($v_{2,s}$), the molecular weight of the polymer chain between two neighboring crosslinking points ($\overline{M_C}$), and the corresponding mesh size (ξ).[96]

The polymer volume fraction describes the amount of fluid imbibed and retained (either chemically or physically) with the hydrogel. Generally, there are three kinds of water in hydrogels which are referred to as: nonfreezing water (or bound water), intermediate water (or secondary bound water), and free water. Nonfreezing water molecules are bound to polymer molecules through hydrogen bonds and are immobilized; intermediate water interact with polymer molecules; free water has greatest degree of mobility in comparison with above two kinds of water molecules. The fraction of free water can be estimated approximately through differential scanning calorimetry (DSC) by the ratio of the endothermic peak during the melting of frozen water.

There are two kinds of polymer volume fraction: $v_{2,r}$ and $v_{2,s}$. $v_{2,r}$ is the polymer volume fraction in the relaxed state, which is defined as the state of the polymer immediately after crosslinking but before swelling, meanwhile $v_{2,s}$ is in swelling state. Ruiz et al. demonstrated the measurement of polymer volume fraction by the gravimetric method. [97] They made hydrogel samples and weighed them in both air and n-heptane. The first measurement was done immediately after hydrogel finished crosslinking (relaxed state). Then hydrogel samples were placed in deionized water. Once they had swelled to equilibrium they were weighed in air and n-

heptane again (swollen state). Finally, hydrogel samples were dried at room temperature and re-weighed in air and n-heptane (dried state).

Flory-Rehner theory can be used to analyze the structure of neutral hydrogels. It states that a crosslinked hydrogel that reaches equilibrium with its surroundings is subject only to two opposing forces: the thermodynamic force of mixing and the retractive force of the polymer chains. The Gibbs free energy of polymer can be defined as:

$$\Delta G_{total} = \Delta G_{mixing} + \Delta G_{elastic} \tag{1.20}$$

where ΔG_{mixing} is the result of the spontaneous mixing of the fluid molecules with the polymer chains, and $\Delta G_{elastic}$ is the contribution due to the elastic retractive forces build within the gel. ΔG_{mixing} is a measure of the compatibility of hydrogel with surrounding fluid. The compatibility is usually expressed by the polymer-solvent interaction parameter χ_1. If we keep temperature and pressure constant, the differentiation of Equation 1.20 results in express of chemical potential (μ):

$$\mu_1 - \mu_{1,0} = \Delta\mu_{mixing} + \Delta\mu_{elastic} \tag{1.21}$$

Here, μ_1 is the chemical potential of the solvent in hydrogel, and $\mu_{1,0}$ is the chemical potential of the pure solvent. At equilibrium, $\mu_1 = \mu_{1,0}$, which means changes in chemical potential due to mixing and elastic forces must balance each other.

The change of chemical potential due to the elastic retractive forces of the polymer chains can be determined from the theory of rubber elasticity. Peppas et al. modified the original Flory-Rehner

theory for hydrogels prepared in the presence of water. The molecular weight between crosslinks in a neutral hydrogel prepared in the presence of water is determined by:

$$\frac{1}{\overline{M_C}} = \frac{2}{\overline{M_n}} - \frac{(\frac{\bar{v}}{V_1})[\ln(1-v_{2,s}) + v_{2,s} + \chi_1 v_{2,s}^2]}{v_{2,r}[(\frac{v_{2,s}}{v_{2,r}})^{1/3} - (\frac{v_{2,s}}{2v_{2,r}})]} \tag{1.22}$$

where $\overline{M_C}$ is molecular weight between two adjacent crosslinks, $\overline{M_n}$ is the molecular weight of the polymer chains prepared under identical conditions but in the absence of the crosslinking agent, $\bar{v}$ is the specific volume of the polymer, V_1 is the molar volume of water, χ_1 is the polymer-solvent interaction parameter.

The space available between macromolecular chains, which is often regarded as the molecular mesh or pore is another important structural parameter for analyzing hydrogels. Correlation length (ξ) is used to describe the size of the pores, which is defined as the linear distance between two adjacent crosslinks:

$$\xi = a(\bar{r}_o^{\,2})^{1/2} \tag{1.23}$$

where *a* is the elongation ratio of the polymer chains in any direction, and $(\bar{r}_o^{\,2})^{1/2}$ is the root-mean-square, unperturbed, end-to-end distance of the polymer chains between two neighboring crosslinks. For an isotropically swollen hydrogel, the elongation ratio (*a*) can be described as:

$$a = v_{2,s}^{\;-1/3} \tag{1.24}$$

And the unperturbed end-to-end distance for the polymer chain between two adjacent crosslinks can be calculated by:

$$(\bar{r}_o^{\,2})^{1/2} = l(C_n N)^{1/2} \tag{1.25}$$

$$N = \frac{2\overline{M_C}}{M_r} \tag{1.26}$$

where l is the length of the bond along the polymer backbone, C_n is the Flory characteristic ratio, N is the number of links per chain, and M_r is the molecular weight of the repeating units of which the polymer chain is composed. Combining Equation 1.23 to 1.26, the correlation distance (ξ) can be calculated as:

$$\xi = v_{2,s}^{\;-1/3}\left(\frac{2C_n\overline{M_C}}{M_r}\right)^{1/2} l \tag{1.27}$$

The adjustment of the structure of hydrogels (e.g., $v_{2,s}$, $\overline{M_C}$, and ξ) enables the tailoring of hydrogels' mechanical, responsive, and diffusive properties. In addition, the properties of hydrogels can greatly modified by the type of crosslinking, which depends on various factors such as covalent bonding, entanglements, hydrogen bonding, ionic bonding, and formation of crystallites.

1.7 Problem Statement and Research Objectives

The design of multifunctional device demands materials with advanced properties, high performance, and good stability.[98] These requirements are difficult to be achieved by single component materials, but can be solved by combining different nanomaterials to utilize the

functions of each component.[99-101] Such heterostructures could be core-shell nanoparticles, alloyed nanoparticles, multisegment nanowires, or nanoparticles-nanowires hybrids.[102-105] The major challenges are the selection of materials, the design of architecture, the incomplete understanding of interaction between different components in a hybrid, and the productivity of high performance nanostructures. In this dissertation, fundamental study of nanoparticle-graphene structure and nanowires heterostructures has been performed and characterized to explore the above mentioned issues. The conducted research strongly provides understanding concerning the growth mechanism and properties of constructed heterostructures. The goal of this dissertation is to develop heterostructures combining carbon and metal nanostructures and explore their applications in chemical/biological sensing and catalysing.[93,106-109] The specific aims of this dissertation are:

(1) To fabricate multisegment nanowires-graphene heterostructure for multifunctional chemical sensors and devices with following sub-tasks:

(a) Studying the mechanism of graphene growth on noble metal nanoparticles.

(b) Understanding the migration of nanomaterials at high temperature.

(c) Synthesizing multi-segment nanowires.

(d) Growing graphene shell on nanowires.

(e) Functionalizing graphene structure.

(f) Fabricating chemical sensor by utilizing functionalized multisegment nanowires-graphene heterostructures.

(2) To fabricate nanowire-hydrogel heterostructure for chemical separation:

(a) Growing nanowires.

(b) Synthesizing PVA hydrogel and nanowire-hydrogel hybrid.

(c) Measuring water absorption and structure parameters of nanowire-hydrogel heterostructure.

(d) Studying chemical releasing/separating behavior of nanowire-hydrogel hybrid.

CHAPTER 2: OXIDATION OF GOLD NANOPARTICLES, EFFECTS OF QUENCHING-INDUCED DEFECTS ON CARBON SHELLS FORMATION

2.1 Introduction

Our group previously observed that surface oxidation of gold nanoparticles (AuNPs) before chemical vapor deposition is a critical step for the fabrication of graphene encapsulated gold nanoparticles. Such plasma oxidized AuNPs inhibit the growth of CNT in a CVD process and rather resulted in graphene shells encapsulating the core AuNPs. However, detailed understanding of the plasma oxidation kinetics of AuNPs, mechanism of the growth of graphene shells, and effect of structural defects in the AuNPs on the graphene shells growth remains unclear. In this chapter, oxidation kinetics of AuNPs was studied. The surface oxidized AuNPs were utilized as catalysts for the growth of graphene shells encapsulated AuNPs (GNPs) in a xylene CVD process. On the other hand, surface oxidized AuNPs with lattice defects were also used as catalysts in a similar xylene CVD process to provide insight into effect of defects on formation of carbon shells.

2.2 Experiment Methods

2.2.1 Materials and Methods.

Gold (III) chloride trihydrate ($HAuCl_4 \cdot 3H_2O$, 99.9%) was purchased from Sigma-Aldrich (St. Louis, MO). Hexadecyltrimethylammonium bromide (CTAB, $C_{19}H_{42}BrN$, 99%), sodium borohydride ($NaBH_4$, powder, 98%), and nitric acid (HNO_3, 69.5%) were bought from Acros Organics. Acetone [$(CH_3)_2CO$] was purchased from VWR International (West Chester, PA). Xylene (o-, m-, p-isomers) and hydrochloric acid (HCl, 37%) were purchased from Fisher

Scientific. All chemicals were used without further purification. A Labnet centrifuge (Edison, NJ) was used to clean, wash, and separate nanoparticles. Wet samples were dried in a VWR vacuum oven (West Chester, PA). Silicon (Si) wafers (100, n-type) were purchased from IWS (Colfax, CA). DI water (18.1 MΩ cm) was obtained using a Barnstead International DI water system (E-pure D4641). Oxygen plasma treatment was performed in a Nordson March Jupiter III Reactive Ion Etcher (Concord, CA). Quenching of solutions was performed in a recirculating bath (model 1162A) purchased from VWR North American (West Chester, PA). Graphene growth processes were conducted inside a Lindberg blue three-zone tube furnace (Watertown, WI). Quartz tube was purchased from ChemGlass (Vineland, NJ). A syringe injector was obtained from Fisher Scientific (Suwanee, GA). Gas flow rates of all chemical vapor deposition processes were controlled by Teledyne Hasting powerpod 400 mass flow controllers (Hampton, VA). Thermocouples and temperature controllers were bought from Omega Engineering (Stamford, CT). H2 (UHP grade, 40% balanced with Ar) and Ar (UHP grade) gas cylinders were purchased from Airgas South (Tuscaloosa, AL).

2.2.2 Synthesis of Gold Nanoparticles.

AuNPs were synthesized in a single-step approach. $HAuCl_4$ (5×10^{-3} or 5×10^{-5} M) water solution was mixed with CTAB (0.03 M). Subsequently, 10 μL of $NaBH_4$ (0.12 M) was added into the above solution and magnetically stirred for 2 h at room temperature or at ~130 °C. On the other hand, to evaluate the effects of quenching on the AuNPs, a similar growth approach was selected, except that the reaction was performed at ~130 °C. After high temperature synthesis (at 130 °C), AuNPs were quenched immediately in a recirculating bath for 1 h at 10, 0, and −20 °C. Table 2.1 shows the growth conditions and result summary. It must be noted that

AuNPs synthesized at room temperature utilized a higher concentration of metal salt (~5×10^{-3} M) as compared to those synthesized at 130 °C or quenched (~5×10^{-5} M).

Table 2.1 Growth conditions and result summary of AuNPs

Sample	Temperature (°C)	Quench Temperature (°C)	Average size (nm)	Shape distribution	Lattice spacing (nm) and corresponding plane
1	25	Not Quenched	67.4±13.2	Hexagon: 1.4% Rhombus: 10.4% Square: 8.1% Triangle: 2.5% Circular: 77.6%	0.20 (200) 0.23 (111) 0.27 (110)
2	130	Not Quenched (Air cooled)	13.9±3.9	Triangle: 10% Square: 9.2% Circular: 80.8%	0.21 (200) 0.23 (111)
3	130	10	28.7±7.8	Triangle: 11.5% Square: 5.1% Rod: 2.6% Circular: 80.8%	0.23 (111)
4	130	0	27.6±7.8	Triangle: 6.3% Square: 3.6% Rod: 2.7% Circular: 87.4%	0.21 (200) 0.24 (111)
5	130	-20	14.5±3.4	Circular: 100%	0.21 (200) 0.23 (111)

2.2.3 Dispersion and Plasma Oxidation of Gold Nanoparticles.

As-synthesized AuNPs were oxidized by a plasma treatment process. At first, Si substrate was soaked in the mixture of H_2SO_4 and H_2O_2 (v/v 5:1) at 100 °C for 30 min. Subsequently, the wafer was rinsed with copious amounts of DI water and dried in air. As a next step, AuNPs were dispersed on cleaned silicon substrate by the drop-casting method. The substrate was then dried in a desiccator, placed in a plasma oxidation chamber, and oxidized at 160 W and 600 mTorr chamber pressure, with flowing O_2. To study the effect of plasma oxidation of room temperature-synthesized AuNPs and kinetics, this process was performed for different durations (15−75 min).

2.2.4 Growth of Graphene Shells Encapsulated Gold Nanoparticle.

Graphene shells were grown in a CVD process. After 30 min plasma oxidation, a Si wafer covered with AuNPs was placed in the center of quartz tube equipped with precursor and gas lines for Ar/H_2 flow. Xylene was utilized as the carbon source and was injected through a syringe injector into a preheated zone (~220 °C) at the rate of 45 mL/h for ~2 min and subsequently transported into the reaction zone (~675 °C) inside the quartz tubes furnace. The xylene flow rate was reduced to 1 mL/h after H_2 mixed with Ar (Ar/H_2 = 1.8 SLM/0.2 SLM or 10% v/v H_2) was introduced in the CVD reactor. Here, H_2 acted as an oxygen scavenger and Ar as a carrier gas or dilutant. The CVD reaction was continued for 1 h after which H_2 and xylene were discontinued, and the furnace was cooled down under Ar flow. AuNPs utilized in the growth of graphene or carbon shells were synthesized according to conditions corresponding to samples 1 and 5 in Table 2.1.

2.2.5 Characterization

Tecnai F-20 was used to collect Transmission Electron Microscopy (TEM) images at 200 kV. TEM samples were prepared by dispersing as-prepared samples on lacey carbon TEM copper grids purchased from Ted Pella Inc. (Redding, CA). The average nanoparticle size was measured from TEM and SEM images, where more than 200 nanoparticles were counted and measured per sample. Diameter was measured for spherical nanoparticles and average side length for triangular ones. For nanoparticles with other shapes, diagonal length average was taken. All the measurements were done using Adobe Photoshop Software. High resolution TEM image for graphene shells encapsulated AuNPs was also converted into FFT image using Digital Micrograph software. X-ray photoelectron spectra (XPS) were gathered by Kratos Axis 165 with mono-Aluminum gun at 160 eV pass energy for full range scan and 40 eV pass energy for detailed scan. Open source program XPSPEAK41 was used for XPS analyzing. The analysis spot was set as "Slot" with >20 μm aperture and 19.05 mm iris setting. Autodesk 3ds Max® was used for drawing illustrations and schematics

2.3 Oxidation Kinetics of Gold Nanoparticles

Detailed theoretical understanding of the oxidation process was done by XPS analyzing, which is used to calculate the accurate thickness of the oxide shell as well as its relationship with the oxide stoichiometry (i.e., x in AuO_x). In order to do these calculations, it is assumed here that the electron emission depth of XPS was 8 nm (less than size of AuNPs),[110] AuNPs were spherical in shape (average diameter ~ 67.4±13.2 nm),[31] charge neutrality was maintained throughout the nanoparticle, and the oxide shell was comprised of a mixture of auric oxide ($AuO_{1.5}$) and aurous oxide ($AuO_{0.5}$). $AuO_{0.5}$ exhibits cuprite structure which has four gold atoms and two oxygen

atoms per cubic unit cell, with lattice constant of 0.48 nm while $AuO_{1.5}$ exhibits orthorhombic unit cell.[111] The density of $AuO_{1.5}$ (MW = $M_{AuO_{1.5}} = 220.97\ g/mol$) is 11.34 g/cm^3.[112] Using all the above information, the density of $AuO_{0.5}$ (MW = $M_{AuO_{0.5}} = 204.97\ g/mol$) is estimated to be ~ 12.31 g/cm^3. Assuming that 1 mol of AuO_x is comprised of *f* mol of $AuO_{0.5}$ and *(1-f)* mol of $AuO_{1.5}$, then $x=1.5-f$

Where $0 \leq f \leq 1$ and $0.5 \leq x \leq 1.5$ (2.1)

Thus, for 1 mol of AuO_x formed, effective molecular weight is given by:

$$M_{(AuO_x)} = f \cdot M_{(AuO_{0.5})} + (1-f) \cdot M_{(AuO_{1.5})} \tag{2.2}$$

Molar volume is given by:

$$V_{mol(AuO_x)} = \frac{f \cdot M_{(AuO_{0.5})}}{\rho_{AuO_{0.5}}} + \frac{(1-f) \cdot M_{(AuO_{1.5})}}{\rho_{AuO_{1.5}}} \tag{2.3}$$

Density is given by:

$$\rho_{(AuO_x)} = \frac{M_{(AuO_x)}}{V_{mol(AuO_x)}} \tag{2.4}$$

Using Equation 2.1 to 2.4, it is possible to derive relationships between *x* and $M_{(AuO_x)}, V_{mol(AuO_x)}, \rho_{(AuO_x)}$. Before oxidation (at *t = 0*), the volume of nanoparticle being detected in XPS is the volume of the spherical cap (V_{cap}) given by:[113]

$$V_{cap} = \frac{\pi}{3} H^2 (3R - H) \tag{2.5}$$

Where R is the radius of AuNPs (~ 33.7 nm) before oxidation (at $t = 0$) and H is the electron emission depth for the sample in XPS (assumed as 8 nm). The fraction of metallic gold remaining in surface oxidized AuNPs as calculated from XPS is F_{Au}, which is also changing with plasma oxidation duration. Thus, at $t = t$, this can be written as:

$$\frac{\frac{\pi}{3}(H-a)^2(3r_1-H+a)}{\frac{\pi}{3}H^2(3r_1+3a-H)} = F_{Au} \tag{2.6}$$

Where r_1 is the radius of remaining metallic core of nanoparticle and a is the thickness of oxide shell, which are functions of oxidation duration (t). The basic chemical reaction governing the conversion of gold into its oxide is: $Au + \frac{x}{2}O_2 \rightarrow AuO_x$ then,

$$n_{(AuO_x)} = n_{(Au)} = \frac{(\frac{4\pi}{3}R^3 - \frac{4\pi}{3}r_1^3)\rho_{Au}}{M_{Au}} \tag{2.7}$$

$$V_{AuO_x} = n_{(AuO_x)}M_{AuO_x} / \rho_{AuO_x} = n_{(AuO_x)} \cdot V_{mol(AuO_x)} \tag{2.8}$$

$$\frac{4\pi}{3}(r_1+a)^3 = \frac{4\pi}{3}(r_1)^3 + V_{AuO_x} \tag{2.9}$$

where n represents the moles of the species, V_{AuO_x} is the volume of oxidized gold, ρ_{Au}, ρ_{AuO_x}, M_{Au} M_{Au}, and M_{AuO_x} are the densities and molar masses of gold and oxidized gold, respectively. Combining Equation 2.6 to 2.9 results in:

$$\frac{\pi}{3}(H-a)^2(3r_1-H+a) = F_{Au} \cdot \frac{\pi}{3}H^2(3r_1+3a-H) \tag{2.10}$$

$$(R^3 - r_1^3) \cdot \frac{\rho_{Au}}{M_{Au}} \cdot V_{mol(AuO_x)} + r_1^3 - (r_1 + a)^3 = 0 \qquad (2.11)$$

Based on above set of equations, the relationship between plasma oxidation time (t), thickness of gold oxide shell (a), and stoichiometric factor (x) for AuO_x can be derived. H, R, M_{Au}, ρ_{Au}, are already known or assumed. It is to be noted that relationship between XPS derived fraction of gold remaining in the nanoparticles (F_{Au}) as a function of oxidation time is shown in the Figure 2.1B and is based on curve fitting of the data points shown. Thus, at a specific oxidation duration and composition of gold oxide ($15 \text{ min} \le t \le 75 \text{ min}$ and $0.5 \le x \le 1.5$), it was possible to estimate thickness of the oxide shell (Figure 2.1C). The calculated oxide shell thicknesses for two different stoichiometries of AuO_x (x= 1.5 and 0.5) were negligibly different, which further implies that oxide shell thickness (AuO_x) was independent of stoichiometric factor 'x'. However, the presence of mixed oxides in our process cannot be ruled out and it is difficult to estimate the actual composition of the gold oxide in our study. In addition, the oxidation kinetics of the nanoparticles was fitted with Cabrera-Mott (CM) kinetics as proposed earlier for other particles.[31,114] The kinetics of oxide film/shell formation is controlled by diffusion of ions and electrons, which further depended on their concentration gradients and self-generated electric potential.[32] In case of thin oxide shell, the electric field is dominating, and the kinetics of oxide growth under this field is described by CM model.[32] It was reported previously that in case of spherical particles, the relationship between oxide shell thickness (a) and time (t) satisfy the following function:[32]

$$f(a) = \frac{1}{2}(a^2 - a_0^2) - \frac{1}{3R}(a^3 - a_0^3) = \Omega t \qquad (2.12)$$

Where a is the oxide thickness, a_0 is the original thickness ($a_0 = 0$, in this study), and Ω is a constant quantity related to the built-in potential across the oxide and ionic mobility. According to Equation 2.12 and from Figure 2.1C, it is possible to plot $f(a)$ as a function of time (Figure 2.1D). This clearly shows the linear region between 15 and 45 min indicating CM theory is applicable to oxidized AuNPs between this duration. The slope of this linear region is Ω and allows for calculating the theoretical oxide shell thickness (a) using Equation 2.12, which further fits closely with the observed shell thickness ($15\ \text{min} \leq t \leq 45\ \text{min}$) as shown in Figure 2.1E.

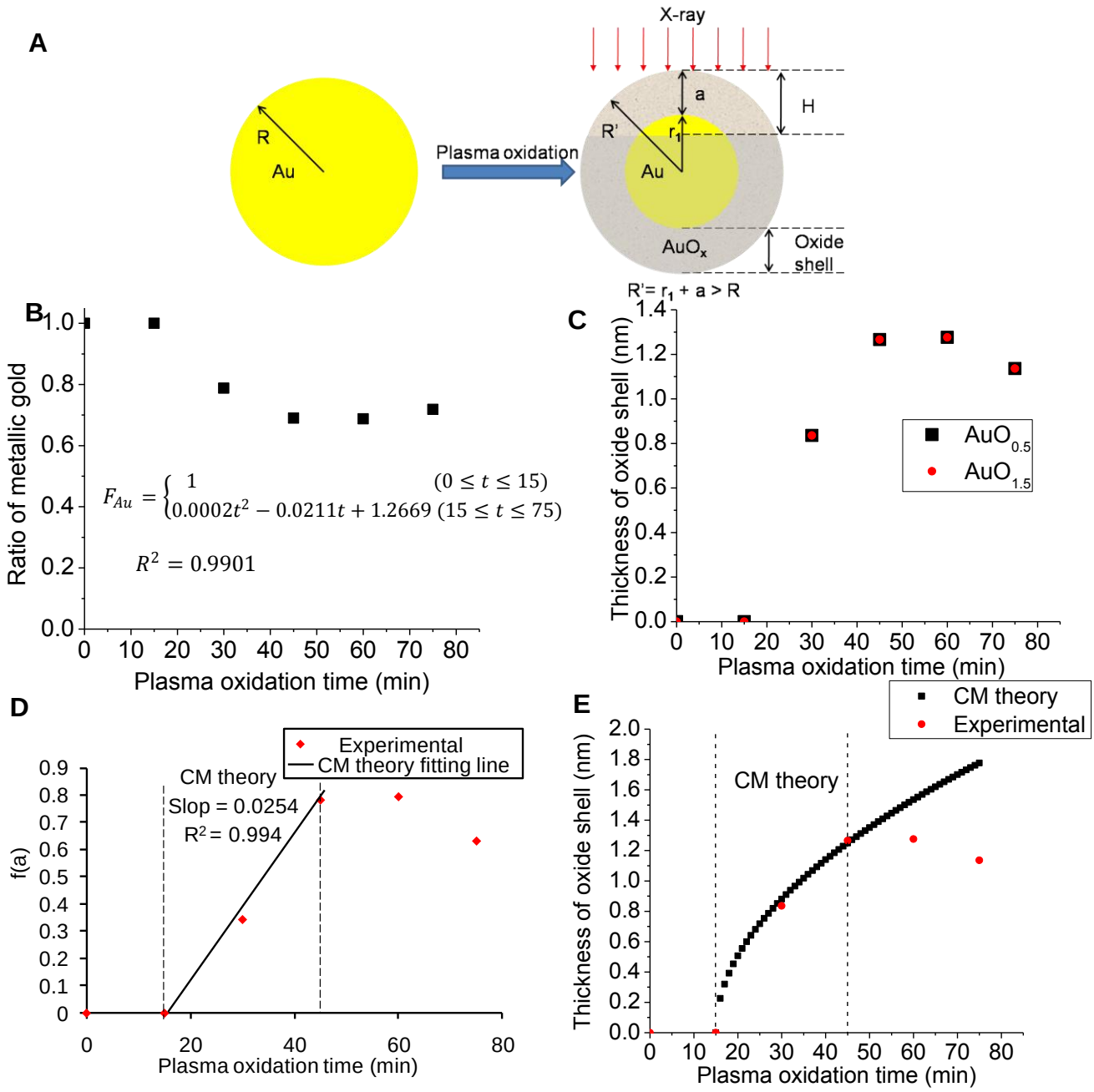

Figure 2.1 (A) Schematic showing formation of gold oxide (AuO_x) shell and XPS analysis showing the detection depth (H) and other geometrical parameters, Graphs showing the relationship between plasma oxidation time and (B) ratio of metallic Au, (C) thickness of oxide shell for AuO_x corresponding to x = 0.5 and 1.5, and (D, E) fitting of Cabrera-Mott (CM) model for oxidation of spherical particles with the observed experimental data.

2.4 Effect of Quenching Induced Defects on Carbon Shells Formation

By using AuNPs synthesized at room temperature (Table 2.1 and sample 1) as catalyst for graphene shells growth, uniform graphene shells encapsulated AuNPs were fabricated after CVD process. Those shells have interlayer spacing of graphene-like carbon layer ~ 0.34 nm, which is consistent with the c-axis spacing of graphite (Figure 2.2A, B). We proposed that the oxide of gold (AuO_x) is unstable at high temperatures,[115] prefers to transform to metallic Au, and necessitates the electron transfer process. Thus, conversion of Au^{x+} to Au^{o} takes place by accepting electrons from the incoming carbon feed resulting in the formation of GNPs (Figure 2.2C). Similar mechanism has been proposed for the formation of carbon shells around surface oxidized AuNPs in a polymer pyrolysis approach.[19]

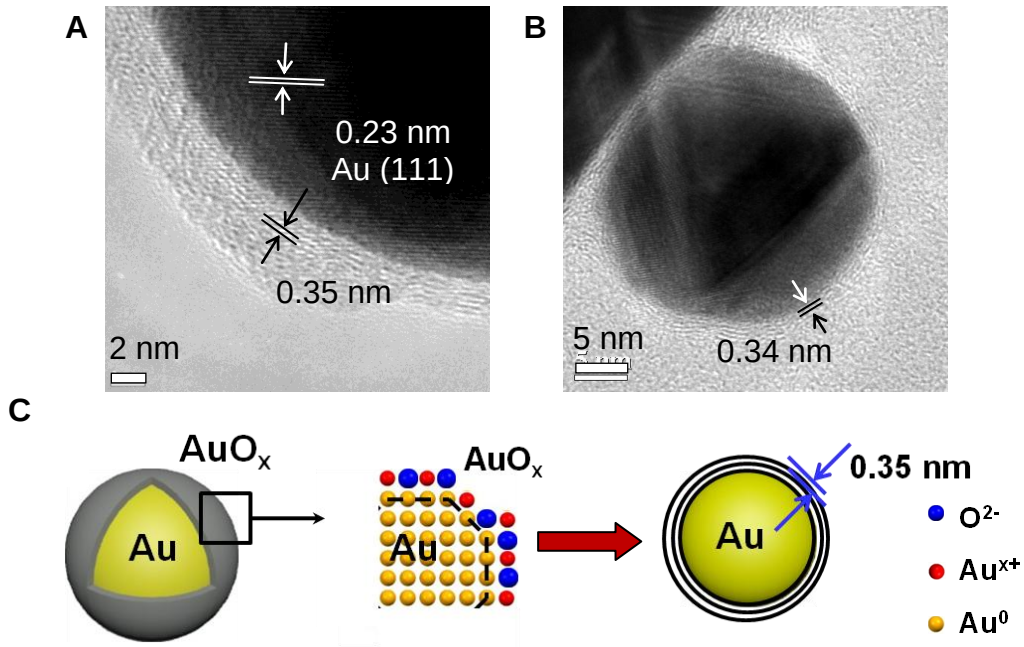

Figure 2.2 (A, B) TEM images show graphene shells encapsulated AuNPs. (C) Schematic illustration of the proposed growth mechanism of GNPs. Surface oxidized AuNPs (grown at room temperature) resulted in graphene shells.

A unique aspect of our study was to understand effects of defects in AuNPs on the growth of graphene shells. Thus, AuNPs with defects prepared by quenching at −20 ^{o}C (Table 2.1 and sample 5) were dispersed on a Si substrate, plasma oxidized for 30 min, and utilized for CVD growth of graphene shells in similar growth conditions. As-synthesized AuNPs (at ~130 °C) were rapidly quenched at different temperatures (10, 0, and −20 °C), and the effects were observed (Figure 2.3) and are reported in Table 2.1. Various kinds of defects such as grain boundaries (Figure 2.3E, G, H), twin boundaries (Figure 2.3I), and vacancies (Figure 2.3J) developed only at low quenching temperatures of 0 and −20 °C. The defects formation at low quenching temperatures could be attributed to sudden cessation ("freezing") of diffusion and growth processes in nanoparticles under significantly high cooling rates.[105] Such processes are known to occur for cubic crystal systems, are very rapid in nature, and are referred to as shock loading.[116] The averages sizes of the quenched AuNPs were between 14 and 30 nm (Figure 2.3K). The percentage of spherical AuNPs increased to 100% (Table 2.1) for the lowest quenching temperatures (−20 °C).

Since the CTAB solubility in the AuNP growth solution decreases with decreasing temperatures,[117] a low CTAB concentration (0.03 M) greater than the critical micelle concentration was chosen in this study.[118] This has been suggested for synthesis of gold nanorods at low temperatures.[24,119] Moreover, the influence of quenching on surfactant (CTAB) micelle shape and its insolubility in growth solution cannot be ruled out.[117] These effects were more dominant for the lowest quenching temperature of −20 °C with high cooling rates (>6000 °C/min). This may result in a decrease in the average AuNP size and spherical shape of the nanoparticles formed at −20 °C quenching (Figure 2.3F). However, an increase of nanoparticle

size was observed (~28 nm) at 10 and 0 °C. This could be attributed to the relatively controlled cooling rates and an optimized jump frequency[120] of gold ions that was most likely favorable for nanoparticle growth as compared to the −20 °C quenched nanoparticles. It is reasonable to consider that 10 °C quenching temperature resulted in a moderate cooling rate because no defect formation in the Au lattice was observed (Figure 2.3A−C).

As a result of high temperature CVD growth, the average size of the core AuNPs was observed to increase from ~ 14.5 nm to ~ 49 nm. Majority of the carbon shells formed were disordered or comprised of amorphous carbon with a shell thickness of ~ 2.71±1.72 nm (Figure 2.4A-D). Several nanoparticles were also observed with graphene-like shells (Figure 2.4E, F, and G) but the inter-layer spacing was significantly higher (~0.45±0.08 nm) than the c-axis spacing between the graphene layers. Thus, we refer to these graphene-like shells as 'relaxed carbon shells'. This interesting observation indicates that the presence of defects in the AuNPs can lead to disordered carbon shells or distorted graphene layers. We propose that defects in AuNPs being the high energy regions or vacant atomic lattice does not allow for electron transfer process to occur between the incoming carbon feed and plasma oxidized and defective AuNPs. These defect sites must be allowing for plasma-generated oxygen species/radicals[121] (during the surface oxidation step) to be trapped in them and also acting as electron donor sites. Thus, as shown schematically in Figure 2.4H, only the partial surface of the AuNPs, which gets oxidized to some extent (shown by 'grey patches' in the Figure 2.4H) is active area for the growth of graphitic carbon. In addition, knowing that carbon solubility in metallic gold is very low (<0.2%),[15] the non-oxidized surface did not participated in the carbon shell growth but disordered carbon formation. Overall, this ineffective surface oxidation of AuNPs resulted in disordered or relaxed carbon shells after

xylene CVD growth. As clearly indicated in TEM images, these hybrid nanoparticles have carbon shells that have some regions with graphitic-like layering while other regions indicating disordered carbon. Increased interlayer spacing in the graphitic regions of the relaxed carbon shells encapsulating AuNPs could also be attributed to the non-uniform surface gold oxide patches present on the AuNPs as well as crystal defects within the core nanoparticle that could lead to improper interfaces.[122] Finally, it could be argued that the defects in surface oxidized AuNPs will be annihilated during the CVD growth process but an earlier report demonstrates that defects in such nanoparticles at high temperature annealing can survive and remain in the structure.[123] Moreover, corresponding to the size of AuNPs in our study (~ 67.4±13.2 nm), the estimated melting temperature[124] is greater than ~ 1000 ^{o}C, which is much higher than the CVD growth temperature employed (~ 675 °C). Thus, the xylene CVD growth will not lead to complete melting of AuNPs but only their coalescence as observed in this study. However, we believe that in such a growth environment, the defects in the surface oxidized AuNPs may have survived for duration much lower than the CVD growth duration (~ 1 h).

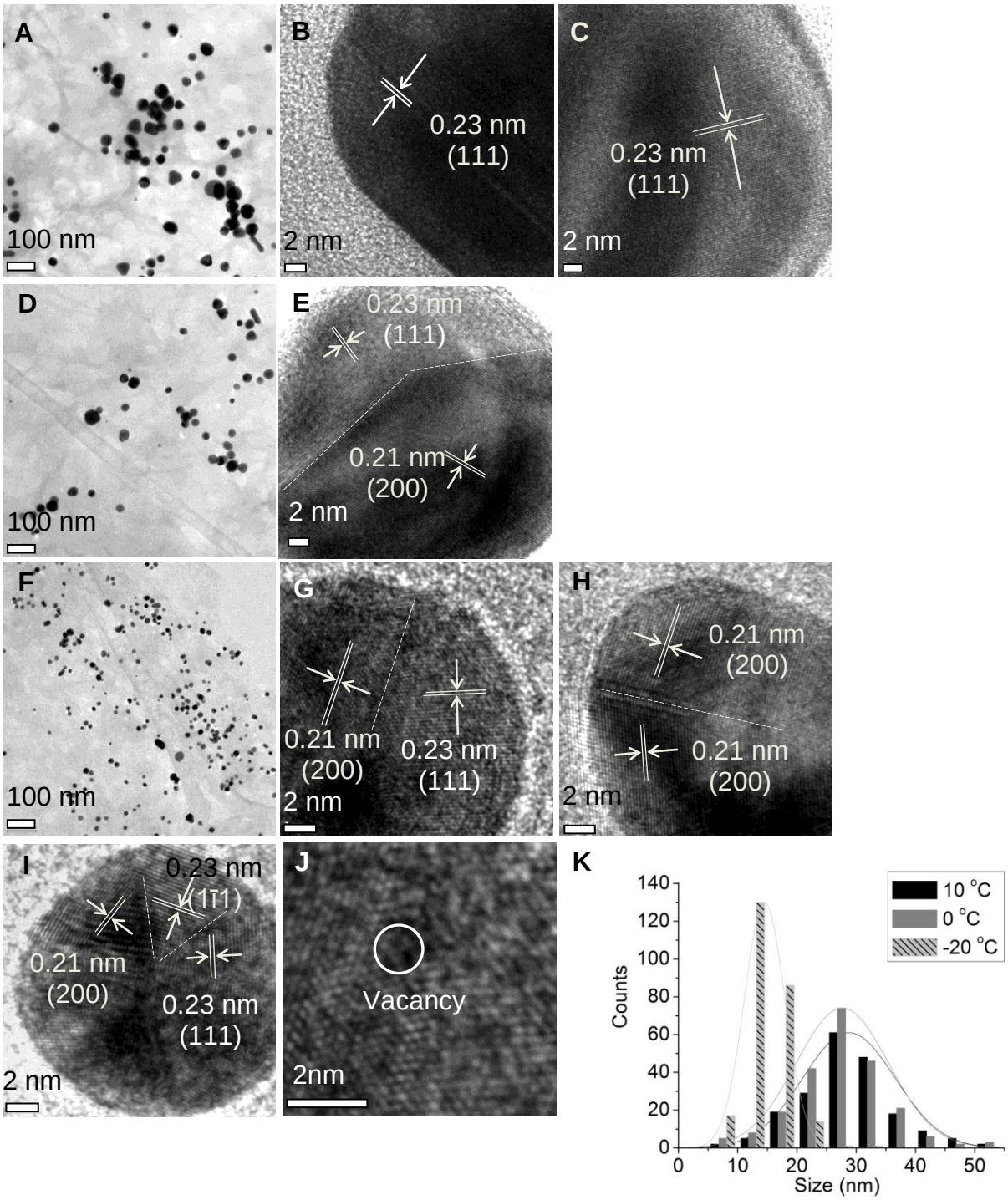

Figure 2.3 TEM images of AuNPs (Table 2.1 and sample 3-5) synthesized at ~ 130 ^{o}C and then quenched at (A, B, C) 10 ^{o}C, (D, E) 0 ^{o}C,(F, G, H, I, J) -20 ^{o}C, and (K) AuNP size distributions as a function of quenching temperatures.

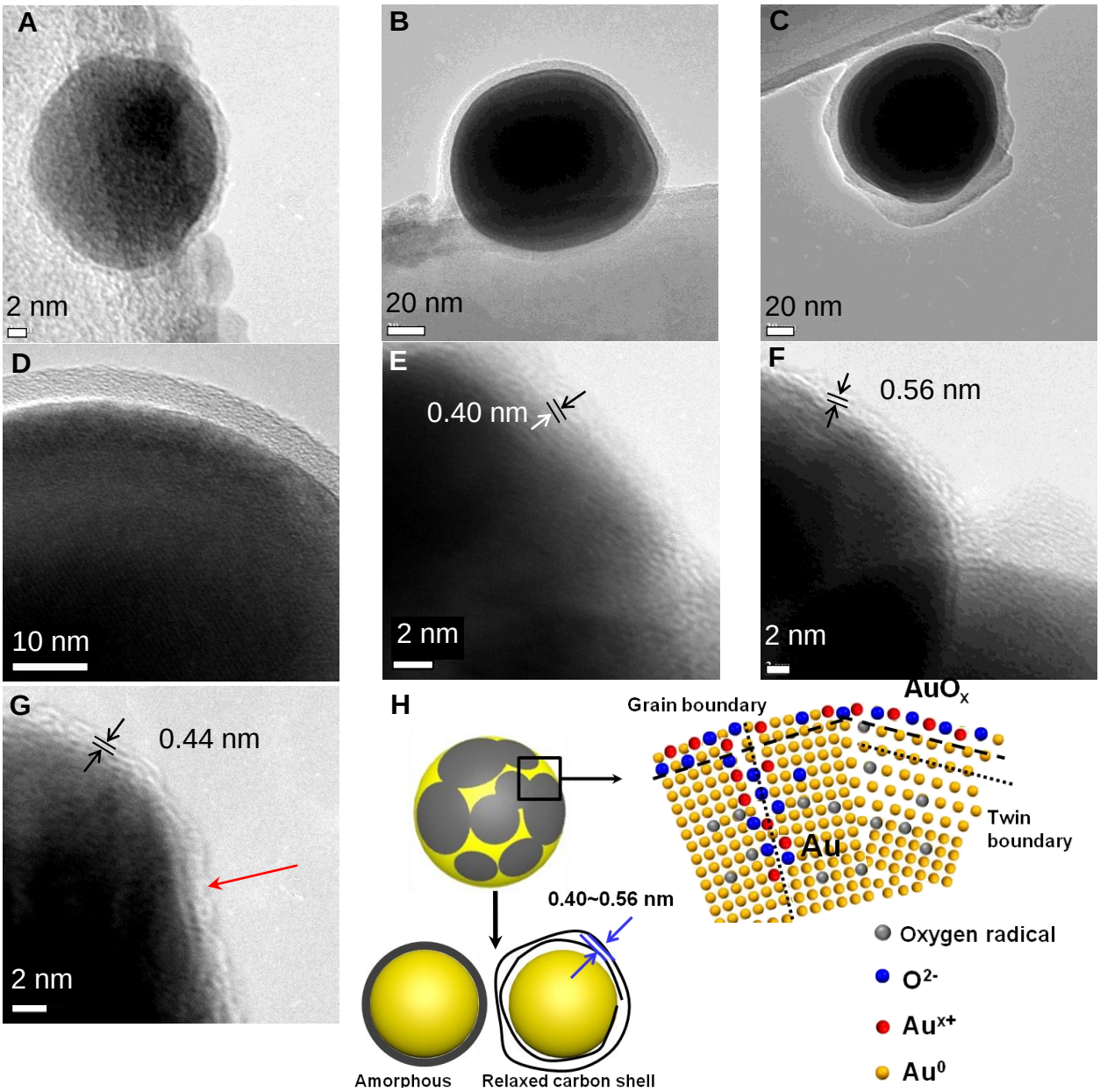

Figure 2.4 (A-G) TEM images for carbon encapsulated AuNPs. Some HRTEM images (E, F, and G) also show the relaxed carbon shells. (H) Schematic illustration of the proposed growth mechanism of GNPs. AuNPs with defects (synthesized at 130 ^{o}C and quenched at -20 ^{o}C) resulted in improper oxidation of AuNPs as well as entrapment of oxygen species from plasma in the defect sites. This led to the formation of amorphous carbon shells or relaxed carbon shells on AuNPs in the CVD process

2.5 Conclusions

In summary, AuNPs were synthesized in a single-step wet-chemical approach. A unique aspect was the post-synthesis quenching of AuNPs (grown at 130 ^{o}C) at 10 ^{o}C, 0 ^{o}C, and - 20 ^{o}C. The percentage of the different shapes of AuNPs decreased with decreasing quenching temperature and ultimately resulted in 100% spherical nanoparticles at lowest (- 20 ^{o}C) quenching temperature. Low quenching temperatures (0 ^{o}C and - 20 ^{o}C) led to defects in the AuNPs such as twin boundaries, grain boundaries, and vacancies. As a next step towards GNP growth, AuNPs synthesized at room temperature were plasma oxidized for different durations (0 – 75 min) in an oxygen plasma process and their oxidation kinetics was studied. The thickness of gold oxide shell on AuNPs was a function of oxidation duration but was independent of stoichiometry (x) of the oxide (AuO_x) formed. Cabrera-Mott oxidation kinetics was observed between 15 and 45 min oxidation, beyond which the etching of oxide occurred. AuNPs that oxidized for 30 min were further selected for catalyzing the growth of GNPs in a xylene CVD process. In regard to the influence of defects in AuNPs (- 20 ^{o}C quenched) on growth of graphene shells, similar xylene CVD growth resulted in amorphous carbon shell and graphene-like layering (relaxed carbon shells). This was attributed to ineffective surface oxidation of defective AuNPs, where the defects also acted as the oxygen species trapping centers during the plasma process. This hindered the electron transfer process between the improperly surface oxidized AuNPs and the incoming carbon feed in CVD growth.

CHAPTER 3: CONTROLLED ASSEMBLY AND PLASMONIC BEHAVIOR OF GRAPHENE SHELLS ENCAPSULATED GOLD NANOPARTICLES AND THEIR INTEGRATION WITH CARBON NANOTUBES

3.1 Introduction

Tight CNT multi-layer networks with homogeneous and uniform distribution and stable CNT-based nanohybrids are highly desired due to their combined properties and effects.[125-127] Various approaches for CNT/nanoparticle complexes were suggested, such as physical evaporation, chemical reaction, and electroless deposition.[128-131] Among these methods, completely eliminating wet chemistry steps of CNT-nanoparticle heterostructure formation will prevent contamination of heterostructures and could be broadly applicable to broad range of materials. Here, we present a systematic study of dewetting procedure of gold film in different conditions (deposition time/film thickness, annealing temperature, time, atmosphere, and substrates). Gold nanoparticles/islands were fabricated through dewetting of gold-film, which was introduced by annealing process. Their size, inter-particle distance, and morphology were analyzed. In order to study the effect of AuNPs' sizes on graphene shells growth, gold nanoparticles/islands with different sizes, which obtained by annealing of gold films with different thicknesses, were subsequently selected as catalysts for the growth of graphene shells. After studied morphology evolution of gold film on planar substrate, gold film with appropriate thickness was also sputtered on the surface of carbon nanotubes (CNTs) for gold nanoparticle formation and further GNPs growth. Discrete dipole approximation (DDA) was employed using the program DDSCAT[38, 132] to model the optical properties of gold nanoparticles/islands and graphene shells encapsulated gold nanoparticles (GNPs).

3.2 Experiment Methods

3.2.1 Materials and Methods.

Sulfuric acid (H_2SO_4, 95%-98% mol.) was bought from VWR (West Chester, PA). Hydrogen peroxide (H_2O_2, 35% w/w) was purchased from Alfa Aesar (Ward Hill, MA). Si wafers (100, n-type) were purchased from IWS (Colfax, CA). Ferrocene ($Fe(C_5H_5)_2$, 98%) was bought from Sigma-Aldrich (St. Louis, MO). DI water (18.0 MΩ-cm) was obtained using a Barnstead International DI water system (E-pure D4641). All chemicals were used without further purification. Sputtering target (Au) and ATC ORION sputtering system were purchased from AJA International, Inc. (North Scituate, MA). The sputtered Au film was annealed in CMF-1100 (MTI Inc, Redmond, CA) compact muffle furnace. Oxygen plasma treatment was performed in a Nordson March Jupiter III Reactive Ion Etcher (Concord, CA). Graphene shells growth was conducted inside a Lindberg blue three-zone tube furnace (Watertown, WI). Quartz tube was purchased from ChemGlass (Vineland, NJ). Xylene (*o*-, *m*-, *p*-isomers) and syringe injector were obtained from Fisher Scientific (Suwanee, GA). Gas flow rate of all annealing and CVD processes were controlled by Teledyne Hasting powerpod 400 mass flow controllers (Hampton, VA). Thermocouples and temperature controllers were bought from Omega Engineering (Stamford, CT). H_2 (UHP grade, 40% balanced with Ar), O_2 (UHP grade, 5% balanced with Ar), N_2 (UHP grade), and Ar (UHP grade) gas cylinders were purchased from Airgas South (Tuscaloosa, AL).

3.2.2 Deposition and Annealing/Dewetting of Gold (Au) Films

Table 3.1 Systematic study of the migration of gold film. Note that sample 4A is the baseline sample.

Sample number	Au Deposition time (s)	Annealing temperature (^oC)	Annealing time (h)	Atmosphere	Substrate
1A	30	700	2	Ar	Si
2A	60	700	2	Ar	Si
3A	90	700	2	Ar	Si
4A	***120***	***700***	***2***	***Ar***	***Si***
5A	150	700	2	Ar	Si
6A	180	700	2	Ar	Si
7A	120	150	2	Ar	Si
8A	120	300	2	Ar	Si
9A	120	600	2	Ar	Si
4A	***120***	***700***	***2***	***Ar***	***Si***
10A	120	800	2	Ar	Si
11A	120	1100	2	Ar	Si
12A	120	700	1/6	Ar	Si
13A	120	700	1/2	Ar	Si
14A	120	700	1	Ar	Si
4A	***120***	***700***	***2***	***Ar***	***Si***
15A	120	700	3	Ar	Si
16A	120	700	4	Ar	Si
17A	120	700	5	Ar	Si
18A	120	700	6	Ar	Si
19A	120	700	10	Ar	Si
20A	120	700	2	H_2 + Ar	Si
21A	120	700	2	N_2	Si
22A	120	700	2	O_2	Si
23A	120	700	2	Ar	Si + Cr
24A	120	700	2	Ar	Si + ITO
25A	120	700	2	Ar	Si + Ta
26A	120	700	2	Ar	Si + Ti

Silicon wafer was soaked in the mixture of H_2SO_4 and H_2O_2 (v/v 5:1) at 100 ^oC for 30 min. Subsequently, the wafer was rinsed with copious amounts of DI water and dried in air. The piranha cleaned silicon wafers were then sputtered gold under 2 kV for 2 min, or sputtered other materials such as Cr, ITO, Ta, or Ti for 30 nm before sputtered gold. To study the influence of different parameters for the migration (size, shape distribution of Au particles after annealing), systematic studies were performed by changing gold deposition time, annealing temperature, time, and atmosphere, and the substrates on which gold was deposited (Table 3.1). For these experiments, only one variable was changed while keeping all the other experimental condition was fixed.

3.2.3 Preparation of Carbon nanotube (CNT)

Multiwalled carbon nanotubes (MWCNTs) were synthesized in a floating catalyst CVD process using ferrocene and xylene as catalyst and carbon source, respectively.[133] A liquid mixture of ferrocene and xylene (Fe:C=0.75% mol.) was injected through a syringe injector into a pre-heated zone (~220 ^oC) and subsequently transported into the reaction zone (~675 ^oC) in the center of a quartz tube furnace. Meanwhile, the gas flow of H_2 (oxygen scavenger) in carrier gas Ar (10% v/v) was also introduced into CVD furnace. The CVD growth reaction continued for 2 h before the furnace was cooled down in Ar gas flow. As-synthesized CNT were collected as black powder from the inner walls of the quartz tube, stored in a solvent, and were dispersed on piranha-cleaned Si wafer by drop-casting method. Followed by CNT substrate drying, Au film was sputtered (2 kV, 40 W, and 0.06 Torr) on this substrate for 30 sec duration. Finally, Au nanoparticles were nucleated, via dewetting process, on CNTs by annealing this substrate at 400 ^oC for 2 h in N_2 atmosphere.

3.2.4 Synthesis of graphene shells encapsulated Au nanoparticles (GNPs)

GNPs were synthesized in a xylene CVD process similar to CNT growth as described earlier. Specifically, samples #1A-6A (Table 3.1) were utilized for this study to understand the influence of Au nanoparticle size on the growth of graphene shells. Prior to the growth of graphene shells, substrates with patterned and dewetted Au nanoparticles were surface plasma oxidized for 30 min. The substrates were placed in the center of quartz tube equipped with precursor and gas lines for Ar/H_2 flow. Xylene was utilized as the carbon source and was injected through a syringe injector into a preheated zone (~220 ^{o}C) at the rate of 45 mL/h for ~ 2 min and subsequently transported into the reaction zone (~675 ^{o}C) inside the quartz tube furnace. The xylene flow rate was reduced to 1 mL/h after H_2 mixed with Ar (Ar/H_2=0.85 LLM/0.3 SLM or 10% v/v H_2) was introduced in the CVD reactor. The CVD reaction was continued for 1 h after which H_2 and xylene were discontinued, and the furnace was cooled down under Ar flow. In a similar CVD approach, graphene shells were also grown on CNT-Au nanoparticles heterostructures dispersed on a Si substrate. In this case, the heterostructures were surface plasma oxidized for 10 min prior to the CVD growth process to result in graphitic shells around Au nanoparticles.

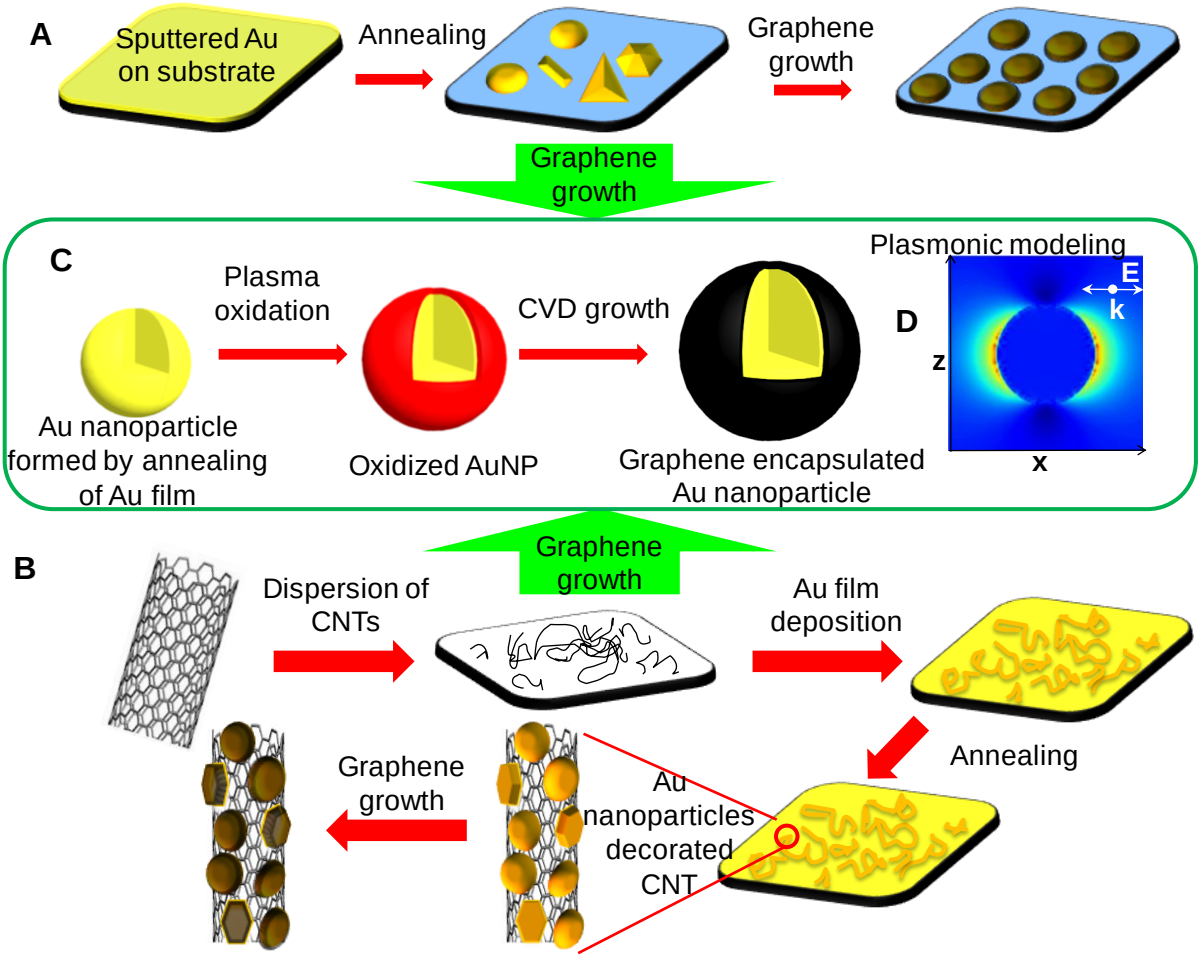

Figure 3.1 Schematic illustration of dewetting of the Au films on (A) Si wafer or on (B) CNTs to result in Au nanoparticles. (C) Surface oxidation of dewetted Au nanoparticles for the CVD growth of GNPs. (D) a representative normalized electric field distribution based on DDA calculations for GNPs. Note: **E** and **k** in (D) represents electric field and wave vector, respectively.

3.2.5 Discrete dipole approximation (DDA) calculations

The optical properties and plasmonic behavior of three nanostructured configurations, namely, Au nanoparticles obtained after dewetting, CNT-Au nanoparticles heterostructure, and GNPs were modeled using discrete dipole approximation (DDA) through the available DDSCAT code (version 7.2) developed by Draine and Flatau.[37,38,132] The nanostructured configurations (or target) in our study were comprised of arrangement of dipoles for which extinction spectra and electric field distributions were numerically solved using the DDSCAT code. The nanostructured configuration studied here was solved for their effective radius (a_{eff}). This is defined as the radius of a sphere with the same volume as that of all the dielectric materials in the target. To obtain accurate simulations of electromagnetic scattering from DDSCAT, the effective radius should meet the following criteria: $2\pi a_{eff}/\lambda < 25$, where λ is the wavelength of the incident electromagnetic wave. In our case, all simulations meet $2\pi a_{eff}/\lambda < 10$ and the dipole spacing is sufficiently small so that $(2\pi d|m|)/\lambda<1$. The dipole spacing d is given $d=(V/N)^{1/3}$, where V is the volume of the effective shape of the nanostructured configuration, N is the number of dipoles comprising that shape, and m is the complex refractive index.[132]

Figure 3.1 outlines the approach for controlled patterning and dewetting of Au nanoparticles on a Si wafer or CNTs and their utilization for the growth of GNPs. It must be noted that the critical step of surface plasma oxidation of Au nanoparticles was performed prior to the CVD growth of graphene shells. This study is divided into four sections: 1) Systematic optimization and morphological evolution of Au nanoparticles by dewetting of Au films coated on substrates such as Si wafer or CNTs. 2) Growth of GNPs as a function of the size of the core Au nanoparticles dispersed on Si wafer. 3) Growth of GNPs directly on CNTs as substrates. 4) Simulation of

optical properties and plasmonic behavior of Au nanoparticles, CNT-Au nanoparticles heterostructures, and GNPs.

3.2.6 Characterization

The morphology and Energy-dispersive X-ray spectra were obtained by Field Emission Scanning Electron Microscope (FE-SEM, JEOL-7000, equipped with Oxford EDX detector). High-resolution transmission electron microscope (HR-TEM, Tecnai FEI-20) was used to obtain TEM images for graphene shells encapsulated Au nanoparticles/islands, as well as CNT-Au heterostructure after graphene shells growth. X-ray diffraction (XRD) data of samples were recorded with a Philips diffractometer (XRG 3100, Cu Ka radiation, 35 mA and 40 kV). X-ray reflectivity (XRR) data of samples were obtained with a Philips X'Pert Diffractometer (X'pert Powder, Cu Ka radiation, 35 mA and 40 kV). Raman spectra were collected using Bruker Senterra system (Bruker Optics Inc. Woodlands, TX) equipped with 785 nm laser source at 10 mW laser powers and 100 × objectives. The integral time and co-additions were set as 15 seconds and 2, respectively. Extinction curves of gold nanoparticles before and after graphene shells growth were calculated by DDSCAT, and visualized by Python(x,y).

3.3 Morphology Evolution of Gold Films

Adjustment of the morphology and optical properties of gold films can be achieved by variation of the film nominal thickness, evaporation rate, and post-deposition annealing conditions.[11] Figure 3.2 shows SEM image and EDS of a thin Au film that was sputtered on piranha-cleaned Si wafer for 2 min. The unannealed film showed a percolated structure with scattered voids/grooves. The deposited Au films were annealed at various conditions (Table 3.1) to obtain monolayer gold islands on substrate. Figure 3.3A exhibits an example of XRD spectra evolution before and after annealing of Au films. The XRD spectrum corresponding to the 2 min-deposition Au films on Si wafer (Figure 3.3A(b)) showed a dominant Au (111) peak. After 2 hours annealing at 700 ^{o}C, the (111) reflection of gold became increasingly sharp and strong, indicating the formation of gold grains with better crystalline (Figure 3.3A(c)).[134]

By controlling the Au sputter deposition conditions, it was possible to control the thickness of as-deposited Au films. Specular X-ray reflectivity (XRR) measurements were used to study the thickness of deposited Au films. The XRR is an accurate, direct, and non-destructive measurement of density, microscopic surface roughness, and thickness of ultrathin films.[135] The measurements were analyzed with a fitting procedure by an open source program “Wingixa”, assuming a single-layer (Au film/Si-substrate) model. Figure 3.3B shows thickness measurement results for Au-films deposited on Si wafer for different durations (from 30 s to 180 s). It suggested a linear increase of film thickness (h) with increasing deposition time (from ~8 nm for 30 s to ~ 45 nm for 180 s).

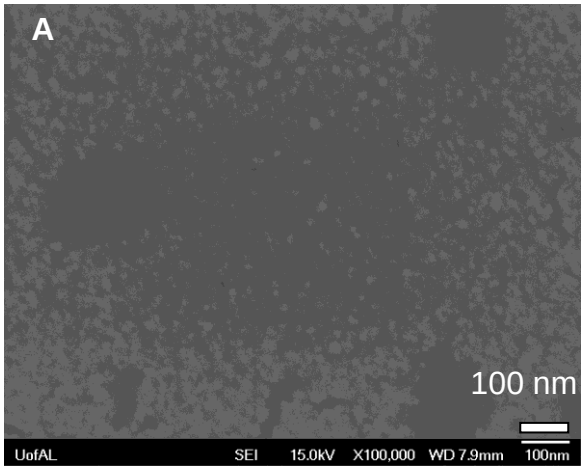

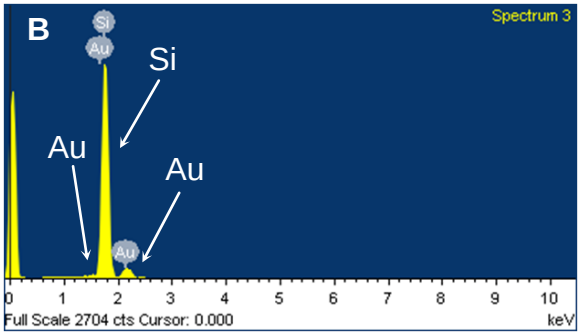

Element	Weight%
Si K	80.29
Au M	19.71
Totals	100.00

Figure 3.2 (A, B) SEM images and (C) EDS of gold film sputtered on piranha cleaned silicon wafer.

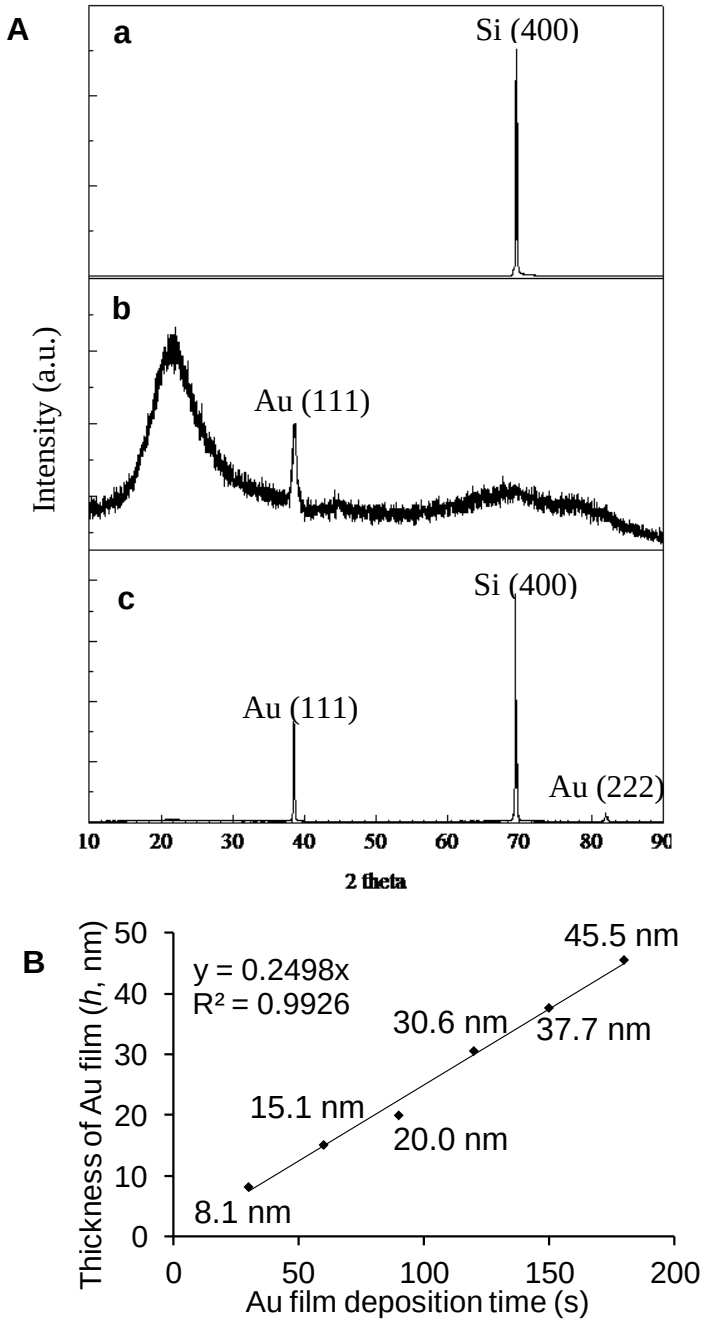

Figure 3.3 (A) XRD of (a) blank Si wafer, (b) Si wafer sputtered gold for 2 min, and (c) Si wafer after dewetting of Au film at 700 ^{o}C for 2 h in Ar. XRD show peaks of Si (JCPDS #: 27-1402) and Au (JCPDS #: 04-0784). (B) XRR-derived Au film thickness as a function of Au film deposition time.

Gold films were deposited on piranha cleaned silicon wafer by sputtering, and then annealed to form a monolayer of gold islands on substrates at different conditions (Table 3.1 and Figure 3.1A). The migration evolution of gold films, including size, inter-particle distance, and shapes of gold islands formed during annealing, were summarized in Table 3.2 and Figure 3.4. It should be noted that since the Au sputtering system has variation, the thickness of sputtered Au film for different batches was variable. To overcome this shortage, samples in the single parameter set were sputtered in the same batch (except the deposition time set), and the annealing baseline condition sample was repeated and characterized for three sets: Au deposition time, annealing temperature, and annealing time. Thus, even though the system error is unavoidable, we can still study and compare the samples within the same set.

Effects of Au deposition time: The XRR measurements showed an increase of film-thickness at longer deposition duration (Table 3.1 sample #1A-6A and Figure 3.3B). The deposited 7.5 nm Au film shows a largely percolated structure with a network of grooves/voids, with the nominal thickness is increased, grooves becoming shorter and less (Figure 3.5A-D left panel), and eventually disappeared when the deposited Au films were thicker (37.5-45 nm, Figure 3.5E, F left panel). High-temperature annealing (700 ^{o}C, 2 h) of the Au films resulted in their dewetting and formed well-patterned islands (Figure 3.5A-F right panel). The average nanoparticles/islands size and inter-particle distance showed a tendency of increasing as the Au nominal thickness became larger, while the fraction of the area covered by islands and the number of particles per unit area decreased (Figure 3.5A-F right panel).

Effects of annealing temperature: The annealing temperature effect on morphology evolution was processed by annealing Au films at different temperatures (from 150 to 1100 ^{o}C, sample

#7A-11A, Table 3.1). Those Au films were deposited on Si wafer with same thickness; other parameters such as annealing time and atmosphere are kept the same (2 h, Ar atmosphere). The dewetting process of Au films can be classified into the following conditions: At low temperature (150-300 ^{o}C), small and circular holes were initiated on the film, subsequently grew and coalesced with each other (Figure 3.6A, B). As temperature increased, the dewetting driving force became higher; holes grew faster to form complex configurations, until the holes covered most of the former thin film area. The remaining elongated structures decomposed into gold islands (Figure 3.6C-E). At elevated temperature, not only the gold islands can be formed within 2 h, but they also reformed into spherical shape to minimize the surface energy (Figure 3.6F). We observed a decrease of gold particle size, which may be induced by the evaporation of gold droplets at elevated temperature.[136,137]

Effects of annealing time: Au films with same thickness were deposited on Si wafer, followed by annealing at 700 ^{o}C for different duration (from 10 min to 10 h, Table 3.1 sample 12A-19A). Figure 3.7 shows similar morphology of samples underwent different annealing durations, indicated that under this annealing condition, the process of void initiation and growth can be accomplished within 10 min. After the formation of gold particles, they were stable at given annealing conditions.

Effects of atmosphere and substrate: Since the driving force of dewetting process is minimizing of surface energy, the annealing environment would have effects on the morphology evolution of Au films. Atmosphere and substrates were varied for the annealing of Au film with same thickness (Table 3.1 sample #20A-22A, 23A-26A). We observed that, a reducing atmosphere (10% H_2 in Ar) would result in more elongated Au islands than inert (N_2) and

oxidizing atmosphere (O_2) (Table 3.2 and Figure 3.8A-C). This can be attributed to the oxidation of gold in O_2 atmosphere, and the change of surface energy during the formation of gold oxide. More isolated gold islands suggested a faster dewetting process than branched islands. Similarly, by pre-sputtering Cr, ITO, Ta, or Ti on Si wafer before deposition of Au, the Au film would have different surface energy on varied substrates, which resulted in different morphology evolution during annealing process (Figure 3.8D-G).

Table 3.2 Result summary for systematic study of gold migration. Note: Sample #4A is the baseline sample (bold and italics) and is repeated in each parameter set to show the trends.

Parameter	Sample number	Average size (nm)	Inter-particle distance (nm)	Shape distribution
Au deposition time	1A	30.4±9.5	25.3±12.5	hexagon-5%
	2A	60.8±30.9	104.9±40.0	hexagon-17.26% pentagon-0.51% worm-1.52%
	3A	248.9±104.7	262.2±69.0	hexagon-17.09% rod-1.51% truncated triangle-0.5% worm-3.53%
	4A	301.5±112.2	484.9±111.2	hexagon-1.42% rod-9.61% worm-16.0%
	5A	362.1±160.0	964.0±294.9	hexagon-15.89% rod-3.27% truncated triangle-0.47% worm-5.14%
	6A	662.3±185.9	1952.6±536.7	hexagon-12.44% pentagon-0.48% rod-7.18% worm-10.53%
Annealing temperature	7A	/	None	None
	8A	/	None	None
	9A	/	None	None
	4A	516.8±208.2	698.9±188.5	branch-4.32% rod-4.75% truncated triangle-1.08% worm-11.66%
	10A	523.5±224.7	828.4±316.3	hexagon-1.84% rod-3.23% truncated triangle-1.38% worm-13.82%
	11A	309.6±113.7	567.6±117.9	hexagon-16.35%
Annealing time	12A	348.9±92.4	444.1±128.4	hexagon-16.83% rod-1.0% worm-5.94%
	13A	369.7±102.8	678.4±194.8	hexagon-34.21% rod-4.74% worm-3.68%

	14A	357.1±141.9	451.3±107.2	hexagon-15.38% rod-2.05% truncated triangle-0.51% worm-2.05%
	4A	319.5±110.0	484.9±111.2	hexagon-4.67% rod-1.40% worm-2.80%
	15A	355.3±80.3	532.7±157.1	hexagon-13.88% rod-9.09% rhmbus-2.39% truncated triangle-5.26% worm-5.74%
	16A	317.4±95.7	416.1±146.2	hexagon-22.01% rod-2.39% rhmbus-0.48% worm-2.39%
	17A	331.2±96.0	358.0±108.8	hexagon-11.33% pentagon-0.49% rod-5.42% truncated triangle-0.49% worm-2.46%
	18A	269.8±77.9	578.8±192.4	hexagon-6.76% rod-1.45% worm-2.9%
	19A	254.0±83.1	355.9±155.2	hexagon-6.67% rod-2.86% worm-0.95%
Atmosphere	20A	437.3±131.0	880.7±302.9	branch-7.53% hexagon-1.43% rod-9.68% worm-16.13%
	21A	447.2±135.4	809.8±208.0	hexagon-12.35% pentagon-0.3% rod-3.92% worm-6.93%
	22A	427.1±167.6	602.3±195.1	hexagon-8.86% pentagon-0.91% rod-6.59% rhmbus-1.36% truncated tringle-1.59% worm-5.91%
Substrate	***4A***	319.5±110.0	484.9±111.2	hexagon-1.42% rod-9.61% worm-16.0%

	23A	372.6±122.2	825.8±303.4	hexagon-19.3% rod-4.35% worm-0.97%
	24A	737.3±239.1	3875.8±1616.1	hexagon-23.23% rod-2.02% rhombus-9.6% truncated triangle-33.84%
	25A	396.9±119.2	518.1±130.1	branch-0.96% hexagon-4.31% pentagon-1.44% rod-2.39% truncated tringle-0.48% worm-3.35%
	26A	327.0±130.0	455.2±122.4	hexagon-7.65% rod-0.51% worm-8.67%

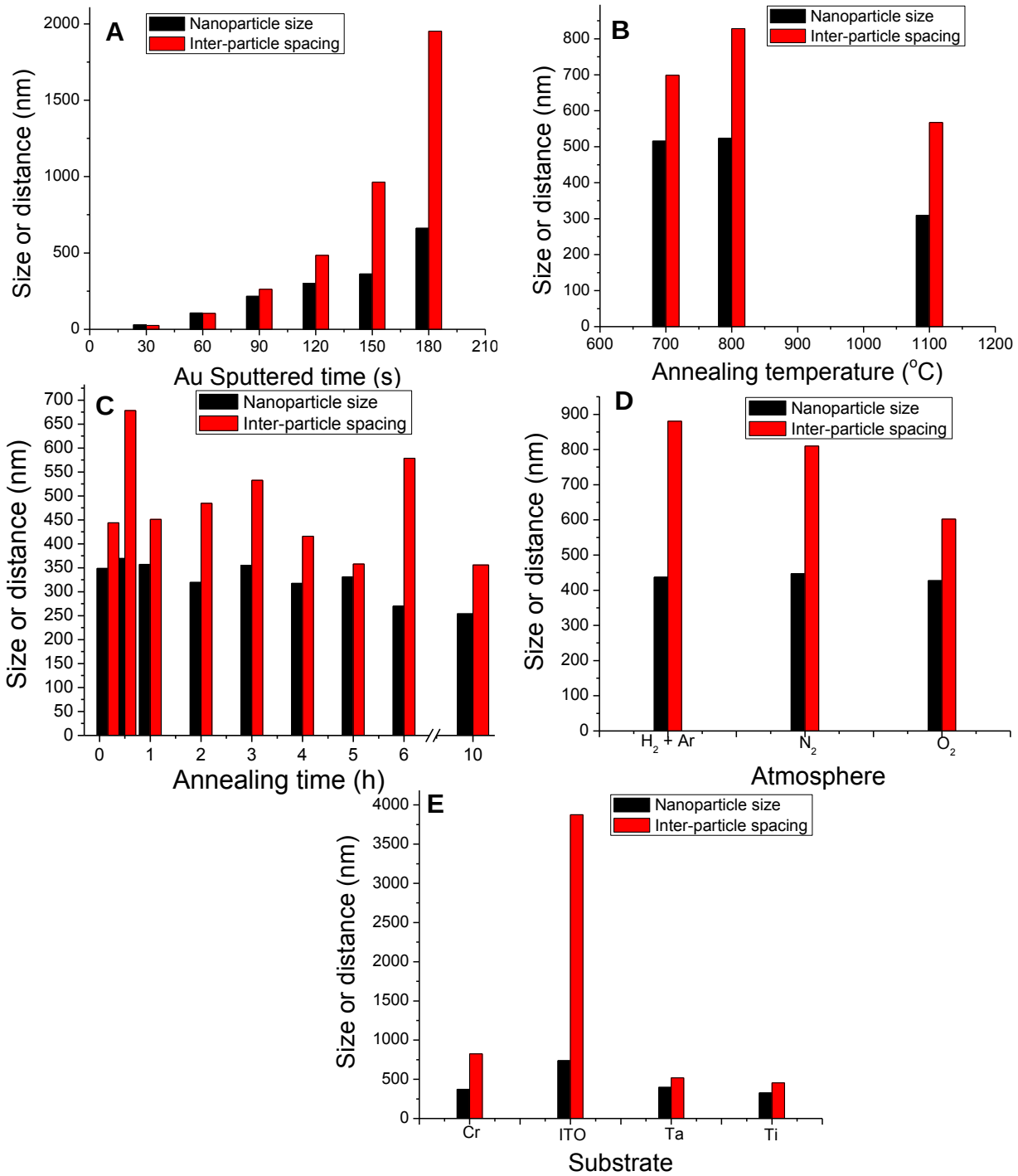

Figure 3.4 Histograms showing the size (black bar) and distance (red bar) of Au nanoparticles in different sets after annealing: (A) Au films with different deposition time, (B) annealed at different temperatures, (C) annealed for different time, (D) annealed in different atmosphere, (E) annealing for Au film sputtered on different substrates.

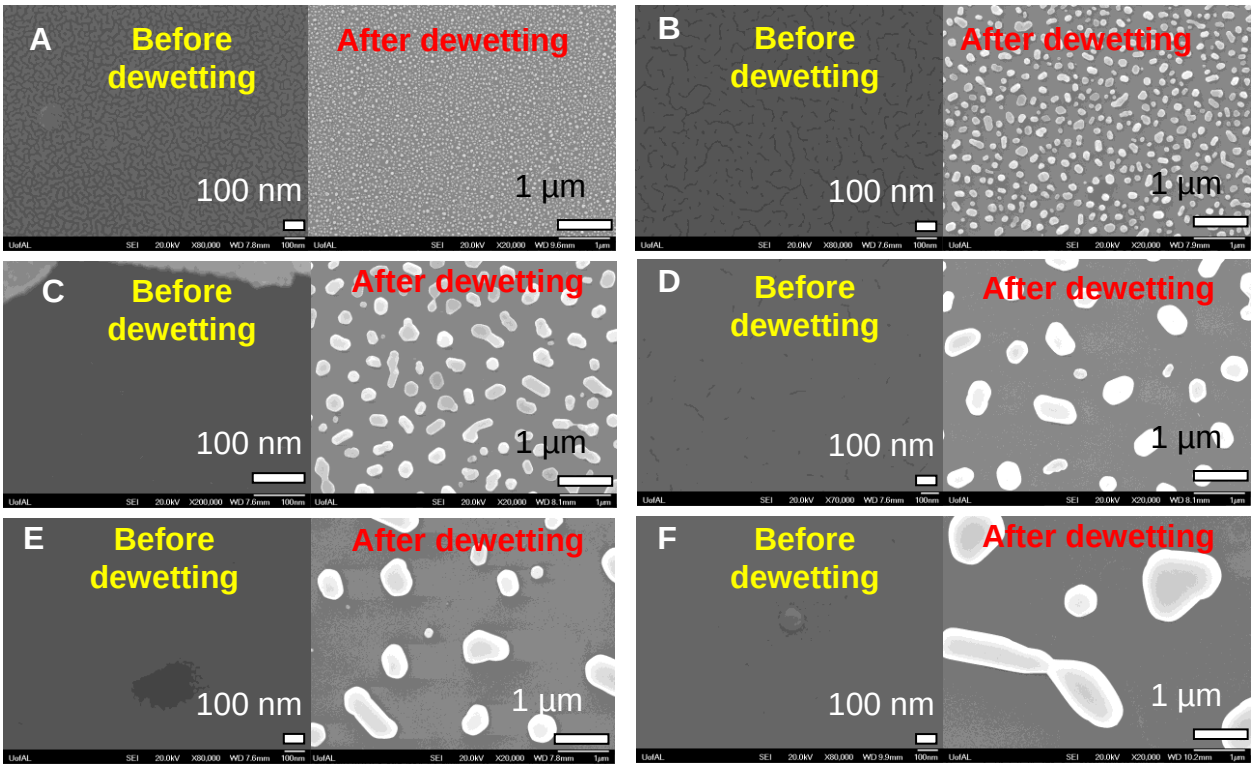

Figure 3.5 SEM images of Au films deposited for different time on piranha-cleaned Si wafer (left panels) and after annealing 2 h at 700 ^{o}C (right panels). Gold film sputtered time are (sample #1A-6A): (A) 30 s, (B) 60 s, (C) 90 s, (D) 120 s, (E) 150 s, (F) 180 s. Note the different scale bars in images before and after annealing.

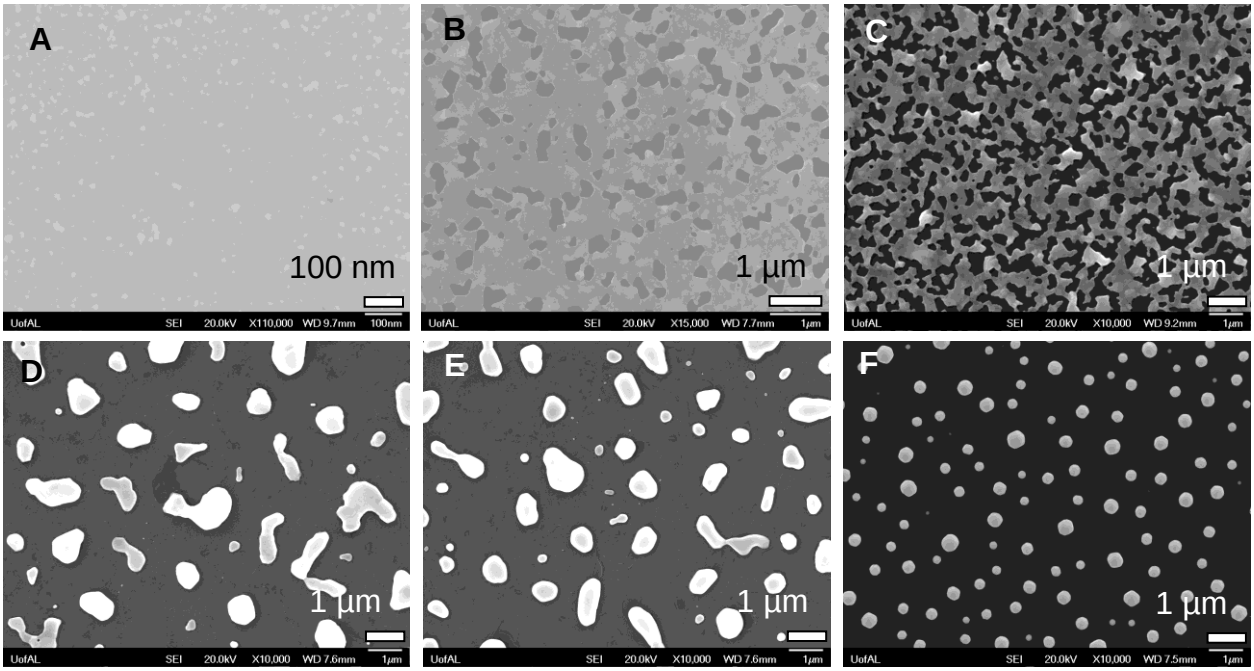

Figure 3.6 SEM images of Au films sputtered on piranha cleaned silicon wafer after annealing 2 h at different temperature (sample #4A, #7A-11A): (A) 150 ^{o}C, (B) 300 ^{o}C, (C) 600 ^{o}C, (D) 700 ^{o}C, (E) 800 ^{o}C, (F) 1100 ^{o}C. Note the different scale bar in (A).

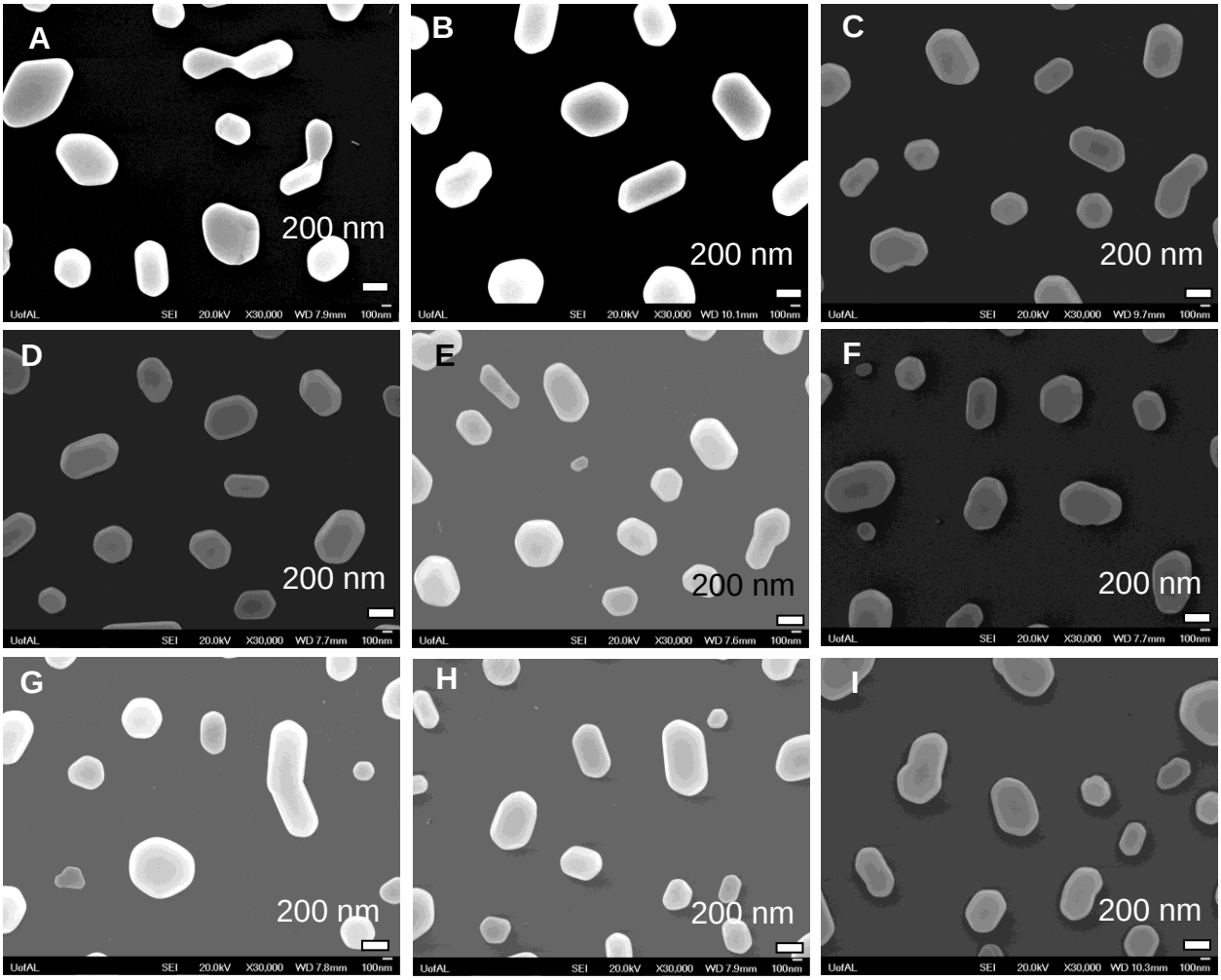

Figure 3.7 SEM images of Au films sputtered on piranha cleaned silicon wafer after annealing at 700 ^{o}C for different duration (sample #4A, 12A-19A): (A) 10 min, (B) 0.5 h, (C) 1 h, (D) 2 h, (E) 3 h, (F) 4 h, (G) 5 h, (H) 6 h, and (I) 10 h.

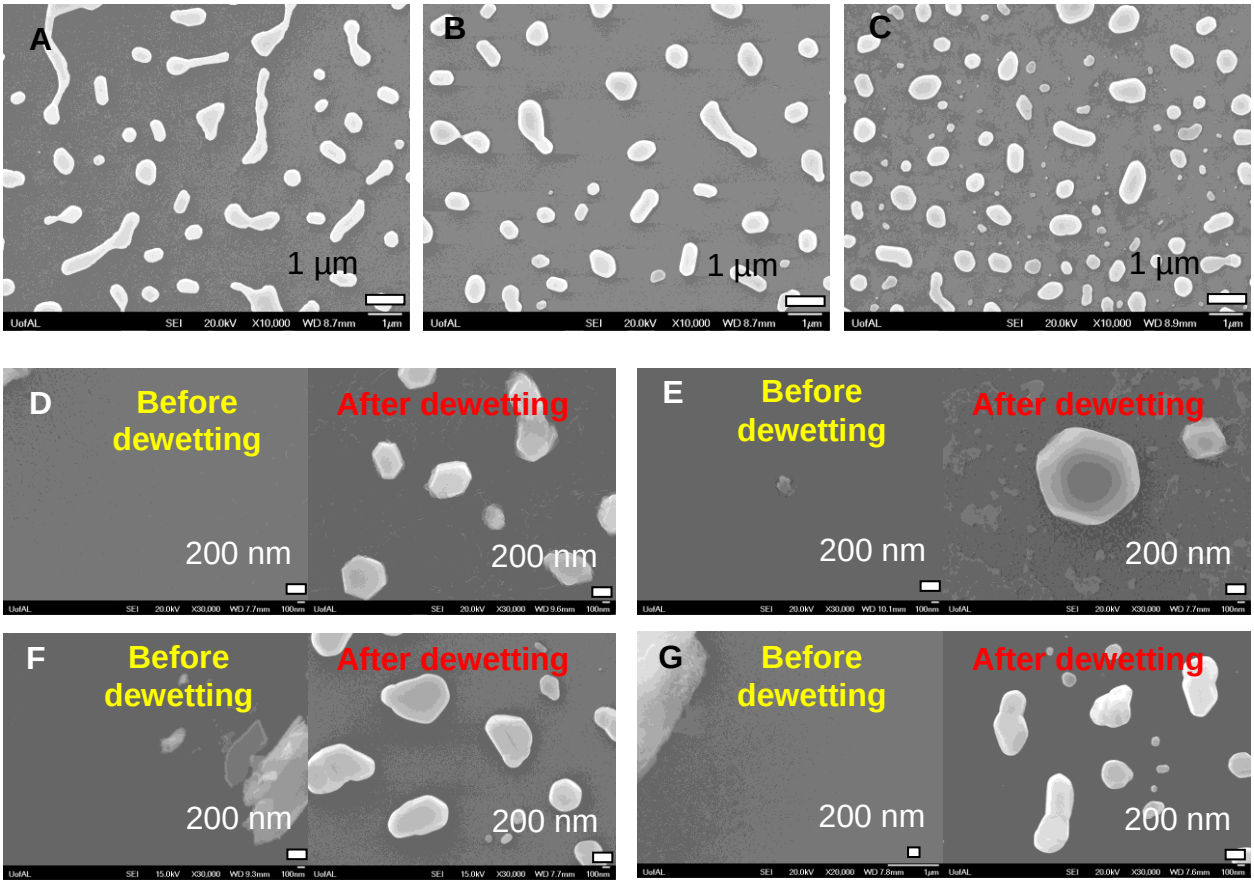

Figure 3.8 (A-C) SEM images of gold films sputtered on piranha cleaned silicon wafer after annealing 2 h at 700 ^{o}C in different atmosphere (sample #20A-22A): (A) 10% H_2 in Ar, (B) N_2, (C) O_2. (D-G) SEM images of different substrates (left panels) and gold films sputtered on those substrates after annealing 2 h at 700 ^{o}C (right panels). Substrates were prepared from sputtering different materials on piranha cleaned silicon wafer (sample #23A-26A): (D) Cr, (E) ITO, (F) Ta, and (G) Ti.

3.4 Graphene shells growth on AuNPs and CNT-Au heterostructure

3.4.1 Size effect of AuNPs on the growth of graphene shells

The migration of gold films provides us a convenient approach to fabricate mono-layer AuNPs dispersed on substrate. The dewetting conditions corresponding to sample #1A-6A resulted in the best control over the average size and pattering (uniform dispersion) of AuNPs. In this case, 6 samples with Au islands size ranging from ~30 to ~660 nm were prepared for graphene shells growth (Table 3.3). These conditions led to stable nanoparticle configurations with an ability to survive multiple processing steps including high temperature CVD growth of graphene shells. This is a critical aspect for understanding the relationship between the Au nanoparticle size and post-CVD graphene shells characteristics (thickness, amorphous content, strains, and inter-planar spacing).

Annealed Au-film samples were treated by oxygen plasma for 30 min before graphene shells growth. Graphene shells were grown on all 6 substrates in a single-batch CVD process,[1, 28] and characterized by HR-TEM (Figure 3.10). It was observed that, the average sizes of the core Au nanoparticles after the CVD growth increased and larger-sized Au nanoparticles resulted in greater increase in their sizes (Table 3.3). However, the size difference for dewetted Au nanoparticles before and after CVD growth is lower than chemically patterned Au nanoparticles that coalesced significantly in our previous report. Another interesting aspect is inter-particle spacing for GNPs that was negligibly changed with respect to dewetted Au nanoparticles before the CVD growth. Thus, as soon as graphene shells grow around Au nanoparticles, it limited the surface migration ability of the encapsulated Au nanoparticles. This also suggests that surface migration of small-sized Au nanoparticles embedded within graphene or carbon shells must have

occurred within a short duration at the beginning of the CVD growth. In regard to the graphene/carbon shell thickness corresponding to sample #1B-6B, it was observed that as the average size of dewetted Au nanoparticle/island increased, the shell thickness also increased from ~2 nm (for sample #1B) to ~11 nm (for sample #6B). It was known that carbon solubility in Au is decreasing when size of Au increased.[15] Thus carbon is easier to be saturated on large Au particles and contribute to the formation of graphene shells. Moreover, as mentioned earlier, the growth of graphene shells around AuNPs was catalyzed by surface metal oxides. Au particles with different sizes may result in different oxidation status (various thickness of gold oxide) after plasma treatment and then lead to a thicker graphene shell in the subsequent CVD process. The c-axis inter-planar spacing was observed to be larger than 0.34 nm (~0.37 nm for sample #1B), showed an increasing trend with increasing Au nanoparticle size, and reaching as high as ~0.4-0.45 nm corresponding to sample #4B, 5B, and 6B. Meanwhile, GNPs with smaller radius of curvature (sample #1B) will exhibit highly strained graphene layer stacking within the shells, this could be further explained with the blue shift of G-band peak location for smaller GNPs respect to flat graphene sheet (Figure 3.9E).[138] I_D/I_G ratio essentially remained the same for all the samples indicating proportional increase in the disordered and graphitic content of the shells, irrespective of the shell thickness (Figure 3E).

Table 3.3 Table summarizing average size of Au nanoparticles before and after CVD growth of graphene shells, corresponding inter-particle spacing, graphene shell thickness, inter-planar c-axis spacing, and G-band position from Raman spectra of the samples after GNP growth. *Note: The samples after GNP growth are referred as B series samples.*

Average size of Au nanoparticles (nm)			After CVD growth of GNPs			
Before CVD growth	After CVD growth	Size change (nm)	Inter-particle spacing (nm)	Shell thickness (nm)	Inter-planar spacing of shells (nm)	G-band location (cm^{-1})
30.4±9.5(#1A)	31.0±8.2(#1B)	0.6	22.7±9.6	2.1±0.7	0.37±0.02	1598.0±3.0
106.8±25(#2A)	112.0±38(#2B)	5.2	107.2±47	4.5±1.8	0.41±0.01	1602.7±1.1
215.2±56(#3A)	235.8±75(#3B)	20.6	256.2±104	10.0±2.1	0.43±0.06	1593.4±2.1
301.5±112(#4A)	380.2±90(#4B)	78.7	557.7±222	10.9±1.0	0.45±0.04	1595.9±3.9
362.1±160(#5A)	509.1±156(#5B)	147	1029.0±447	11.4±1.5	0.42±0.02	1593.5±2.5
662.3±186(#6A)	844.0±236(#6B)	181.7	1900.6±637	10.6±1.6	0.40±0.04	1591.2±9.0

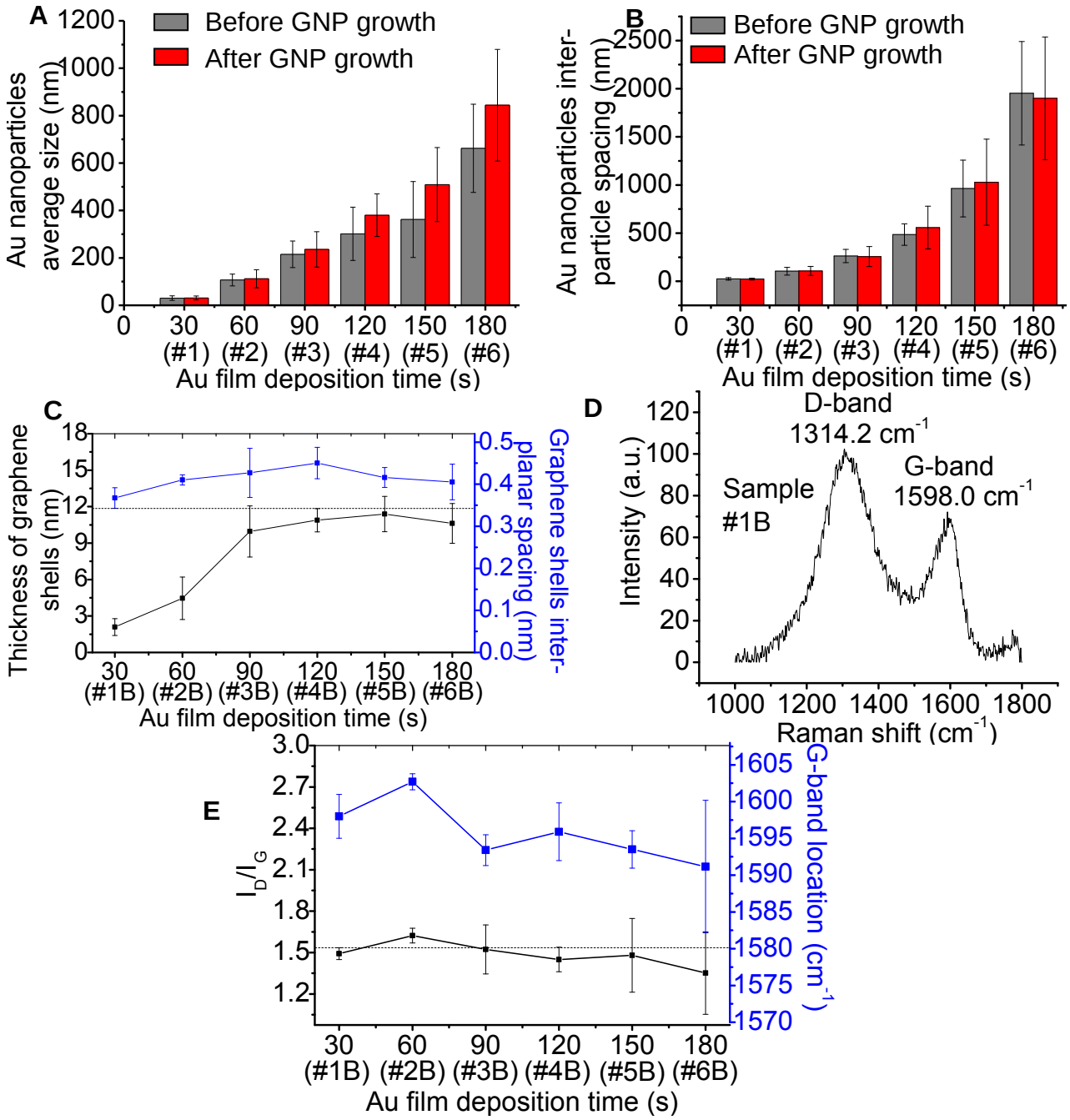

Figure 3.9 Histograms showing (A) size and (B) inter-particle spacing distributions for AuNPs before (gray) and after (red) CVD process. (C) Average thickness (black) and average lattice spacing (blue) for graphene shells in GNPs. (D) A representative Raman spectrum for GNPs (sample #1B). (E) Average I_D/I_G ratio and G-band peak location from Raman spectroscopy.

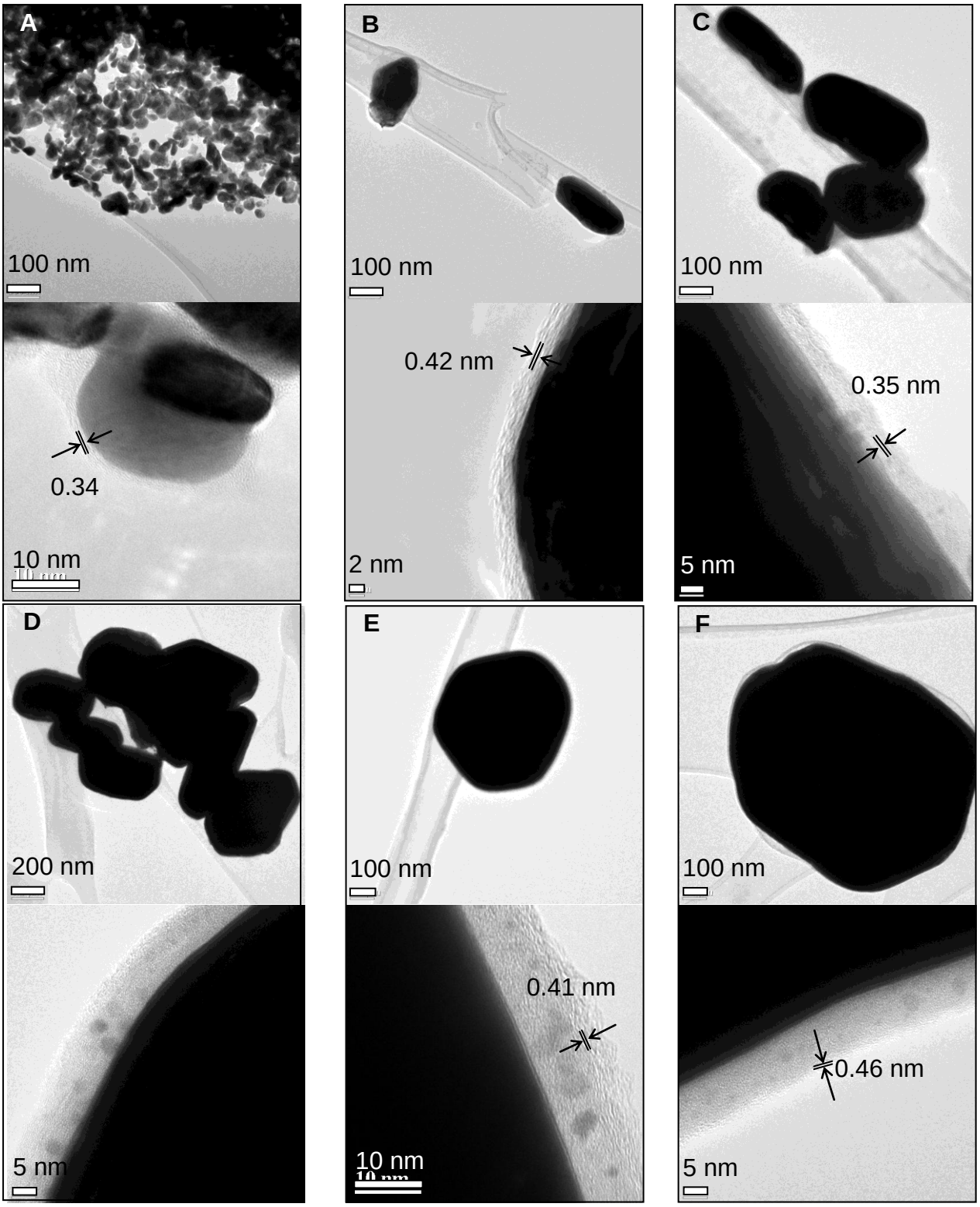

Figure 3.10 TEM images of GNPs corresponding to (A) Sample #1B, (B) Sample #2B, (C) Sample #3B, (D) Sample #4B, (E) Sample #5B, (F) sample #6B.

3.4.2 Formation of CNT-Au heterostructure and graphene shells growth

The inert and pristine surface of as-prepared CNT makes it difficult for the attachment of metal precursors by wet impregnation.[139,140,141] The dewetting methods, on the other hand, does not have problem of dispersion and attachment of AuNPs because it is a dry-process leads to a decrease of surface energy of gold. We selected gold sputtering and annealing conditions based on our dewetting systematic study to fabricate CNT-Au heterostructures. In order to prepare CNT-Au nanoparticle heterostructures, dewetting (annealing) temperature of ~400 ^{o}C was selected because CNTs are stable at this temperature. After the dewetting process, graphene shells were further formed on this hybrid (referred as CNT-Au-C). CNT, CNT-Au, and CNT-Au-C heterostructures were characterized by SEM (Figure 3.11 and 3.12). Figure 3.11A summarized the diameter distribution of CNT after annealing and graphene shells growth, Figure 3.11B-C compared the size, inter-particle distance of AuNPs on CNT before and after graphene shells growth. SEM image of unannealed CNT-Au was shown in Figure 3.12A (left panel). Before annealing, CNTs were uniformly covered with gold, and no individual nanoparticles can be seen. After annealing at 400 ^{o}C for 2 h, the deposited Au-film on CNTs and on Si substrate underwent dewetting process and resulted in Au islands (Figure 3.12A right panel). Due to the shadow effect,[142] Au must be deposited on CNTs in a form of stripes with thin edges on the sides of CNTs.[143] After CVD process, semitransparent shells formed on the gold segment, indicating the deposition of carbon on gold surface (Figure 3.12B). HR-TEM images showed the interlayer spacing of shell is ~0.3-0.5 nm, suggesting it is graphene shell (Figure 3.13).

A decreasing trend in the CNT average diameters is observed and in the following order (Figure 3.11A): As synthesized CNTs (~43.8±18.2 nm) > CNTs with dewetted Au nanoparticles

(~29.4±11.9 nm) > CNTs with GNPs (~19.9±4.2 nm). This indicates that CNT walls were etched during the dewetting process as well as CVD growth of graphene shells. Further reduction in CNT diameters after the CVD growth of GNPs can be attributed to both their vulnerability at high process temperature (>600 ^{o}C) as well as reducing H_2 environment. So it is necessary to use multi-walled CNT with large diameter to sacrifice part of walls. Both size and inter-particle spacing of AuNPs were slightly increased after graphene shells growth (size from ~21 to ~24 nm, inter-particle distance from ~9 to ~12 nm, Figure 3.11B, C). The maintaining of AuNPs size holds a significant role for applications of CNT-Au-C heterostructures due to the importance of morphology to nanostructures. The thin graphene shell can protect AuNPs on CNTs from aggregation, and AuNPs majorly maintained their original morphology before high temperature CVD process.

Raman spectra hold important information about graphite samples, from which the quality of CNTs, and the potential of Raman enhancement of CNT-Au-C heterostructures can be shown. Even though CNTs were etched during the processes of sputtering Au and graphene shells growth, the Raman intensity of CNT followed a increasing trend in the order of CNT-Au-C > CNT-Au > CNT (Figure 3.14B, D, E). It indicates that AuNPs on CNTs formed through dewetting process have Raman enhancement effect.[144] Moreover, the Raman enhanced effect maintains after graphene shells formed on AuNPs. The intensity of D-, G-band for graphene structure even increased after CVD process, due to the graphene shell formation. As-grown CNTs showed the lowest I_D/I_G ratio (Figure 3.14C) as compared to after dewetting process, which confirmed that CNT structural damage occurred during the latter process. However, this ratio decreased again after the growth of graphene shells due to their well-ordered and defect-

free structure that dominated the Raman spectrum. In addition, the blue shift (Figure 3.14E) in the G-band peak location (~1590 cm^{-1}) for CNTs coated with GNPs as compared to as-grown CNTs (~1581 cm^{-1}) re-confirms our argument about the strained lattice in the former.

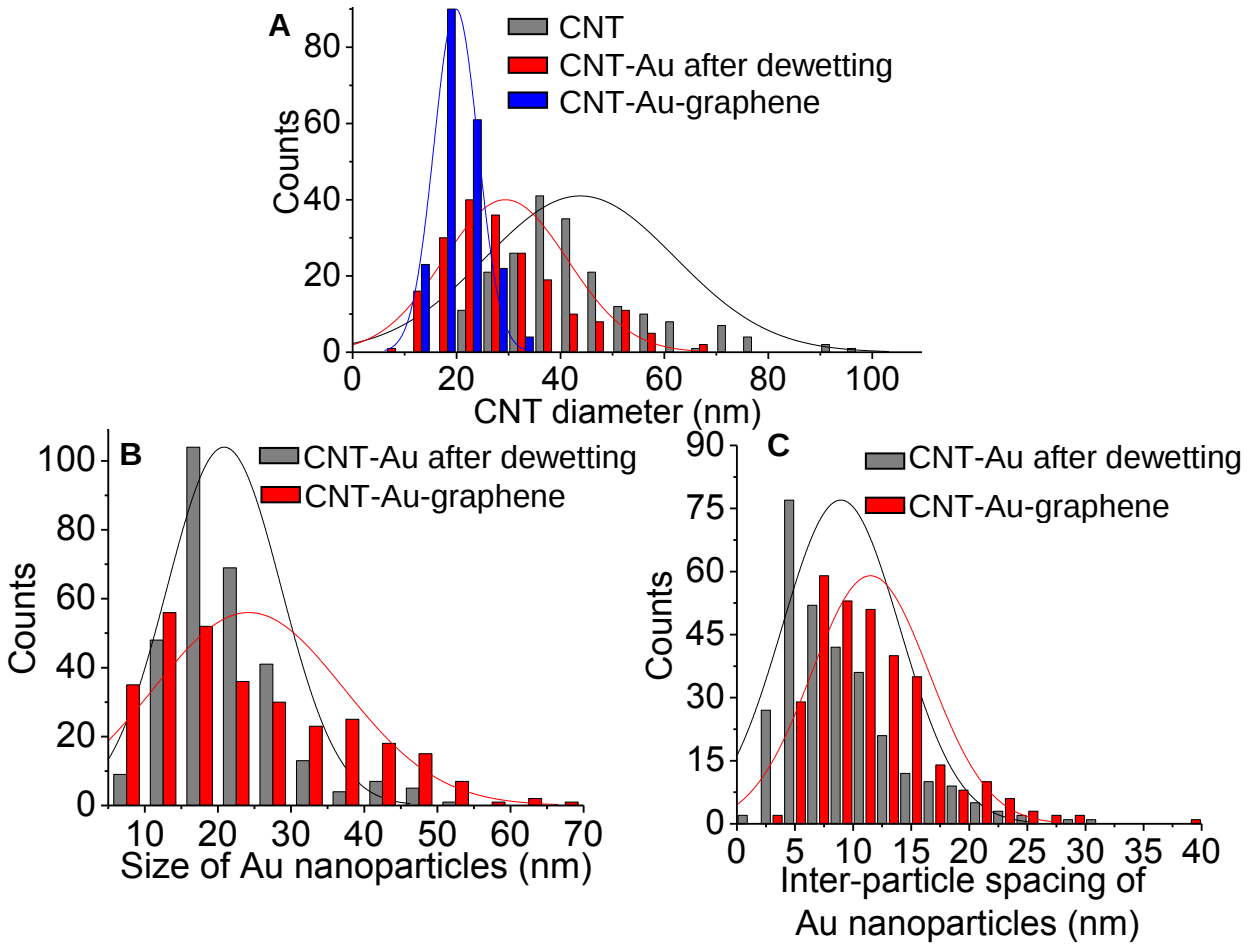

Figure 3.11 Histograms showing (A) diameter distributions of as-synthesized CNTs (black, average ~43.8±18.2 nm), annealed CNTs with dewetted Au nanoparticles (red, average ~29.4±11.9 nm), and CNTs with GNPs (blue, average ~19.9±4.2 nm). (B) Size and (C) inter-particle spacing distributions of dewetted Au nanoparticles on CNTs before (average size ~20.8±7.8 nm, average spacing ~8.9±5.1 nm) and after CVD growth of graphene shells (average size ~24.2±13.0 nm, average spacing ~11.5±5.1 nm).

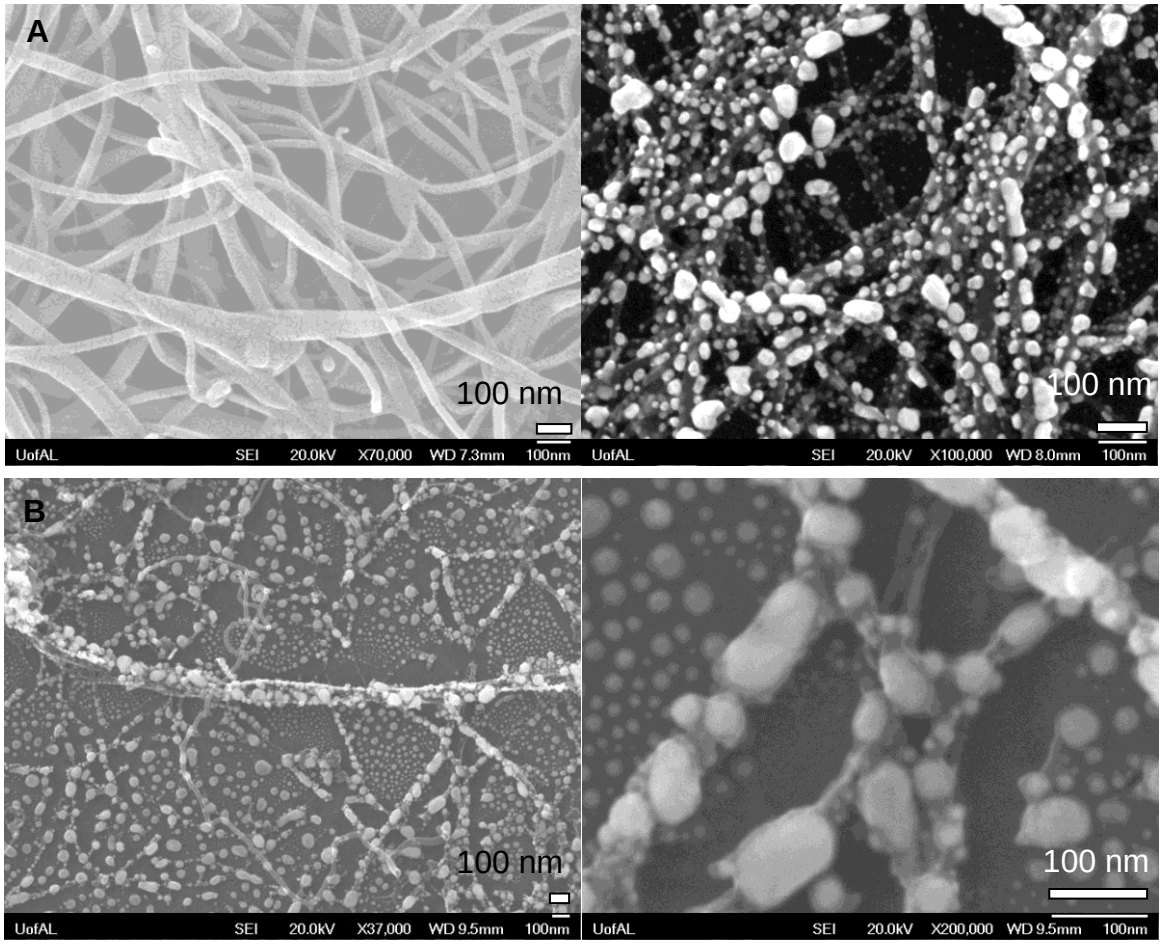

Figure 3.12 SEM images showing substrates of Au sputtered on CNT for (A) 30 s, before (left panel) and after (right panel) annealing, (B) graphene shells encapsulated Au on CNT (CNT-Au-C) using CNT-AuNPs obtained from annealing of 30s sputtered Au film on CNT.

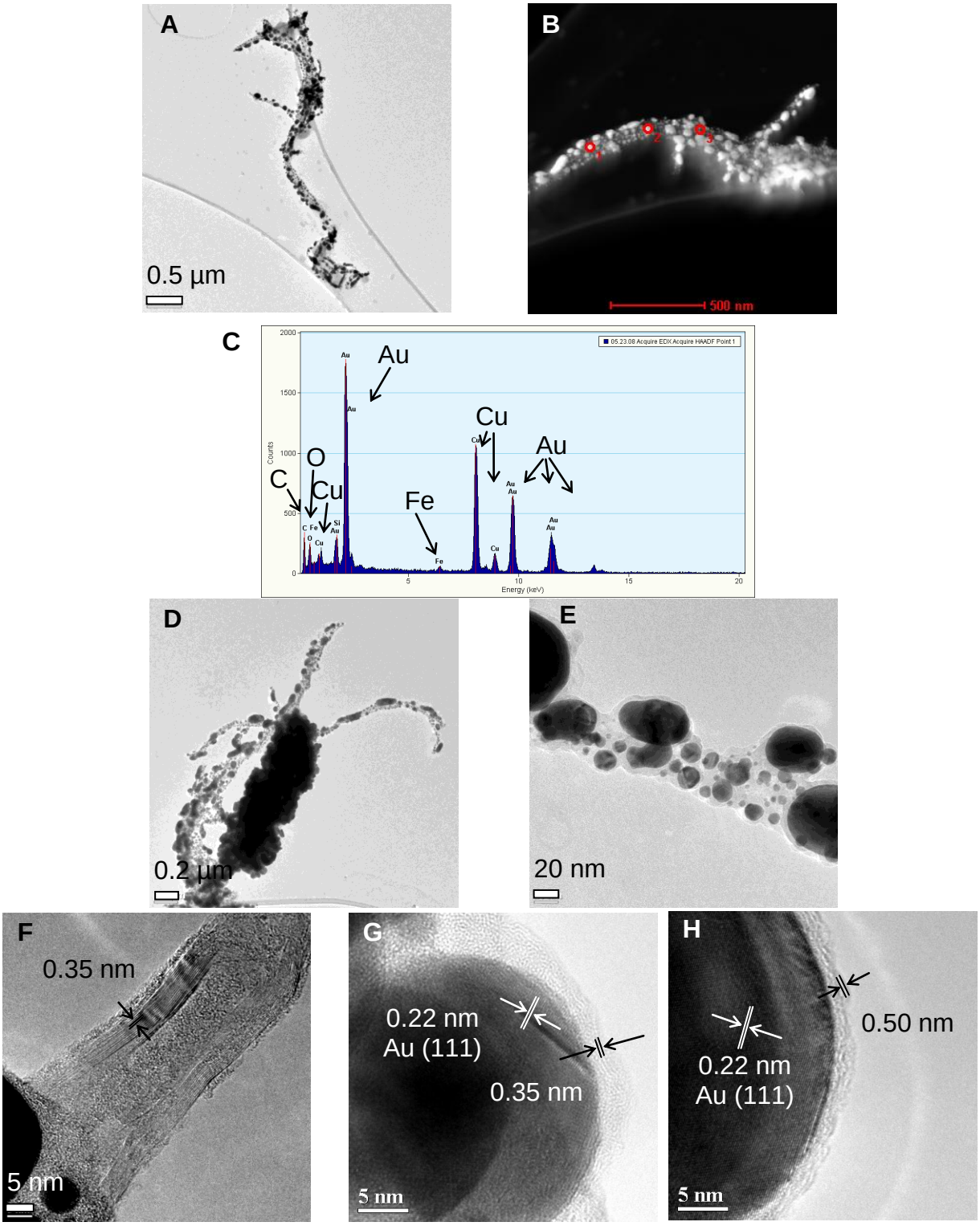

Figure 3.13 TEM images, STEM image, and EDS of graphene shells encapsulated Au on CNT using CNT-Au nanoparticles obtained from annealing of 30s sputtered Au film on CNT.

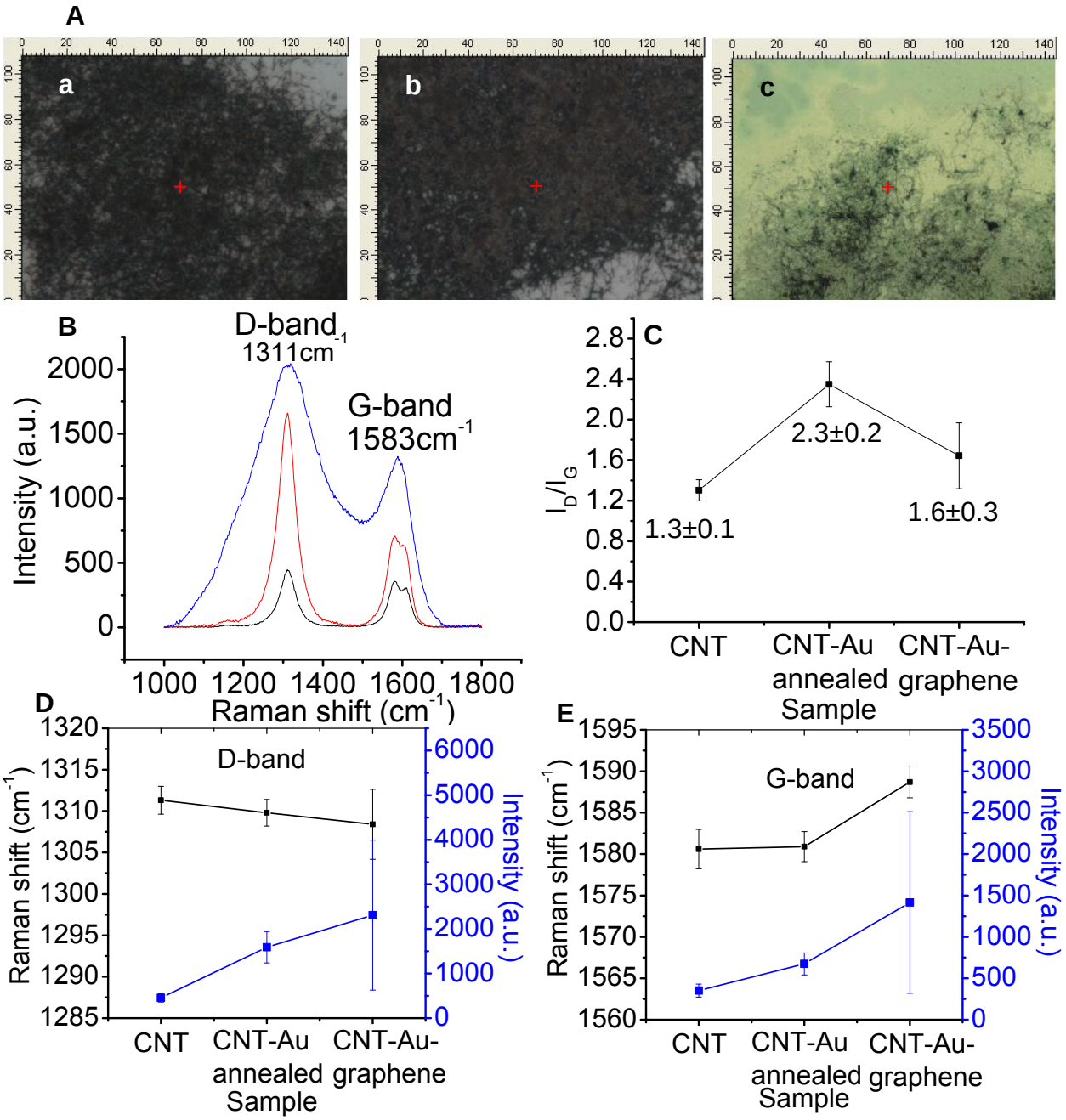

Figure 3.14 (A) Optical images for (a) CNT, (b) CNT sputtered with Au after annealing, and (c) annealed CNT-sputtered Au after graphene shells growth. (B) Raman spectra for as-synthesized CNTs (black), CNTs with Au nanoparticles after dewetting (red) and CNTs with GNPs after CVD growth (blue). (C) I_D/I_G ratio estimated using spectra in (B). (D, E) Comparison of D-, G-band intensity and Raman shift for each sample.

3.5 Discrete dipole approximation calculations for AuNPs, GNPs, and CNT-AuNPs heterostructures.

Numerical simulations using open source program DDSCAT developed by Draine and Flatau[132] based on the discrete dipole approximation (DDA) were employed in order to model the optical properties of Au islands formed by dewetting, graphene shells encapsulated AuNPs (GNPs), and CNT-Au heterostructure. The dielectric function of Au and graphene was from program build-in database. For convenience, the simulations were carried out for nanostructures in vacuum with a refractive index of $n=1.0$. The direction of incident light was assumed through *x-axis*. The island shape was modeled as sphere. Flowchart of modeling for AuNPs, GNPs, CNT and CNT-Au heterostructures were shown in Figure 3.15 and Figure 3.16, parameters were shown in Table 3.4 and 3.5.

The surface plasmon extinction of AuNPs and GNPs has been studied as the basis for potential application in chemical and biological sensing.[145,146] During our simulation, the selection of AuNPs size and graphene shell thickness was based on experimental results. Figure 3.17 displays extinction spectra for AuNPs with different sizes (~30- 660 nm), which were obtained by dewetting of Au-films deposited for different thickness. The extinction was given by:

$$Q_{ext} = Q_{sca} + Q_{abs} \tag{3.1}$$

where Q_{ext} is extinction efficiency factor, Q_{sca} is scattering efficiency factor, and Q_{abs} is absorbance factor.

The extinction peaks for AuNPs with size ranging from ~30 to 100 nm exhibit typical surface plasmon resonance of AuNPs, showing maximum location around 500-550 nm.[147] More precisely, the peaks located around 527 nm, and became sharp and stronger as AuNPs size

increased from 30.4 nm to 106.8 nm. As the size of AuNPs increased to ~200 nm, extinction peak red-shifted, exhibited a complex structure with a shoulder around 527 nm and a broad main band around 611 nm. Further increase the size of AuNPs to ~300-600 nm, their plasmon resonance peak still located around 500-650 nm. However, the intensity of extinction decreased. Besides the typical surface resonance of gold around 550 nm, the extinction spectra also exhibited shoulders in ultraviolet region. The extinction efficiency factor is constructed by absorbance and scattering. It has been reported that for islands with a major axis smaller than ca. 50 nm the extinction is dominated by the absorbance.[148,149] Above this size, the contribution of scattering to the total extinction gradually increases, eventually becoming dominant. At the same time, the surface plasmon peak red-shifts considerably to longer wavelengths and becomes much broader. Hence, in our case, the shoulders located in ultraviolet region were attributed to the absorbance; for peaks located around 550 nm, their red-shift and broadening are influenced primarily by scattering.

Extinction spectra for GNPs were shown in Figure 3.17B. Since the fabrication of GNPs have similar size of AuNPs-cores with their corresponding original AuNPs, their spectra showed similar tendency with AuNPs. The difference is that GNPs exhibits a stronger shoulder in ultraviolet region (~200-250 nm), which is attributed to the absorbance effect from their graphene shell.

Figure 3.18 and Figure 3.199 presents visualization of normalized electric near field intensity (defined as the ratio between the near field and incident field, $|E|/|E_0|$) of AuNPs and corresponding GNPs.[150] AuNPs with size within ~110 nm (obtained from sputtering Au for 30 s and 60 s) showed large electric field surround the spherical nanoparticles and the dipolar field

due to plasmon resonance (Figure 3.18A, C). As size increased larger than 200 nm, the dipoles location gradually shifted along with the light direction (Figure 3.18E, Figure 3.19A, C, E), and normalized near field intensity decreased. That is due to the dominant of scattering as size increasing. Also, when the size of AuNPs close or larger than the incident light wavelength, the incoming light would be blocked and left shadow behind gold particles. Their corresponding GNPs presented similar trend (Figure 3.18B, D, F, and Figure 3.19B, D, F).Moreover, even though the absolute intensity of normalized electric field slightly decreased comparing to their original AuNPs before graphene shells growth, the interaction between graphene shells with AuNPs-core resulted in a larger electric field with more hot-spots on the edge of GNPs. The visualization of normalized near field of AuNPs and GNPs predict the potential of our GNPs in application of SERS, which theoretically proved our experimental observation of Raman signal enhancement of graphene after putting AuNPs on CNT and grow graphene shells (Figure 3.14B).

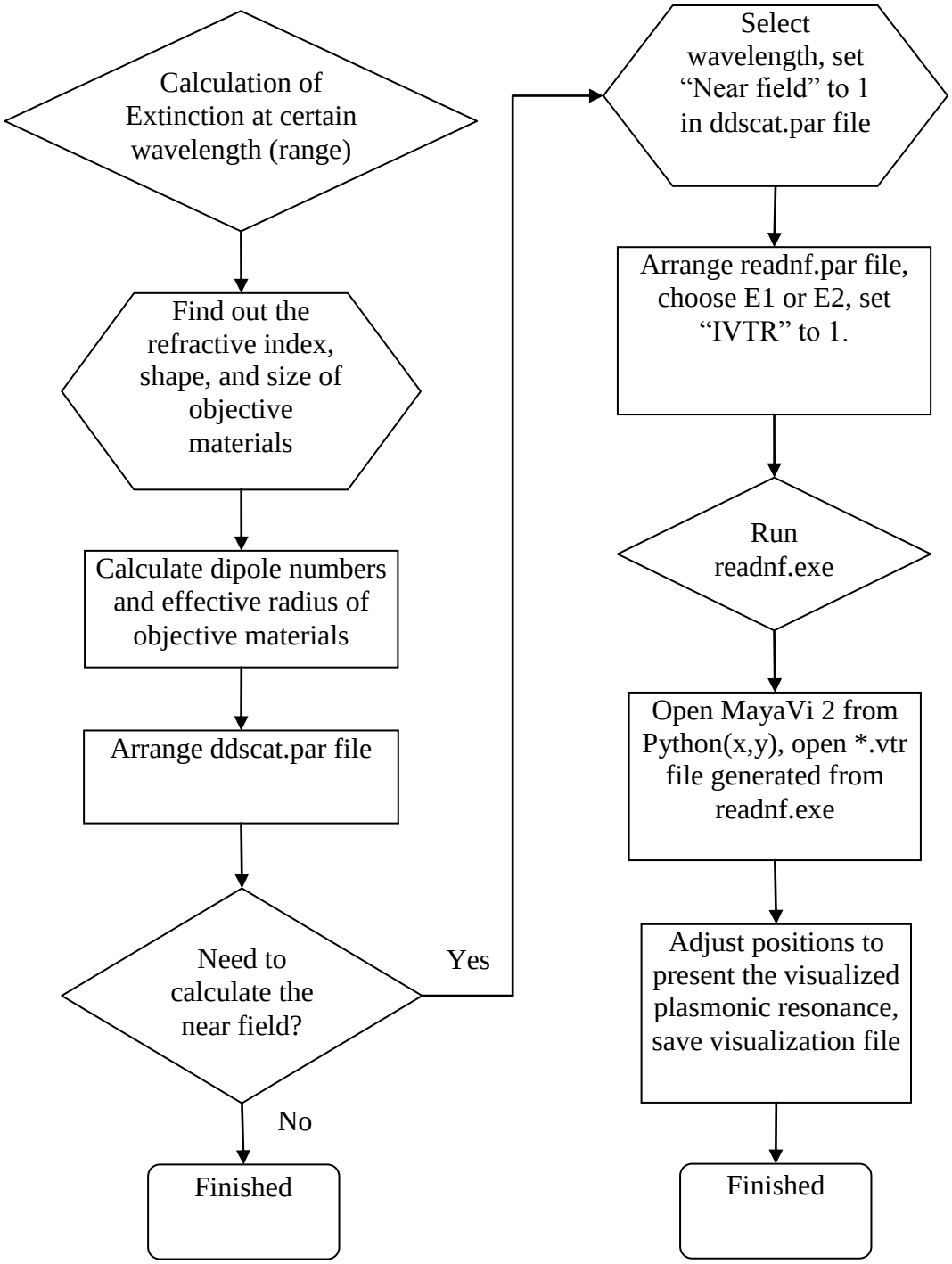

Figure 3.15 Flowchart shows plasmonic modeling for AuNPs and GNPs.

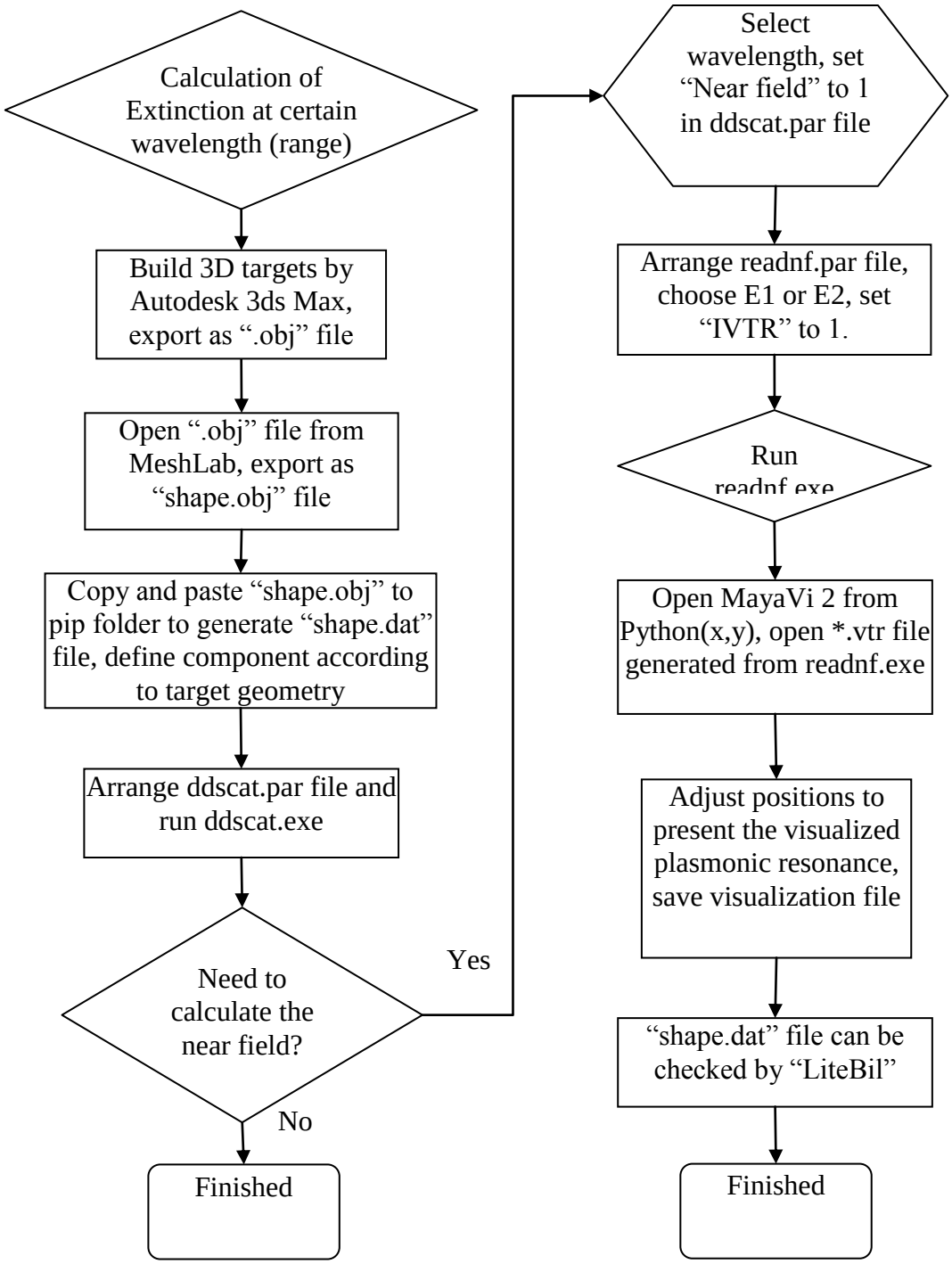

Figure 3.16 Flowchart shows plasmonic modeling for CNT and CNT-Au heterostructures.

Table 3.4 Parameters used in DDA calculations for bare AuNPs

Au film deposition time (s, sample #)	Effective radius (μm)	Dipole-number	Shape parameter	Dipole spacing (nm)	Experimentally observed average size of Au nanoparticles (nm)
30 (#1A)	0.0152	65752	50	0.608	30.4
60 (#2A)	0.0535	65752	50	2.136	106.8
90 (#3A)	0.1078	65752	50	4.304	215.2
120 (#4A)	0.1510	65752	50	6.030	301.5
150 (#5A)	0.1813	65752	50	7.242	362.1
180 (#6A)	0.3317	65752	50	13.246	662.3

Table 3.5 Parameters used in DDA calculations for GNPs. Average size of GNPs, core AuNP, and average graphene shells thickness are consistent with experimental observations.

Au film deposition time (s, sample #)	Effective radius (μm)	Dipole-number	Shape parameter	Dipole spacing (nm)	Core Au nanoparticle size (nm)	Average graphene shell thickness (nm)	Experimentally observed Average size of GNPs (nm)
30 (#1B)	0.0176	22887	35.2	1	31	2.1	35.2
60 (#2B)	0.0605	116129	60.5	2	112	4.5	121
90 (#3B)	0.1291	72072	51.16	5	235.8	10	255.8
120 (#4B)	0.2010	272200	80.4	5	380.2	10.9	402
150 (#5B)	0.2661	154088	66.4875	8	509.1	11.4	531.9
180 (#6B)	0.4325	338947	86.52	10	844	10.6	865.2

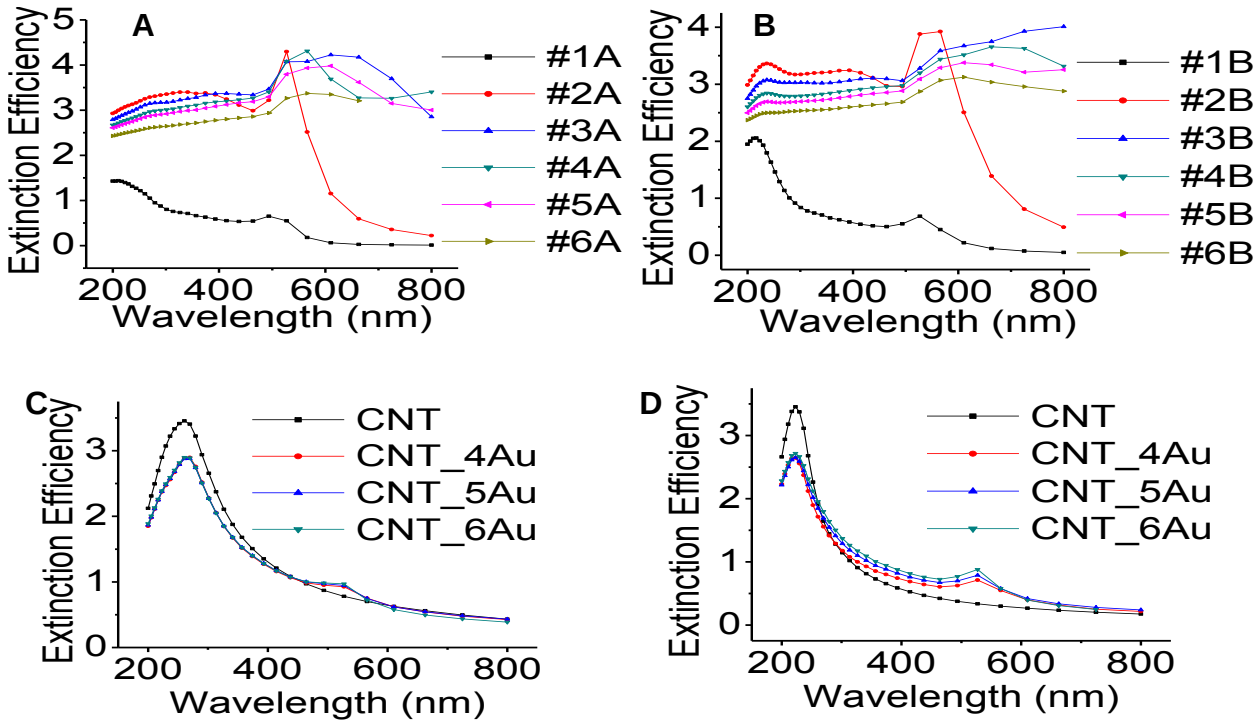

Figure 3.17 Extinction efficiency spectra for (A) spherical Au nanoparticles, and (B) GNPs. Extinction efficiency spectra for CNT, CNT-Au when incidence light is (C) vertical to CNT, and (D) along axial direction of CNT.

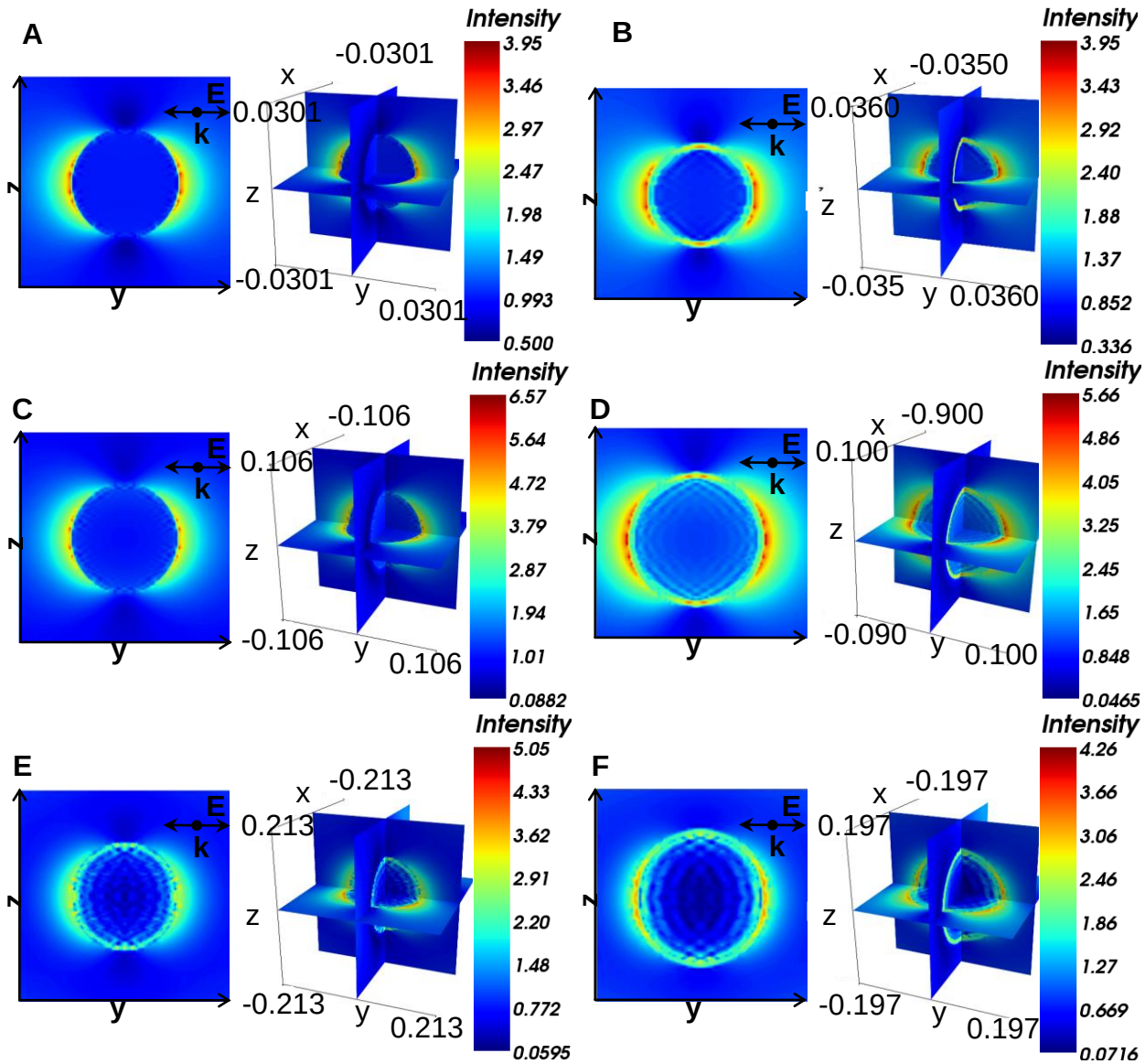

Figure 3.18 DDSCAT calculations showing normalized electric field around Au nanoparticles before and after graphene shells growth. The calculations were performed using average dimensions for bare Au nanoparticles and GNPs as given in Table S5 and S7 (A) sample #1A at 494 nm, (B) sample #1B at 527 nm, (C) sample #2A at 527 nm, (D) sample #2B at 566 nm, (E) sample #3A at 611 nm, (F) sample #3B at 611 nm. *Note: The selected wavelength corresponds to the extinction efficiency spectrum peak location for Au.*

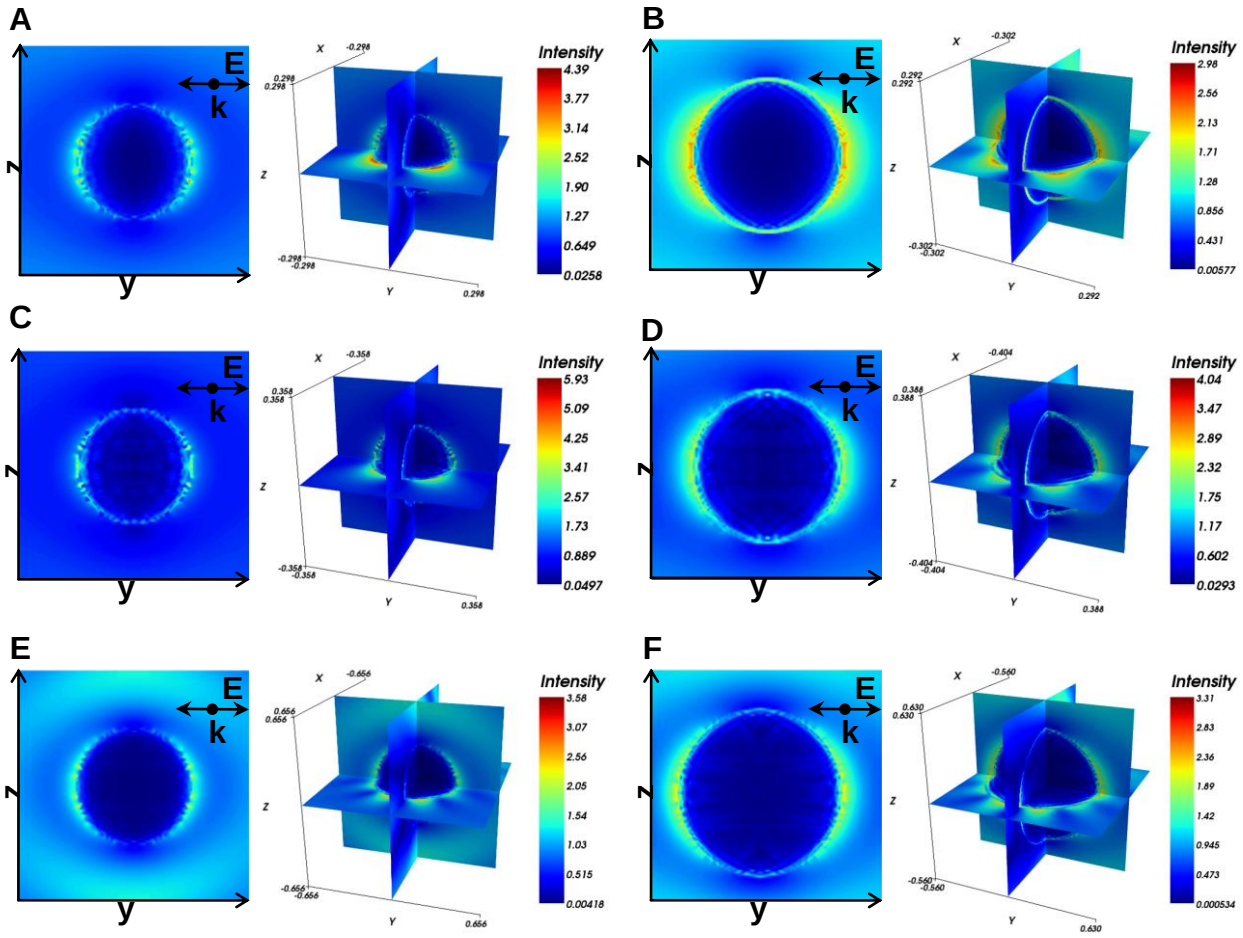

Figure 3.19 DDSCAT calculations showing normalized electric field around Au nanoparticles before and after graphene shells growth. The calculations were performed using average dimensions for bare Au nanoparticles and GNPs as given in Table S5 and S7 (A) sample #4Aat 566 nm, (B) sample #4B at 566 nm, (C) sample #5A at 611 nm, (D) sample #5B at 611 nm, (E) sample #6A at 566 nm, (F) sample #6B at 611 nm. *Note: The selected wavelength corresponds to the extinction efficiency spectrum peak location for Au*.

Figure 3.17C-D showed extinction spectra for CNT and CNT-Au heterostructures. The diameter of CNT and AuNPs were selected based on our experimental data (Table 3.6). Three conditions were simulated by arranging the number of AuNPs attached on radial plane of CNT (4, 5, and 6 AuNPs, respectively). The 3-D geometry of CNT and CNT-Au heterostructures were shown in Figure 3.20-3.23. Since the incident light direction is assumed along x-axis during DDSCAT calculation, we can adjust the space direction when we were building the 3-D structures to obtain different angles of incident light on our nanostructures (on radical direction or axial direction).

In Figure 3.17C, incident light is vertical to CNT (on radical direction); whereas incoming light is along axial direction of CNT in Figure 3.17D. Extinction curve of CNT only exhibited strong absorbance peak located around 200-300 nm. By adding AuNPs on radical plane of CNT, CNT-Au heterostructure showed extinction peak around 527 nm. Adding the number of AuNPs attached on CNT reduced the inter-particle spacing between each AuNPs. In case of incident light along axial direction of CNT, we observed increasing of gold extinction peak as more AuNPs attached on CNT (Figure 3.17D).

Comparing the visualization of near field for CNT and CNT-Au heterostructure (Figure 3.20-3.23), we observed strong enhancement of surface plasmon resonance after AuNPs attachment, and after reducing the inter-particle distance between AuNPs. In case of 4-AuNPs (Figure 3.21), plasmons between AuNPs almost do not couple; while the AuNPs number increased to 5, and 6, as they were getting closed to each other (Figure 3.22 and Figure 3.23), strongly coupled contribution to the gold absorption. The enhancement of near field intensity reveals the importance of manipulating geometry of nanostructure and polarization of light in application of SERS.

Table 3.6 Parameters used in DDA calculations for CNT and CNT-AuNPs heterostructure. The CNT radius and AuNP radius are consistent with the experimental observations.

Target	CNT inner wall radius (nm)	CNT outer wall radius (nm)	CNT length (nm)	Radius of Au nanoparticles (nm)	Dipole-number (N)	Dipole spacing (nm)	Effective radius (μm)
As-synthesized CNT	4	22	80	10	86724	1	0.0275
CNT with 4 Au nanoparticles	4	15	80	10	51504	1	0.0231
CNT with 5 Au nanoparticles	4	15	80	10	54296	1	0.0235
CNT with 6 Au nanoparticles	4	15	80	10	57716	1	0.0240

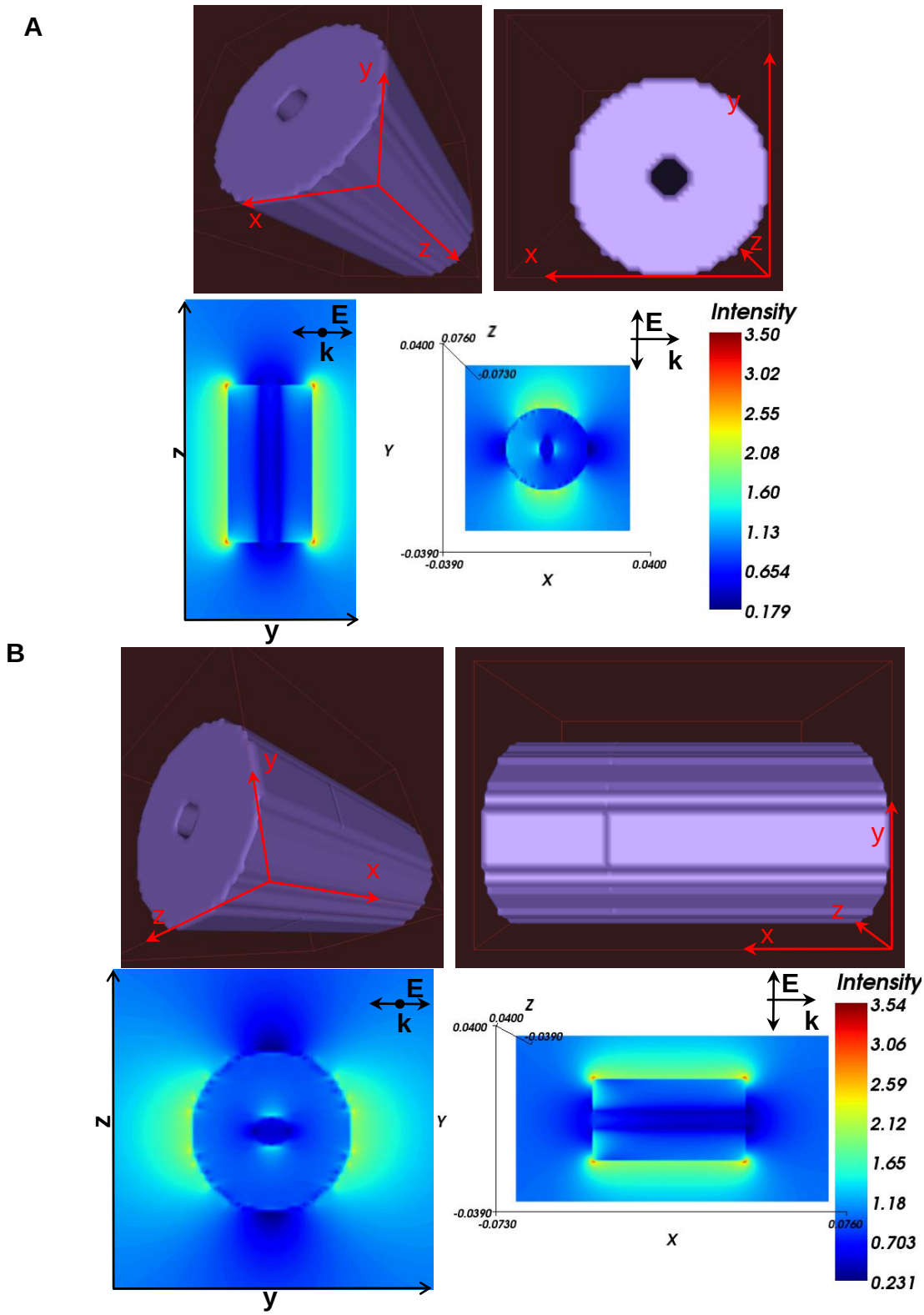

Figure 3.20 3D image of CNT normalized electric field intensity at 527 nm wavelength when incidence light **k** is (A) vertical to CNT, and (B) along axis of CNT.

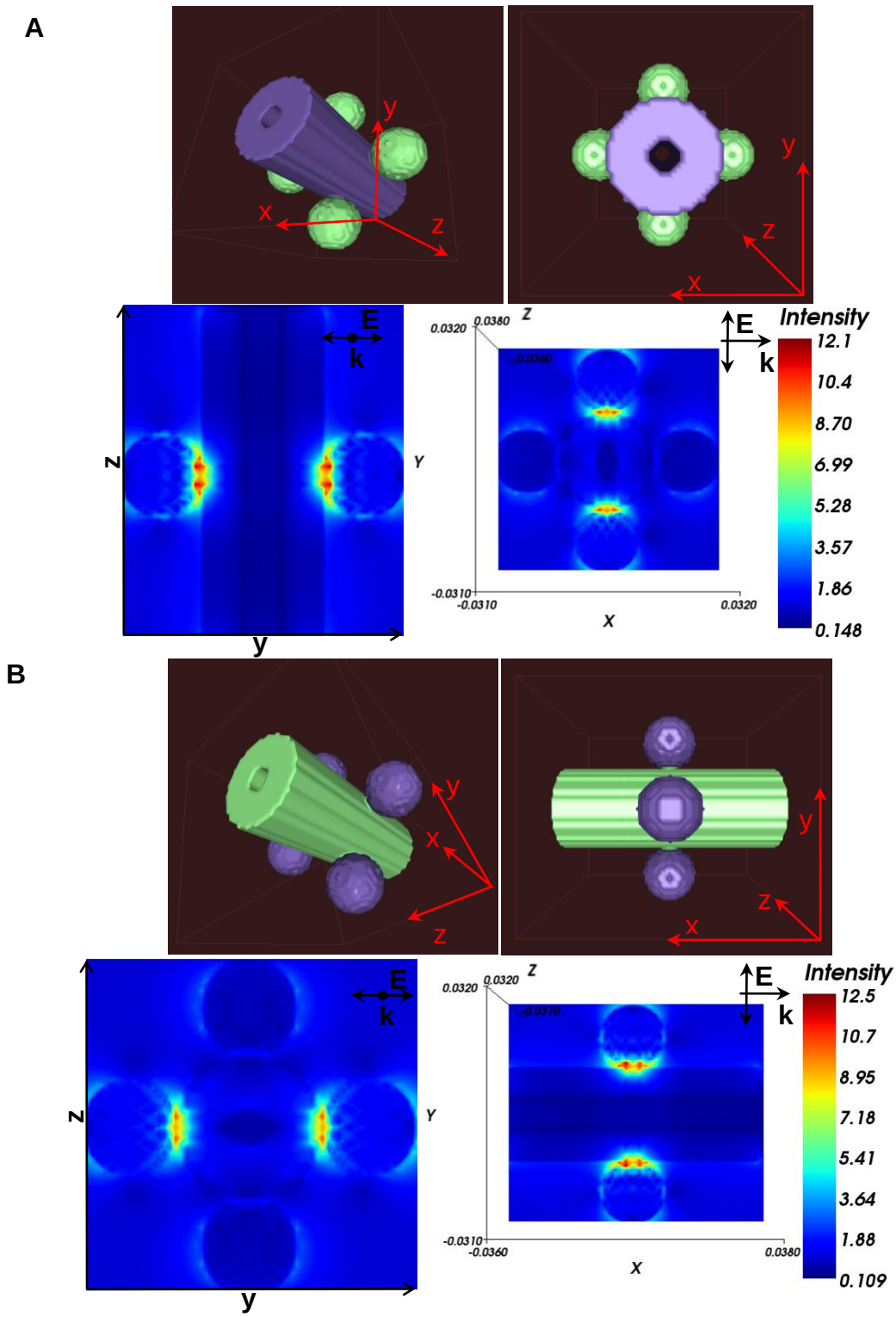

Figure 3.21 3D image of CNT decorated with 4 AuNPs and near field image at 527 nm wavelength when incidence light is (A) vertical to CNT, and (B) along axis of CNT.

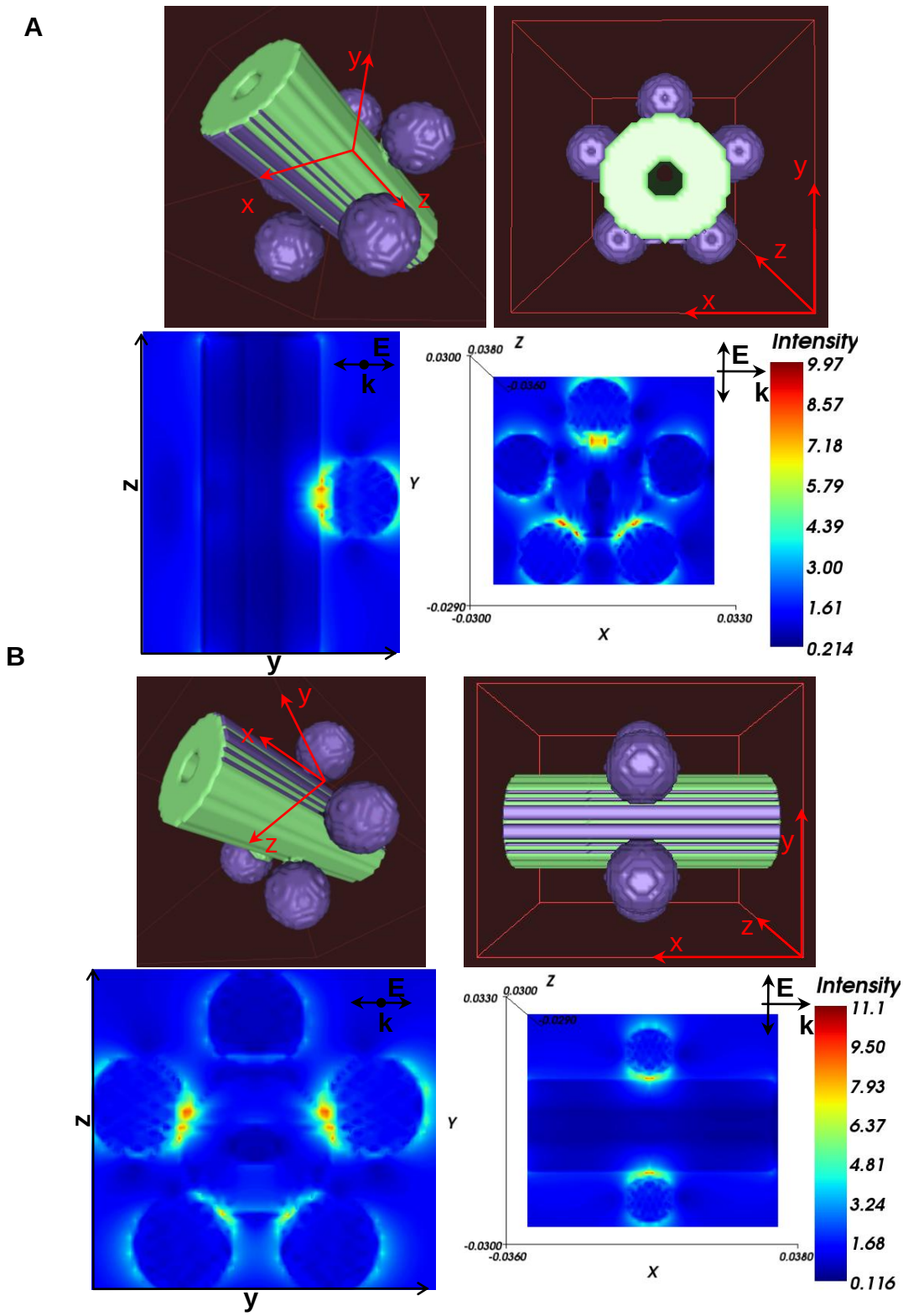

Figure 3.22 3D image of CNT decorated with 5 AuNPs and near field image at 527 nm wavelength when incidence light is (A) vertical to CNT, and (B) along axis of CNT.

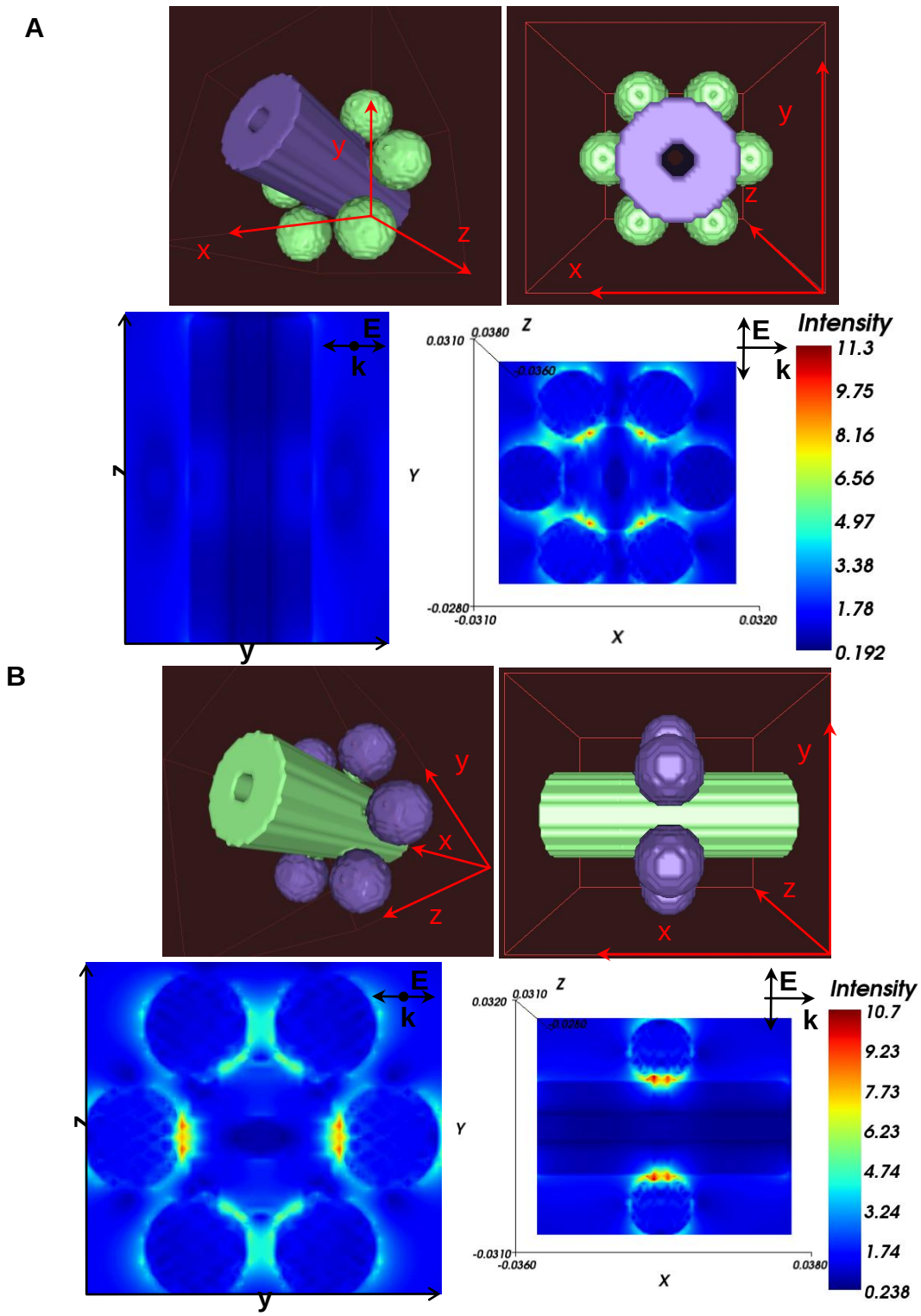

Figure 3.23 3D image of CNT decorated with 6 AuNPs and near field image at 527 nm wavelength when incidence light is (A) vertical to CNT, (B) along axis of CNT.

3.6 Conclusions

In summary, monodispersed Au islands on substrate were synthesized, and the morphology evolution of this dewetting process was systematically studied by varying deposition time/film thickness, annealing temperature, time, atmosphere, and substrates. The solid state dewetting process is driven by minimization of surface and strain energy, which involves the initiation of voids on deposited Au films and the growth of holes. Given enough temperature, the dewetting can be accomplished within several minutes, and thicker gold films would result in bigger Au islands with decreased fraction of area covered by islands on substrate. The variation of substrates and annealing temperature changes surface energy of Au film and lead to different morphology of Au islands. Monodispersity of Au islands allows us to study the size effect of Au islands on the growth of graphene shell. It indicated that larger Au islands helped to form thicker graphene shells. This morphology evolution study also allows us to select appropriate conditions to fabricate CNT-Au heterostructure, and further grown graphene shells to stabilize AuNPs on CNT. Detailed study on optical properties of AuNPs, GNPs, and CNT-Au were conducted through DDSCAT calculation, which theoretically explained the Raman signal enhancement effect after attached AuNPs on CNT, and predict the significant potential of our CNT-Au-C heterostructure in application of optical sensing.

CHAPTER 4: GRAPHENE SHELLS ENCAPSULATED PALLADIUM NANOPARTICLES AND THEIR OPTICAL PROPERTIES

4.1 Introduction

In order to explore versatility of our CVD approach and verify the influence of plasma oxidation on graphene shells growth, here we report the fabrication of graphene shells encapsulated PdNPs (GNPs), using PdNPs that have been treated through different oxidation conditions. The as-synthesized cubic PdNPs, oxidation and graphene shells encapsulated products were characterized for their morphology, crystal structures, and chemical compositions. The usage of palladium in surface enhanced Raman spectroscopy (SERS) has just been studied in recent 20 years, and more effort needs to be invested in this field. In the application of SERS, thick carbon shells may hinder the enhancement of chemical signal. In this regard, thin graphene shells are expected. Additionally, various chemistry of graphene provides potential for this heterostructure in the field of selective sensing. To study the potential application of palladium in SERS, plasmonic modeling for palladium nanoparticles with different shape, size, and shell thickness for palladium/graphene core/shell heterostructures have been done by discrete dipole approximation (DDA) through DDSCAT 7.2. Figure 4.1 outlines steps investigated in this chapter, including: 1) Synthesis of cubic PdNPs; 2) The oxidation kinetics of cubic PdNPs in a plasma oxidation process was studied by varying the plasma treatment duration; 3) The effect of palladium oxide formation for the CVD growth of carbon/graphene shell encapsulating PdNPs

(GNPs) was evaluated using PdNPs that have been plasma oxidized for different time as catalysts during the growth of graphene shell.

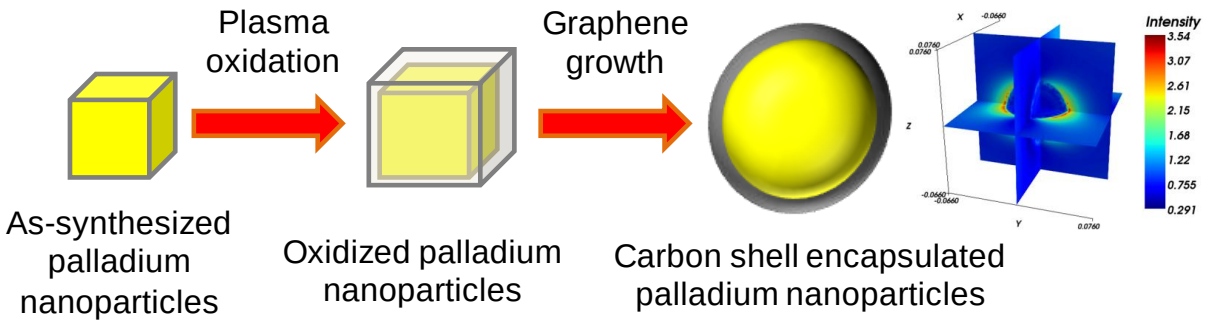

Figure 4.1 Schematic shows various steps including controlled synthesis of cubic PdNPs, their plasma oxidation, and subsequent utilization as catalysts for the growth of GNPs. Finally, the optical property of GNPs was studied by plasmonic modeling.

4.2 Experiment Methods

4.2.1 Materials and Methods

Potassium bromide (KBr) and L-ascorbic acid (AA) were purchased from Acros Organics (New Jersey). Potassium chloride (KCl) and Xylene (o-, m-, p- isomers) were bought from Fisher Scientific (New Jersey). Sodium tetrachloropalladate (II) hexahydrate ($Na_2PdCl_4 \cdot xH_2O$ ($x \approx 3$), 99.999%) was purchased from Alfa Aesar (Ward Hill, MA). Polyvinylpyrrolidone (PVP, $(C_6H_9NO)_n$ average mol wt 40,000) was bought from Sigma-Aldrich (Louis, MO). 3-Mercaptopropyltrimethoxysilane (MPTMS, $HSCH_2CH_2CH_2Si(OCH_3)_3$, 97+ %) was bought from TCI America (Portland, OR). All chemicals were used without further purification. Labnet centrifuge (Edison, NJ) was used to clean, wash, and separate nanoparticles. Wet samples were dried in a VWR vacuum oven (West Chester, PA). Silicon (Si) wafers (100, n-type) were purchased from IWS (Colfax, CA). DI water (18.1 MΩ-cm) was obtained using a Barnstead International DI water system (E-pure D4641). Oxygen plasma treatment was performed in Model 1021 plasma cleaner (E.A. Fischione Instruments, PA). Graphene shells growth was conducted inside Lindberg blue 3-zone tube furnace (Watertown, WI). Quartz tubes were purchased from ChemGlass (Vineland, NJ). Syringe injector was obtained from Fisher Scientific (Suwannee, GA). Thermocouples and temperature controllers were bought from Omega Engineering (Stamford, CT). H_2 (UHP grade, 40% balanced with Ar) and Ar (UHP grade) gas cylinders were purchased from Airgas South (Tuscaloosa, AL). Gas flow rates of all chemical vapor deposition processes were controlled by Teledyne Hasting power pod 400 mass flow controllers (Hampton, VA).

4.2.2 Synthesize Cubic Palladium Nanoparticles

KBr and KCl were added as shape-control additives. An aqueous solution (~ 8.0 mL), containing ~ 0.945 mmol PVP, ~ 0.341 mmol AA, ~ 5.042 mmol KBr, ~ 2.482 mmol KCl were placed in a volumetric flask, refluxed and pre-heated in oil bath under magnetic stirring at 80 ^{o}C for 10 min. Subsequently, ~ 3.0 mL of an aqueous solution containing ~ 0.194 mmol $Na_2PdCl_4 \cdot xH_2O$ was added using a pipette. The solution was stirred and refluxed at 80 ^{o}C for 3 h. The dark brown solution was centrifuged, washed with DI water to remove excess PVP, and re-dispersed in 11 mL DI water.

As-synthesized cubic PdNPs were dispersed on piranha cleaned silicon wafer by MPTMS functionalization method and dried in vacuum oven. Firstly, silicon wafer was cleaned by piranha acid (H_2SO_4:H_2O_2=5:1 v/v) at 100 ^{o}C for 30 min, followed by washing in copious deionized water. Secondly, cleaned silicon wafer was fully dried and then immersed in reagent alcohol containing 2 mM MPTMS, gently shaking for 12 h. After silanization, the substrate was rinsed with reagent alcohol and baked at 80 ^{o}C for 1 h. Finally, PdNPs were dispersed on substrate by immersing functionalized Si wafer in PtNPs reagent alcohol solution for 12 h. After dispersion, the substrates were rinsed with reagent alcohol, dried and stored in vacuum oven.

4.2.3 Plasma Oxidation of Palladium Nanoparticles

The oxidation was performed in Model 1021 plasma cleaner at ~40 W and ~36 mTorr of mixture gas (25% O_2 and 75% Ar) pressure. The dispersed PdNPs were plasma oxidized from 5 to 90 min to result in surface oxide. As compare, as-synthesized PdNPs also been reduced by H_2 in Ar (Ar/H_2=0.18 SLM: 0.3 SLM, 25% v/v) at 300 ^{o}C for 30 min.

4.2.4 Growth of graphene shells encapsulated Palladium Nanoparticle

Substrates with as-synthesized PdNPs, H_2 reduced PdNPs, as well as PdNPs been plasma treated for different times were placed in the center of quartz tube equipped with precursor and gas lines for Ar/H_2 flow. Xylene was utilized as the carbon source and was injected through a syringe injector into a preheated zone at the rate of 45 mL/h for ~ 2 min and subsequently transported into the reaction zone (~800 ^{o}C) inside the quartz tube furnace. The xylene flow rate was reduced to 5 mL/h after H_2 mixed with Ar (Ar/H_2=0.85 LLM/0.3 SLM or 10% v/v H_2) was introduced in the CVD reactor. Here, H_2 acted as an oxygen scavenger and Ar as a carrier gas or dilutant. The CVD reaction was continued for 30 min after which H_2 and xylene were discontinued, and the furnace was cooled down under Ar flow.

4.2.5 Characterization

Tecnai F-20 was used to collect Transmission Electron Microscopy (TEM) images at 200 kV. TEM samples were prepared by dispersing as-prepared samples on lacey carbon TEM copper grids. The average nanoparticle size was measured from TEM images, where 200 nanoparticles were counted and measured per sample. Diameter was measured for spherical nanoparticles, average side length for triangular, and for nanoparticles with other shapes, diagonal length average was taken. All the measurements were done using Adobe Photoshop Software. X-ray photoelectron spectra (XPS) were gathered by Kratos Axis 165 with mono-aluminum gun. The analysis spot was set as "Slot" with >20 μm aperture and 19.05 mm iris setting. XPS was used to characterize elements' chemical states. Raman spectra were collected using Bruker Senterra system (Bruker Optics Inc. Woodlands, TX) equipped with 785 nm laser source at 10 mW laser powers and 100 × objective. The integral time and co-additions were set as 15 seconds and 2, respectively. The Raman mapping conditions for map acquisition were set at the spectral resolution of 3-5 cm-1 in the range of 102-2658 cm^{-1} with 10 mW laser power. A rectangular grid of 15 μm × 15 μm of the sample surface was chosen and 100 points on the grid were scanned in full range. OPUS Spectroscopy Software coupled with Raman spectrometer allows one to select the frequency range for populating the chemical map. The range is defined from 1500 to 1700 cm^{-1}, and then software integrated the peak area in this range and showed the spectral changes as a function of position on the substrate. The contour mapping enables one to subdivide the absorption intensity into several levels and to visualize them by a color scheme. Extinction curves of Pd nanoparticles with and without graphene shells were calculated by DDSCAT, and visualized by Python(x,y).

4.3 Shape Control of Palladium Nanoparticles

It has been demonstrated that Pd {100} facets have a higher catalytic activity than both {110} and {111} facets for CO oxidation.[151] Thus PdNPs enclosed by {100} facets are selected to be used as catalysts for graphene shells growth in this study. The synthesis of cubic PdNPs can be achieved by introducing halide ions (Br^- and Cl^-) as capping agent to selective adsorb on {100} facets.[152] Na_2PdCl_4 was used as metal salt and injected into an aqueous solution containing ascorbic acid (AA) held at 80 ^oC, with poly(vinyl pyrrolidone) (PVP) acting as a stabilizer for PdNPs.[153] Figure 4.2A, B show high resolution TEM images of the produced cubic PdNPs enclosed by (200) crystal plane. The size distribution of Pd cubes was derived from TEM images by counting around 200 nanoparticles (Figure 4.2C). The mean size of cubic Pd was found to be ~18 nm (width: 17.50±3.14 nm, average aspect ratio: 1.14). The STEM image and EDS also confirmed the cubic nanoparticles are palladium (Figure 4.2D).

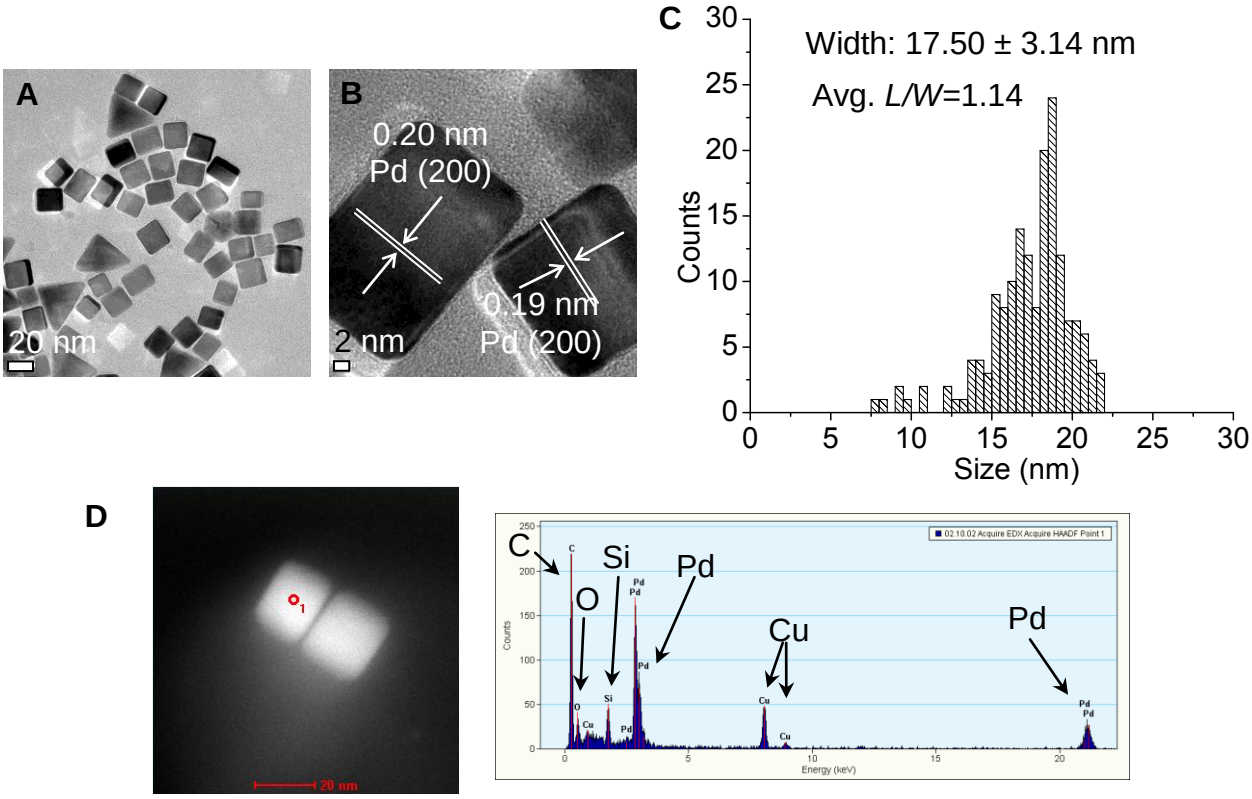

Figure 4.2 (A, B) TEM images, (C) histogram of size distribution (both width and average aspect ratio are used to describe their sizes), (D) STEM image and EDS of as-synthesized cubic PdNPs

4.4 Oxidation Kinetics of Palladium Nanoparticles

To study the oxidation behavior of cubic PdNPs, as-synthesized PdNPs were drop-casted on piranha cleaned silicon wafers and placed in oxygen plasma chamber for oxidation treatment. The substrates were oxidized in the same environment (40W, 36 mTorr pressure of 25% O_2 balanced in Ar) with various duration (from 5 min to 90 min). Yujie and coworkers observed the transformation of Pd nanocubes into Pd/PdO core-shell-type particles with pores in the shell by just expose Pd nanoparticles in air[154]. In our case, from high resolution TEM (Figure 4.3A-C) of PdNPs after plasma oxidized for 90 min, it was found that cubic PdNPs became porous core-shell heterostructures. The shell was constructed by single-crystalline particles with lattice fringe distance of 0.27 nm, which could be indexed to the (200) plane of face-centered cubic PdO (JCPDS Card No. 46-1211, lattice constant: 0.5637 nm). The lattice fringe distance of core was 0.19 nm, which matches the (200) crystal plane of Pd (Figure 4.3A-C). It indicates that the surface of Pd would be oxidized into PdO, while remains cubic shape during the formation of porous oxidized shell on the surface.

In order to make quantitative conclusions, XPS was utilized to determine the composition of nanoparticles in different oxidation states. Figure 4.3D shows an over-lapped XPS spectra with binding energy ranging from 1000 to 0 eV for H_2 reduced PdNPs, as-synthesized PdNPs and PdNPs been plasma oxidized from 5 min to 90 min. Peaks of Pd, Na, C, and Si presented in spectra were generated from PdNPs, metal salt, PVP, and Si substrate, respectively.[155] The existence of O peaks can be attributed to several origins, such as palladium oxide, the absorbed

organic molecules, and surface SiO_2 from substrates, thus the formation of palladium oxide could only be distinguished by detailed analysis of Pd 3d peaks (Figure 4.4 and Table 4.1).

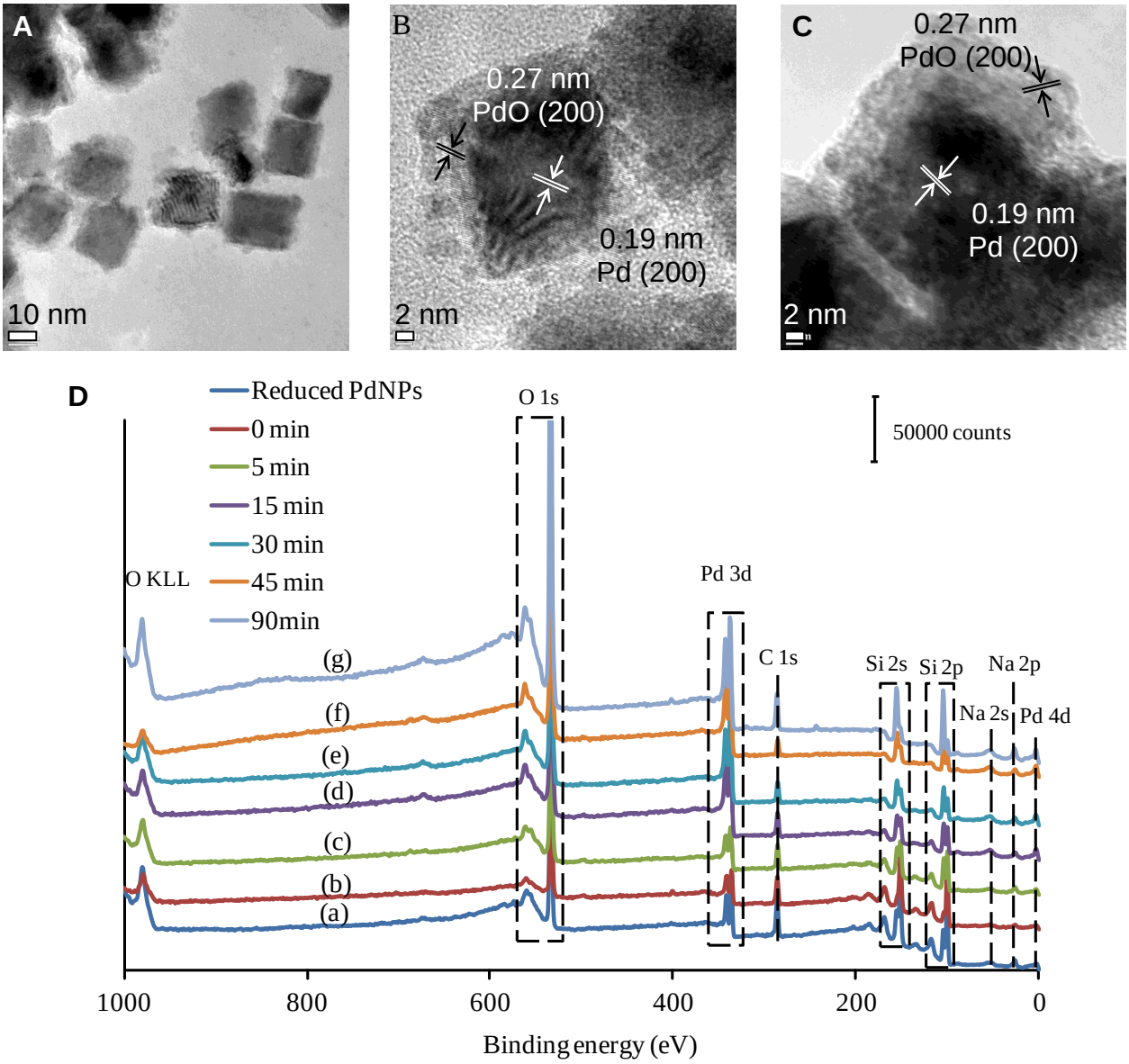

Figure 4.3 (A-C) TEM images showing core-shell structure of PdNPs encapsulated in PdO after plasma oxidation for 90 min. (D) XPS spectra corresponding to PdNPs (a) PdNPs reduced by H_2, (b) as-synthesized PdNPs and after (c) 5 min, (d) 15 min, (e) 30 min, (f) 45 min, and (g) 90 min of plasma oxidation duration. *Note: Cubic PdNPs were dispersed on Si wafer by drop casting method.*

Table 4.1 Binding energy (eV) derived from XPS study for shape controlled PdNPs with different oxidation conditions corresponding to the spectra as shown in Figure 4.4

Plasma condition (min)	Binding Energy (eV)					
	Pd $3d_{3/2}$			Pd $3d_{5/2}$		
	PdO_2	PdO	Pd^0	PdO_2	PdO	Pd^0
Reduced	343.06	341.95	340.49	338.06	336.64	335.21
0	343.09	341.81	340.44	338.12	336.50	335.16
5	343.09	341.94	340.37	338.14	336.64	335.10
15	343.16	342.11	340.42	338.14	336.76	335.12
30	343.06	342.11	340.39	338.05	336.78	335.12
45	343.06	342.11	340.37	338.06	336.81	335.11
90	343.06	342.18	340.37	338.10	336.64	335.21

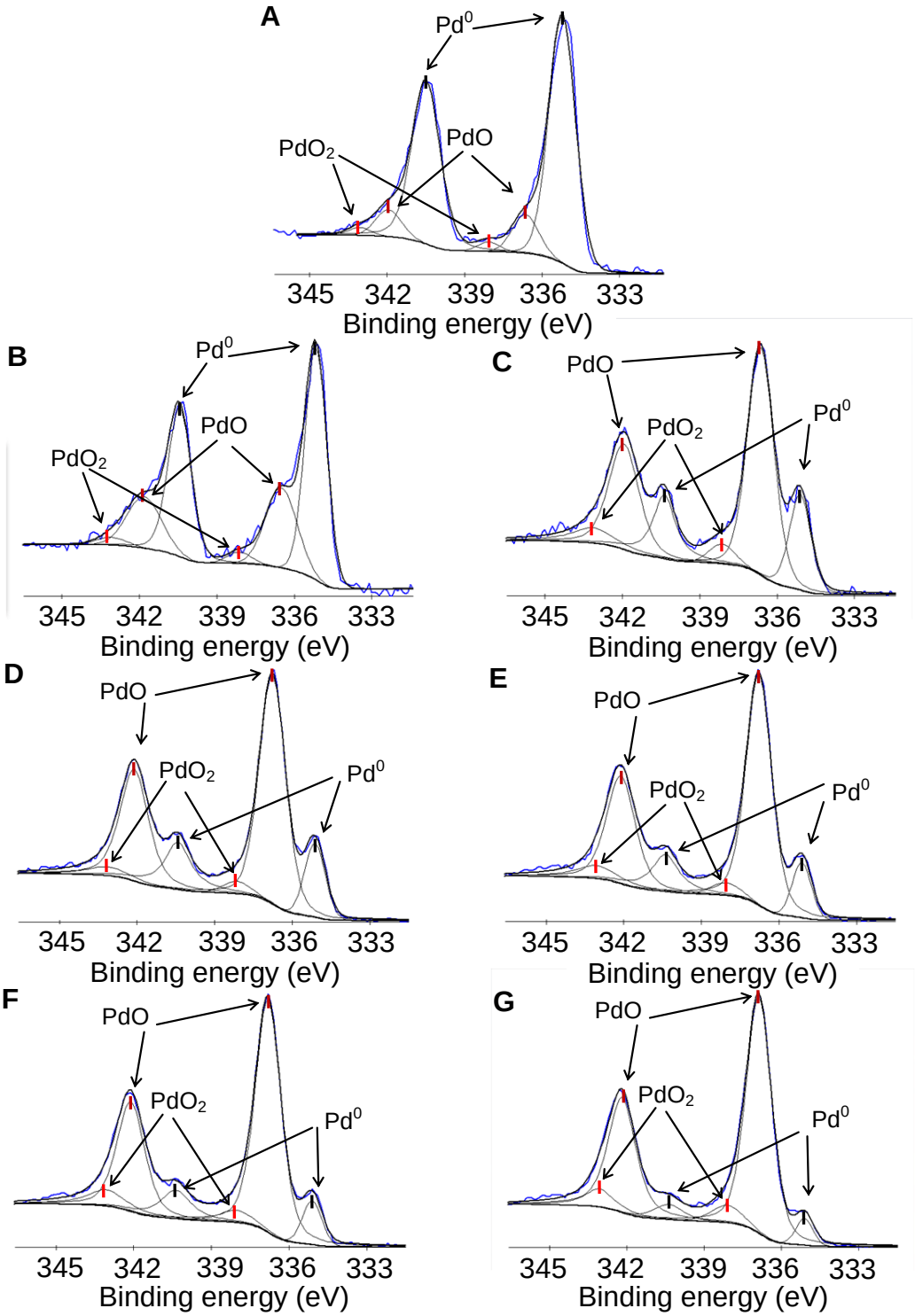

Figure 4.4 Deconvoluted XPS spectra subtracted by Shirley background, and fitted with Pd 3d peaks corresponding to PdNPs (A) reduced by H_2, (B) as synthesized, and after plasma oxidation for (C) 5 min, (D) 15 min, (E) 30 min, (F) 45 min (G) 90 min.

The Pd $3d_{5/2, 3/2}$ peaks indicate the existence of three forms of Pd in as-synthesized cubic PdNPs: the metallic palladium at 335.16 eV and 340.49 eV, the PdO at 336.50 eV and 341.81 eV, the PdO_2 at 338.12 eV and 343.09 eV, respectively.[156] The generation of palladium oxide in as-synthesized PdNPs could be attributed to the oxidation of Pd by air during synthesis and handling. As the increase of plasma oxidation time, the peaks corresponding to palladium oxide increased while the metallic peaks decreased, indicating the process of surface oxidation of PdNPs. As-synthesized PdNPs also been reduced by hydrogen gas for half hour, whose deconvoluted Pd 3d showing dominate component of metallic palladium and lowest fraction of oxide form.

The percentage of the metallic palladium and surface oxides could be obtained by analyzing the areas under each Pd 3d peaks (Table 4.2), which can help us to understand the oxidation kinetics of PdNPs. This quantitative analysis (Figure 4.5) showed the formation of PdO and PdO_2 during the oxygen plasma process. The amount of oxides, with PdO as major component, was dramatically increased within 5 min plasma oxidation and kept increasing during the prolonged plasma treatment. Overall, it was observed that 92.46% surface oxides (molar percentage, including PdO and PdO_2) were detected by XPS after 90 min oxidation.

Table 4.2 The ratio of Pd calculated as peak area of Pd over the sum of Pd and PdO_x peaks area as shown as Figure 4.4

Plasma time (min)	Pd peaks area	PdO peaks area	PdO_2 peaks area	Metallic Pd ratio (%) (Pd/ (Pd+ PdO_x) ×100%)
H_2 Reduced	26422.78	3773.75	891.39	85.00
0	14921.18	7209.07	854.14	64.92
5	8092.54	19174.82	2742.53	26.97
15	15898.07	49369.34	4160.40	22.90
30	12049.58	49778.17	5559.61	17.88
45	10199.6	51773.81	7035.27	14.78
90	5069.74	55059.17	7071.30	7.54

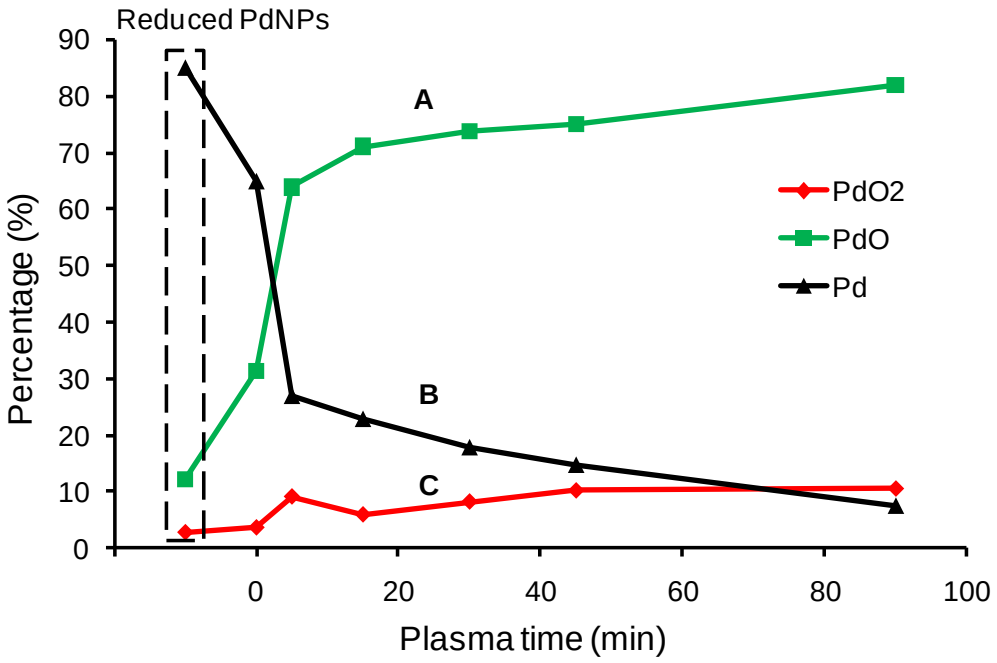

Figure 4.5 Oxidation behavior of cubic PdNPs as a function of plasma time, derived from the XPS results (Table 4.2): percentages of (A) PdO, (B) Pd, and (C) PdO_2.

The evaluation of XPS results allows us to theoretically understand oxidation process and calculate the accurate thickness of the oxide shell. The XPS analysis shows that PdO is the dominant oxide (Figure 4.4 and Table 4.2), so we can consider all palladium oxide as PdO during the calculation. Due to the lower density of PdO (8.3 g/cm^3) than Pd (12.023 g/cm^3), the size of PdNPs would increase after oxidation. Considering a certain amount of palladium film has been oxidized, the change of thickness after oxidation is:

$$\frac{a_0 \cdot A \cdot \rho_{Pd}}{M_{Pd}} = \frac{a \cdot A \cdot \rho_{PdO}}{M_{PdO}} \tag{4.1}$$

where a_0 is original thickness of palladium film, a is the thickness of oxidized palladium film (PdO), A is the area of palladium film, ρ_{Pd}, ρ_{PdO} are density of Pd and PdO, M_{Pd}, M_{PdO} are molecular weight of Pd and PdO (106.42 g/mol and 122.42 g/mol, respectively). Submit density and molecular weight into Equation 4.1 we have:

$$a_0 = \frac{\rho_{PdO}}{\rho_{Pd}} \cdot \frac{M_{Pd}}{M_{PdO}} \cdot a \approx 0.6a \tag{4.2}$$

For a cubic PdNPs, the width after oxidation (B') becomes:

$$B' = B - 2a_0 + 2a = B + 2(a - a_o) = B + 0.8a \tag{4.3}$$

where B is initial width of cubic PdNPs (17.50 nm). Assuming the electron emission depth of XPS (H) was 3 nm (less than the size of cubic PdNPs), the detected percentage of metallic palladium (F_{Pd}) by XPS is (Figure 4.6A):

$$\frac{(H-a)\cdot(B^{'})^{2}-4a\cdot(H-a)\cdot(B^{'})+4a^{2}\cdot(H-a)}{H(B^{'})^{2}}=F_{Pd} \tag{4.4}$$

Submit *H*=3 nm, *B*=17.50 nm, and Equation 4.3 into Equation 4.4 we have:

$$\frac{(3-a)\cdot(17.5+0.8a)^{2}-4a\cdot(3-a)\cdot(17.5+0.8a)+4a^{2}\cdot(3-a)}{3\times(17.5+0.8a)^{2}}=F_{Pd} \tag{4.5}$$

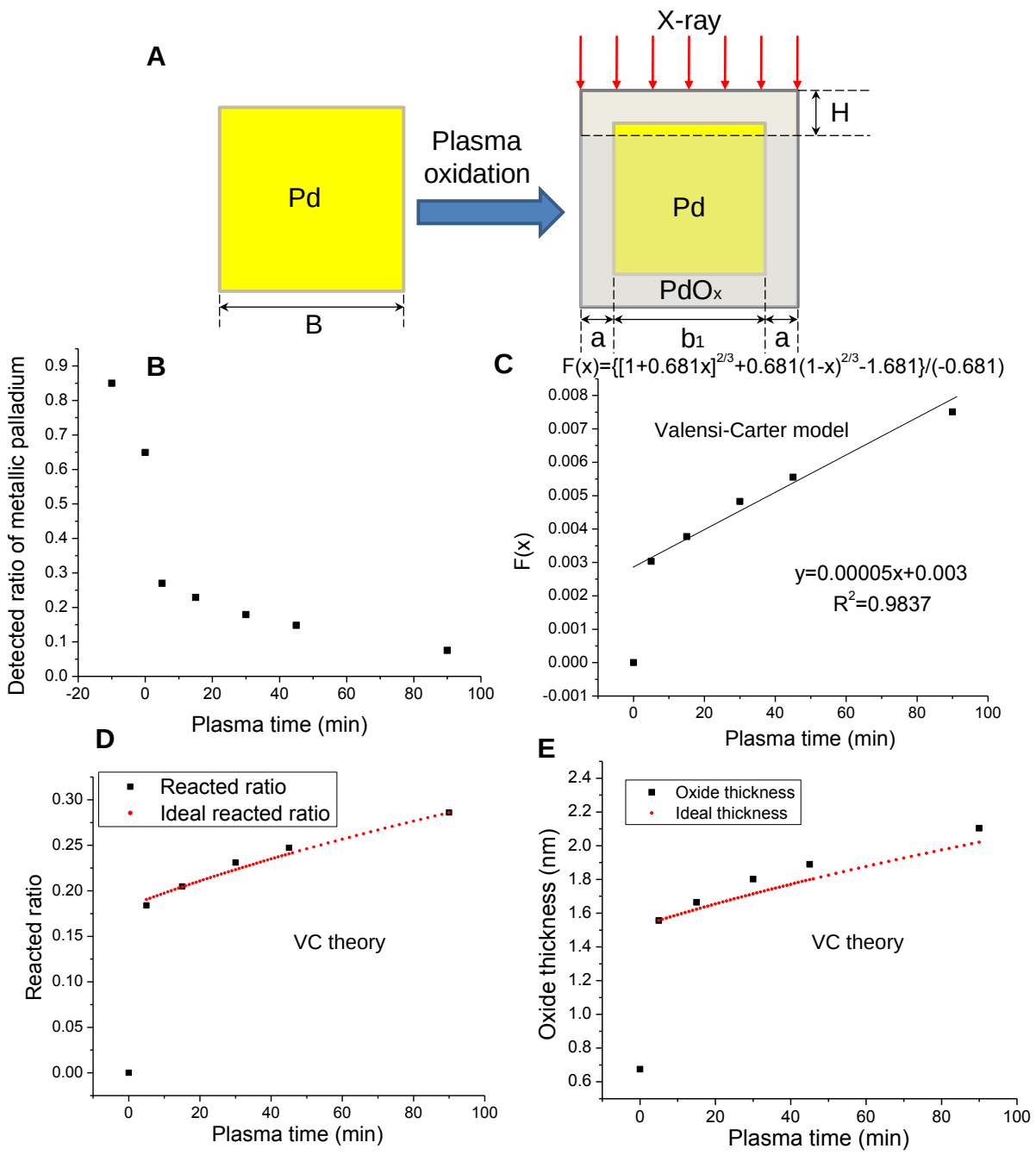

Figure 4.6 (A) Schematic showing formation of palladium oxide (PdOx) shell on cubic particle and XPS analysis showing the detection depth (H) and other geometrical parameters. Graphs showing the relationship between plasma time and (B) XPS detected ratio of metallic Pd, (C) Valensi-Carter function F(x), (D, E) Fitting of Valensi-Carter (VC) model for oxidation of cubic particles with the observed experimental data.

The XPS derived fraction of metallic palladium remaining in the cubic PdNPs (F_{Pd}) as a function of plasma oxidation time is shown in Figure 4.6B and Table 4.2, which is based on comparing the peaks area of the data points shown. Thus the thickness of the oxide shell can be estimated for each sample (H_2 reduced PdNPs, as-synthesized PdNPs, and plasma oxidized PdNPs). In addition, the oxidation kinetics of the nanoparticles was fitted with Valensi-Carter model as proposed earlier for the oxidation kinetics of palladium powder.[34] The Valensi-Carter equation is given by:

$$[\{1+(z-1)x\}^{2/3}+(z-1)(1-x)^{2/3}-z]/(1-z)=Kt \qquad (4.6)$$

z is the volume of product formed per unit volume of reactant consumed, for reaction $Pd+0.5O_2 \rightarrow PdO$, z is 1.681. x is the reaction ratio of palladium, which can be calculated from the size of cubic PdNPs and thickness of oxide shell. K is a kinetic constant, t is the oxidation time. Submit z=1.681 into Equation 4.6 we have:

$$F(x)=[(1+0.681x)^{2/3}+0.681(1-x)^{2/3}-1.681]/(-0.681)=Kt \qquad (4.7)$$

According to Equation 4.7 and the thickness calculation for each sample, the *F(x)* can be plotted as a function of plasma time (Figure 4.6C). The oxidation occurred very fast in the first 5 min, and became gradually slow in the later stage of the reaction, and the plot after 5 min oxidation can be fitted to a good straight line. The Valensi-Carter equation is used to describe the reaction controlled by diffusion process, implies the diffusion of either O or Pd during plasma treatment is the control-step during oxidation.[153] From the obtained *F(x)* fitted line, we can calculate the

ideal reacted ratio and oxide thickness inversely. Figure 4.6D and 6E show the comparison of theoretical data from Valensi-Carter model and the calculated data from XPS analyzing, the two sets data closely matched.

4.5 Effect of Oxidation on Carbon Shell Formation

To evaluate the influence of palladium oxide on graphene shell-formation, PdNPs with different oxidation states (Table 4.1 and 4.2) were used as catalysts in the xylene CVD process. After graphene shells growth, the shape of PdNPs transformed from cubic to near-spherical with exposed crystal plane from {100} to {111} to attain a minimum surface energy configuration (Figure 4.7). Some extent of amorphous/graphitic carbon was also observed surround those nanoparticles. PdNPs were encapsulated in uniform graphene-like carbon shells with interlayer spacing of 0.34~0.39 nm, which is consistent with the c-axis spacing of graphite. Due to the drop-casting method, the density of PdNPs on substrate was high. Thus some adjacent PdNPs tend to aggregate together during high temperature CVD procedure, and resulted in the increase of particle size from originally less than 20 nm to 35~63 nm after graphene shells growth (Figure 4.8A and Table 4.3).

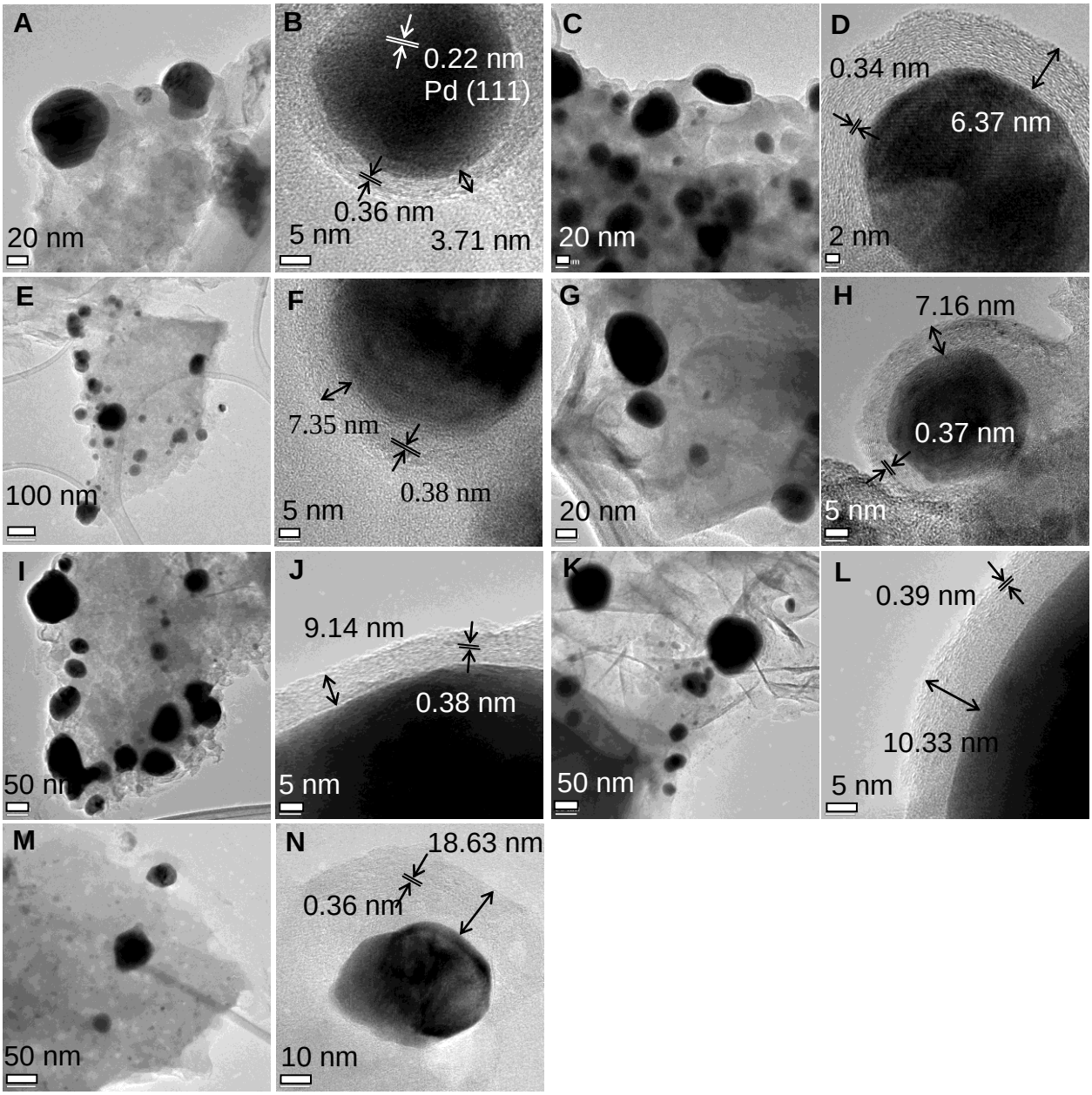

Figure 4.7 TEM images showing graphene shells growth on (A, B) PdNPs reduced in H_2 for 30 min, (C, D) as-synthesized PdNPs, and PdNPs been plasma oxidized for (E, F) 5 min, (G, H) 15 min, (I, J) 30 min, (K, L) 45 min, and (M, N) 90 min

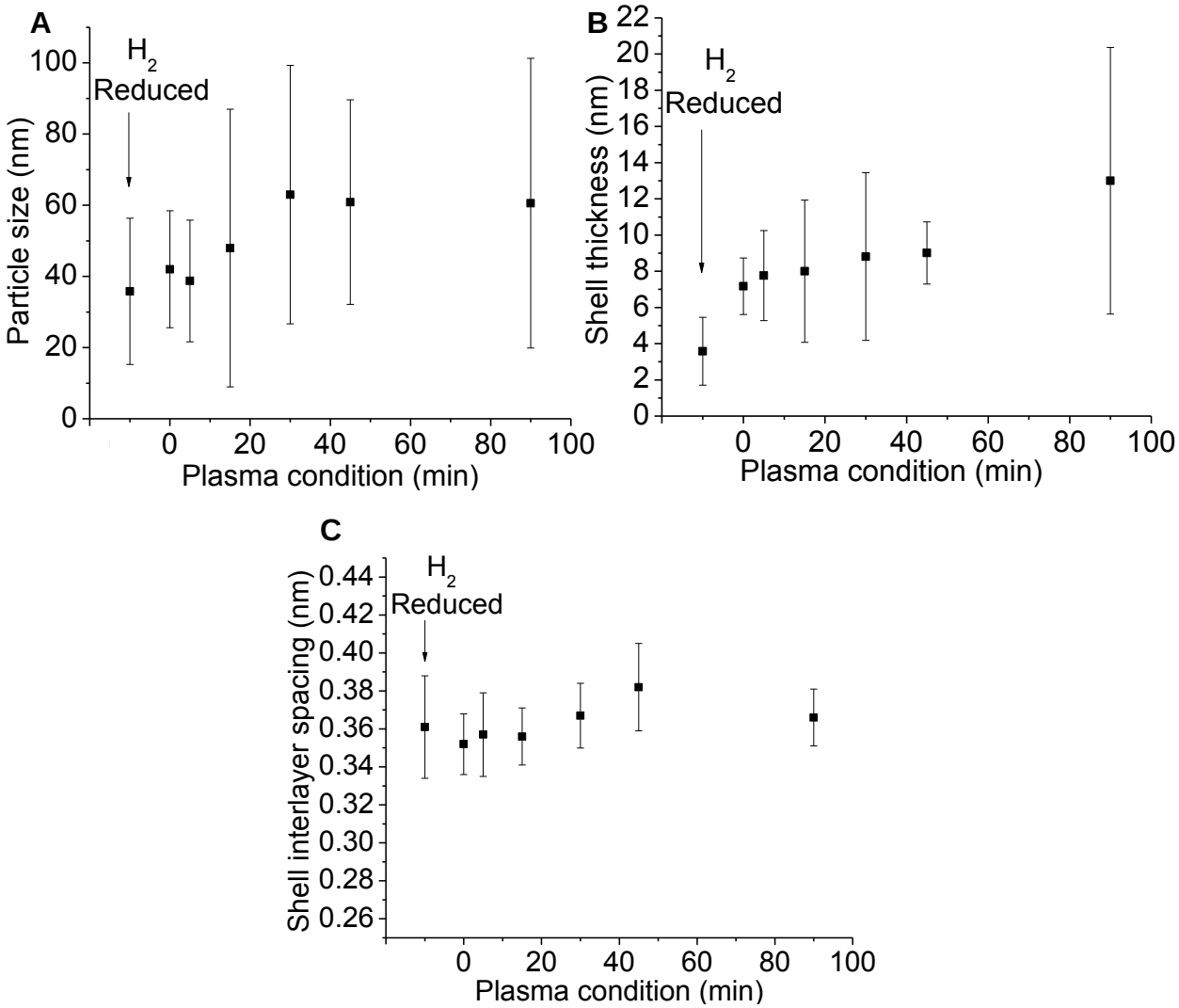

Figure 4.8 Plots showing the change of (A) particle size, (B) shell thickness, and (C) shell interlayer spacing as a function of plasma condition.

Table 4.3 Average size of Pd core, thickness and interlayer spacing of shell, and D-, G-band intensity ratio (I_D/I_G) of PdNPs in different oxidation states after graphene shells growth.

Oxidation condition (min)	Particle size (nm)	Shell thickness (nm)	Shell interlayer spacing (nm)	I_D/I_G
H_2 Reduced	35.8±20.6	3.6±1.9	0.36±0.03	1.39±0.20
0	42.0±15.4	7.2±1.6	0.35±0.02	1.54±0.12
5	38.7±17.1	7.8±2.5	0.36±0.02	1.38±0.14
15	48.0±39.0	8.0±3.9	0.36±0.02	1.45±0.09
30	63.0±36.3	8.8±4.6	0.37±0.02	1.53±0.13
45	60.9±28.8	9.0±1.7	0.38±0.02	1.64±0.16
90	60.6±40.7	13.0±7.4	0.37±0.02	1.55±0.21

In same graphene shells growth condition, PdNPs with longer oxidation time obtained larger size after CVD process. This may due to sintering of nanoparticles caused by long-time plasma treatment. It was reported that high energy plasma interacts with ceramics and enhanced grain boundary diffusion[157]. The select of RF power would ensure homogeneous and stable plasma conditions. Reinhold and co-workers reported sintering of inkjet-printed Ag nanoparticles using low-pressure Ar plasma[158]. The low pressure in the barrel reactor favors the evaporation of surfactants from the nanoparticles surface, and allows the uncoated particles contact directly and sinter. As the generated high energy plasma arrives on the surface of PdNPs, it leads the recombination of PdNPs through atomic diffusion. Thus a longer plasma treatment allows more PdNPs sinter together and form larger clusters, which melted into larger particles during high temperature CVD process. Increase oxidation duration also leads to the formation of thicker carbon shells (from ~3.6 nm to ~13 nm, Figure 4.8B and Table 4.3). Since noble metal oxide can act as electron-receptor and assist the formation of graphene shells during CVD process, thicker palladium oxide shell would last longer in high temperature, reducing environment, thus resulted in more formation of carbon shells. Graphene shell obtained from as-synthesized PdNPs has smallest interlayer spacing (0.35±0.02 nm), and the interlayer spacing increases as plasma time increase, which reached maximum (0.38±0.02 nm) for PdNPs oxidized for 45 min (Figure 4.8C, Table 4.3). But the shell interlayer spacing for plasma oxidized 90 min PdNPs decreased to 0.37±0.02 nm. The rise of interlayer spacing attributed to uncorrelated atomic positions between carbon atoms on two adjacent shell layers[159].

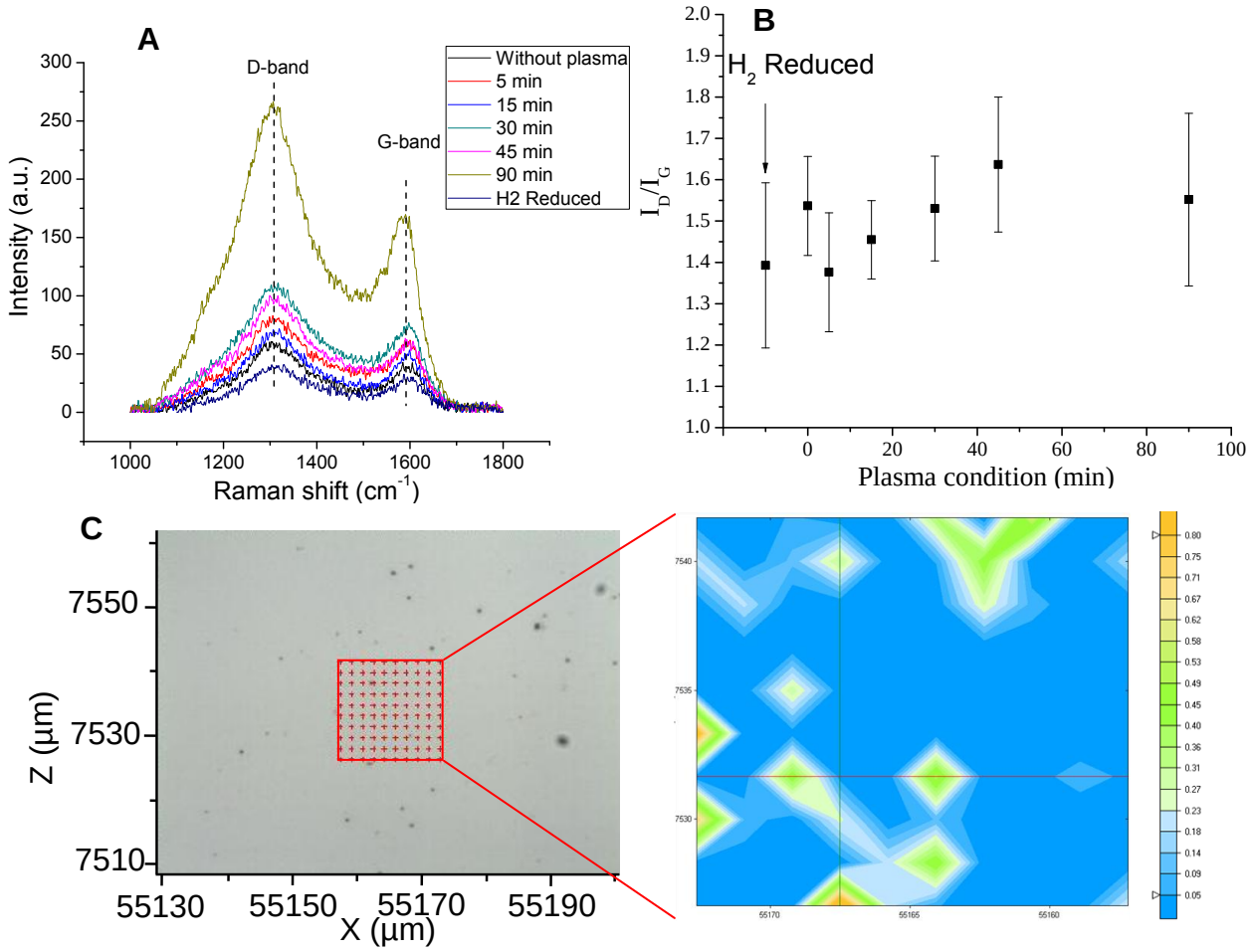

Figure 4.9 (A) Raman spectra showing graphene shells growth on PdNPs been plasma oxidized for different duration. (B) Plot showing the ratio of D-, G-band peak intensity as a function of plasma condition. (C) Raman chemical mapping for graphene shells growth on PdNPs been plasma oxidized for 5 min.

Raman spectra (Figure 4.9A) for GNPs showed D and G-band, which consistent with disordered and graphitic carbon content, centered at ~1308 and 1591 cm^{-1}, respectively. The intensity of D, G-band Raman spectra has similar tendency with the change of shell thickness for each sample. PdNPs reduced by hydrogen resulted in thinnest graphene shell and lowest Raman intensity, while PdNPs plasma-treated for 90 min produced thickest graphene shell and highest Raman intensity. The intensity ratio of D-, G-band (I_D/I_G) was ranging from 1.39 to 1.64 (Figure 4.9B and Table 4.3). The PdNPs plasma oxidized from 5 min to 45 min showed that I_D/I_G increased as increasing plasma oxidation duration, indicating that more disordered carbon formed on longer oxidized PdNPs. However, it was observed that as-synthesized PdNPs resulted in higher I_D/I_G than PdNPs oxidized within 30 min. The surface of as-synthesized PdNPs was surrounded by surfactant (PVP), which could be carbonized into disordered carbon at high temperature. Meanwhile, plasma treatment may clean the surface of PdNPs and remove reagent residue. Thus the plasma treated PdNPs could produce less disordered carbon shell than as-synthesized PdNPs. Similarly, the hydrogen reducing process may also help to clean the surface of PdNPs to produce higher quality carbon shell. Raman chemical mapping over large substrate area was performed (Figure 4.9C) and the color scheme represents the normalized intensity of the G-band peak (with regard to the highest G-band peak intensity in the scanned area). The mapping showed uniform intensity over the most area, and high intensity corresponding to “black spots” on the substrates, which may contained large amount of particles encapsulated in carbon. This indicates that the high-throughput CVD growth process resulted in large area growth of GNPs. The specific

surface area of graphene shell can be estimated from TEM images. The shell thickness ($b_{observed}$) and core-particle size (R) can be measured from TEM images, and we know the density of palladium (ρ_{PdNP}=12.023 g/cm^3), thus the specific surface area of graphene shell can be estimated as:

$$\frac{S_{grapheneobserved}}{m_{PdNP}} = \frac{4\pi(R+b_{observed})^2}{V_{PdNP}\cdot\rho_{PdNP}} = \frac{4\pi(R+b_{observed})^2}{\frac{4}{3}\pi R^3\cdot\rho_{PdNP}} \quad (4.8)$$

After submitting shell thickness and core size for each sample to Equation 8, we obtained the average specific area of graphene shell per unit palladium particle mass is (5.78 ± 1.36) ×10^5 cm^2/g.

The importance of palladium oxide to the growth of graphene shell has been proved by the fact that PdNPs with longer oxidation duration resulted in thicker graphene shell. The proposed mechanism is that the oxide of palladium (PdO_x) is unstable at high temperature with the existence of H_2, prefers to accept electrons and transform to metallic Pd. It would assist the decomposition of incoming carbon feed (xylene), resulting in the formation of GNPs. A similar mechanism has been proposed by our group for the formation of carbon shells around surface oxidized AuNPs CVD approach. XPS was utilized to study the chemical states of palladium before and after graphene shells growth. Since the graphene shells formed from as-synthesized PdNPs and plasma oxidized PdNPs were thicker than detection depth of XPS (~3 nm), no Pd signal was obtained (Figure 4.10, 4.11). Because the detection area of XPS was in the scale of micron, it proved that graphene shells were uniformly covered on the surface of PdNPs, and

became thicker by using PdNPs at higher oxidized conditions. Weak Pd signal was obtained from H_2 reduced PdNPs after graphene shells growth. Survey scans for H_2 reduced PdNPs before and after graphene shells growth are shown in Figure 4.12A. Pd 3d peaks were further deconvoluted as shown in Figure 4.12B and were assigned accordingly (Table 4.4). An interesting observation was that only PdO peaks exist after graphene shells growth. This may attribute to the high activity of metallic palladium in the air and the stability of PdO at room temperature. Sample would unavoidable expose to the air during handling and form palladium oxide on the surface of palladium core. XPS can only detect angstrom scale depth of core surface after penetrate the carbon shell (~3 nm), thus only PdO would be detected. However, we can also compare the intensity of PdO peaks before and after graphene shells growth on this H_2 reduced PdNPs sample. Before graphene shells growth, the PdO peak area is 3772.745, after graphene shells growth, PdO peak area is 323.65, so the detected of PdO after graphene shells growth is estimated as just 8.6% compare to its pre-graphene growth counter. Carbon 1s peaks obtained from XPS were also deconvoluted (Figure 4.12C and Table 4.5). The peak located at 284.8 eV corresponds to C 1s peak or sp2 carbon. Peaks located at 288.98 and 286.12 eV could be attributed to C-O and C=O bonds, respectively. π-π^* transition loss peak (291.57 eV) was also observed, which is associated with the formation of graphitic carbon.

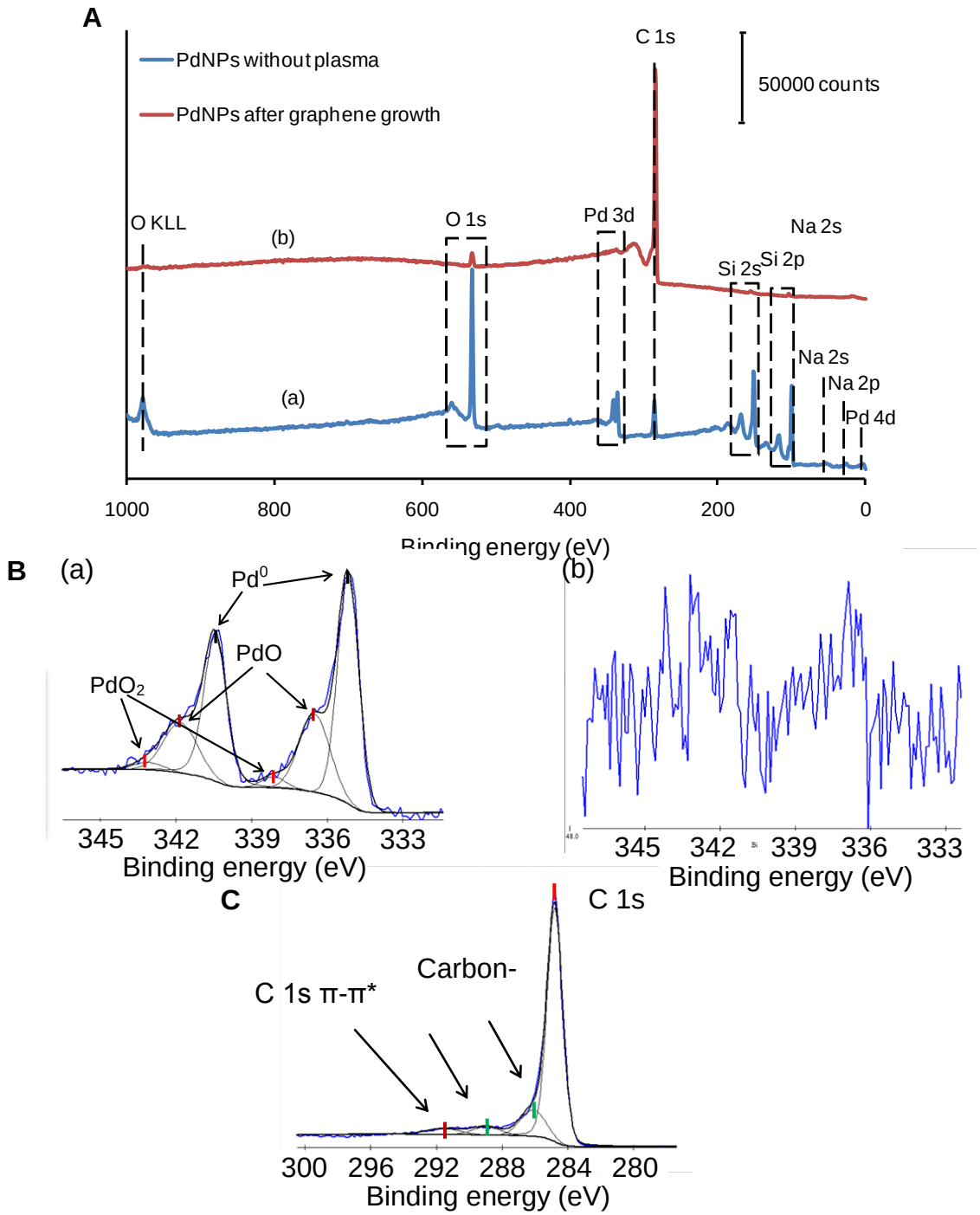

Figure 4.10 (A) XPS spectra corresponding to PdNPs (a) as synthesized, (b) after 0.5 h graphene growth. (B) Deconvoluted XPS spectra, subtracted by Shirley background, and fitted with Pd 3d peaks (a) before and (b) after graphene growth. (C) Deconvoluted XPS spectra, subtracted by Shirley background, and fitted with C 1s peak after graphene growth.

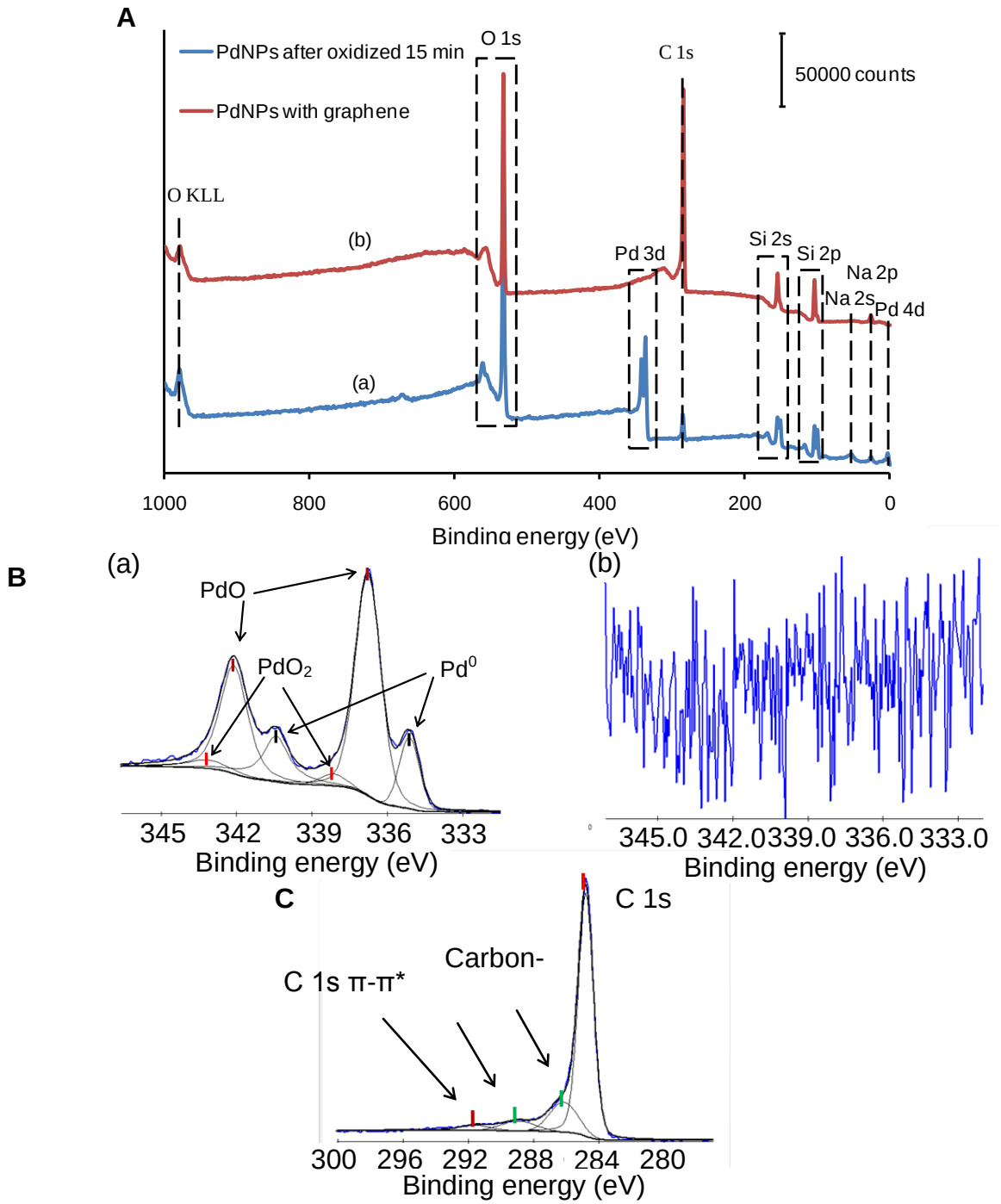

Figure 4.11 (A) XPS spectra corresponding to PdNPs (a) after plasma oxidation 15 min, (b) after 0.5 h graphene growth. (B) Deconvoluted XPS spectra, subtracted by Shirley background, and fitted with Pd 3d peaks (a) before and (b) after graphene growth. (C) Deconvoluted XPS spectra, subtracted by Shirley background, and fitted with C 1s peak after graphene growth.

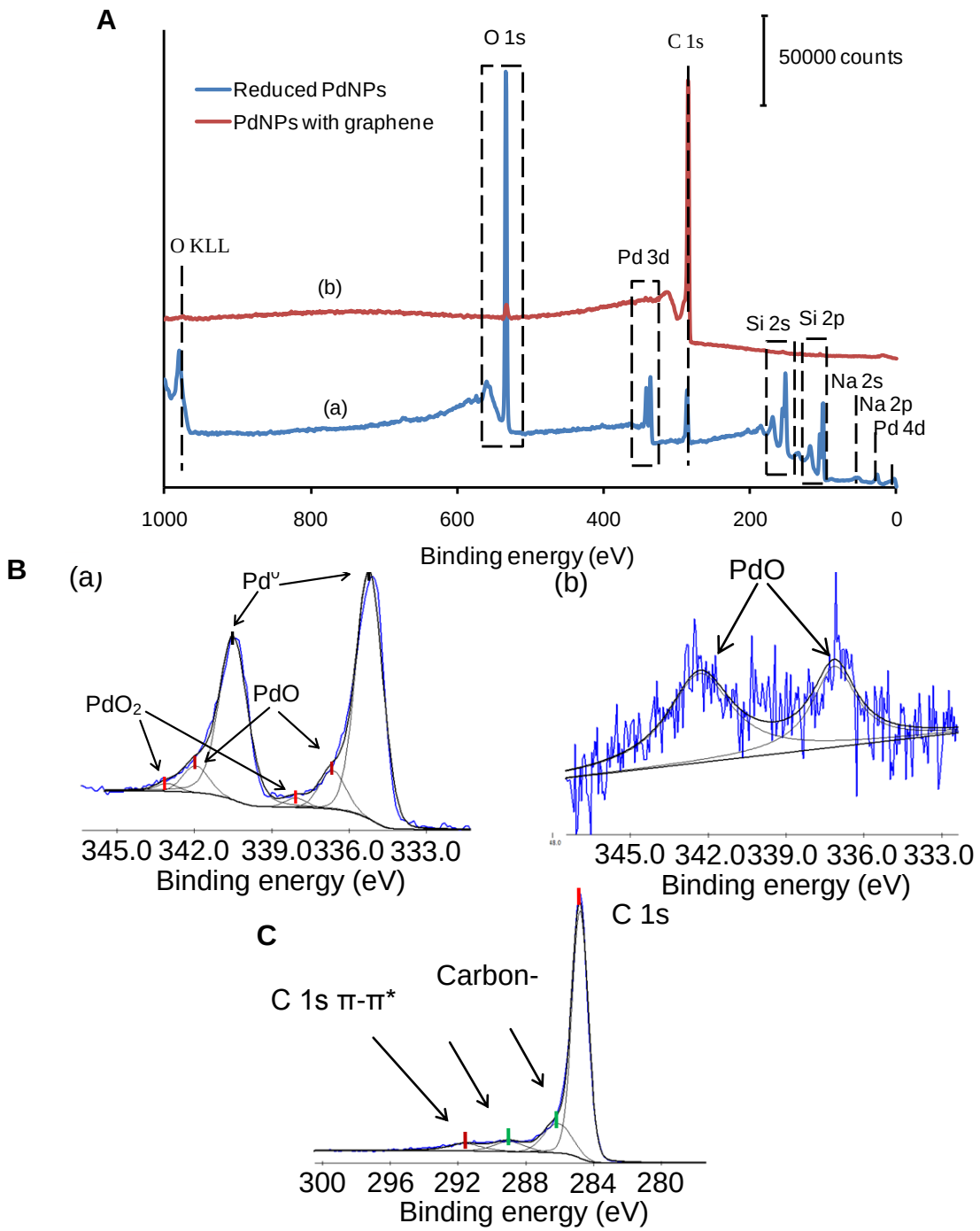

Figure 4.12 (A) XPS spectra corresponding to PdNPs (a) reduced by H_2 for half hour, (b) after 0.5 h graphene growth. (B) Deconvoluted XPS spectra, subtracted by Shirley background, and fitted with Pd 3d peaks (a) before and (b) after graphene growth. (C) Deconvoluted XPS spectra, subtracted by Shirley background, and fitted with C 1s peak after graphene growth.

Table 4.4 Binding energy (eV) chart derived from XPS analysis for reduced PdNPs before and after graphene shells growth corresponding to the spectra as shown in Figure 4.12B

Conditions	Binding Energy (eV)					
	Pd $3d_{3/2}$			Pd $3d_{5/2}$		
	PdO_2	PdO	Pd^0	PdO_2	PdO	Pd^0
After reduced	343.06	341.95	340.49	338.06	336.64	335.21
With Graphene	/	342.32	/	/	337.13	/

Table 4.5 Binding energy (eV) chart derived from XPS analysis for PdNPs corresponding to the spectra as shown in Figure 4.12C. *Note: The values in parenthesis indicate the area under the peaks.*

Condition	C 1s Binding Energy (eV)			
	C 1s	Carbon-Oxygen links	Carbon-Oxygen links	C π-π*
After Graphene growth	284.80 (59024.97)	286.12 (11872.82)	288.98 (5107.45)	291.57 (4672.31)

4.6 Plasmonic Properties of PdNPs and GNPs

The optical properties of PdNPs with different shapes, sizes, and GNPs with different core size and shell thickness have been analyzed by discrete dipole approximation (DDA) calculations. These computational studies have already been proved to fit well with real case, and can be utilized to predict how to achieve good optical properties by controlling the morphology (size and shape) of metal nanostructures. Using the DDSCAT code developed by Draine and Flatau, [132] we calculated the extinction cross section for each structure at wavelength ranged from 200 nm to 800 nm of incident light. The calculate target was chosen to be in vacuum. The dielectric function of palladium was taken from online refractive index database, and the built-in dielectric function of graphite in DDSCAT was utilized for the graphene shell.

Extinction spectra (Figure 4.13A) for cubic PdNPs with different size (width) show the red-shift of peak from around 200 nm to 740 nm when particle size increased from ~10 nm to ~300 nm. Further increase the size would broaden the peak and flatten the extinction curve. Extinction spectra (Figure 4.13B) for spherical PdNPs with different size (diameter) show similar red-shift of peak as increasing size of particles. Compare with the extinction spectra for cubic PdNPs with similar effective radius, it was observed that cubic PdNPs present red-shifted, broaden peak features. The red-shift of extinction peak holds significant importance for PdNPs. As a noble metal, palladium nowadays primarily serves as catalyst for purification of automobile gas waste and organic reactions. The optical property of PdNPs remains unexplored relatively. That's because the surface plasmon resonance (SPR) peak of small PdNPs with size smaller than 10 nm

is located in the UV zone. The lights in that region are absorbed strongly by glass and most solvents, which makes PdNPs' SPR characteristics much more difficult to probe. If the position of the SPR peak of PdNPs could be shifted to visible region, at which the maximum electromagnetic field enhancement would be obtained, it could lead to applications of PdNPs in various field such as colorimetric sensing, plasmonic waveguiding, enhancement of Raman, and optical sensing of hydrogen. The calculation through DDA proved that by increasing PdNPs size or changing shapes, their SPR features could be tailored to locate in visible region. The extinction peaks of large PdNPs are relatively broad, that can be attributed to the dielectric function of palladium. Cubic PdNPs exhibit better optical properties compare to spherical PdNPs with similar effective radius. That is due to metal nanostructures with sharp corners or edges are especially active surface enhanced Raman spectra (SERS) substrates.

Table 4.6 Parameters used in DDA calculations for bare PdNPs.

Shape	Effective radius (μm)	Dipole-number	Shape parameter	Size (nm)
Cubic	0.0063	125000	50	10.15
Cubic	0.01326	125000	50	21.38
Cubic	0.0307	125000	50	49.49
Cubic	0.614	125000	50	98.98
Cubic	0.0921	125000	50	148.46
Cubic	0.1229	125000	50	198.11
Cubic	0.1541	125000	50	248.41
Cubic	0.1843	125000	50	297.09
Cubic	0.2456	125000	50	395.91
Cubic	0.39789	110592	48.49	647.94
Spherical	0.0063	65752	50	12.58
Spherical	0.01326	65752	50	26.49
Spherical	0.0307	65752	50	61.31
Spherical	0.0492	65752	50	98.25
Spherical	0.0614	65752	50	122.61
Spherical	0.0921	65752	50	183.92
Spherical	0.1229	65752	50	245.42
Spherical	0.2456	65752	50	490.45
Spherical	0.39789	59728	48.49	795.64

Table 4.7 Parameters used in DDA calculations for graphene shells encapsulated PdNPs. Average size of GNPs, core PdNP, and average graphene shells thickness are consistent with experimental observations.

Effective radius (μm)	Dipole-number	Shape parameter	Core size (nm)	Shell thickness (nm)	Total size (nm)
0.02152	41755	42.98	35.82	3.58	42.98
0.02817	93656	56.35	42.01	7.17	56.35
0.02716	83888	54.24	38.72	7.76	54.24
0.03195	136584	63.96	47.96	8	63.96
0.04029	273977	80.61	62.99	8.81	80.61
0.03946	257295	78.9	60.88	9.01	78.9
0.04329	339883	86.58	60.58	13	86.58
0.02602	73824	52	50	1	52
0.02703	82712	54	50	2	54
0.029	102208	58	50	4	58
0.031	124800	62	50	6	62
0.03303	150920	66	50	8	66
0.03502	179944	70	50	10	70
0.03702	212472	74	50	12	74

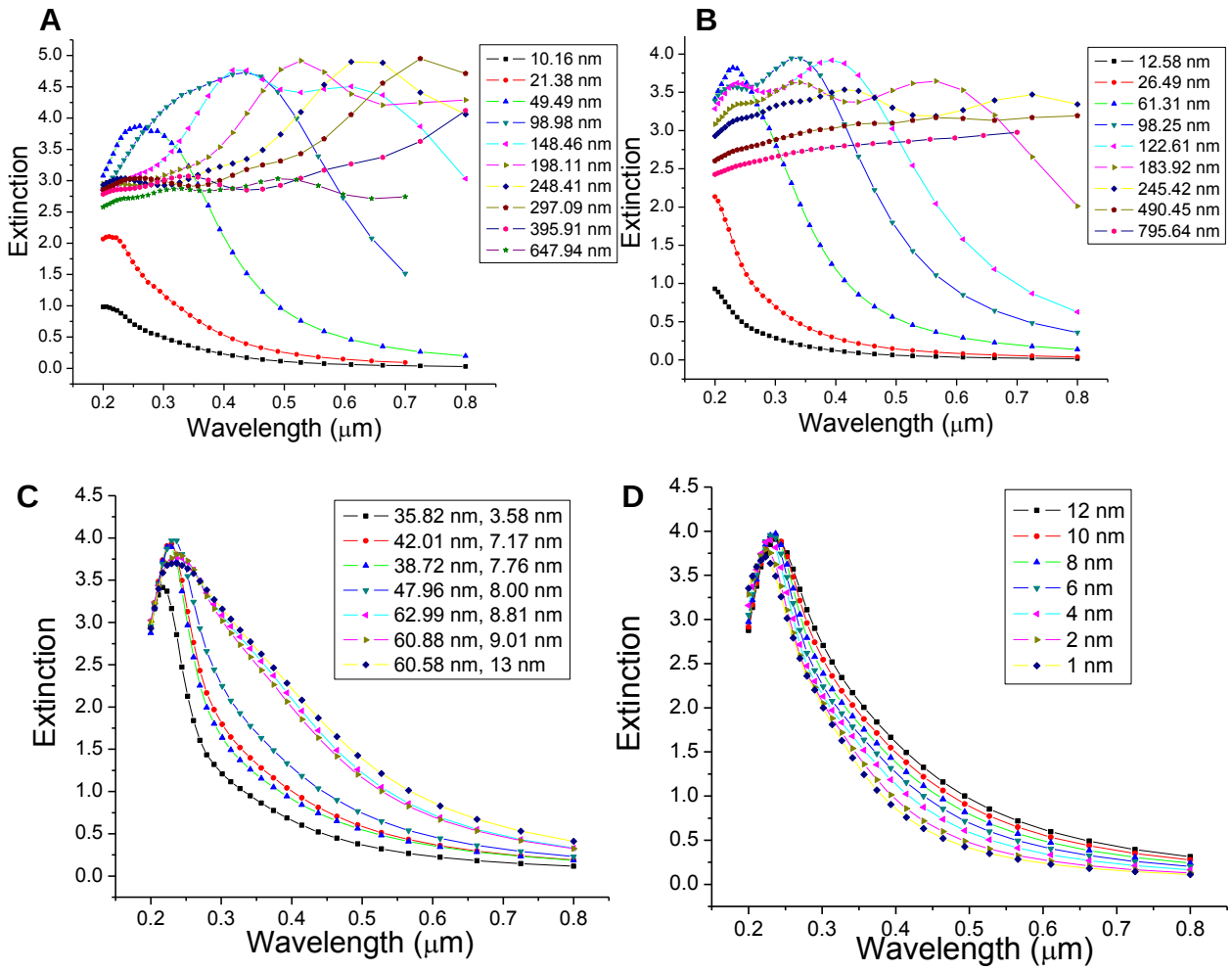

Figure 4.13 (A) Graph of the extinction curve of cubic Pd nanoparticles with different sizes; (B) Graph of the extinction curve of spherical Pd nanoparticles with different sizes; (C) Graph of the extinction curve of spherical graphene shells encapsulated Pd nanoparticles with different sizes of core and shell thickness; (D) Graph of the extinction curve of spherical graphene shells encapsulated Pd nanoparticles with 50 nm core and different shell thickness.

In this paper, we extend optical property study from single PdNPs to Pd-graphene core-shell heterostructures. The size of PdNPs and thickness of graphene shell were selected based on our experimental data (Table 4.6, 4.7). Graphene shell can serve as barrier that preserves the PdNPs from aggregation. However, it is unknown that whether or how much the graphene shell would hinder the SPR on palladium core. DDA provides a convenient approach to characterize the optical properties of GNPs core-shell heterostructures with different core size and shell thickness. Figure 4.13C shows extinction spectra of graphene shells encapsulated PdNPs obtained from different oxidation conditions. Their core size and shell thickness were calculated from TEM images (Figure 4.7, Figure 4.8A, B) and listed in the inserted panel. Red-shift was observed for GPNs with larger core size. It was observed that the extinction of GNPs is majorly affected by the Pd core size. Red-shift, broaden and increase of extinction peak were observed as increasing core size from around 36 nm to 50 nm. To understand the affect of graphene shell thickness on plasmon resonance of GNPs, we also processed plasmonic modeling of a certain size Pd core (50 nm) with various shell thickness (1-12 nm), as shown in Figure 4.13D. It indicated that when keep the Pd cores same, thicker graphene shells would lead to red-shift and broaden of extinction peak. The extinction peak also became higher in the case of thicker shells (3.71 with 1 nm shell, and 3.91 with 12 nm shell), which may due to the absorbance of light in graphene shell.

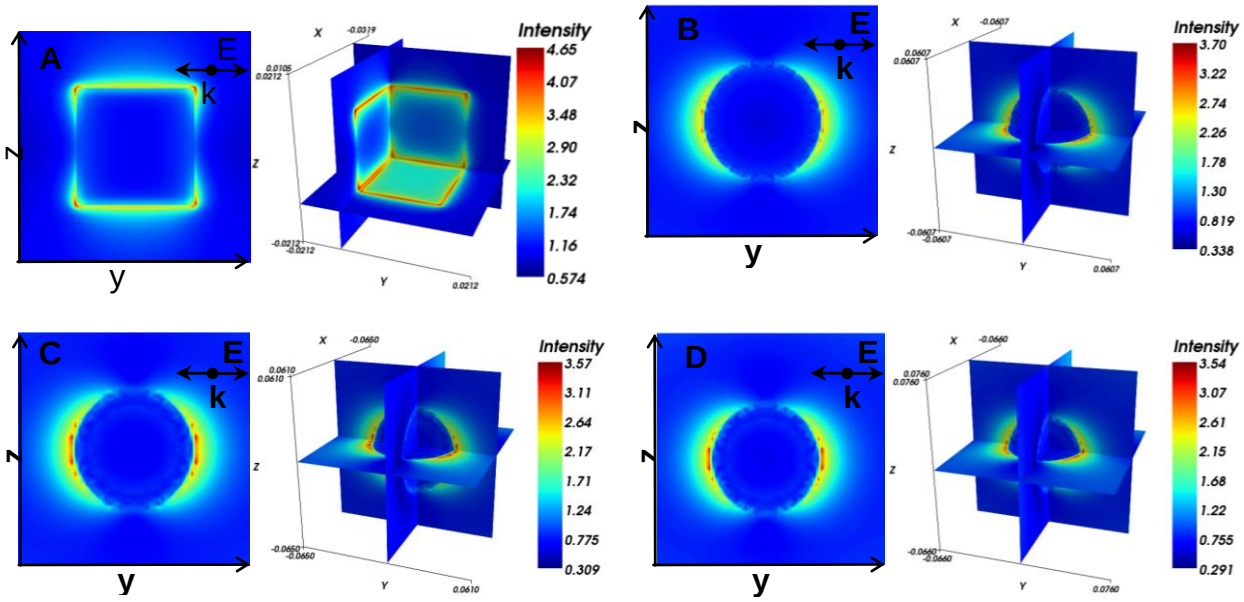

Figure 4.14 (A) Near field image of cubic Pd nanoparticles with size of 21.38 nm at 210 nm wavelength; (B) Near field image of spherical Pd nanoparticles with size of 61.31 nm at 223 nm wavelength; (C) Near field image of spherical graphene shells encapsulated Pd nanoparticles with 47.96 nm core and 8.0 nm shell at 230 nm wavelength; (D) Near field image of spherical graphene shells encapsulated Pd nanoparticles with 50 nm core and 8.0 nm shell at 230 nm wavelength.

Figure 4.14A shows the visualized near field image of a 21.38 nm cubic PdNP in vacuum at localized surface plasmon resonance (210 nm).[150] The strongest field intensity located around the four edges. Figure 4.14B shows the visualized near field image of a 61.31 nm spherical PdNP in vacuum at localized surface plasmon resonance (223 nm). It shows large electric field at the edges of the nanoparticle and dipolar field due to plasmon resonance. Figure 4.14C presents near field image of a 47.96 nm spherical PdNP encapsulated in 8 nm thick graphene shell at localized surface plasmon resonance (230 nm). With graphene shell, there are still large electric field at the edges of the spherical particle and generated dipolar filed. Figure 4.14D is the visualization of near field for spherical GNPs with 50 nm-size core and 8 nm-thick graphene shells at localized surface plasmon resonance (230 nm). Similarly, large electric field at the edges and dipolar field was observed. The plasmonic modeling shows the potential of application of PdNPs and GNPs in the field of optical sensing, and proves that the formation of graphene shell won't destroy the plasmonic resonance of palladium core. Figure 4.15 shows the visualized near field image of a 49.85 nm spherical PdNP without (Figure 4.15 A) and with (Figure 4.15 B) 8.19 nm-thick graphene shells at localized surface plasmon resonance (785 nm). The selection of wavelength is based on the Raman system we have in the lab. It was proved that the graphene shell would not decrease too much plasma resonance for the same size PdNPs.

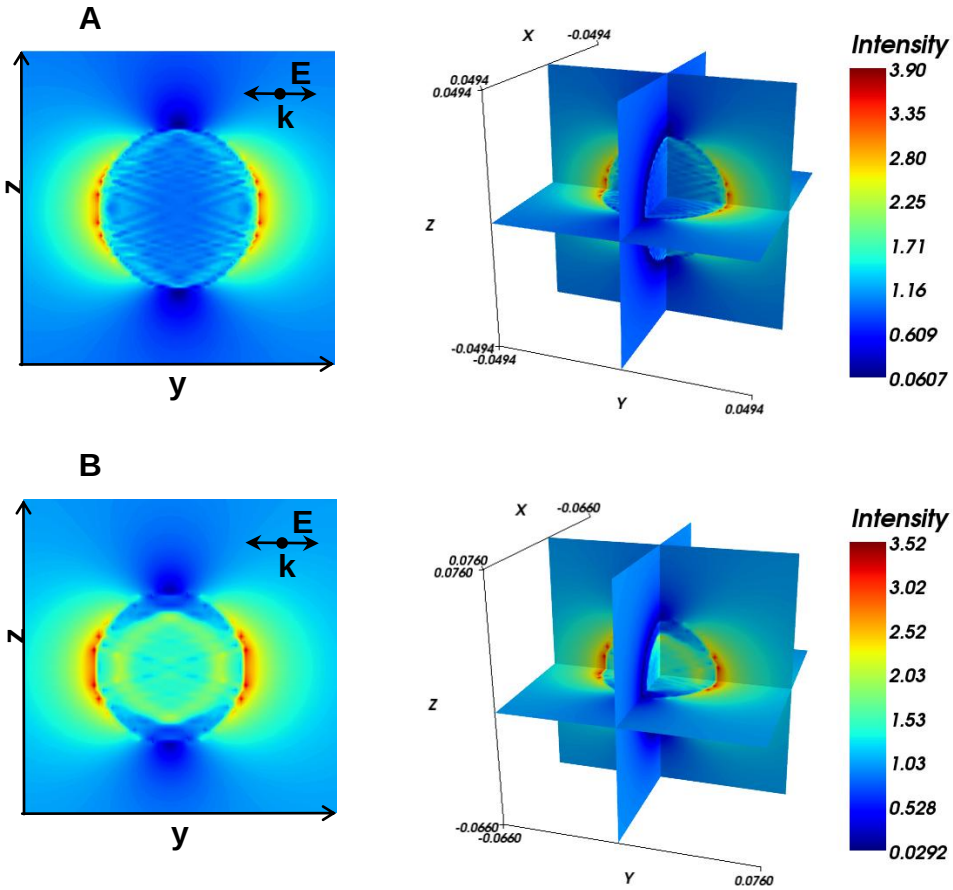

Figure 4.15 (A) Near field image of spherical Pd nanoparticles with size of 49.85 nm at 785 nm wavelength; (B) Near field image of spherical graphene shells encapsulated Pd nanoparticles with 49.85 nm core and 8.19 nm shell at 785 nm wavelength

4.7 Conclusions

In summary, cubic PdNPs were grown in a single-step wet chemical synthesis. As a next step toward GNP growth, as-synthesized PdNPs were plasma –oxidized for different durations (0-90 min) in an oxygen plasma process, palladium/oxides core/shell heterostructures were observed for 90 min oxidation sample. PdNPs also been reduced by hydrogen for 30 min as a compare sample. Oxidation kinetics of PdNPs was studied by XPS, and found to obey Valensi-Carter model. The PdNPs with different oxidation states were used as catalysts for the growth of graphene shell. The increase of shell thickness as increasing of oxidation proved that the palladium oxide shell was consumed during the graphene shell growth process. This supported the hypothesis that unstable palladium oxide at CVD growth temperature allowed for the favorable electron transfer between the palladium oxide and incoming carbon feed, where the latter converts into the graphene shell. The fact that only GNPs using H_2 reduced PdNPs for graphene shells growth can show Pd signal indicates that graphene shells are uniform on nanoparticle surface for each sample. The total yield of ~5.78×10^5 cm^2 of graphene shell surface area per unit gram of PdNPs was observed. (DDA) calculations were performed for PdNPs with different sizes and shapes, as well as Pd-graphene core-shell heterostructures with different core-size and shell-thickness. Red-shift was found for cubic PdNPs, compare to its spherical counters. As increasing the size of PdNPs, the extinction peak of nanoparticles shifts to higher wavelengths. The visualized near field images show strong field intensity located on the edges and corners of cubic PdNPs, and large electric field at the edges of spherical PdNPs/GNPs and dipolar field due to plasmon resonance. The plasmonic modeling spherical PdNPs with/without graphene shells indicates that graphene will just slightly decrease the plasmonic resonance of PdNPs, which is important for the future application of PdNPs in optical sensing.

CHAPTER 5: GRAPHENE SHELLS ENCAPSULATED PLATINUM NANOPARTICLES, THEIR CATALITIC AND OPTICAL PROPERTIES

5.1 Introduction

Similar with PdNPs, in order to explore versatility of our CVD approach and verify the influence of plasma oxidation on graphene shells growth, here we report the fabrication of graphene shells encapsulated PtNPs, using PtNPs that have been treated through different oxidation conditions. The as-synthesized PtNPs, oxidation and graphene shells encapsulated products were characterized for their morphology, crystal structures, and chemical compositions. To study the potential application in SERS, plasmonic modeling for platinum nanoparticles with different size, and shell thickness for platinum/graphene core/shell heterostructures have been done by discrete dipole approximation (DDA) through DDSCAT 7.2, and the near field of above products have been visualized. Since platinum is an important catalyzing material, we also studied the catalytic property of graphene shells encapsulated PtNPs (GNPs), and compared their stability to their counter PtNPs. Figure 5.1 outlines steps investigated in this chapter, including: 1) Synthesis of PtNPs; 2) The oxidation kinetics of PtNPs in plasma oxidation process was studied by varying the plasma treatment duration; 3) The effect of platinum oxide formation for the CVD growth of carbon/graphene shell encapsulating PtNPs (C-PtNPs) was evaluated using PtNPs that have been plasma oxidized for different time as catalysts during the growth of graphene shell; 4) The investment of optical and catalytic properties of C-PtNPs.

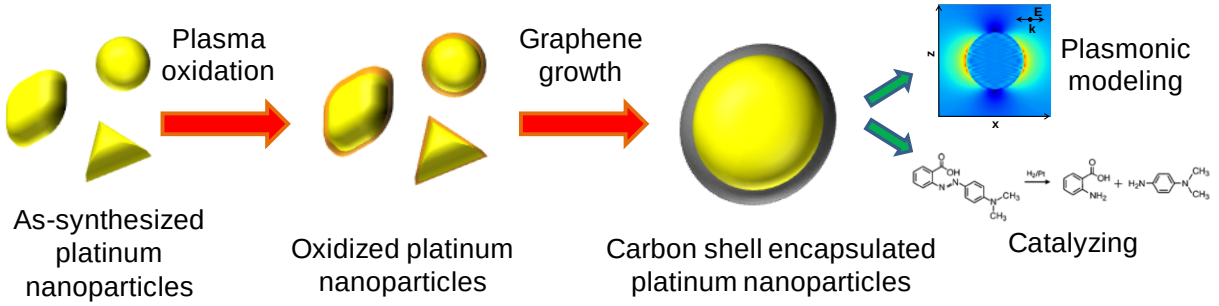

Figure 5.1 Schematic shows various steps including controlled synthesis of PtNPs, their plasma oxidation, and subsequent utilization as catalysts for the growth of C-PtNPs. The optical and catalytic properties of C-PtNPs were also studied.

5.2 Experimental Methods

5.2.1 Materials and methods

Polyvinylpyrrolidone (PVP, $(C_6H_9NO)x$, *Mw* 40,000) was purchased from Sigma-Aldrich (St. Louis, MO). Dihydrogen hexachloroplatinate (IV) hexahydrate ($H_2PtCl_6{\cdot}_6H_2O$, 99.9%) was bought from Alfa Aesar (Ward Hill, MA). Silver nitrate ($AgNO_3$, reagent ACS, electrophoresis grade) was purchased from Acros Organics (New Jersey, NJ). Ethylene Glycol (EG, HOCH2CH2OH) was bought from VWR International (West Chester, PA). Xylene (o-, m-, p-isomers) was purchased from Fisher scientific (New Jersey). 3-Mercaptopropyltrimethoxysilane (MPTMS, $HSCH_2CH_2CH_2Si(OCH_3)_3$, 97+ %) was bought from TCI America (Portland, OR). All chemicals were used without further purification. Silicon wafers (100, n-type) were purchased from IWS (Colfax, CA). DI water (18.1 MΩ-cm) was obtained using a Barnstead International DI water system (E-pure D4641). Labnet centrifuge (Edison, NJ) was used to wash and separate nanoparticles. Wet samples were dried and stored in a VWR vacuum oven (West Chester, PA). Oxygen plasma treatment was performed in Model 1021 plasma cleaner (E.A. Fischione Instruments, PA). Graphene shells growth was conducted inside Lindberg blue 3-zone tube furnace (Watertown, WI). Quartz tubes were purchased from ChemGlass (Vineland, NJ). Syringe injector was obtained from Fisher Scientific (Suwannee, GA). Thermocouples and temperature controllers were bought from Omega Engineering (Stamford, CT). H_2 (UHP grade, 40% balanced with Ar) and Ar (UHP grade) gas cylinders were purchased from Airgas South (Tuscaloosa, AL). Gas flow rates of all chemical vapor deposition processes were controlled by Teledyne Hasting power pod 400 mass flow controllers (Hampton, VA).

5.2.2 Synthesis of Platinum Nanoparticles

To control the morphology of PtNPs, AgNO3 was added as shape-control additive. First, 2.5 mL of EG was magnetic stirred and refluxed at 200 ^{o}C for 5 min in an oil heating bath. Second, 0.5 mL 0.002 M $AgNO_3$ in EG was added to above EG. Third, 3 mL 0.375 M PVP and 1.5 mL 0.0625 M H_2PtCl_6 in EG were mixed together, then 140.7 μL of PVP and H_2PtCl_6 in EG mixture was added into the volumetric flask every 30 s over a 16 min period (4.5 mL totally). The resultant mixture was heated and refluxed at 200 ^{o}C for an additional 5 min. After cooling down, the solution was centrifuged at 5000 rpm for 15 min to remove AgCl. The supernatant was collected and precipitated by adding triple volume (21 mL) of acetone, and centrifuged at 3000 rpm for 5 min. The precipitate was dispersed in 3 mL ethanol by sonication, then added 9 mL of hexane. Repeating the centrifugation step twice, and finally the product was dispersed in ethanol. As-synthesized PtNPs were dispersed on piranha cleaned silicon wafer by MPTMS functionalization method and dried in vacuum oven. Firstly, silicon wafer was cleaned by piranha acid (H_2SO_4:H_2O_2=5:1 v/v) at 100 ^{o}C for 30 min, followed by washing in copious deionized water. Secondly, cleaned silicon wafer was fully dried and then immersed in reagent alcohol containing 2 mM MPTMS, gently shaking for 12 h. After silanization, the substrate was rinsed with reagent alcohol and baked at 80 ^{o}C for 1 h. Finally, PtNPs were dispersed on substrate by immersing functionalized Si wafer in PtNPs reagent alcohol solution for 12 h. After dispersion, the substrates were rinsed with reagent alcohol, dried and stored in vacuum oven.

5.2.3 Plasma Oxidation of Platinum Nanoparticles

The oxidation was performed in Model 1021 plasma cleaner at ~40 W and ~36 mTorr of mixture gas (25% O_2 and 75% Ar) pressure. The dispersed PtNPs were plasma oxidized from 5 to 90 min

to result in surface oxide. The oxidized samples were sent to next graphene shells growth step immediately after plasma treatment.

5.2.4 Fabrication of Graphene Shells Encapsulated PtNPs to Study the Effect of Plasma Oxidation

Substrates with as-synthesized PtNPs, as well as PtNPs been plasma treated for different times were placed in the center of quartz tube equipped with precursor and gas lines for Ar/H_2 flow. Xylene was utilized as the carbon source and was injected through a syringe injector into a preheated zone at the rate of 45 mL/h for ~ 2 min and subsequently transported into the reaction zone (~800 ^{o}C) inside the quartz tube furnace. The xylene flow rate was reduced to 5 mL/h after H_2 mixed with Ar (Ar/H_2=0.85 LLM/0.3 SLM or 10% v/v H_2) was introduced in the CVD reactor. Here, H_2 acted as an oxygen scavenger and Ar as a carrier gas or dilutant. The CVD reaction was continued for 30 min after which H_2 and xylene were discontinued, and the furnace was cooled down under Ar flow.

5.2.5 Hydrogenation of Methyl Red Using Graphene Shells Encapsulated Platinum Nanoparticles

To invest the catalytic property of C-PtNPs, larger amount of PtNPs were loaded on substrate to obtain a notable catalyzing effect. PtNPs were dispersed on cleaned silicon substrate (with area around 1 cm^2) by drop-casting 20 μL as-synthesized PtNPs solution and dried in a desiccator. Then PtNPs were plasma oxidized for 30 min, and grow graphene shells at 675 ^{o}C for 1h, with xylene flow rate 10 mL/h, resulted in C-PtNPs. To study their stability and catalytic property, different treatment such as aqua regia etching, plasma oxidation or high temperature annealing were applied on C-PtNPs. Each substrate has the same load of PtNPs to obtain comparable results.

Dissolution of C-PtNPs in Aqua Regia: In order to estimate the tightness of graphene shell on C-PtNPs, dissolution experiment in aqua regia were performed. The substrate patterned with C-PtNPs were immersed in ~6 mL aqua regia ($HCl:HNO_3$=3:1 v/v) solution for 1 h. Then, the substrate was washed in an abundant amount of DI water to remove any remaining acid after the dissolution experiment, followed by drying in a desiccator.

Oxygen plasma treatment of C-PtNPs: To study their catalytic property, as prepared C-PtNPs would be treated with oxygen plasma. The C-PtNPs substrates were placed in plasma chamber, and oxidized for 15 s, 30 s, or 60 s at 120W and 300 mTorr chamber pressures, with flowing O_2.

Annealing treatment of PtNPs or C-PtNPs: To study their stability at high-temperature, substrates patterned with PtNPs or C-PtNPs were placed in quartz tube, followed by annealing at 350 ^oC, 550 ^oC, 750 ^oC, or 1000 ^oC in Ar atmosphere for 2 h.

Evaluation of catalytic activity by Methyl red hydrogenation: The hydrogenation of methyl red has been chosen to gain an insight into the catalytic activity of C-PtNPs. Methyl red solution was prepared by dissolving 3.9 mg methyl red in 25 mL reagent alcohol, then added 100 mL of pH 4.0 buffer solution (made from mixing 0.1 M citric acid and 0.2 M Na_2HPO_4). The solution was diluted into 1000 mL with DI water, yielding a 14.5 μM methyl red stock solution. The substrate with as-prepared PtNPs, annealed PtNPs, plasma treated or annealed C-PtNPs was incubated in 2 mL methyl red solution, and then bubbled with 40% (v/v) H_2 balanced in Ar for hydrogenation of methyl red. The samples for this test came from the same batch and have the same Pt loading. The dynamic of hydrogenation has been tested by measure UV-Vis after every 1 min hydrogenation.

To determine the recycling property, the C-PtNPs annealed at 750 ^{o}C was used for catalysis cycling. After annealed at 750 ^{o}C for 2 h, the substrate was repeatedly used for hydrogenation 5 times, each time the UV-Vis was tested after 5 min, 10 min hydrogenation, respectively. Then the substrate was recovered by immersing in DI water for 24 h, and used for hydrogenation again. After that, the substrate was repeated for annealing – hydrogenation for 5 cycles.

5.2.6 Characterization

Tecnai F-20 was used to collect Transmission Electron Microscopy (TEM) images at 200 kV. TEM samples were prepared by dispersing as-prepared samples on lacey carbon TEM copper grids. The average nanoparticle size was measured from TEM images, where 200 nanoparticles were counted and measured per sample. Diameter was measured for spherical nanoparticles, and for nanoparticles with other shapes, diagonal length average was taken. All the measurements were done using Adobe Photoshop Software. X-ray photoelectron spectra (XPS) were gathered by Kratos Axis 165 with mono-Aluminum gun. The analysis spot was set as “Slot” with >20 µm aperture and 19.05 mm iris setting. XPS was used to characterize elements’ chemical states. Raman spectra were collected using Bruker Senterra system (Bruker Optics Inc. Woodlands, TX) equipped with a 785 nm laser source at 10 mW laser powers and 100X objective. The integral time and co-additions were set as 15 seconds and 2, respectively. The Raman mapping conditions for map acquisition were set at the resolution of 3-5 cm^{-1} in the range of 102-2658 cm^{-1} with 10 mW laser power. A rectangular grid of 15 µm × 15 µm of the sample surface was chosen and 100 points on the grid were scanned in full range. OPUS Spectroscopy Software coupled with Raman spectrometer allows to select the frequency range for populating the chemical map. The range is defined from 1500 – 1700 cm^{-1}, and then software integrated the

peak area in this range and shows the spectral changes as a function of position on the substrate. The contour mapping enables to subdivide the absorption intensity into several levels and to visualize them by a color scheme. The UV-Vis-NIR spectroscopy was performed using USB 4000 spectrometer from Ocean Optics Inc. The UV-Vis-NIR light source was using Mikropack DH-2000 Deuterium-Tungsten Halogen light source.

5.3. Morphology Control of Platinum Nanoparticles

The process we utilized is a standard approach for producing PtNPs with controlled shape and size[160]. Ethylene glycol (EG) was served as solvent for metal salt (H_2PtCl_6) and surfactant (PVP), meanwhile it acted as reducing agent to produce PtNPs. For face-centered cubic (fcc) structured metal particles, the surface energy for different facets usually follow the sequence: $\gamma\{111\} < \gamma\{100\} < \gamma\{110\}$[160]. So the platinum atoms will tend to form on the high-energy facets during reduction and the low-energy facets were achieved. Meanwhile, silver species preferentially adsorbs on {100} surfaces of PtNPs than {111} surfaces, enhances the growth along <100>, and/or suppresses the growth along <111>.[161] During the process, $AgNO_3$ is unstable, it decomposes at high temperature (200 ^{o}C), and Ag species was adsorbed on {100} surface of PtNPs. H_2PtCl_6 was continuously added into solution, favorable electrochemical reaction took place between Pt salt and Ag species, and subsequently the growth rate along the <100> direction was enhanced. Eventually, octahedra and tetrahedra PtNPs was obtained. HRTEM image shows that PtNPs exhibit stable {111} faces and {200} facets (Figure 5.2). After synthesis, the AgCl byproducts and excess PVP were easily removed by repetitive precipitation, only left the PVP monolayer coating on surface of PtNPs to stabilize them from aggregation.

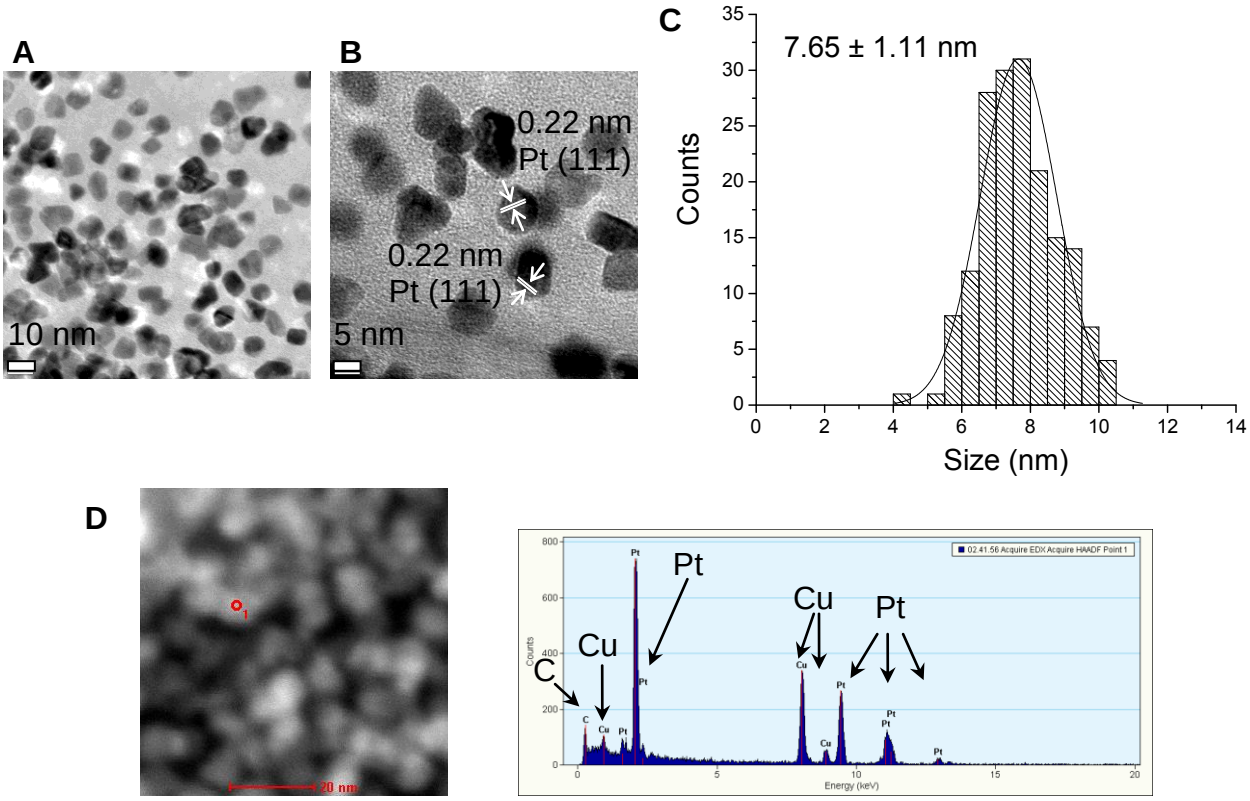

Figure 5.2 (A, B) TEM images, (C) histogram of size distribution, (D) STEM image and EDS of as-synthesized PtNPs

5.4 Oxidation Kinetics of PtNPs

To study the oxidation behavior of PtNPs under oxygen plasma, as-synthesized PtNPs were drop-casted on piranha cleaned silicon wafers and placed in oxygen plasma chamber for oxidation treatment. The substrates were oxidized in the same environment (40 W, 36 mTorr pressure of 25% O_2 balanced in Ar) with various duration (from 5 min to 90 min).

In order to make quantitative conclusions on oxidation status, XPS was utilized to determine the composition of nanoparticles in different oxidation states. Figure 5.3 shows over-lapped XPS spectra with binding energy ranging from 1000 to 0 eV for as-synthesized PtNPs and PtNPs been plasma oxidized from 5 min to 90 min. Peaks of Pt, N, C, and Si presented in spectra were generated from PtNPs, PVP, and Si substrate, respectively. The existence of O peaks can be attributed to several origins, such as platinum oxide, the absorbed organic molecules, and surface SiO_2 from substrates, thus the formation of platinum oxide could only be distinguished by detailed analysis of Pt 4f peaks (Figure 5.4 and Table 5.1).

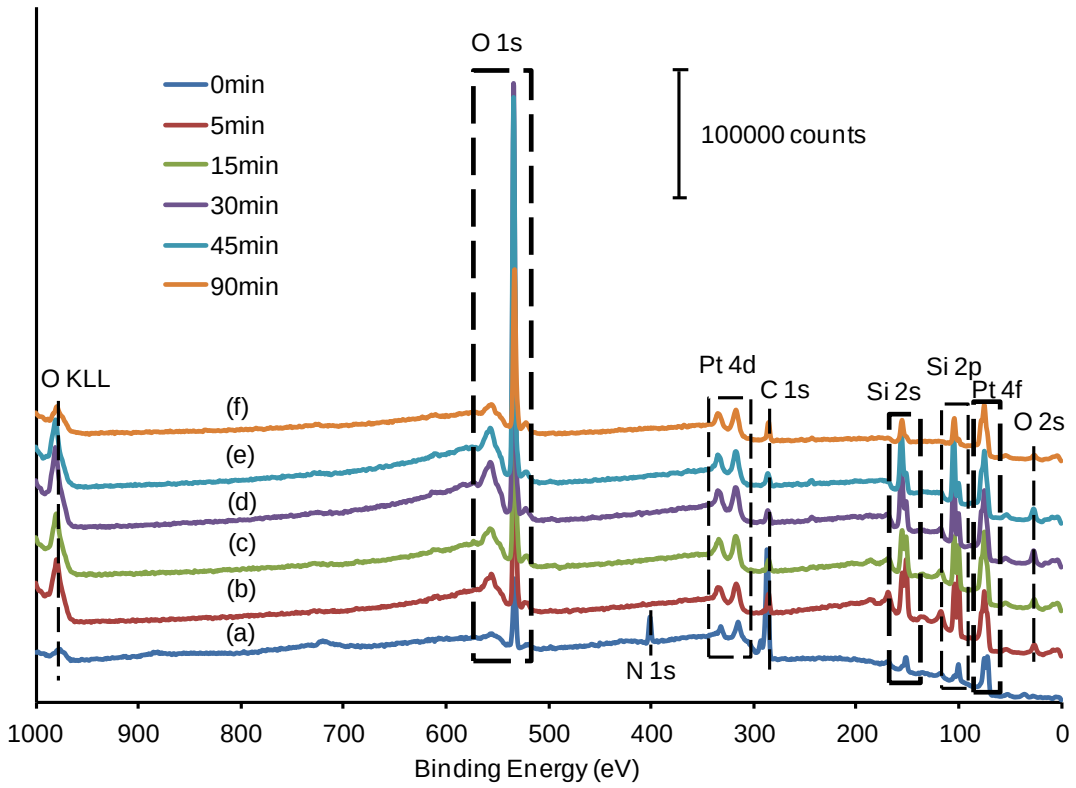

Figure 5.3 XPS spectra corresponding to PtNPs (a) as-synthesized PdNPs and after (b) 5 min, (c) 15 min, (d) 30 min, (e) 45 min, (f) 90 min of plasma oxidation duration. *Note: PtNPs were dispersed on Si wafer by drop-casting method.*

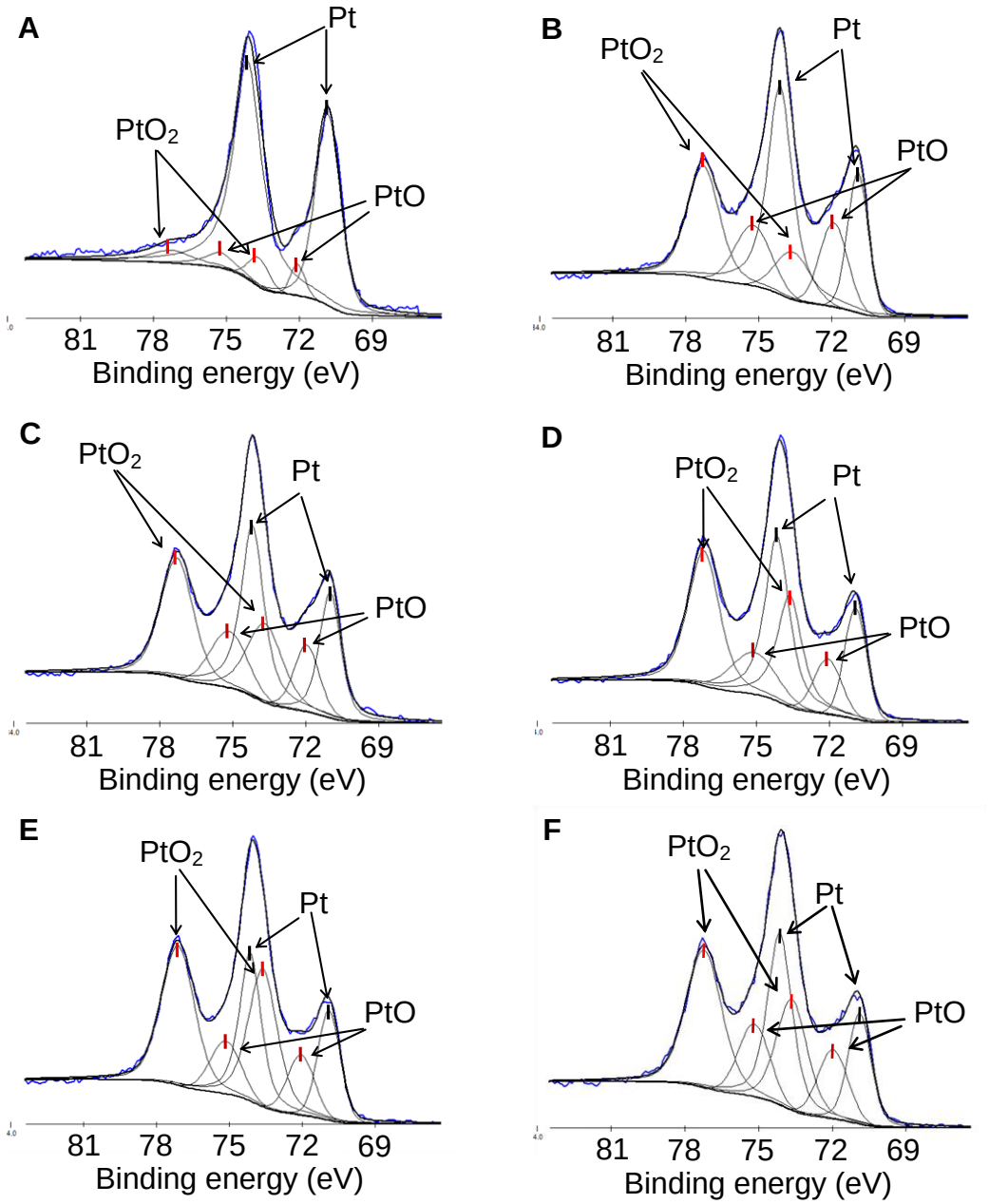

Figure 5.4 Deconvoluted XPS spectra subtracted by Shirley background, and fitted with Pt 4f peaks corresponding to PtNPs (A) as synthesized, and after plasma oxidation for (B) 5 min, (C) 15 min, (D) 30 min, (E) 45 min, (F) 90 min.

Table 5.1 Binding energy (eV) derived from XPS study for shape controlled PtNPs with different oxidation conditions corresponding to the spectra as shown in Figure 5.4

Plasma condition (min)	Binding Energy (eV)					
	Pt $4f_{5/2}$			Pt $4f_{7/2}$		
	PtO_2	PtO	Pt^0	PtO_2	PtO	Pt^0
0	77.28	75.26	74.13	73.67	72.07	70.83
5	77.26	75.22	74.12	73.58	71.91	70.91
15	77.28	75.15	74.18	73.67	71.95	70.99
30	77.16	75.10	74.15	73.63	72.07	70.93
45	77.12	75.15	74.14	73.62	72.05	70.90
90	77.22	75.18	74.13	73.65	71.97	70.89

The Pt $4f_{7/2,\ 5/2}$ peaks indicate the existence of three forms of Pt in as-synthesized PtNPs: the metallic platinum at 70.83 eV and 74.13 eV, the PtO at 72.07 eV and 75.26 eV, the PtO_2 at 73.67 eV and 77.28 eV, respectively. The generation of platinum oxide in as-synthesized PtNPs could be attributed to the oxidation of Pt by air during synthesis and handling. As the increase of plasma oxidation time, the peaks corresponding to platinum oxide generally increased while the metallic peaks decreased, indicating the process of surface oxidation of PtNPs.

The percentage of the metallic platinum and surface oxides could be obtained by analyzing the areas under each Pt 4f peaks (Table 5.2), which can help us to understand the oxidation kinetics of PtNPs. The quantitative analysis (Figure 5.5) showed the formation of PtO and PtO_2 during the oxygen plasma process. The amount of oxides, with PtO_2 as major component, was dramatically increased within 5 min plasma oxidation and maximized at 45 min duration, then slightly reduced at 90 min. This could be attributed to the etching of platinum oxides beyond 45 min plasma oxidation due to the prolonged plasma processing. Overall, it was observed that 66.74%, 63.54% surface oxides (molar percentage, including PtO and PtO_2) were detected by XPS after oxidation for 45 min and 90 min, respectively.

Table 5.2 The ratio of Pt calculated as peak area of Pt over the sum of Pt and PtO_x peaks area as shown as Figure 5.4

Plasma time (min)	Pt peaks area	PtO peaks area	PtO_2 peaks area	Metallic Pt ratio (%) (Pt/ (Pt+ PtO_x) ×100%)
0	26243.57	2063.83	2618.2	84.86
5	23092.98	10633.11	13729.16	48.66
15	24189.9	11274.75	22197.85	41.95
30	22103.3	9995.2	24989.3	38.72
45	17627.07	8681.198	26685.97	33.26
90	14909.38	8174.854	17809.05	36.46

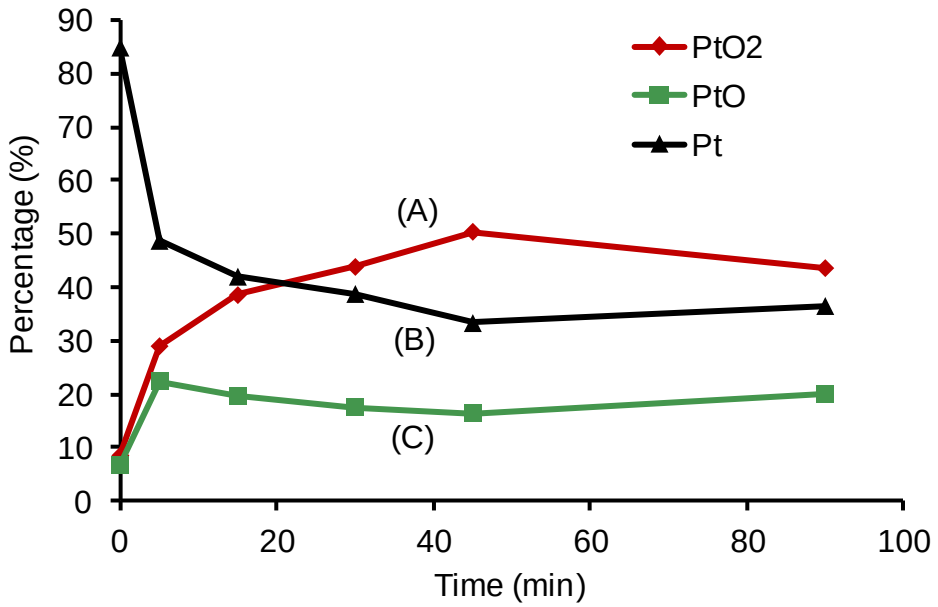

Figure 5.5 Oxidation behavior of cubic PdNPs as a function of plasma time, derived from the XPS results (Table 5.2): percentages of (A) Pt, (B) PtO_2, and (C) PtO.

The evaluation of XPS results allows us to theoretically understand oxidation process and calculate the accurate thickness of the oxide shell. The XPS analysis shows that PtO_2 is the dominant oxide (Figure 5.4 and Table5.2), so we can consider all platinum oxide as PtO_2 during the calculation. Due to the lower density of PtO_2 (10.2 g/cm^3) than Pt (21.45 g/cm^3), the size of PtNPs would increase after oxidation. Considering spherical PtNPs, as indicated in Figure 5.6A, before oxidation (at t=0), the XPS detected volume (V_{cap}) is given by

$$V_{cap} = \frac{\pi}{3} H^2 (3R - H) \tag{5.1}$$

where R is the radius of PtNPs (~3.83 nm) before plasma oxidation (at $t=0$) and H is the electron emission depth of the sample in XPS (assumed as 3 nm). The fraction of metallic platinum remaining in surface-oxidized PtNPs as calculated from XPS is F_{Pt} (Table 5.2), which is also changing with plasma oxidation duration. Thus, at $t=t$, this can be written as

$$\frac{\frac{\pi}{3}(H-a)^2(3r_1 - H + a)}{\frac{\pi}{3}H^2(3r_1 + 3a - H)} = F_{Pt} \tag{5.2}$$

where r_1 is the radius of remaining metallic core of nanoparticle and a is the thickness of oxide shell, which are functions of oxidation duration (t). The basic chemical reaction governing the conversion of platinum into its oxide is $Pt + O_2 \rightarrow PtO_2$; then,

$$n_{PtO_2} = n_{Pt} = \frac{(\frac{4\pi}{3}R^3 - \frac{4\pi}{3}r_1^3)\rho_{Pt}}{M_{Pt}} \tag{5.3}$$

$$V_{PtO_2} = n_{PtO_2} M_{PtO_2} / \rho_{PtO_2} \tag{5.4}$$

$$\frac{4\pi}{3}(r_1 + a)^3 = \frac{4\pi}{3}r_1^3 + V_{PtO_2} \tag{5.5}$$

where n represents the moles of the species, V_{PtO2} is the volume of oxidized platinum, ρ_{Pt}, ρ_{PtO2}, M_{Pt}, and M_{PtO2} are the densities and molar masses of platinum and platinum oxide, respectively. Combining Equation 5.2-5.5 results in

$$\frac{\pi}{3}(H - a)^2(3r_1 - H + a) = F_{Pt}\frac{\pi}{3}H^2(3r_1 + 3a - H) \tag{5.6}$$

$$(R^3 - r_1^3)\frac{M_{PtO_2}\rho_{Pt}}{M_{Pt}\rho_{PtO2}} + r_1^3 - (r_1 + a)^3 = 0 \tag{5.7}$$

On the basis of above set of equations, the relations between plasma oxidation time (t) and thickness of platinum oxide shell (a) can be derived. H, R, M, and ρ are known parameters. The relationship between XPS-derived fractions of metallic platinum remaining in the nanoparticles (F_{pt}) with oxidation time (t) is shown in Figure 5.6B. Thus the thickness of the oxide shell can be estimated for each sample. The oxidation kinetics of the nanoparticles was fitted with Valensi-Carter model as proposed earlier for the oxidation kinetics of palladium powder. The Valensi-Carter equation is given by:

$$[\{1+(z-1)x\}^{2/3}+(z-1)(1-x)^{2/3}-z]/(1-z)=Kt \quad (5.8)$$

z is the volume of product formed per unit volume of reactant consumed, for reaction $Pt+O_2 \rightarrow PtO_2$, z is 2.448. x is the reaction ratio of palladium, which can be calculated from the size of cubic PdNPs and thickness of oxide shell. K is a kinetic constant, t is the oxidation time. Submit z=2.448 into Equation 5.8 we have:

$$F(x)=[(1+1.448x)^{2/3}+1.448(1-x)^{2/3}-2.448]/(-1.448)=Kt \quad (5.9)$$

According to Equation 5.7 and the thickness calculation for each sample, the *F(x)* can be plotted as a function of plasma time (Figure 5.6C). The oxidation occurred very fast in the first 5 min, and gradually slowed down in the later stage of reaction. After 45 min, the detected oxidation ratio reduced because of the plasma etching effect. The Valensi-Carter equation is used to describe the reaction controlled by diffusion process, implies the diffusion of either O or Pt during plasma treatment is the control-step during oxidation. From the obtained *F(x)* fitted line, we can calculate the ideal reacted ratio and oxide thickness inversely. Figure 5.6D and 6E show the comparison of theoretical data from Valensi-Carter model and the calculated data from XPS analyzing, the two sets data closely matched within 45 min oxidation.

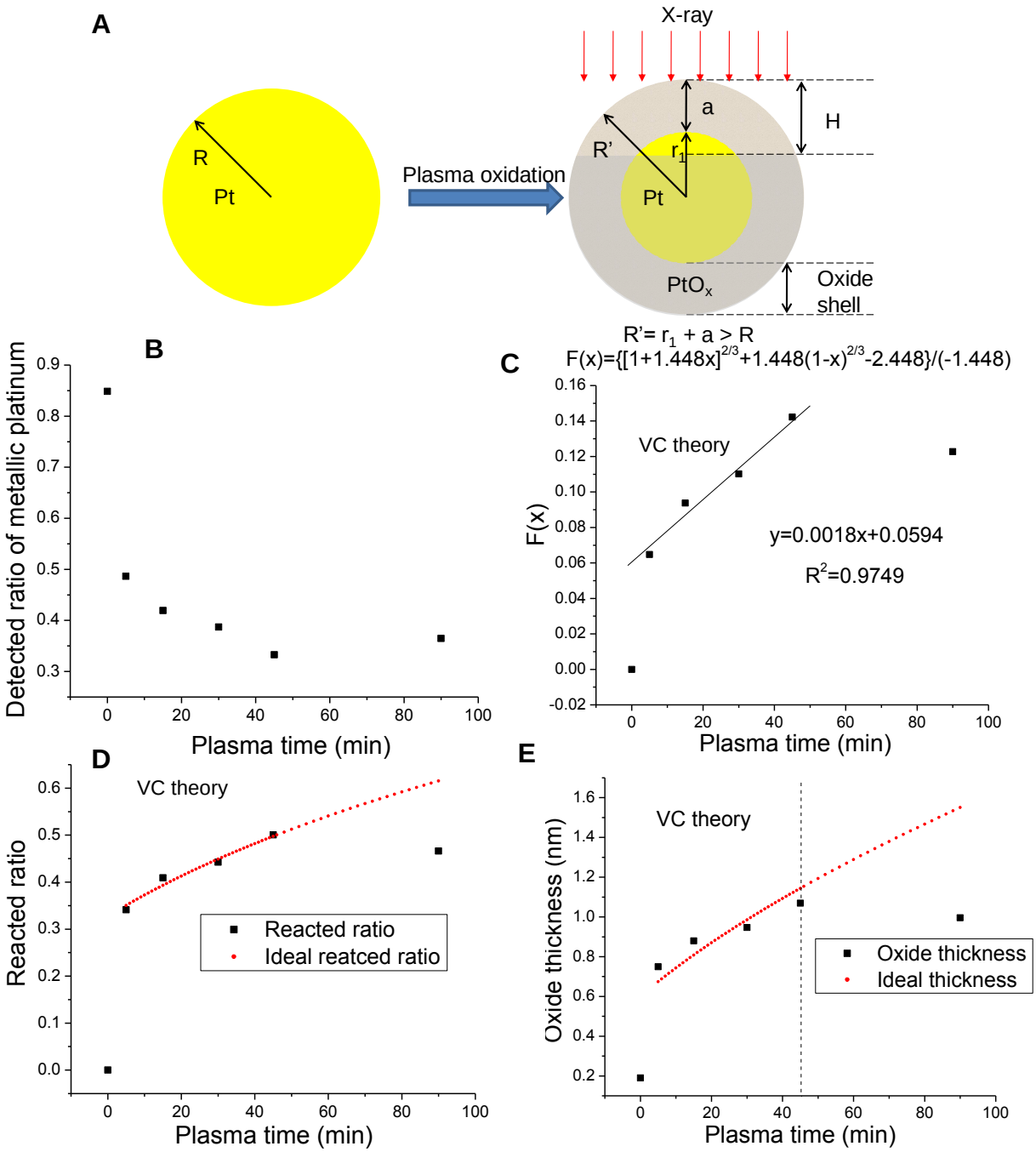

Figure 5.6 (A) Schematic showing formation of platinum oxide (PtOx) shell on as-synthesized particle and XPS analysis showing the detection depth (H) and other geometrical parameters. Graphs showing the relationship between plasma time and (B) XPS detected ratio of metallic Pt,

(C) Valensi-Carter function F(x), (D, E) Fitting of Valensi-Carter (VC) model for oxidation of cubic particles with the observed experimental data.

5.5 Effect of oxidation on graphene shells growth

To evaluate the influence of platinum oxide on graphene shell-formation, PtNPs with different oxidation states (Table 5.1 and 5.2) were used as catalysts in the xylene CVD process. After graphene shells growth, PtNPs increased size and exposed {111} to attain a minimum surface energy configuration (Figure 5.7). Some extent of amorphous/graphitic carbon and loosen carbon shells were observed surround those nanoparticles. PtNPs were encapsulated in graphene-like carbon shells with interlayer spacing of 0.34~0.39 nm, which is consistent with the c-axis spacing of graphite. At high temperature during CVD process, some adjacent PtNPs tend to aggregate together, and resulted in the increase of particle size from originally less than 10 nm to 10~30 nm after graphene shells growth (Figure 5.8A and Table 5.3).

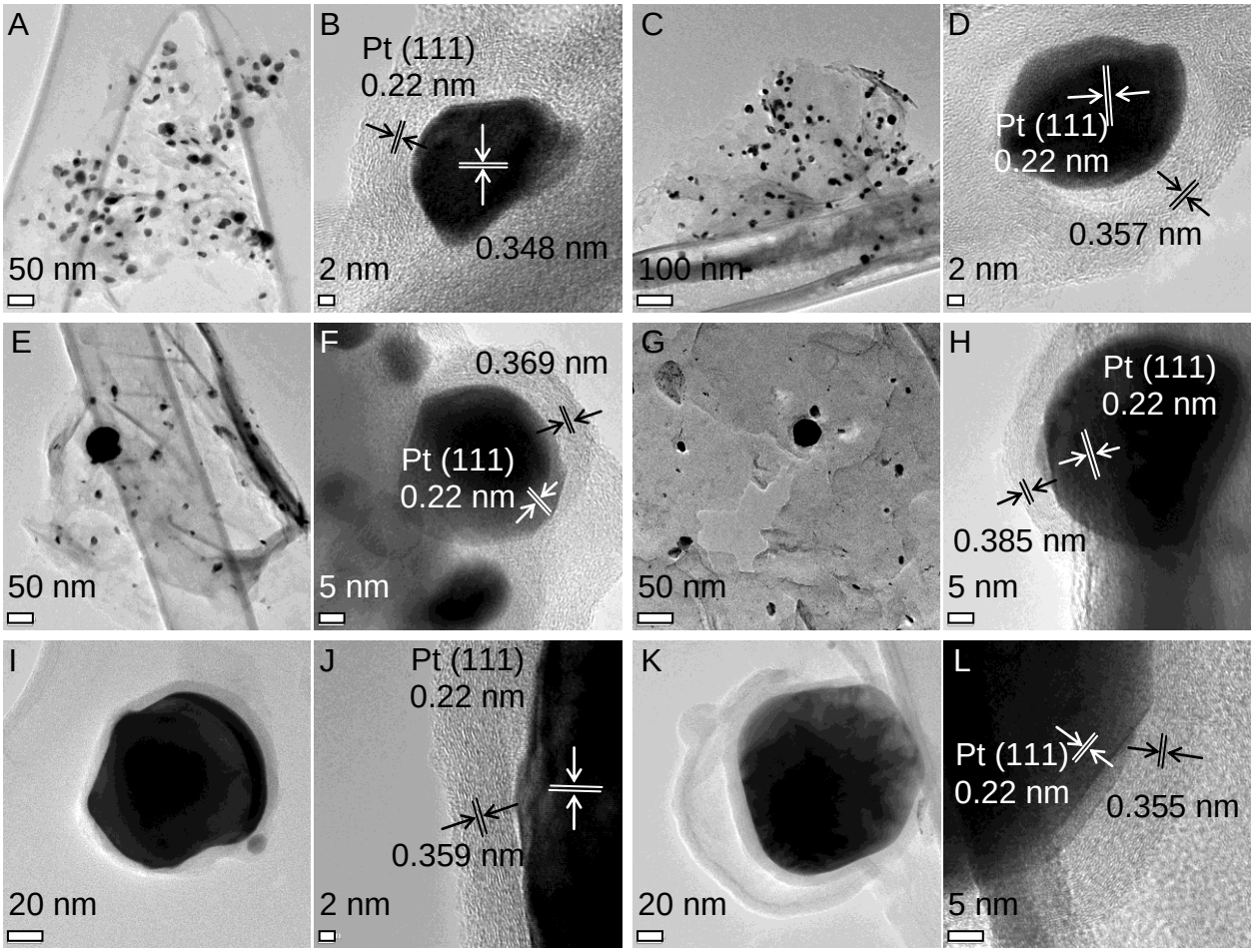

Figure 5.7 TEM images showing graphene shells growth on (A, B) as-synthesized PtNPs, and PtNPs been plasma oxidized for (C, D) 5 min, (E, F) 15 min, (G, H) 30 min, (I, J) 45 min, (K, L) 90 min

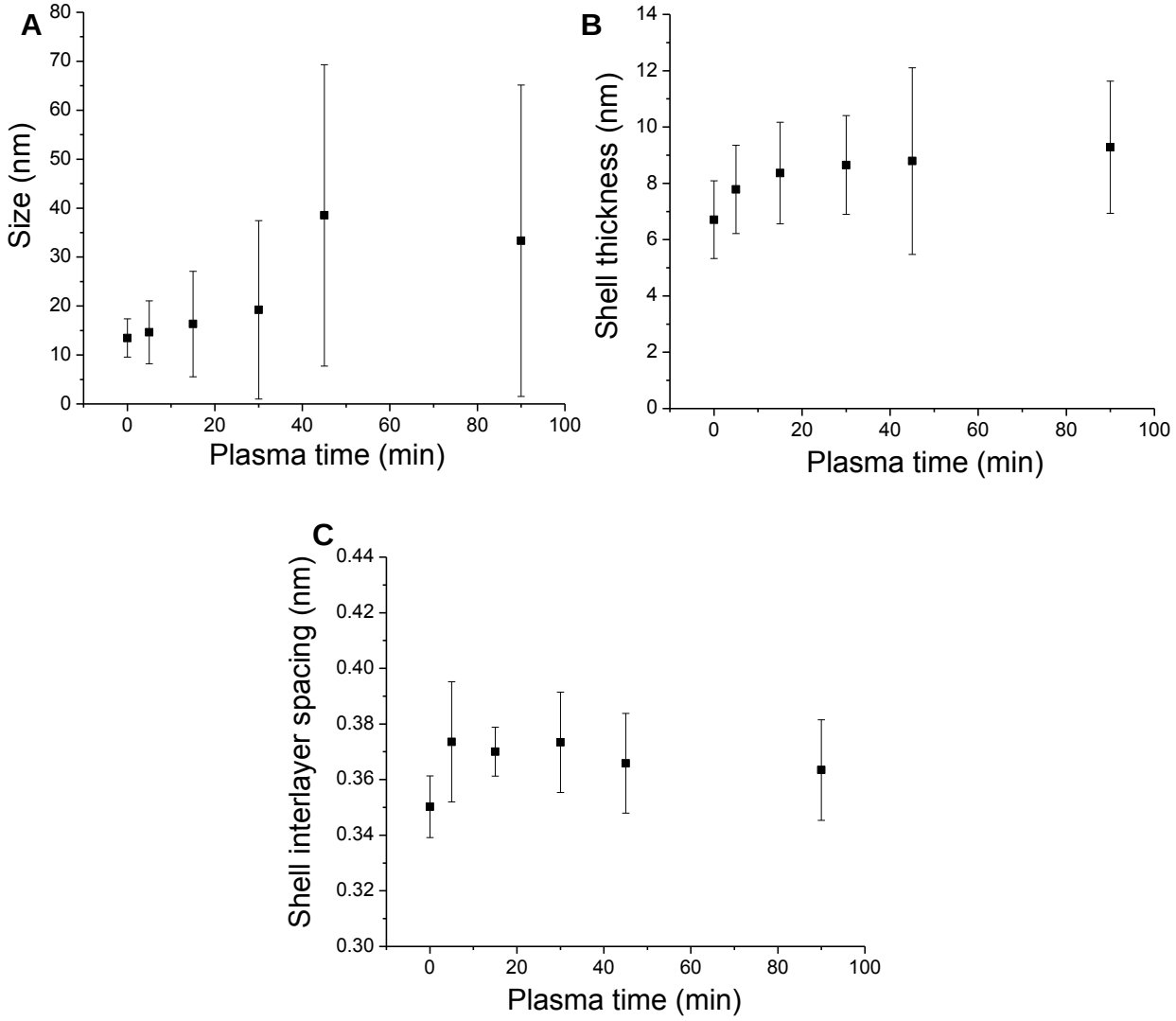

Figure 5.8 Plots showing the change of (A) particle size, (B) shell thickness, and (C) shell interlayer spacing as a function of plasma condition.

Table 5.3 Average size of platinum core, thickness and interlayer spacing of shells, and D-, G-band intensity ratio (I_D/I_G) of graphene shells encapsulated PtNPs (PtNPs were treated by plasma oxidation for different duration).

Oxidation condition (min)	Particle size (nm)	Shell thickness (nm)	Shell interlayer spacing (nm)	I_D/I_G
0	13.5±3.9	6.7±1.4	0.35±0.01	1.42±0.10
5	14.6±6.4	7.8±1.6	0.37±0.02	1.52±0.09
15	16.3±10.8	8.4±1.8	0.37±0.01	1.55±0.11
30	19.2±18.2	8.7±1.8	0.37±0.02	1.38±0.12
45	38.5±30.8	8.8±3.3	0.37±0.02	1.43±0.10
90	33.3±31.8	9.3±2.3	0.36±0.02	1.39±0.14

In same graphene shells growth condition, PtNPs with longer oxidation time obtained larger size after CVD process. This may due to sintering of neighbor nanoparticles caused by long-time plasma treatment. Under low pressure plasma reactor, the condition favors the evaporation of surfactants from the nanoparticles surface, and helps the uncoated particles contact directly and sinter. Thus a longer plasma treatment allows more PtNPs sinter together and form larger clusters, which melted into bigger particles during high temperature graphene shells growth process. Since noble metal oxide can act as electron-receptor to assist the formation of graphene shells during CVD process, thicker platinum oxide shell would last longer in harsh environment (high temperature, reducing atmosphere), thus resulted in more formation of carbon shells. So as oxidation duration was increased, we observed the trend of thicker carbon shells formation (from ~6.7 to ~9.3 nm average, Figure 5.8B and Table 5.3). Graphene shell obtained from as-synthesized PtNPs has smallest interlayer spacing (0.35±0.01 nm), and the interlayer spacing increases as plasma time increased to 45 min (0.37±0.02 nm, Figure 5.8C, Table 5.3). But the shell interlayer spacing for plasma oxidized 90 min PtNPs decreased to 0.36±0.02 nm. The rise of interlayer spacing attributed to uncorrelated atomic positions between carbon atoms on two adjacent shell layers.

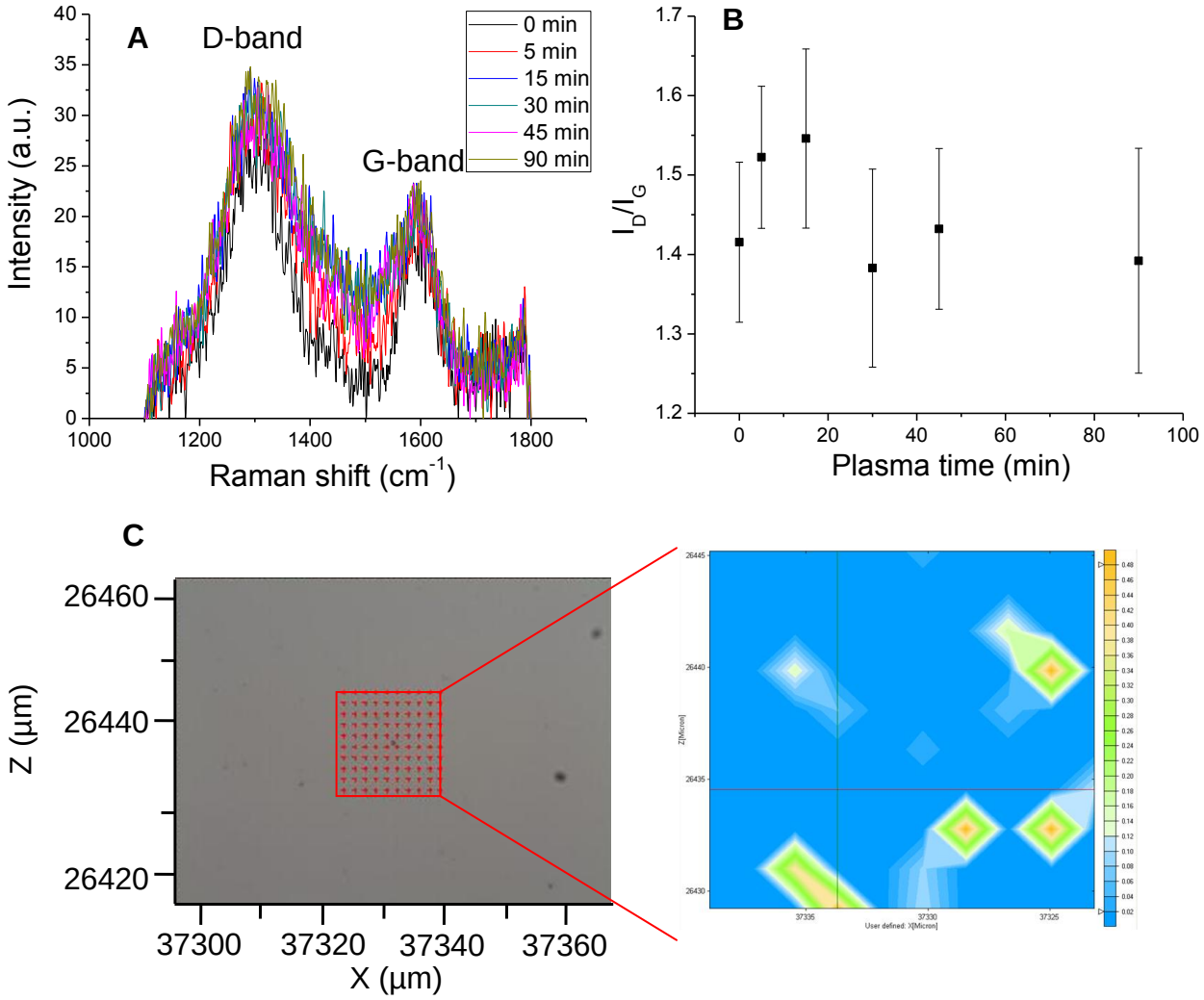

Figure 5.9 (A) Raman spectra showing graphene shells growth on PtNPs been plasma oxidized for different duration. (B) Plot showing the ratio of D-, G-band peak intensity as a function of plasma condition. (C) Raman chemical mapping for graphene shells growth on PtNPs been plasma oxidized for 30 min.

Raman spectra (Figure 5.9A) for C-PtNPs showed D and G-band, which consistent with disordered and graphitic carbon content, centered at ~1308 and 1596 cm^{-1}, respectively. The intensity of D-, G-band Raman spectra has similar tendency with the change of shell thickness for each sample. However, since the difference of average shell thickness between samples is small, there was no big difference between Raman spectra intensity either. The intensity ratio of D-, G-band (I_D/I_G) was ranging from 1.38 to 1.55 (Figure 5.9B and Table 5.3). The PtNPs plasma oxidized within 15 min showed that I_D/I_G increased at longer oxidation duration, indicating that more disordered carbon formed on longer oxidized PtNPs. After 15 min oxidation, I_D/I_G remained similar to each other among graphene samples. Raman chemical mapping over large substrate area was performed (Figure 5.9C) and the color scheme represents the normalized intensity of the G-band peak (with regard to the highest G-band peak intensity in the scanned area). The mapping showed uniform intensity over the most area, and high intensity corresponding to large amount of particles encapsulated in carbon. This indicates that the high-throughput CVD growth process resulted in large area growth of C-PtNPs. The specific surface area of graphene shell can be estimated from TEM images. The shell thickness ($b_{observed}$) and core-particle size (R) can be measured from TEM images, and we know the density of platinum (ρ_{PtNP}=21.45 g/cm^3), thus the specific surface area of graphene shell can be estimated as:

$$\frac{S_{grapheneobserved}}{m_{PtNP}} = \frac{4\pi(R+b_{observed})^2}{V_{PtNP}\cdot\rho_{PtNP}} = \frac{4\pi(R+b_{observed})^2}{\frac{4}{3}\pi R^3\cdot\rho_{PtNP}} \tag{5.10}$$

After submitting shell thickness and core size for each sample to eq. 10, we obtained the average specific area of graphene shell per unit palladium particle mass is $(1.69 \pm 0.94) \times 10^6$ cm^2/g.

The importance of platinum oxide to the growth of graphene shell has been proved by the fact that PtNPs with longer oxidation duration resulted in thicker graphene shell. The proposed mechanism is that the oxidized platinum (PtO_x) is unstable at high temperature with the existence of H_2, prefers to accept electrons and transform to metallic Pt. It would assist the decomposition of incoming carbon feed (xylene), resulting in the formation of C-PtNPs. A similar mechanism has been proposed by our group for the formation of carbon shells around surface oxidized AuNPs CVD approach. XPS was utilized to study the chemical states of platinum before and after graphene shells growth. Survey scans for as-synthesized PtNPs before and after graphene shells growth are shown in Figure 5.10A. Pt 4f peaks were further deconvoluted as shown in Figure 5.10B and were assigned accordingly (Table 5.4). An interesting observation was that PtO and PtO_2 peaks still exist after graphene shells growth but weaker than before graphene shells growth. This may attributed to the high activity of metallic platinum nanoparticles in the air and the stability of PtO_2 at room temperature. Carbon 1s peaks obtained from XPS were also deconvoluted (Figure 5.10C and Table 5.5). The peak located at 284.88 eV corresponds to C 1s peak or sp2 carbon. Peaks located at 286.27 and 288.98 eV could be attributed to C-O and C=O bonds, respectively. π-π^* transition loss peak (291.57 eV) was also observed, which is associated with the formation of graphitic carbon.

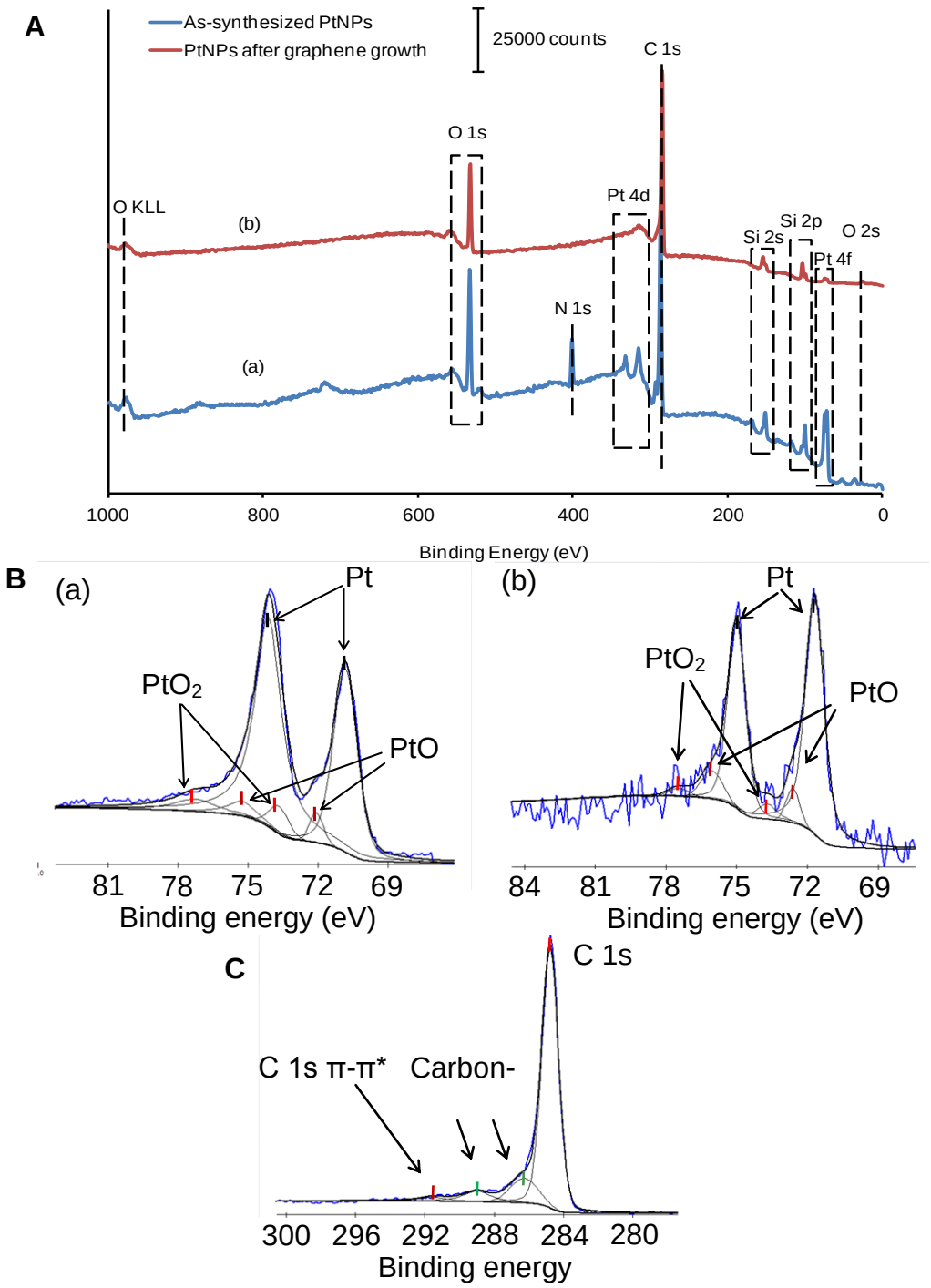

Figure 5.10 (A) XPS spectra corresponding to (a) as-synthesized PtNPs, (b) after 0.5 h graphene growth. (B) Deconvoluted XPS spectra, subtracted by Shirley background, and fitted with Pt 4f peaks (a) before and (b) after graphene growth. (C) Deconvoluted XPS spectra, subtracted by Shirley background, and fitted with C 1s peak after graphene growth.

Table 5.4 Binding energy (eV) chart derived from XPS analysis for PtNPs before and after graphene shells growth corresponding to the spectra as shown in Figure 5.10B

Conditions	Binding Energy (eV)					
	Pt			Pt		
	PtO_2	PtO	Pt^0	PtO_2	PtO	Pt^0
As-synthesized	77.28	75.26	74.13	73.67	72.07	70.83
With Graphene	77.43	76.05	75.00	73.69	72.61	71.69

Table 5.5 Binding energy (eV) chart derived from XPS analysis for PtNPs corresponding to the spectra as shown in Figure 5.10C. *Note: The values in parenthesis indicate the area under the peaks.*

Condition	C 1s Binding Energy (eV)			
	C 1s	Carbon-Oxygen links	Carbon-Oxygen links	C π-π*
After Graphene growth	284.77	286.27	288.98	291.57

5.6 Plasmonic Properties of PtNPs and C-PtNPs

The optical properties of PtNPs with different sizes, and C-PtNPs with different core size and shell thickness have been analyzed by discrete dipole approximation (DDA) calculations. These computational studies have already been proved to fit well with real case, and can be utilized to predict how to achieve good optical properties by controlling the morphology (size and shape) of metal nanostructures. Using the DDSCAT code developed by Draine and Flatau, we calculated the extinction cross section for each structure at wavelength ranged from 200 nm to 800 nm of incident light. The calculate target was chosen to be in vacuum. The dielectric function of platinum was taken from online refractive index database, and the built-in dielectric function of graphite in DDSCAT was utilized for the graphene shell. Extinction spectra (Figure 5.11A) for spherical PtNPs with different size show the red-shift of peak from less than 200 nm to ~367 nm when particle size increased from ~5 nm to ~300 nm. Further increase the size would broaden the peak and flatten the extinction curve. The red-shift of extinction peak holds significant importance for PtNPs. As a noble metal, platinum normally serves as catalyst for various applications. The optical property of PtNPs remains unexplored relatively. That's because the surface plasmon resonance (SPR) peak of small PtNPs with size smaller than 10 nm is located in the UV zone, where the lights in that region are easily absorbed by glass and most solvents and makes PtNPs' SPR characteristics much more difficult to probe. If the position of the SPR peak of PtNPs could be shifted to visible region, at which the maximum electromagnetic field enhancement would be obtained, it could lead to applications of PtNPs in various field such as colorimetric sensing, plasmonic waveguiding, enhancement of Raman, and optical sensing of hydrogen. The calculation through DDA proved that by increasing PtNPs size, their SPR features could be tailored to locate in visible region.

Table 5.6 Parameters used in DDA calculations for bare PtNPs.

Shape	Effective radius (μm)	Dipole-number	Shape parameter	Size (nm)
Spherical	0.0025038	65752	50	5
Spherical	0.00383	65752	50	7.65
Spherical	0.0050077	65752	50	10
Spherical	0.0075115	65752	50	15
Spherical	0.010015	65752	50	20
Spherical	0.012519	65752	50	25
Spherical	0.015023	65752	50	30
Spherical	0.017527	65752	50	35
Spherical	0.02003	65752	50	40
Spherical	0.02504	65752	50	50
Spherical	0.050077	65752	50	100

Table 5.7 Parameters used in DDA calculations for C-PtNPs. Average size of C-PtNPs, core PtNP, and average graphene shells thickness are consistent with experimental observations.

Effective radius (μm)	Dipole-number	Shape parameter	Core size (nm)	Shell thickness (nm)	Total size (nm)
0.0134	10131	26.9	13.5	6.7	26.9
0.0151	14400	30.2	14.6	7.8	30.2
0.0165	18949	33.1	16.3	8.4	33.1
0.0183	25677	36.6	19.2	8.7	36.6
0.0281	92576	56.1	38.5	8.8	56.1
0.0260	73464	51.9	33.3	9.3	51.9

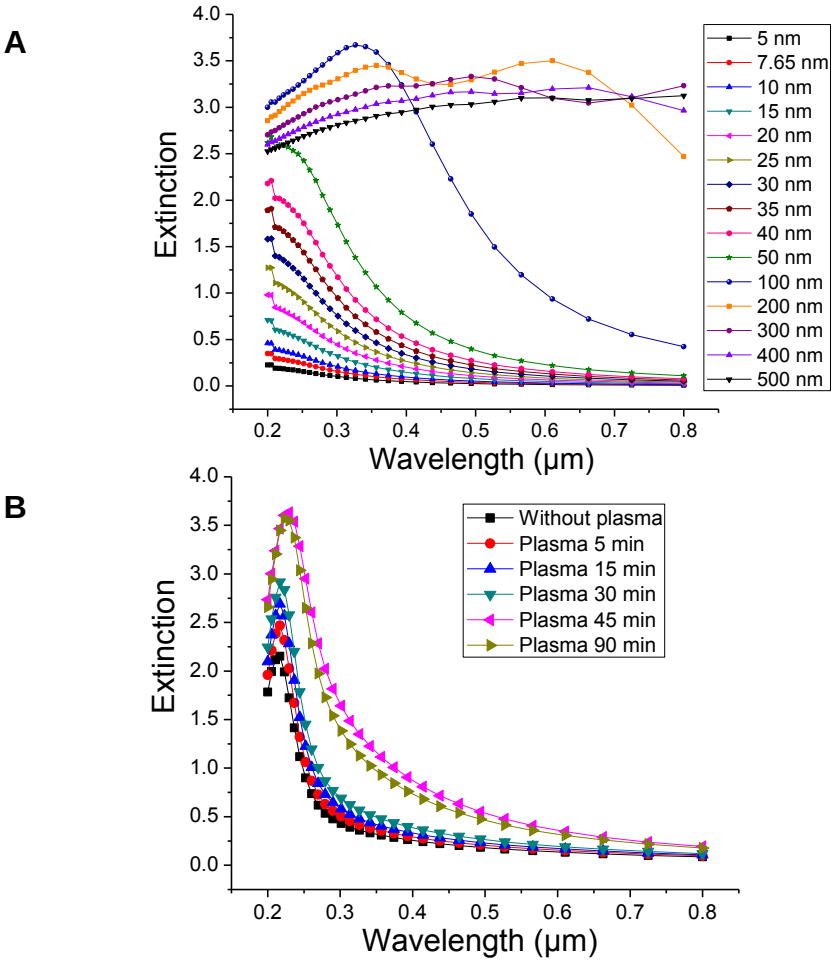

Figure 5.11 (A) Graph of the extinction curve of spherical Pt nanoparticles with different sizes; (B) Graph of the extinction curve of spherical graphene shells encapsulated Pt nanoparticles with different plasma duration; (C) Graph of the extinction curve of spherical graphene shells encapsulated Pt nanoparticles with 50 nm core and different shell thickness.

In this paper, we extend optical property study from single PtNPs to Pt-graphene core-shell heterostructures. Graphene shell can serve as barrier that preserves the PtNPs from aggregation. However, it is unknown that whether or how much the graphene shell would hinder the SPR on platinum core. DDA provides a convenient approach to characterize the optical properties of C-PtNPs core-shell heterostructures with different core size and shell thickness. The size of PtNPs and thickness of graphene shells were selected based on our experimental data (Table 5.6, 5.7). Figure 5.11B shows extinction spectra of graphene shells encapsulated PtNPs obtained from different oxidation conditions. Their core size and shell thickness were measured from TEM images (Figure 5.7, Figure 5.8A, B). Red-shift and increase of peak intensity were observed as increasing core size and shell thickness.

Figure 5.12 shows some visualized near field images of PtNPs and C-PtNPs in vacuum at localized surface plasmon resonance (785 nm). Large electric field at the edges of spherical particle and generated dipolar filed. The selection of wavelength is based on the Raman system we have in the lab. It was proved that the graphene shell would not decrease too much plasma resonance for the platinum core.

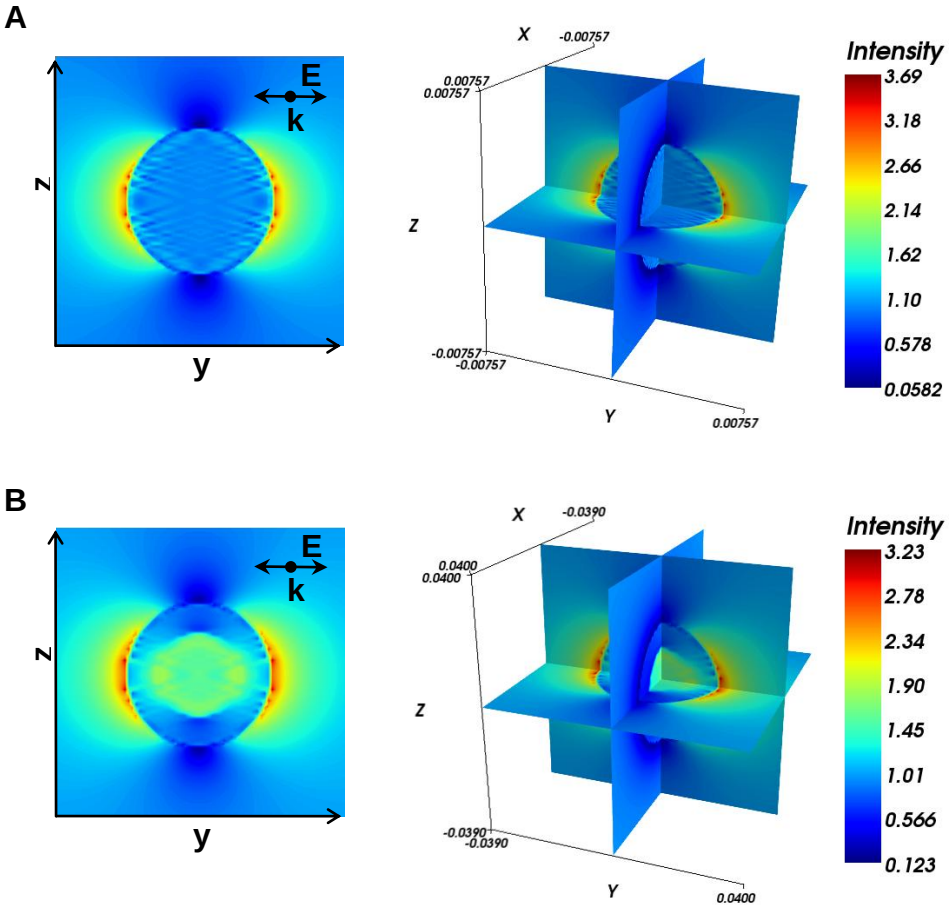

Figure 5.12 (A) Near field image of spherical Pt nanoparticles with size of 7.65 nm at 785 nm wavelength; (B) Near field image of spherical graphene shells encapsulated Pt nanoparticles with 22.6 nm core and 8.3 nm shell at 785 nm wavelength

5.7 Catalyzing property of C-PtNPs

5.7.1 Dissolution of C-PtNPs in aqua regia

Platinum is an important catalyst in many industrial processes such as CO oxidation in catalytic converters, oxidation and reduction reactions in fuel cells, nitric acid production, and petroleum cracking.[162,163,164] To prevent particle aggregation during their application, a normal method is immobilization of PtNPs inside framework of shells. However, the coverage of PtNPs surface will reduce chemical contact areas and result in regression of their catalyzing ability.[165] With this particular concern, porous shell or hollow cage are more preferred than tightly covered shells around nanoparticles.[25,166] In order to study the porosity of graphene shells on our C-PtNPs, C-PtNPs were treated with aqua regia. If the graphene shells are tightly covered on Pt-cores, C-PtNPs would survive in this hash-environment. On the other hand, if the shells are porous or easy to be penetrated, Pt-core would be dissolved after aqua regia etching.

Figure 5.13 shows SEM images of PtNPs, oxidized PtNPs, C-PtNPs, C-PtNPs after aqua regia dissolution, and Raman spectrum of etched C-PtNPs. PtNPs were dispersed on Si wafer by drop-casting, and then formed C-PtNPs with similar size through CVD process. C-PtNPs patterned on Si wafer uniformly. The substrate was immersed in aqua regia for 1 h and characterized by SEM and Raman. It was observed by SEM that most encapsulated PtNPs were dissolved and empty graphene shells remained in those locations, which indicates that aqua regia penetrated the graphene shell and etched away Pt-cores. Raman spectrum showed the decrease of D-, G-band intensity and the increased I_D/I_G ratio (~1.6), suggesting aqua regia is strong enough to attack graphene shells. Since the graphene shells were not been totally etched away, the

sacrificed part should be amorphous carbon, which is easier to be removed. It indicates that the shells on C-PtNPs can provide access of chemicals when they are used as catalysts.

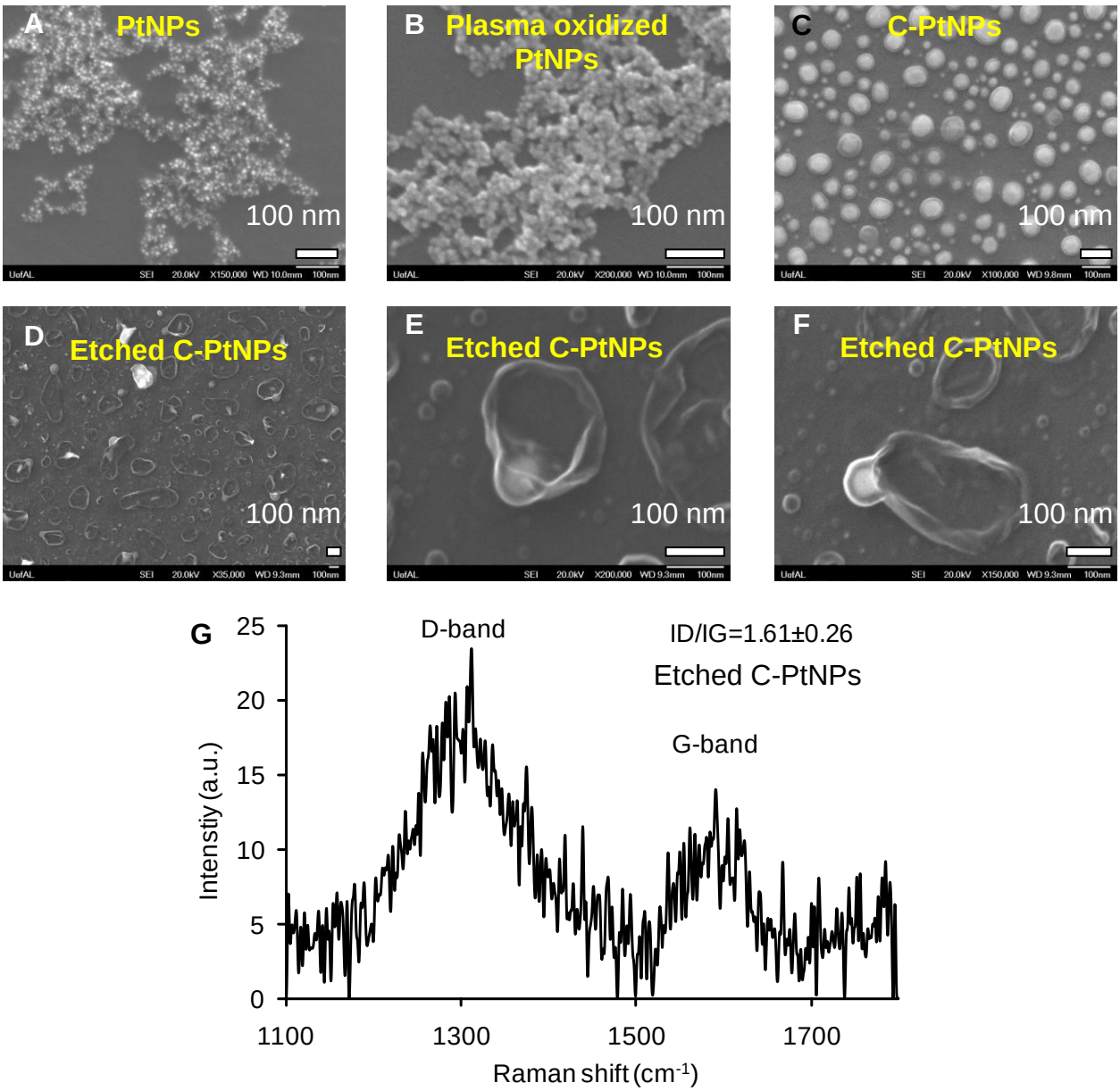

Figure 5.13 SEM images show (A) Drop-casted PtNPs, (B) Plasma oxidized PtNPs, (C) C-PtNPs patterned on Si wafer, (D-F) C-PtNPs after dissolution in aqua regia for 1 h. (G) Raman spectrum of aqua regia treated C-PtNPs.

5.7.2 Plasma treatment for C-PtNPs

Stable oxygen functionalities can by introduced on carbon structures by means of oxygen plasma.[167] Oxygen functional groups, many of which are of acidic and hydrophilic character,[168,169] can improve the surface properties by increasing the wettability, the chemisorptions activity, and the adhesion potential.[170],[171] Moreover, the oxygen plasma can also be used to partially etch our carbon shells of C-PtNPs, in order to increase the access ability of chemicals during catalyzing process.

As-synthesized C-PtNPs were treated with 120 W oxygen plasma for 15 s, 30 s, and 60 s, respectively. Shell morphology and quality were characterized by TEM and Raman (Figure 5.14, Table 5.18). Comparing their HR-TEM, plasma oxidation does not appear to greatly affect the thickness of graphene shells (Figure 5.14A-D). However, some carbon atoms on the shell must be removed due to their reaction with the active species from the plasma (oxygen atoms); we expect that at least the defect sites of carbon shell (amorphous carbon) should react from the surface with the treatment. As a matter of fact, this is proved in Raman measurement (Figure 5.14E). After been treated by oxygen plasma, it is very clear that the intensity of D-, G-band for graphene was reduced, and I_D/I_G ratio increased, suggesting the consuming of carbon materials and reduced quality of graphene. It was reported that during oxygen plasma treatment on carbon materials, oxygen concentration reached its maximum after a short exposure, and longer, more intense treatments were not able to provide higher levels of surface oxidation.167 This might be the reason why all three plasma treated samples, although have different oxidation duration, exhibit similar HR-TEM images. We should notice that the as-synthesized C-PtNPs showed clear graphene layer with interlayer spacing around 0.4 nm consistent with the c-axis spacing of

graphite. After plasma treatment, however, the shells do not show clear interlayer spacing anymore. On the other hand, the inserted FFT image for as-synthesized C-PtNPs showed two bright dots labeled as the Pt (111) plane and a diffused ring for graphitic carbon. After plasma oxidation, FFT images only show Pt (111) plane and the graphitic diffuse ring disappeared.

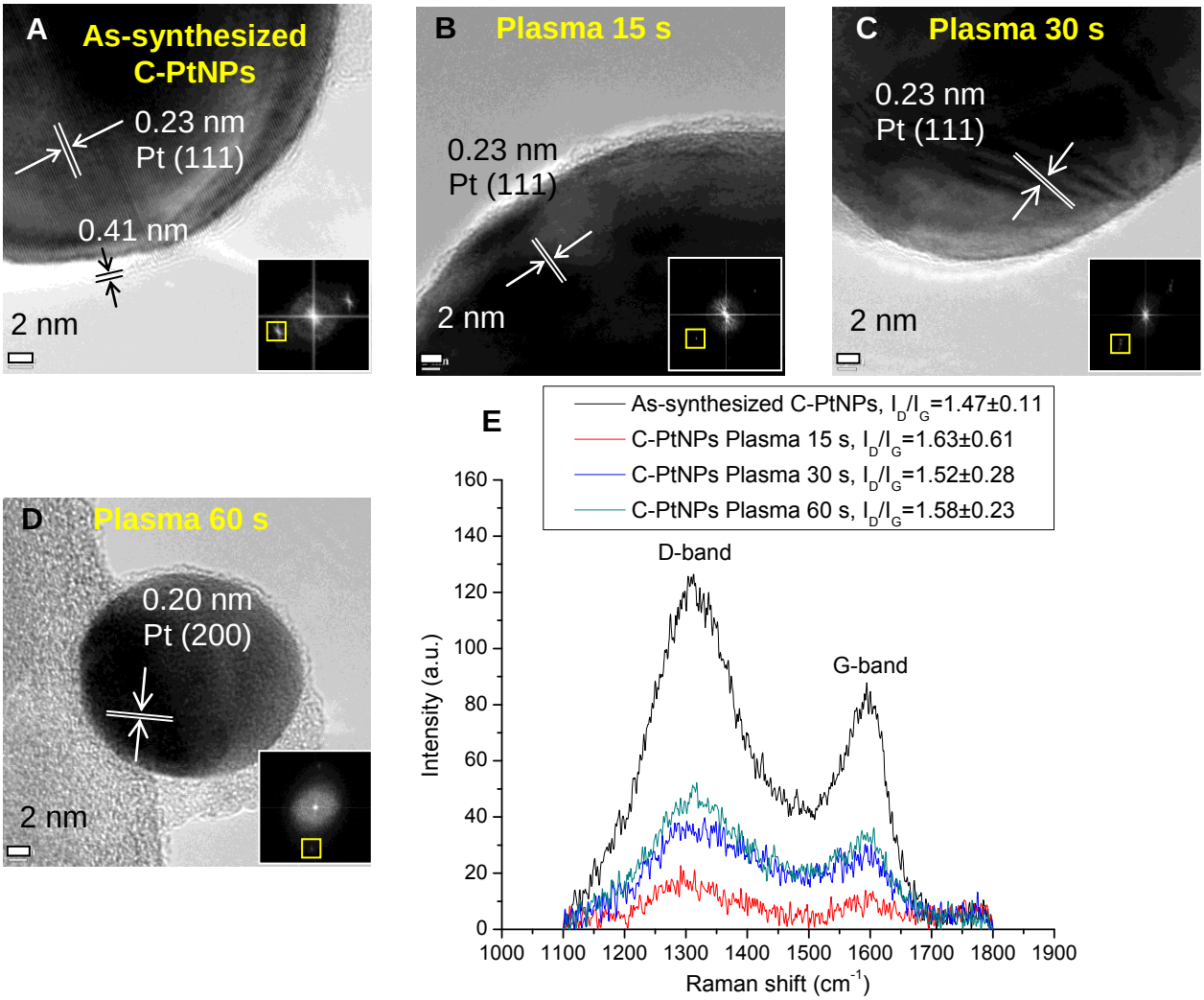

Figure 5.14 TEM images show (A) as-synthesized C-PtNPs, and C-PtNPs after plasma treated for (B)15 s, (C) 30 s, and (D) 60 s. The inserted FFT on the bottom right of TEM images show Pt (111) plane (spot marked by yellow frame). (D) Raman spectra comparing D-, G-band of graphene before and after plasma treatment.

Table 5.8 Raman results of C-PtNPs before and after plasma treatment

Sample	I_D/I_G	D-band peak		G-band peak	
		Location (cm^{-1})	Intensity (a.u.)	Location (cm^{-1})	Intensity (a.u.)
As-synthesized C-PtNPs	1.47±0.11	1303.4±1.7	113.5±25.8	1583.4±2.6	77.1±14.6
C-PtNPs plasma 15 s	1.63±0.61	1296.5±2.9	25.4±6.8	1587.2±6.33	17.1±8.1
C-PtNPs plasma 30 s	1.52±0.28	1300±2.0	30.2±7.3	1583.4±5.2	21.4±4.6
C-PtNPs plasma 60 s	1.58±0.23	1304.9±5.3	32.9±16.9	1583.2±3.0	21.4±10.9

5.7.3 Thermal stability of PtNPs and C-PtNPs

In practical applications that involve high temperatures (typically higher than 300 ^{o}C), the PtNPs tend to aggregate and lose their catalytic activity during operation because of sintering.[172,173,174,175] To demonstrate that our graphene shell can prevent Pt-cores aggregate at high temperature, two group of substrate (Group A were drop-casted with as-synthesized PtNPs, Group B were patterned with C-PtNPs that fabricated from Group A through CVD process) were annealed at high temperature (350 ^{o}C, 550 ^{o}C, 750 ^{o}C, and 1000 oC) in Ar atmosphere, and their morphology evolution were compared by SEM (Figure 5.15).

The changes of size and inter-particle distance of PtNPs/Pt-cores were summarized in Table 5.9. Histograms exhibit the size and inter-particle distance distribution for annealed PtNPs (Figure 5.16) and C-PtNPs (Figure 5.17). Without any protection, PtNPs undergo serious aggregation, their average size increases dramatically (from initially less than 10 nm increased to more than 180 nm) and size-distribution became broadened (Figure 5.15A, B, Table 5.9, Figure 5.16). Especially when annealing temperature increased to ~1000 ^{o}C, the substrate drop-casted with PtNPs exhibits rough surface with transparent bubble-like structures. It was reported that Pt and Si can form alloys at high temperature, and XRD peak for Pt will disappear when the annealing temperature is higher than 800 ^{o}C.[176] Thus complicated processes must have taken place during the annealing of PtNPs. Platinum particles may migrate, aggregate into large particles, and then interact with Si substrate, partially diffused in the substrate.

In case of C-PtNPs, the Pt-core size of as-synthesized C-PtNPs is larger than as-synthesized PtNPs (~17 nm compare to ~7 nm, Table 5.9) because of migration during graphene shells growth step. However, with the protection of carbon shell, the Pt-cores exhibit much higher

thermal stability than PtNPs. As shown in SEM (Figure 5.15C-F), C-PtNPs showed uniform dispersion on Si wafer even after annealing at 1000 ^{o}C for 2 h. The average Pt-core size for C-PtNPs maintained less than 20 nm and exhibit relatively narrow distribution comparing to unprotected PtNPs (Table 5.9, Figure 5.16, 5.17). The effective control of platinum size and dispersion plays significant role in its applications. The high thermal stability of C-PtNPs suggests that they can exhibit higher catalyzing performance in practical environment. The quality of annealed graphene shell was studied by Raman spectroscopy; results are summarized in Table 5.10 and Figure 5.18. Similar with oxygen plasma treatment, the annealing process would reduce the intensity of carbon D-, G-band. The difference is that plasma oxidation increased defects of graphene shell (I_D/I_G increased), whereas the annealing process, especially at elevated temperature (~1000 ^{o}C) resulted in higher quality of graphene shell (I_D/I_G decreased). Since both graphitic carbon and amorphous carbon were deposited on substrate during CVD process, the annealing process may remove most of amorphous carbon on the large area substrate, only left high quality graphitic shell surrounding PtNPs.

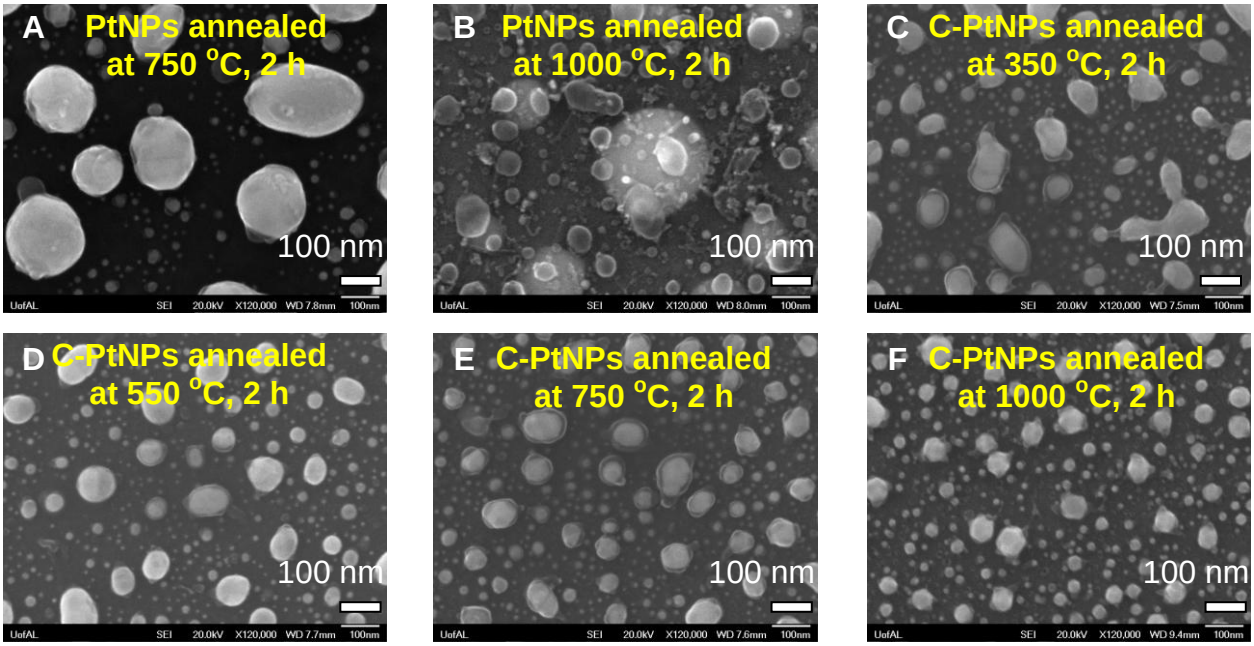

Figure 5.15 SEM images exhibit samples after been annealed at different temperatures for 2 h: PtNPs after been annealed at (A) 750 ^{o}C, (B) 1000 ^{o}C; comparing with C-PtNPs after been annealed at (C) 350 ^{o}C, (D) 550 ^{o}C, (E) 750 ^{o}C, and (F) 1000 ^{o}C

Table 5.9 Size of PtNPs cores and inter-particle spacing before and after annealing (from observed from SEM images)

Sample	Average size (nm)	Inter-particle spacing (nm)
As-synthesized PtNPs	7.36 ± 1.04	3.36 ± 1.50
PtNPs annealed at 750 ^{o}C for 2 h	20.89 ± 29.66	29.37 ± 20.55
PtNPs annealed at 750 ^{o}C for 10 h	33.10 ± 23.70	36.01 ± 21.26
PtNPs annealed at 1000 ^{o}C for 2 h	185.50 ± 66.90	231.14 ± 102.42
As-synthesized C-PtNPs	17.22 ± 7.42	15.57 ±7.42
C-PtNPs annealed at 350 ^{o}C for 2 h	16.40 ± 14.68	18.13 ± 8.55
C-PtNPs annealed at 550 ^{o}C for 2 h	15.66 ± 14.61	19.43 ± 10.29
C-PtNPs annealed at 750 ^{o}C for 2 h	17.76 ± 13.30	17.04 ± 7.67
C-PtNPs annealed at 1000 ^{o}C for 2 h	19.98 ± 12.40	26.61 ± 13.87

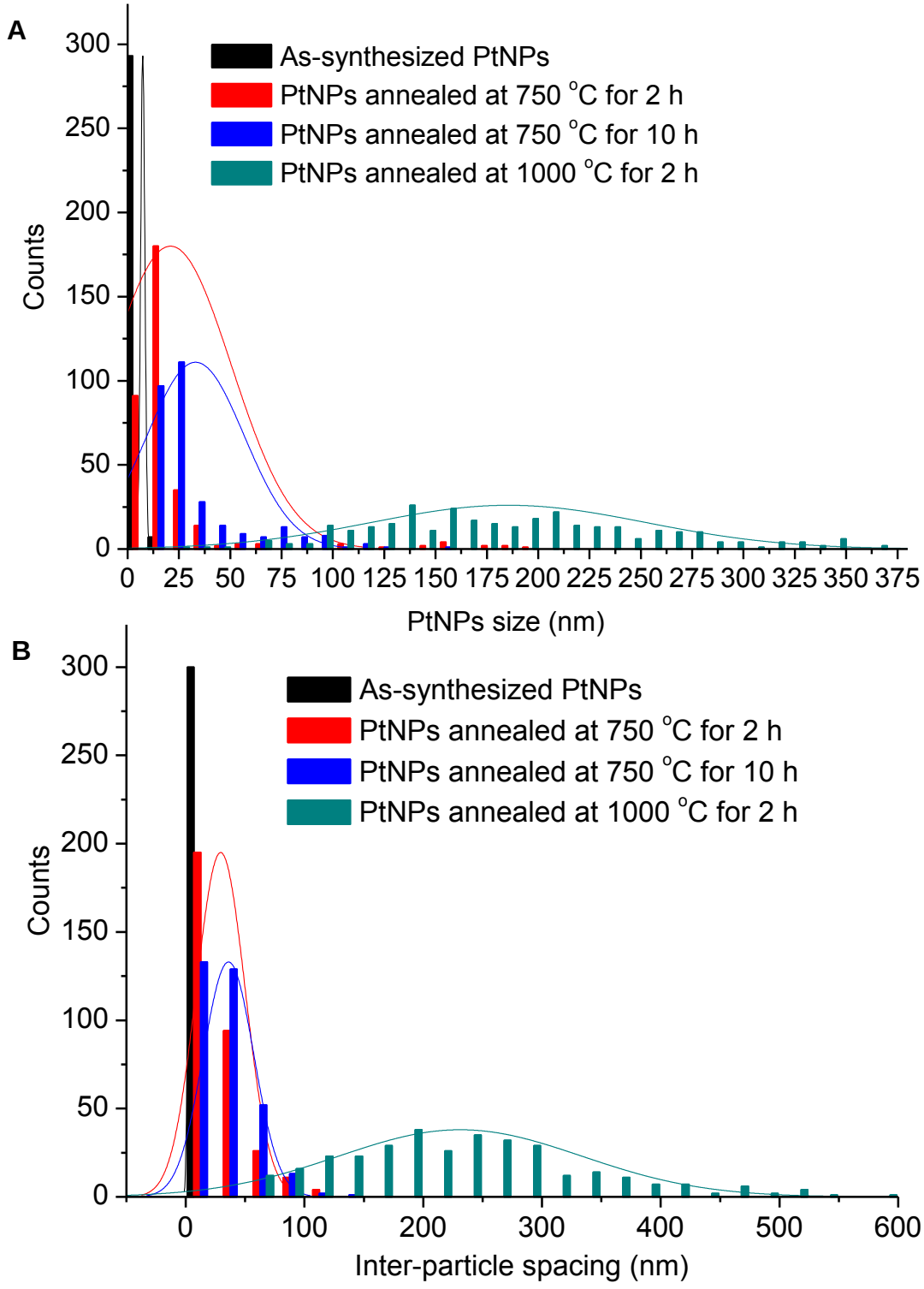

Figure 5.16 (A) Size and (B) inter-particle spacing of PtNPs before and after annealing

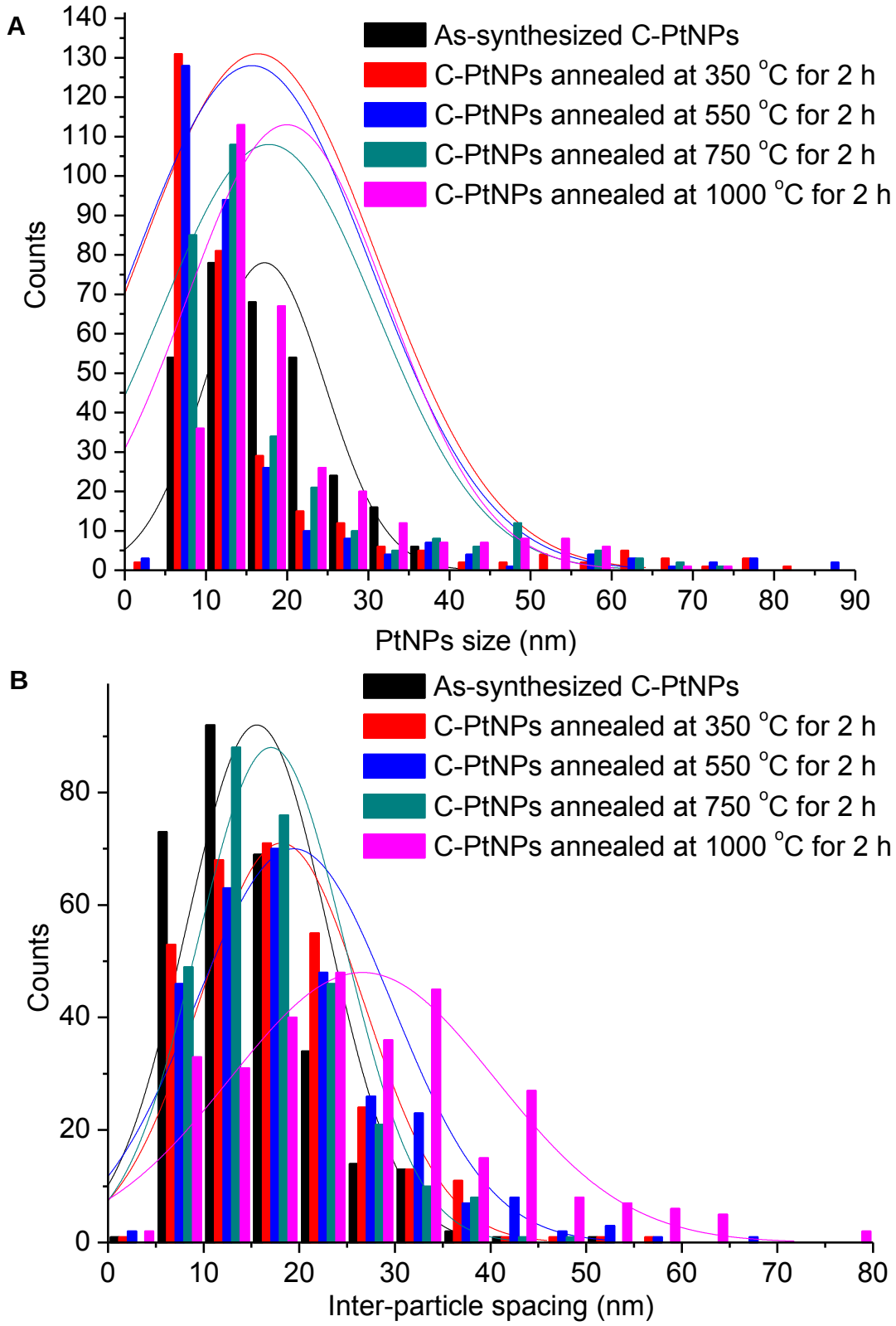

Figure 5.17 (A) Size and (B) inter-particle spacing of C-PtNPs before and after annealing

Table 5.10 Summary of Raman results for different C-PtNPs (before and after annealing treatment).

Sample	I_D/I_G	D-band peak		G-band peak	
		Location (cm^{-1})	Intensity (a.u.)	Location (cm^{-1})	Intensity (a.u.)
As-synthesized C-PtNPs	1.47±0.11	1303.4±1.7	113.5±25.8	1583.4±2.6	77.1±14.6
C-PtNPs annealed at 350 ^{o}C for 2 h	1.44±0.09	1302.4±1.7	108.4±37.2	1583.4±1.9	74.4±21.2
C-PtNPs annealed at 550 ^{o}C for 2 h	1.40±0.04	1304.6±5.3	87.1±19.4	1581.5±1.3	62.2±13.5
C-PtNPs annealed at 750 ^{o}C for 2 h	1.48±0.12	1298.8±2.1	62.2±7.3	1581.6±3.0	42.0±2.8
C-PtNPs annealed at 1000 ^{o}C for 2 h	0.79±0.26	1285.3±1.9	15.0±4.1	1589.7±3.8	21.2±9.2

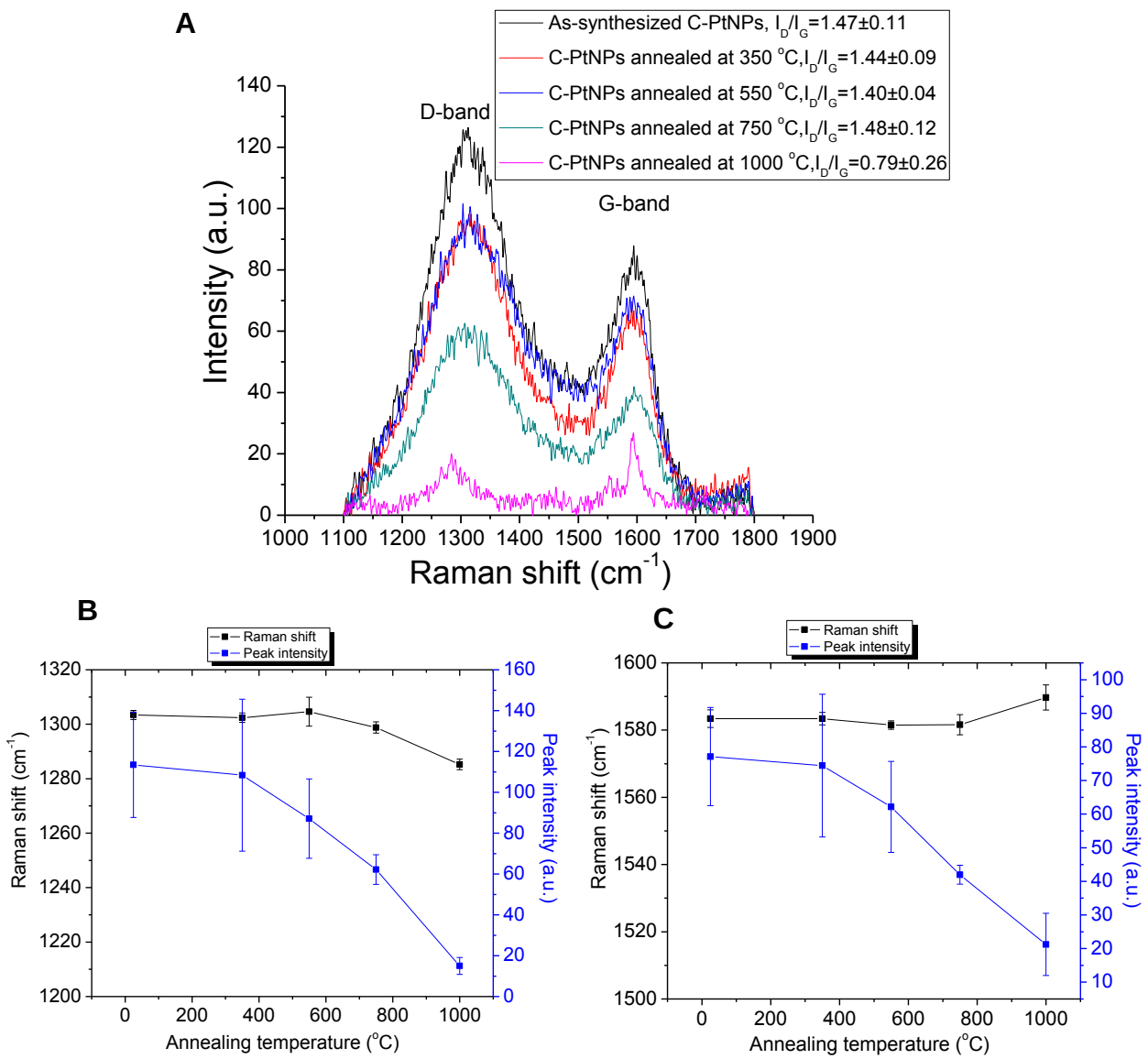

Figure 5.18 (A) Raman spectra, (B) Raman shift and peak intensity of D-band, and (C) Raman shift and peak intensity of G-band for C-PtNPs before and after annealing at different temperatures.

5.7.4 Sinter-Resistant Catalytic System for Hydrogenation of Methyl Red

We also investigated the catalytic property of the graphene shells encapsulated PtNPs (C-PtNPs) by employing the hydrogenation of methyl red (MR) as a model reaction. The hydrogenation of the N=N hydrogen molecules were able to diffuse through the porous graphene shells to the surface of Pt-cores. To compare the catalyzing efficiency, different samples were used including as-synthesized PtNPs, as-synthesized C-PtNPs, annealed PtNPs, plasma-oxidized C-PtNPs, and annealed C-PtNPs (Table 5.11). Enable to compare the conversion results, each sample maintained same load of platinum (each substrate has been loaded 20 µL as-synthesized PtNPs solution for graphene shells growth or annealing treatment). For each conditions, there were 5 samples been tested for MR hydrogenation and calculated the average conversion. UV-Vis of methyl red was utilized to measure the conversion of hydrogenation; the standard line was calculated in Figure 5.19.

The highest catalytic activity was achieved from the as-synthesized PtNPs (100% conversion in 5 min). However, the conversion of MR using unprotected PtNPs dropped to as low as ~26% after annealing (Table 5.11, Figure 5.20, 5.21), which is attributed to the aggregation and the surface reconstruction of PtNPs. As-synthesized C-PtNPs have a moderate activity, which resulted in ~28% conversion. The activity of C-PtNPs was increased by plasma treatment and annealing treatment. By plasma oxidizing C-PtNPs for a longer duration, the conversion of MR can be increased from ~30% to 37%. It was reported that plasma etching will proceed by initially creating tiny voids which may subsequently widen with increased treatment severity.[167] This means the pore size of graphene shell may be increased as processing further plasma oxidation to C-PtNPs, provide more access to chemicals during hydrogenation. Comparing the annealed

samples, the highest catalytic activity was obtained from C-PtNPs annealed at 750 ^{o}C, with an average conversion of ~45% (Table 5.11, Figure 5.20, 5.21). As discussed before, the annealing process can remove amorphous carbon; this process may also provide more access for the diffusion of chemicals. We also confirmed the hydrogenation will only process with appearance of both Pt and H_2 by two control samples: 1. Flowing H_2 without catalyst (Pt) and 2. C-PtNPs bubbled with Ar. The conversion for above two control samples was zero. Compare to bare PtNPs, C-PtNPs have high thermal stability and can be used in practical process. Moreover, since C-PtNPs were patterned on Si substrate, we do not need a centrifuge step to collect catalysts dispersed in solution, which will dramatically increase the efficiency.

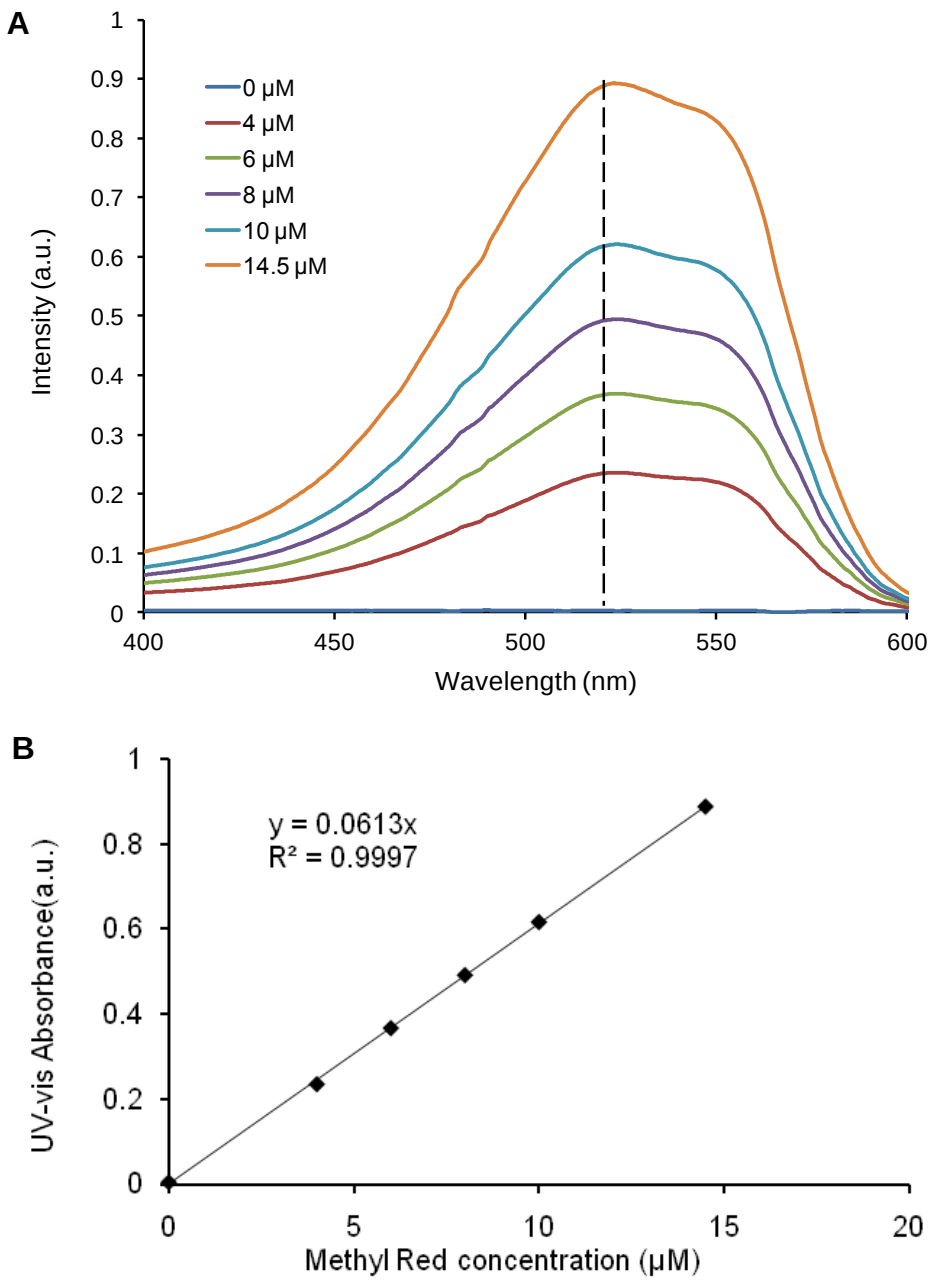

Figure 5.19 (A) UV-Vis and (B) standard line for methyl red in pH=4.0 buffer solution.

Table 5.11 Conversion of methyl red using different samples for hydrogenation after 5 min

Sample	MR conversion after 5 min (%)
Without catalysts, bubbled with H_2	0.69±0.44
C-PtNPs, bubbled with Ar	0.62±0.44
As-synthesized PtNPs	100
PtNPs annealed at 750 ^{o}C for 2 h	26.82±2.37
PtNPs annealed at 750 ^{o}C for 10 h	26.34±4.73
PtNPs annealed at 1000 ^{o}C for 2 h	28.17±3.81
As-synthesized C-PtNPs	28.34±7.80
C-PtNPs plasma treated for 15s	29.99±3.56
C-PtNPs plasma treated for 30s	30.61±5.57
C-PtNPs plasma treated for 60s	37.00±3.80
C-PtNPs annealed at 350 ^{o}C for 2 h	39.11±6.02
C-PtNPs annealed at 550 ^{o}C for 2 h	42.55±2.87
C-PtNPs annealed at 750 ^{o}C for 2 h	45.19±4.63
C- PtNPs annealed at 1000 ^{o}C for 2 h	31.25±3.78

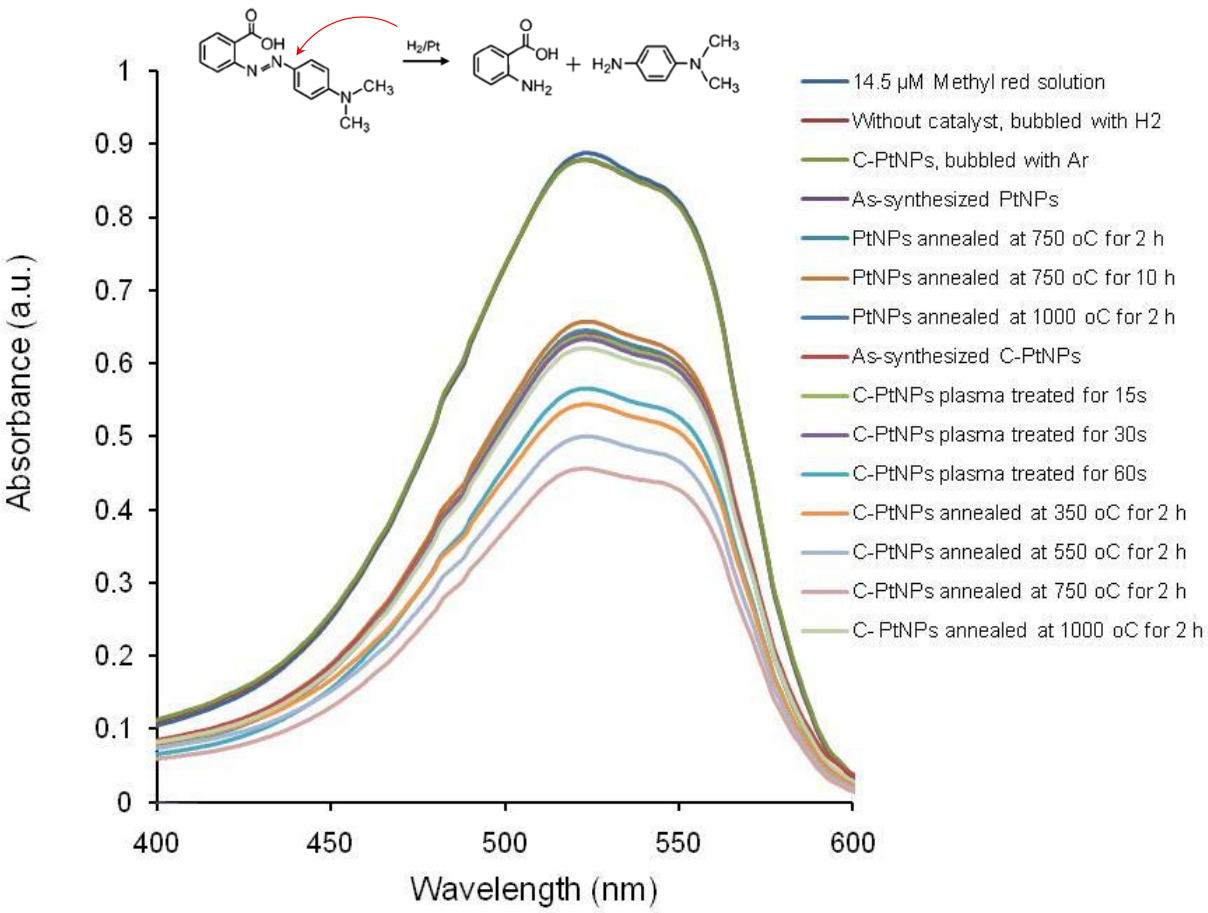

Figure 5.20 UV-Vis of methyl red solution using different samples for hydrogenation after 5 min. Note that there was almost no change for the solution without catalyst and just bubbled with H_2.

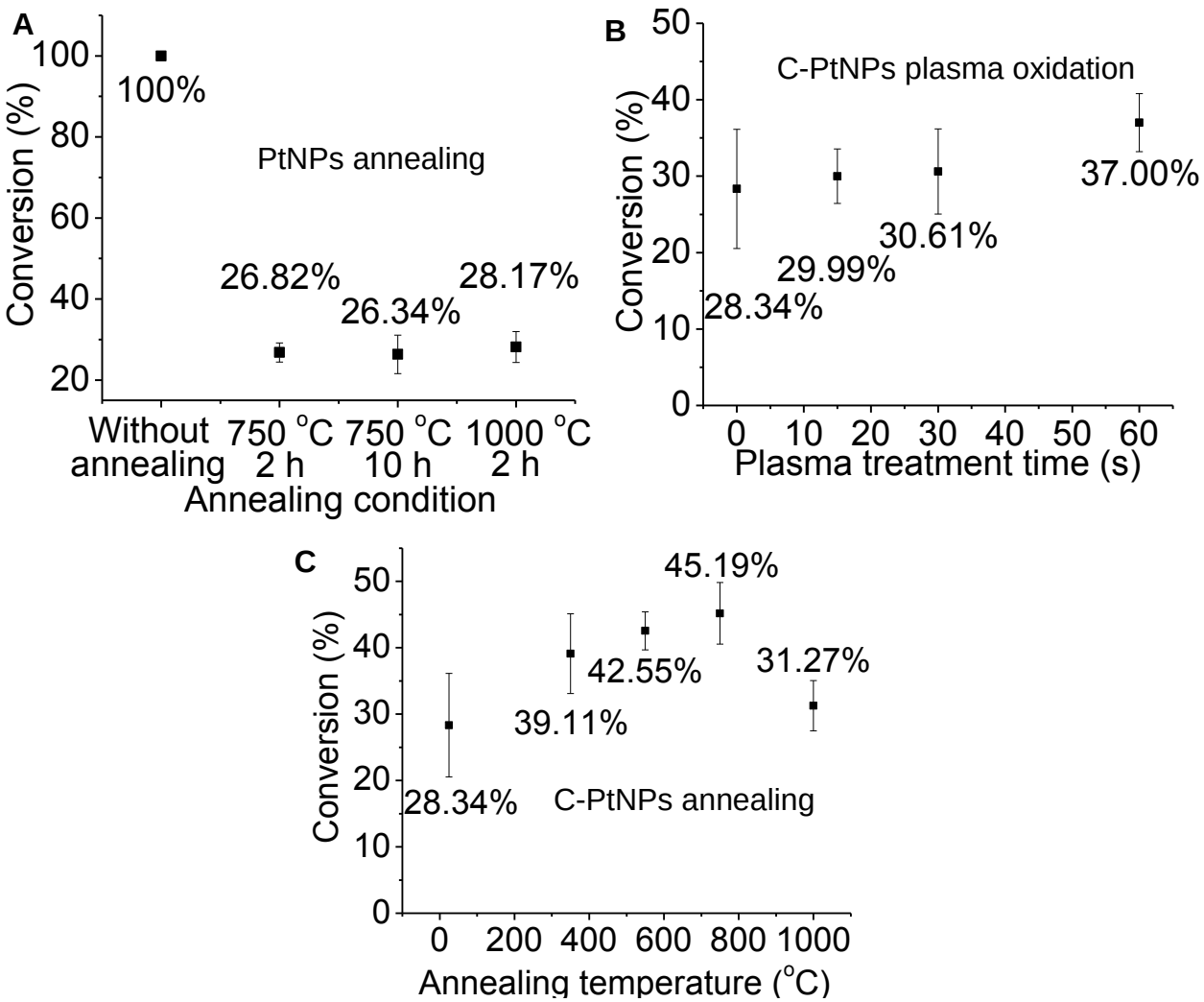

Figure 5.21 Conversion of methyl red solution using different samples for hydrogenation after 5 min (A) As-synthesized PtNPs before and after annealing, (B) As-synthesized C-PtNPs before and after plasma treatment, (C) As-synthesized C-PtNPs before and after annealing at different temperature for 2 h.

The major concerns of using catalyst substrate repeatedly are the lost of catalyst from substrate, and the poisoning of catalysts. A Si wafer patterned with C-PtNPs used to invest its recycling property. Firstly, the substrate was annealed at 750 ^{o}C for 2 h, and then used hydrogenation of MR for 5 times without washing (MR solution was refreshed every time). The UV-Vis was tested after 5 min and 10 min hydrogenation for each solution. Secondly, the same substrate was recovered by immersing in DI water for 24 h before hydrogenation again. After that, repeated annealing-hydrogenation processes were conducted on this substrate for 5 times.

The substrate was dried and characterized by SEM after repeatedly hydrogenation without washing for 5 times (Figure 5.22A-B), and then be characterized again after it underwent 5 times annealing-hydrogenation process (Figure 5.22C-D). The size of Pt-core and inter-particle spacing results were summarized in Table 5.12 and Figure 5.22. It was observed that the size of Pt-core, after recycling, maintains ~20 nm. And their catalysis performance maintains above 55% of conversion for 10 min hydrogenation all the time (Table 5.13, Figure 5.24). This indicated that C-PtNPs are catalytically active toward hydrogenation of methyl red even after high-temperature annealing for multiple times, thus demonstrating our C-PtNPs patterned substrates are recyclable for application of catalyzing.

Table 5.12 Size of C-PtNPs cores and inter-particle spacing after annealing and repeated catalyzing (from observed from SEM images)

Sample	Average size (nm)	Inter-particle spacing (nm)
C-PtNPs annealed at 750 ^{o}C for 2 h, and after 5 catalysis cycles	19.74 ± 15.36	24.02 ± 12.24
C-PtNPs annealed at 750 ^{o}C for totally 12 h, and after totally 11 catalysis cycles	21.62 ± 17.13	21.36 ± 11.65

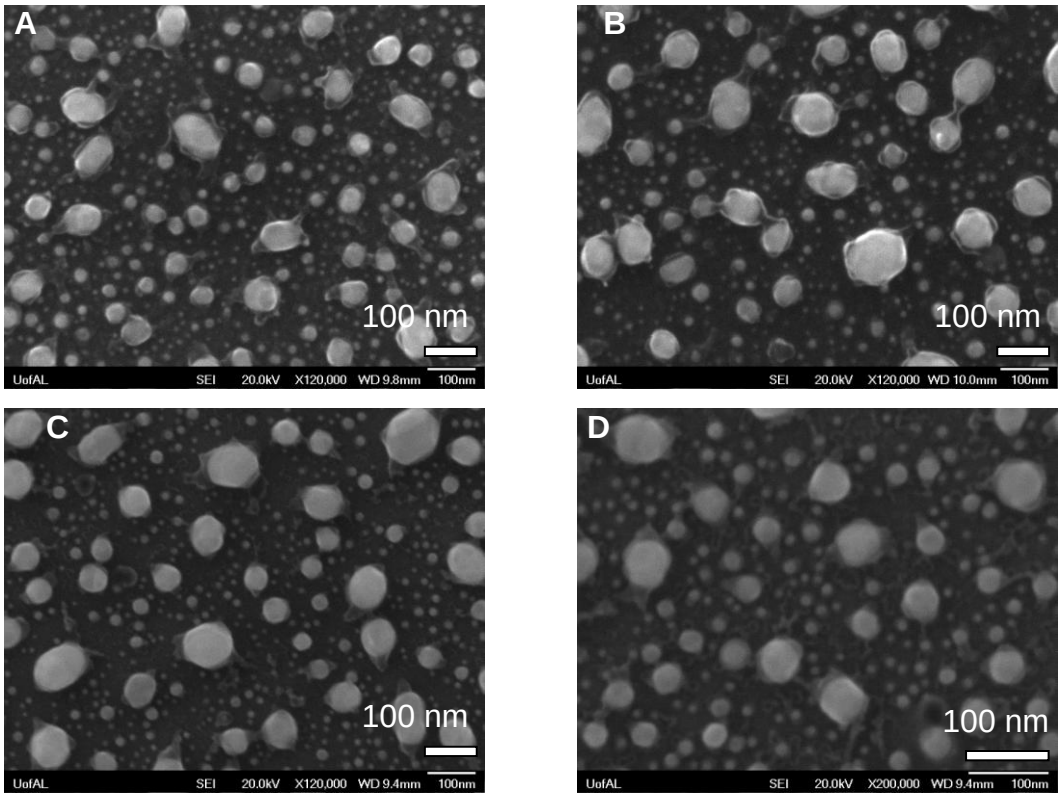

Figure 5.22 SEM images exhibiting (A-B) C-PtNPs annealed at 750 ^{o}C for 2 h, and after 5 catalysis cycles; (C-D) C-PtNPs annealed at 750 ^{o}C for totally 12 h, and after totally 11 catalysis cycles.

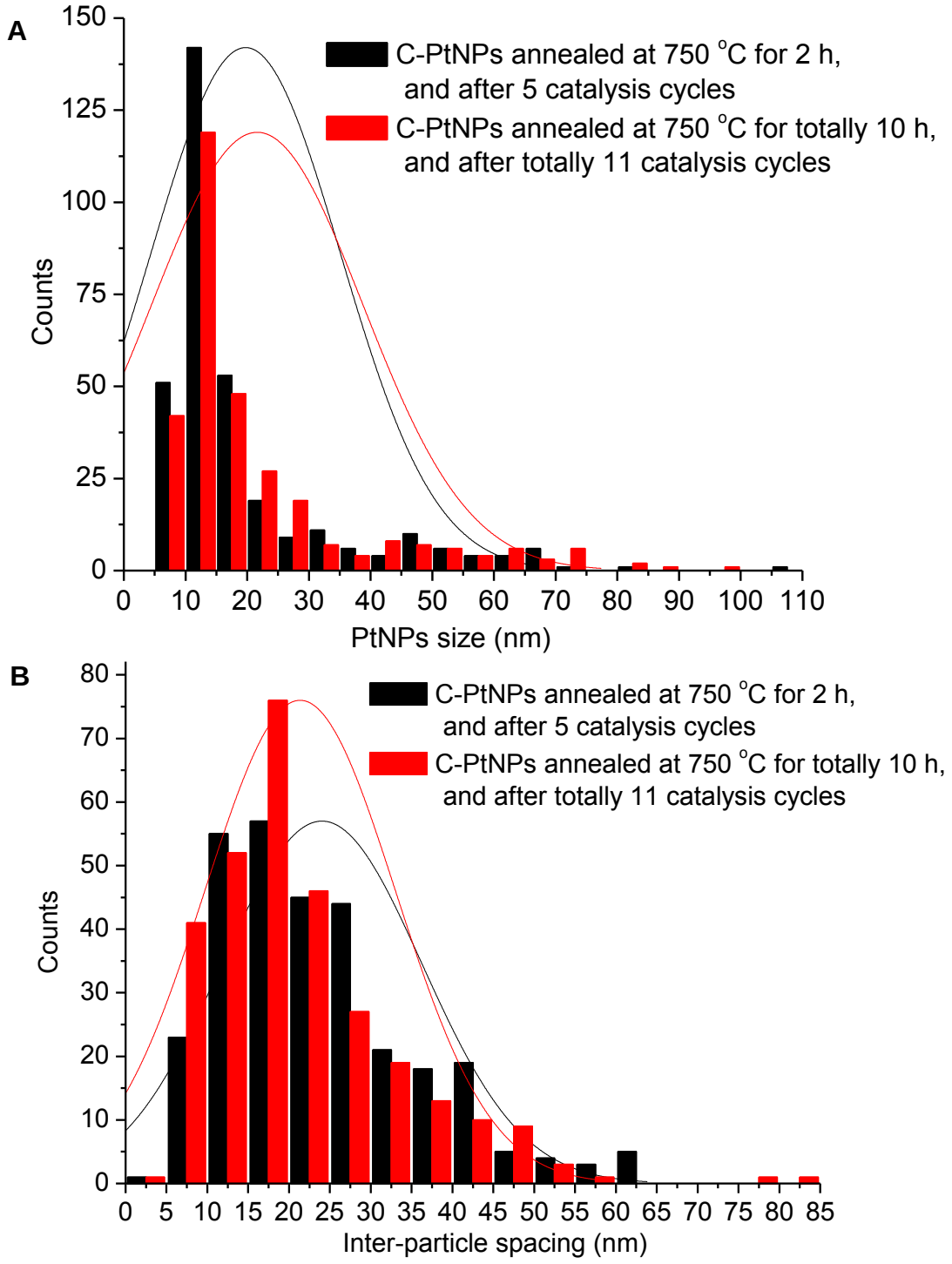

Figure 5.23 (A) Size and (B) inter-particle spacing of C-PtNPs after annealing and catalysis cycles

Table 5.13 Methyl Red hydrogenation cycle study for treated C-PtNPs

Sample	Cycle	Conversion (%)	
		After 5 min	After 10 min
Annealed at 750 ºC for 2h, then cycled 5 times	1	50.12	84.80
	2	37.01	60.56
	3	32.02	56.03
	4	28.07	51.62
	5	29.58	53.94
Recover C-PtNPs by immersing in DI water for 24 h before hydrogenation	6	40.50	69.34
Repeat annealing at 750 ºC for 2h each time before hydrogenation	7	47.28	71.83
	8	36.08	62.36
	9	32.11	55.57
	10	33.07	57.99
	11	32.76	55.02

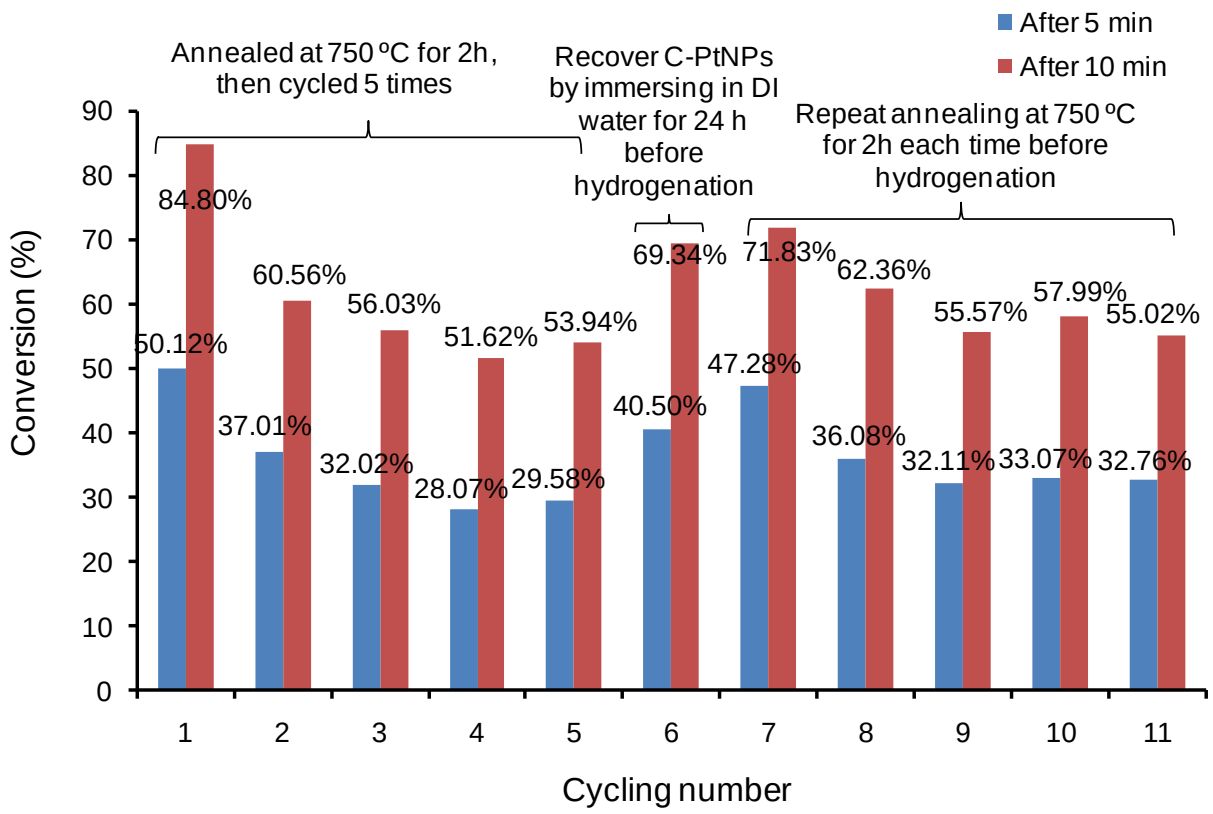

Figure 5.24 Methyl Red hydrogenation cycle study for C-PtNPs annealed at 750 ^{o}C

5.8 Conclusions

In summary, octahedra and tetrahedra PtNPs were grown in a single-step wet chemical synthesis. As a next step toward C-PtNPs growth, as-synthesized PtNPs were plasma-oxidized from 0-90 min in an oxygen plasma process. Oxidation kinetics of PtNPs was studied by XPS, and found to obey Valensi-Carter model. The PtNPs with different oxidation states were used as catalysts for the growth of graphene shell. The increase of graphene shell thickness as increasing of oxidation duration was observed, similar with the trend for PdNPs.DDA calculations were performed for PtNPs with different sizes and C-PtNPs heterostructures. As increasing the size of PtNPs, the extinction peak of nanoparticles shifts to higher wavelengths. The plasmonic modeling of PtNPs and corresponding C-PtNPs indicates that graphene will only slightly decrease the plasmonic resonance of PtNPs.

To explore the application of C-PtNPs in practical environment, we compared the thermal stability of PtNPs and C-PtNPs. The porous graphene shell could serve as an effective barrier to prevent the migration of PtNPs during annealing, thus enabling the Pt-cores to become sinter-resistant. C-PtNPs maintained good catalysis activity underwent high-temperature annealing treatment, while the performance of PtNPs dramatically decreased. Finally, we demonstrated that C-PtNPs are recyclable for repeating annealing-hydrogenation process, and the substrate-patterned C-PtNPs do not need particle-collection process after catalyzing, which would greatly improve the producing efficiency.

CHAPTER 6: METAL NANOWIRE-CARBON NANOSTRUCTURE HETEROSTRUCTURES

6.1 Introduction

There is an increasing interest on synthesis arrays of highly ordered and uniform nanostructures. Among various approaches of one dimensional (1-D) nanostructures fabrication such as chemical vapor deposition, photolithography, and electrodeposition, the bottom-up approaches (CVD process using patterned catalysts, or membrane with aligned channels as template) are more efficient than top-down approach (e.g., electron beam lithography).

Here, we fabricated vertically aligned and axially heterostructured metal nanowires inside anodized aluminum oxide template (AAO) by a wet-chemical deposition process. Subsequently, two kinds of nanowires-carbon hybrids were fabricated: graphene shells encapsulated nanowires, and nanowires-carbon nanotubes (NWs-CNT) heterostructures. The graphene shells encapsulated nanowires using nanowires as templates for the graphene shell growth. The thermal stability of nanowires was studied. NWs-CNT hybrid was synthesized within the pores of AAO membrane using Ni nanowires as catalysts. The length of nanowires and CNT could be controlled by varying the duration of electrodeposition and CVD process. After removing AAO template, ordered arrays of NWs-CNT heterostructures have been coated by nickel nanoparticles through a direct wet-chemical nucleation approach, fabricated hybrid materials denoted as NWs-CNC heterostructures. The capacitive behavior of NWs-CNC was invested in 9 M KOH using cyclic voltammetry (CV) and ac electrochemical impedance spectroscopy (EIS).

6.2 Experimental Methods

6.2.1 Materials and Methods

Cupric sulfate pentahydrate ($CuSO_4 \cdot 5H_2O$) and Sodium hydroxide (NaOH), sodium chloride (NaCl) were purchased from Fisher Scientific (New Jersey), Niceklous sulfate 6-hydrate ($NiSO_4 \cdot 6H_2O$) and Ammonium hydroxide ($NH_3 \cdot H_2O$) were bought from Mallinckrodt Baker, Inc. (New Jersey). Gold (I) potassium cyanide ($KAu(CN)_2$), Sodium hydrogen carbonate ($NaHCO_3$, 99.7~100.3%), Sodium tetrachloropalladate (II) hydrate (Na_2PdCl_4, 99.999%), Dihydrogen hexachloroplatinate (IV) hexahydrate (99.9%), Tri-n-octylphosphine oxide (TOPO, 98%) were purchased from Alfa Aesar (Ward Hill, MA). Potassium hydroxide (KOH) and Ammonium chloride (NH_4Cl) were bought from Acros Organics (New Jersey). Nickel acetate tetrahydrate ($(CH_3CO_2)_2Ni \cdot 4H_2O$, 98%), Oleylamine ($C_{18}H_{37}N$), Trioctylphosphine (TOP, 90%) were purchased from Sigma-Aldrich (St. Louis). All chemicals were used without further purification. DI water (18.1 MΩ-cm) was obtained using a Barnstead International DI water system (E-pure D4641).

Parastat2273 (Princeton Applied Research) was used for electrodeposition and electrochemical characterization. Labnet centrifuge (Edison, NJ) was used to wash and separate nanoparticles. Wet samples were dried and stored in a VWR vacuum oven (West Chester, PA). Oxygen plasma treatment was performed in Model 1021 plasma cleaner (E.A. Fischione Instruments, PA). Growth of graphene shells was conducted inside Lindberg blue 3-zone tube furnace (Watertown, WI). Quartz tubes were purchased from ChemGlass (Vineland, NJ). Syringe injector was obtained from Fisher Scientific (Suwannee, GA). Thermocouples and temperature controllers were bought from Omega Engineering (Stamford, CT). H_2 (UHP grade, 40% balanced with Ar)

and Ar (UHP grade) gas cylinders were purchased from Airgas South (Tuscaloosa, AL). Gas flow rates of all chemical vapor deposition processes were controlled by Teledyne Hasting power pod 400 mass flow controllers (Hampton, VA).

6.2.2 Synthesis of Nanowires

An Au or Ag layer with ~45 nm thickness was sputtered on one side of porous alumina (AAO, pore size ~200nm) as the conductive part of working electrode. Copper wire was connected with the Au face of AAO using silver paint, works as extensive part of working electrode to connect with electrochemical workstation Parastat2273 (Princeton Applied Research).

Gold nanowires were potentiostatic deposited from 0.02M $KAu(CN)_2$ solution in pH=10.0 $NaHCO_3$/NaOH buffer solution. Palladium nanowires were potentiostatic deposited from 2.5 g/L Na_2PdCl_4 solution in pH=8 $NH_4Cl/NH_3{\cdot}H_2O$ buffer solution. Platinum nanowires were potentiostatic deposited from 2 g/L H_2PtCl_6 solution with 30 g/L H_3BO_3 and using $NH_3{\cdot}H_2O$ adjusted pH to 7.4. Nickel nanowires and copper nanowires were potentiostatic deposited using their sulfate solutions with boric acid adjusting pH. Multisegment nanowires were obtained by subsequently deposition of each segment from the corresponding electrolyte. The whole processes were performed at room temperature. After electro-deposition, products were washed with DI water and dried in vacuum oven. Array of nanowires were obtained by etching AAO template by 3M KOH.

6.2.3 Annealing of Nanowires

After removing AAO template, Cu-Au-Cu multi-segment nanowires were annealed in quartz tube furnace in Ar atmosphere. The effect of temperature and annealing duration were studied. On the one hand, nanowires were annealed at temperature ranging from 100 ^{o}C to 800 ^{o}C for 1 h.

On the other hand, nanowires were annealed at 675 ^{o}C for different time (from 15 s to 60 min). The annealing temperature (675 ^{o}C) was selected based on optimized graphene shells growth temperature for gold as discussed in previous chapter. To avoid being heated in temperature ramping process, a quick heating test was made by loading nanowires after furnace temperature arrived 300 ^{o}C. The nanowires were then heated at 300 ^{o}C for 15 s, 5 min, and 30 min, respectively.

6.2.4 Graphene Shells Growth on Nanowires

Graphene shell was grown in a CVD process with similar procedure in previous chapters. Single segment nanowires Au NWs, Cu NWs, Pd NWs, and Pt NWs were used for graphene shell growth. Growth temperature was 675 ^{o}C for Au NWs and Cu NWs, and 800 ^{o}C for Pd NWs and Pt NWs, respectively.

6.2.5 Fabrication of Nanowire-CNT Heterostructure

After reducing oxidized Ni by hydrogen (with flux of 0.3 SLM at 675 ^{o}C for 15 min), carbon nanotube (CNT) was grown on the tip of Au-Ni nanowires in a chemical vapor deposition (CVD) process, involving xylene as a carbon source. Pure xylene precursor was injected through a syringe injector into a pre-heated zone (~ 220 ^{o}C) at the rate of 45 mL/h for ~2 min and subsequently transported into the reaction zone (~ 675 °C) inside the quartz tubes furnace. The xylene flow rate was reduced to 1 mL/h when H_2 in Ar (Ar/H_2=1.8 SLM: 0.2 SLM 10% v/v) carrier gas was introduced in the CVD reactor, where H_2 acted as an oxygen scavenger. The CVD reaction was continued for 1 h after which H_2 and xylene flow was discontinued and furnace was cooled down under Ar flow. After CNT growth, AAO template was etched away in 3 M KOH at 70 ^{o}C.

6.2.6 Attaching Ni Nanoparticles on Nanowire-CNT Heterostructure

After being removed of AAO template, the brush-like NWs-CNT heterostructures were mixed with nickel acetate and Oleylamine in a three-neck round bottom flask. The mixture was heated in ~90 ^{o}C oil bath under N_2 atmosphere for 40 min, followed by adding TOPO and TOP as stabilizer for nickel nanoparticles. The temperature was increased from 90 ^{o}C to 250 ^{o}C at rate of10 ^{o}C/min and then held at 250 ^{o}C for 30 min. After reaction, the product was washed several times with a mixture of hexane and acetone, and then dried in vacuum oven at 80 ^{o}C overnight and stored in Petri dish in air for further experimentation and characterization. The obtained materials were referred as NWs-CNC heterostructure.

6.2.7 Electrochemical measurements of the electrodes

Electrochemical capacitive behavior of the synthesized Au-Ni NWs, NWs-CNT heterostructure, and NWs-CNC heterostructure were determined by cyclic voltammetry in a three-electrode cell equipped with the working electrode (samples), a platinum wire counter electrode, and a saturated Ag/AgCl reference electrode. A typical electrolyte was 9 M KOH aqueous solution. The cells were cycled at different scan rates in the range of -1.2 to 0.45 V versus a saturated Ag/AgCl reference electrode.

6.2.8 Characterization

X-ray diffraction (XRD) patterns were recorded with a Philips diffractometer (XRG 3100, Cu Ka radiation, 35 mA and 40 kV). The morphology and Energy-dispersive X-ray spectra were obtained by Field Emission Scanning Electron Microscope (FE-SEM, JEOL-7000, equipped with Oxford EDX detector). Tecnai F-20 was used to collect Transmission Electron Microscopy (TEM) images at 200 kV. TEM samples were prepared by dispersing as-prepared samples on

lacey carbon TEM copper grids purchased from Ted Pella Inc. (Redding, CA). All the measurements were done using Adobe Photoshop Software. Raman spectra were collected using Bruker Senterra system (Bruker Optics Inc. Woodlands, TX) equipped with a 785 nm laser source at 10 mW laser powers and 100X objective. Optical microscopy was also utilized Bruker Senterra system. Parastat2273 (Princeton Applied Research) was used for electrodeposition and electrochemical characterization.

6.3 Electrodeposition of Nanowires

Figure 6.1 shows the electrodeposition process within AAO template. A concentration boundary layer of metal ion under diffusion control may develop through the nanoscale pores to the bulk electrolyte solution. Thus, the result is presumably caused by a kind of natural convection accompany metal deposition in and around such a small and high aspect ratio pore, which must enhance the ionic mass transfer rate around the bottom of the pore, as is illustrated schematically in Figure 6.1. The purpose of magnetically stirring is also to enhance the mass transfer of metal ions.

Figure 6.2 shows some optical images of multi-segment nanowires. Those images were obtained by ultrasonic-dispersion of nanowire arrays in solution and drop-casted on piranha cleaned Si wafer. The Cu, Ni, and Au segments show different colors under optical microscopy, especially when Cu segment been oxidized and show rusty contrast. Figure 6.3 shows typical XRD patterns for Ni NWs, Au NWs, Ni-Cu NWs, and Au-Ni-Cu NWs. Considering the individual surface planes of FCC materials, their stability decrease in the order {111} > {100} > {110}. Thus for low overpotential, the {111} is preferred due to its low surface energy. However, it was reported that, in electrochemical growth of FCC metals under a large overpotential, they present a

preferred crystallographic orientation along the [220] direction.[177] Our XRD patterns show a stronger (220) plane over (111) plane, confirmed high overpotential during deposition of Au, Ni, and Cu. SEM and EDS of single-, multi-segment nanowires arrays were shown in Figure 6.4. Those nanowires, after removing AAO templates, remain vertical standing because of a layer of metal film formed during electrodeposition. Different metals exhibit different contrast under SEM image, metals with higher atomic number show brighter contrast in SEM.

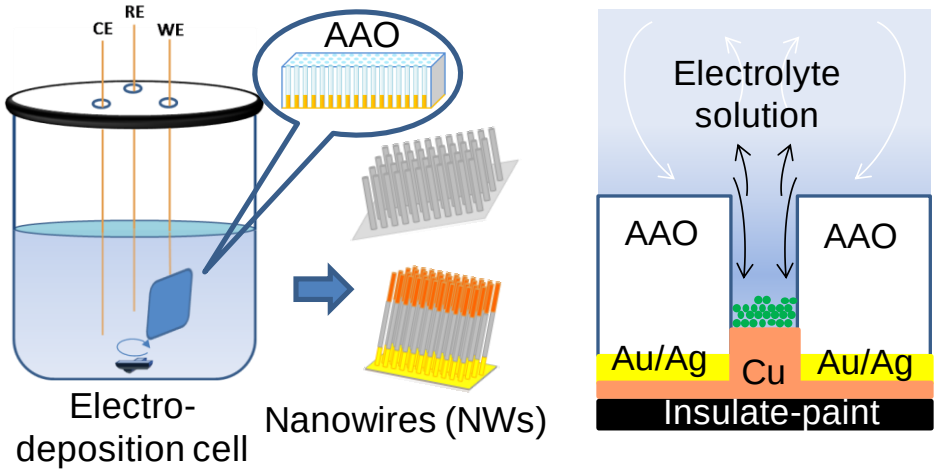

Figure 6.1 Schematic shows electrodeposition of nanowires in anodic aluminum oxide (AAO) template.

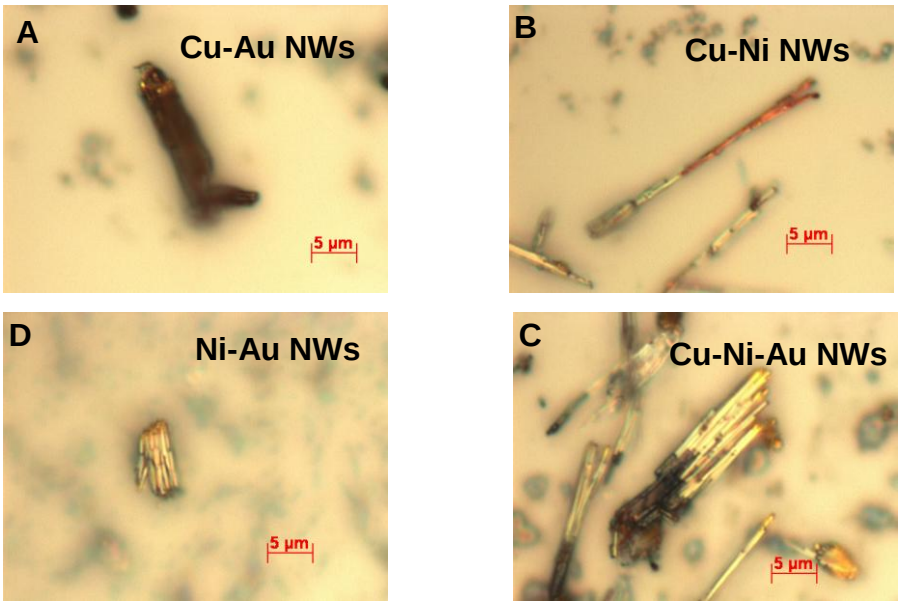

Figure 6.2 Optical images show nanowires: (A) Cu-Au NWs, (B) Cu-Ni NWs, (C) Ni-Au NWs, and (D) Cu-Ni-Au NWs

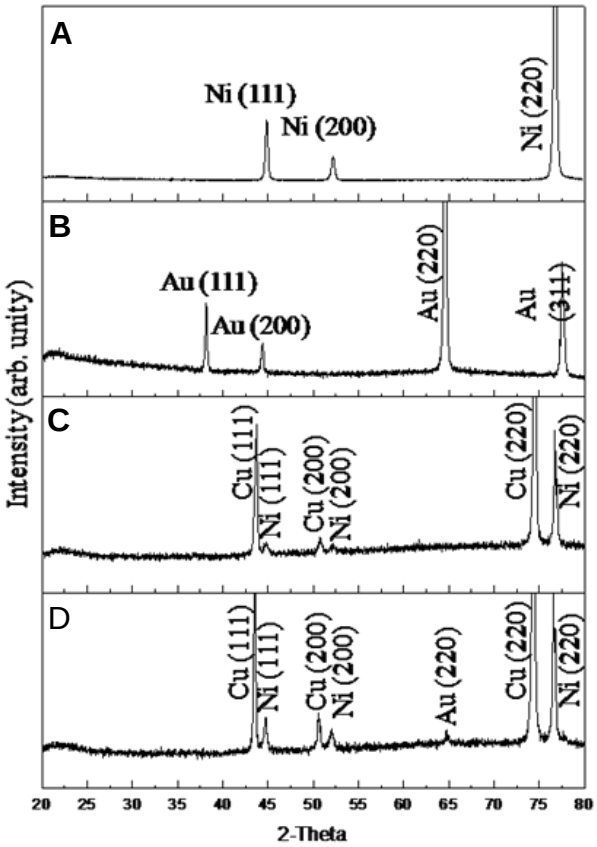

Figure 6.3 XRD of (A) Ni NWs, (B) Au NWs, (C) Ni-Cu NWs, (D) Au-Ni-Cu NWs

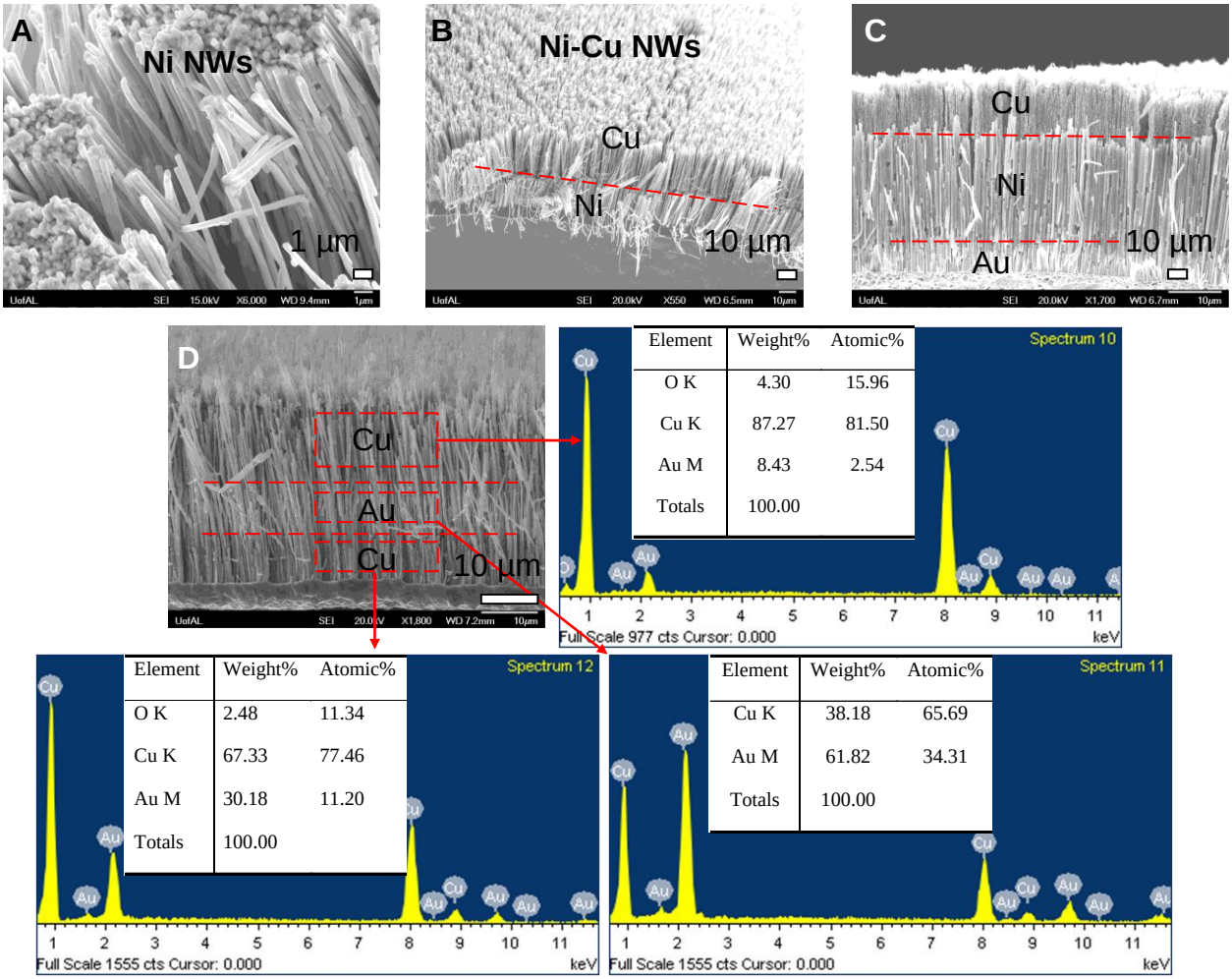

Figure 6.4 SEM images and EDS show (A) Ni NWs, (B) Ni-Cu NWs, (C) Au-Ni-Cu NWs, and (D) Cu-Au-Cu NWs.

The growth kinetics of nanowires was studied by depositing Cu NWs, Au NWs for different durations and measuring the length nanowires (Figure 6.5). It was shown that length of nanowires increases proportional with electrodeposition duration. (Figure 6.5B, C). For Cu NWs, however, since it exhibited a fast growth behavior and some nanowires grow faster on the edge of AAO template, the average length of nanowire in AAO membrane stopped increasing beyond 45 min deposition. That is due to preferential deposition on the surface of AAO supported by heterogeneous deposition on some coming-out, fast-grown nanowires on the edge.

We also observed a coarse appearance of Au NWs in high HR-SEM, comparing to Cu NWs with smooth surface (Figure 6.5D, E). This may due to the competitive growth rates for gold atoms entering the crystal lattice, that is $v_{//}$ (growth rate parallel to AAO channel) and $v_{\perp}$ (growth rate perpendicular to AAO channel).[178] When a low current density (electronic field) is applied, it has little influence on the values of $v_{//}$ and $v_{\perp}$, which means that $v_{//}$ is similar to $v_{\perp}$. As time increases, metal atoms fill most of the template pores and produce wire-like 1-D nanostructures. However, if a growth direction parallel to the current direction is the preferential direction, which means that $v_{//} \gg v_{\perp}$. In this case, metal atoms deposit straightforwardly to generate a tubular structure. The coarse appearance of Au NWs suggesting the tendency of forming Au nanotubes, which means the gold atom deposition rate parallel to AAO channel is considering high in our case.

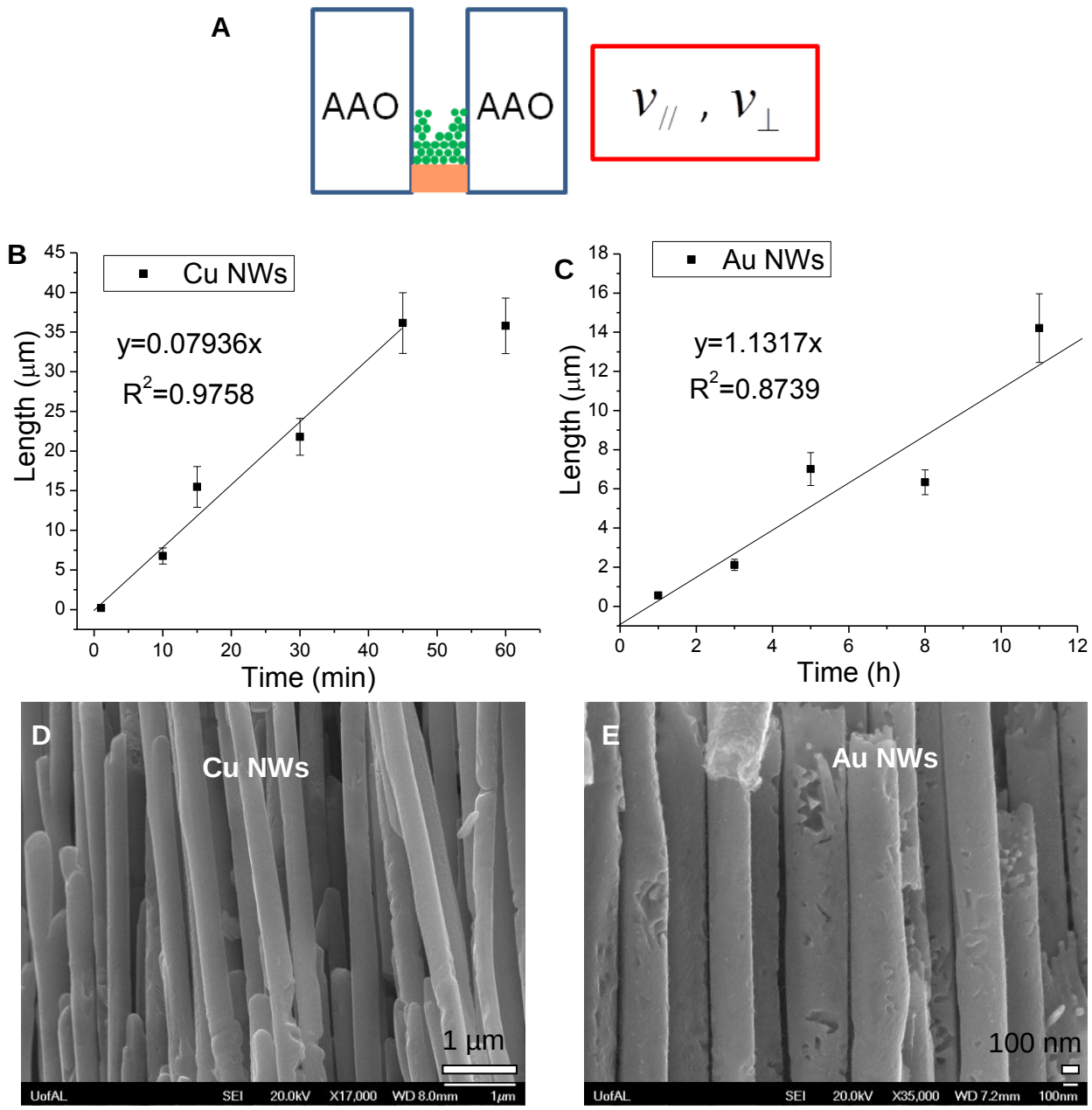

Figure 6.5 (A) Schematic shows the formation of nanowire/nanotube depending on the growth rate vertical to AAO wall ($v_{\perp}$) and growth rate parallel to AAO wall ($v_{//}$). Plots show the length of nanowires verse deposition time for (B) Cu NWs, (C) Au NWs. (D, E) SEM images show Cu NWs, Au NWs, respectively.

6.4 Graphene Shells Encapsulated Nanowires

Our interest was extended from growing graphene shell on nanoparticles to fabricating graphene shell on nanowires. The chemical vapor deposition process was similar with we applied on nanoparticle system and illustrated in Figure 6.6. Nanowires were synthesized through electrodeposition; they had been placed in quartz tube furnace after removing AAO template.

6.4.1 Thermal Stability of Nanowires

Knowledge of the thermal stability of nanowires is a prerequisite for the graphene shell growth. It was demonstrated that metal nanowires become unstable at temperatures far below the bulk melting point.[179] The fragment of nanowires when exposed to high temperature is due to the so-called Rayleigh instability.[180] On the other hand, the optimized temperature we used for graphene shells growth on previous nanoparticles was high (675 ^{o}C for AuNPs, and 800 ^{o}C for PdNPs, PtNPs). Our purpose of study the thermal stability of nanowires is to find out what the lowest temperature we can apply to our nanowires system, and how fast those nanowires would melt at optimized graphene shells growth temperature.

Cu-Au-Cu three-segment nanowires were select for the thermal stability study. The chosen of multisegment enable us to observe morphology change for both copper and gold within a single experiment. One group of Cu-Au-Cu NWs was annealed at different temperature (ranging from 100 ^{o}C to 800 ^{o}C) in Ar atmosphere for 1 h (Figure 6.7). It was observed that nanowires maintained their morphology well below 300 ^{o}C (Figure 6.7A-B). As temperature increased to 300-400 ^{o}C, sintering took place and neighboring nanowires start to aggregate together (Figure 6.7C-D). Keep increasing temperature higher than 500 ^{o}C, nanowires were totally melted and finally formed crystal particles at temperature higher than 600 ^{o}C (Figure 6.7E-H). This indicated

that under our optimized graphene shells growth temperature for noble nanoparticles (675-800 ^{o}C) the nanowires would not be able to maintain their morphology.

To further understand how fast the Cu-Au-Cu NWs would melt, they had been heated at 675 ^{o}C in Ar atmosphere for different durations (from 15 s to 60 min). It was shown that Cu-Au-Cu NWs can maintain wire-like morphology by heated at 675 ^{o}C less than 1 min, only some sintering took place (Figure 6.8A-C). As increasing annealing duration, sintering and melting of nanowires became obvious (Figure 6.8D-G), and nanowires transformed into firm-like structure by annealing longer than 40 min (Figure 6.9H-I). The gold segment in the center of nanowires seems melted earlier than copper segment, probably due to the coarse structure of gold segment.

Due to temperature ramping process of the furnace, the actual heating time for nanowires was longer than what we set. To precisely control the annealing duration, we annealed nanowires by inserting the sample after temperature ramped up to 300 ^{o}C, and then heated three nanowire samples at 300 ^{o}C for 15 s, 5 min, and 30 min, respectively. It showed that nanowires would be sintered at 300 ^{o}C beyond 5 min annealing (Figure 6.10).

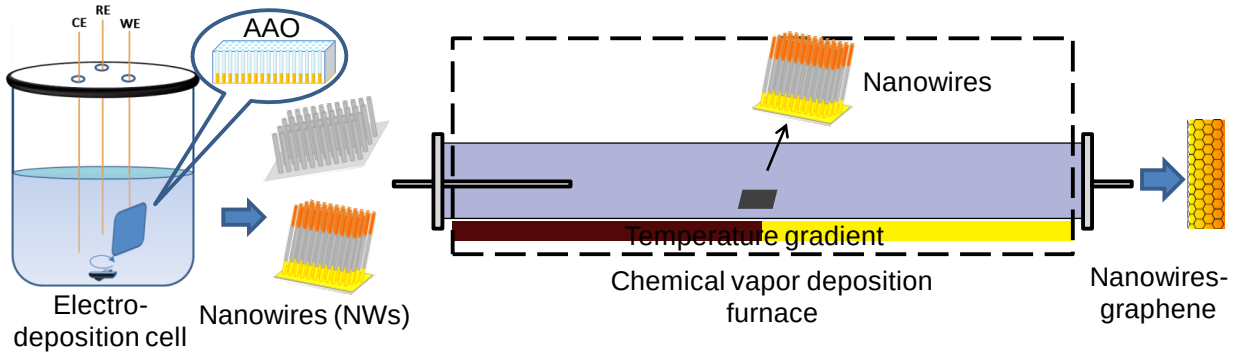

Figure 6.6 Schematic show processes of graphene shells growth on nanowires.

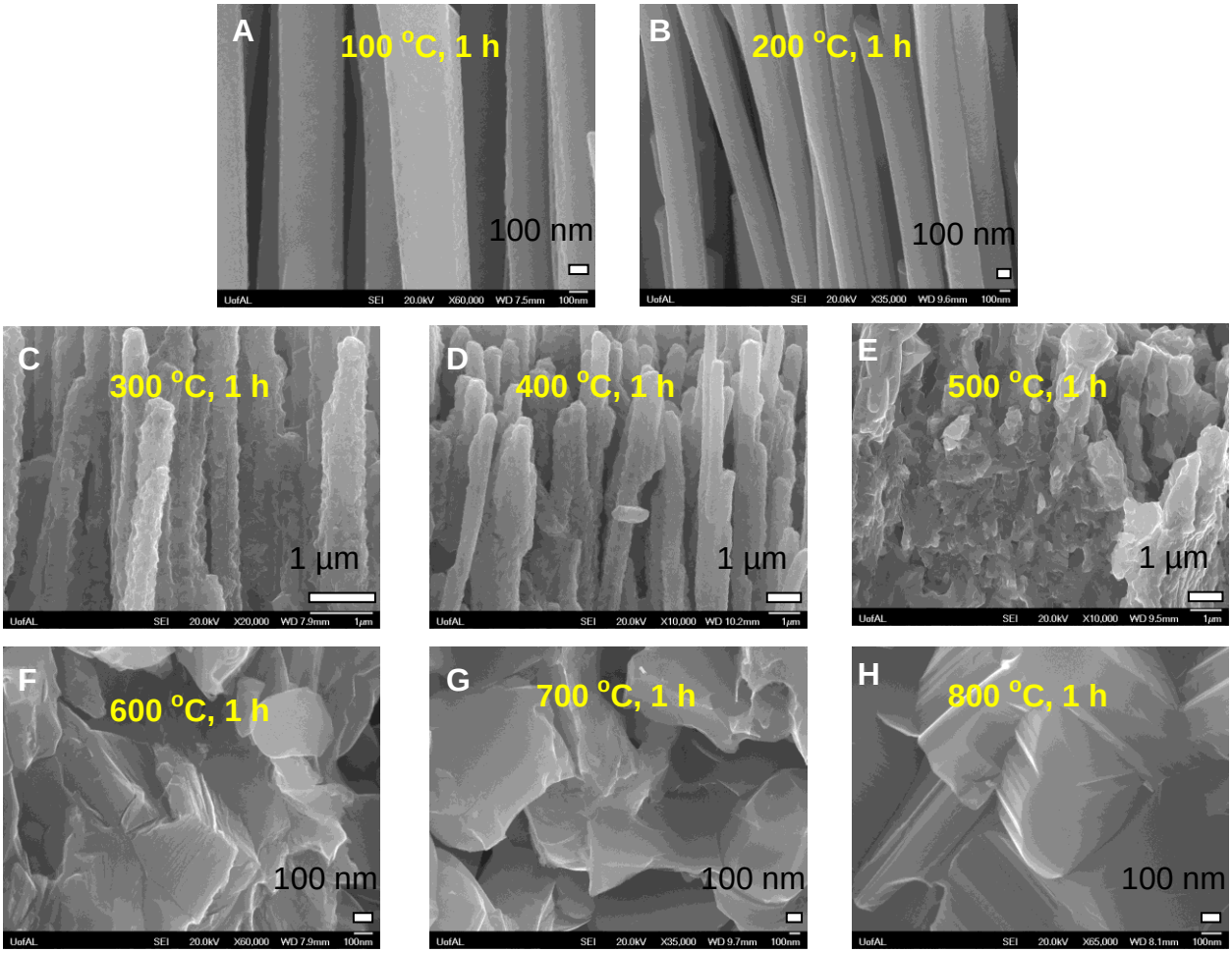

Figure 6.7 SEM show Cu-Au-Cu NWs been annealed 1 h at different temperatures: (A) 100 ^{o}C, (B) 200 ^{o}C, (C) 300 ^{o}C, (D) 400 ^{o}C, (E) 500 ^{o}C, (F) 600 ^{o}C, (G) 700 ^{o}C, (H) 800 ^{o}C.

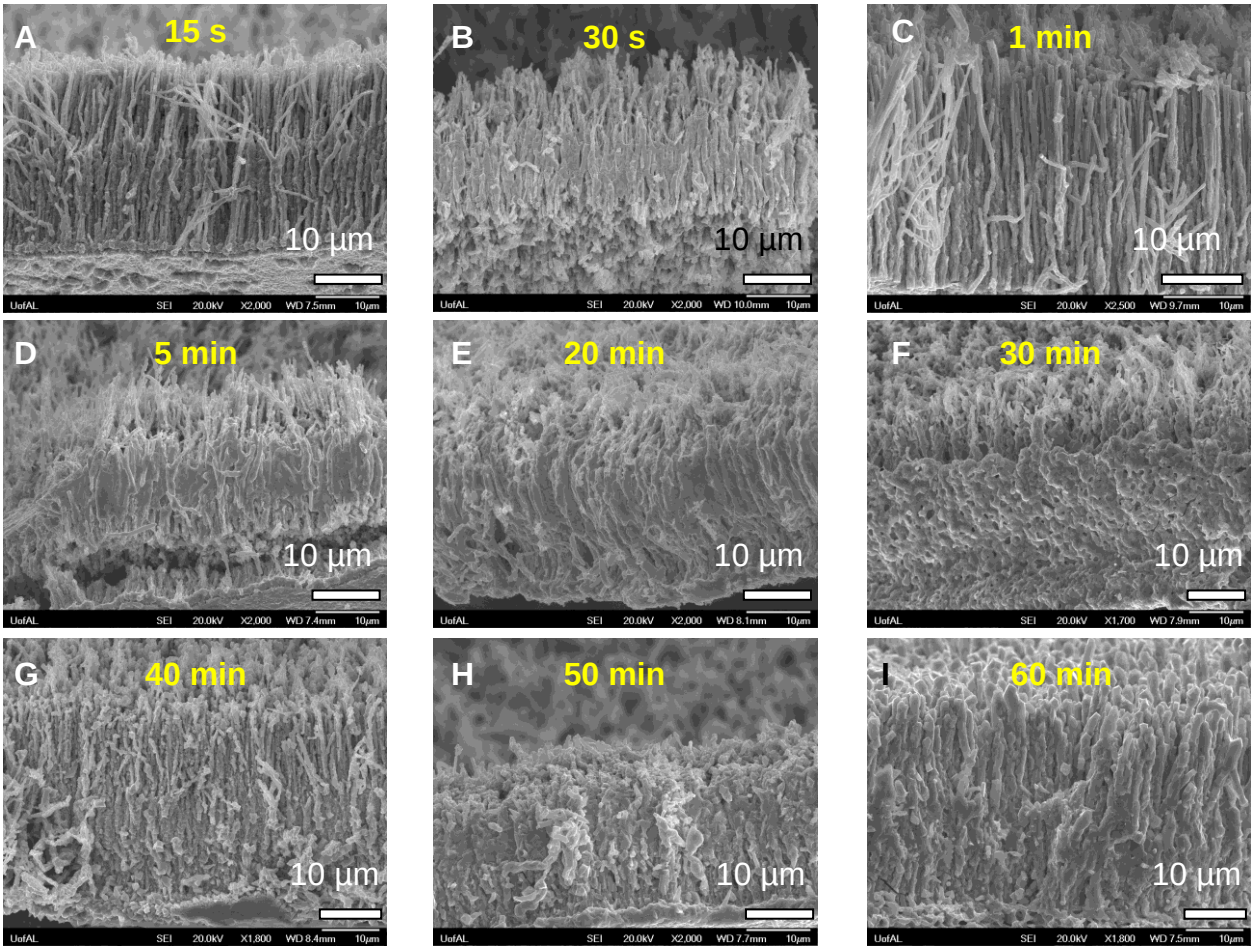

Figure 6.8 SEM showing Cu-Au-Cu NWs after been annealed at 675 ^{o}C for different duration: (A) 15 s, (B) 30 s, (C) 1 min, (D) 5 min, (E) 20 min, (F) 30 min, (G) 40 min, (H) 50 min, and (I) 60 min.

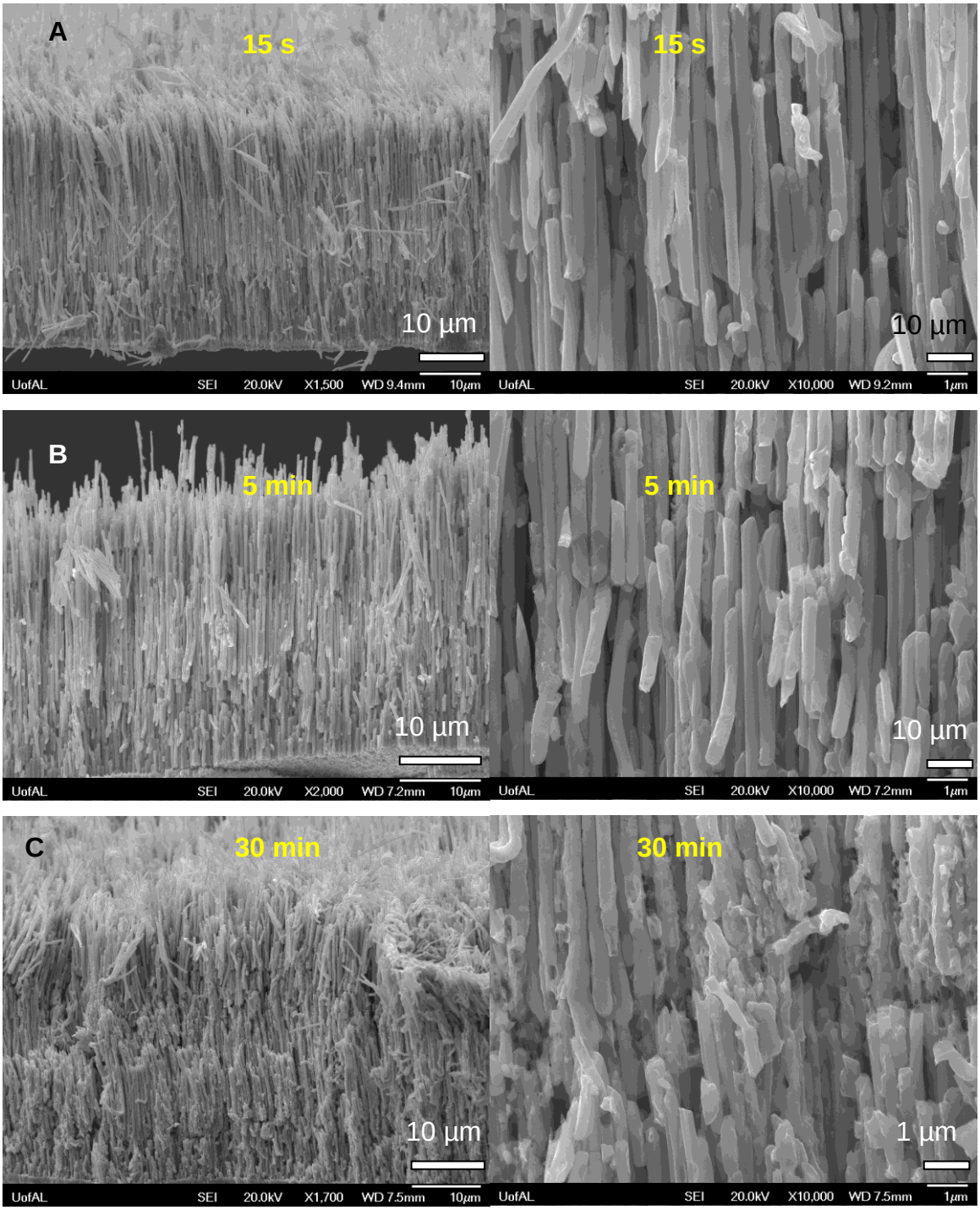

Figure 6.9 SEM show Cu-Au-Cu NWs been quickly inserted for annealing at 300 ^{o}C for different duration: (A) 15 s, (B) 5 min, and (C) 30 min

6.4.2 Graphene shells growth for Nanowires

An exciting research direction is to grow single-walled or few layered graphene tubes using nanowires as template. The number of carbon layers in a CNT is strongly influenced by its diameter, and single-walled CNTs are typically at most 2-5 nm in diameter, while larger-diameter CNT are usually multiwalled with diameters ranging between 2 to 100 nm.[181],[182] Using nanowires with large diameters, we may get graphene shells with large diameter, and the number of graphene layers can be controlled through tuning the graphene shells growth duration. Thus single-walled or few layered graphene tubes would be obtained through a post-etching process of the nanowire-template.[79]

Even though we observed melting of nanowires at high temperature in last section, we also found that nanowires can maintain wire-like structure within 1 min annealing at 675 ^{o}C. In chapter 5, we demonstrate that the as-formed carbon/graphene shell can prevent PtNPs from further aggregation even at 1000 ^{o}C, so we were expecting that if we can synthesize graphene shell on nanowires fast enough, the fabricated graphene shell would protect nanowires from further melting. In this regard, single-segment nanowires Au NWs, Cu NWs, Pd NWs, and Pt NWs were utilized for graphene shells growth study. The effects of plasma oxidation and temperature on graphene shell formation were investigated.

The plasma oxidation effect on the growth of graphene shell was studied on Au NWs and Cu NWs. Two pieces of Au NWs arrays (one was plasma oxidized for 30 min, the other one was untreated by oxygen plasma) were placed in quartz tube for graphene shells growth at the same condition. It showed that no observable shell was formed on non-oxidized Au NWs under SEM (Figure 6.10A), while only oxidized Au NWs can form graphene shells (Figure 6.10B-C). For Cu

NWs, both plasma-treated sample and non-treated sample melted after graphene shells growth, but the plasma oxidized Cu NWs exhibited a smoother surface with some sheath-like pieces (Figure 6.11).

Single Pd NWs and Pt NWs were used to investigate the temperature effect on graphene shell growth. Studies in chapters 4 and 5 indicated that palladium and platinum tend to form surface-oxides at room temperature even without any plasma oxidation. Thus Pd NWs and Pt NWs were placed in quartz furnace for graphene growth without plasma treatment. Two temperatures (675 ^{o}C and 800 ^{o}C) were used in chemical deposition process, and graphene shells only formed on Pd NWs and Pt NWs at higher temperature (Figure 6.12B and Figure 6.13B). After graphene shells growth, even though sintering was observed for all nanowires, but Au NWs, and Pd NWs maintained wire-like morphology with the help of their graphene shell.

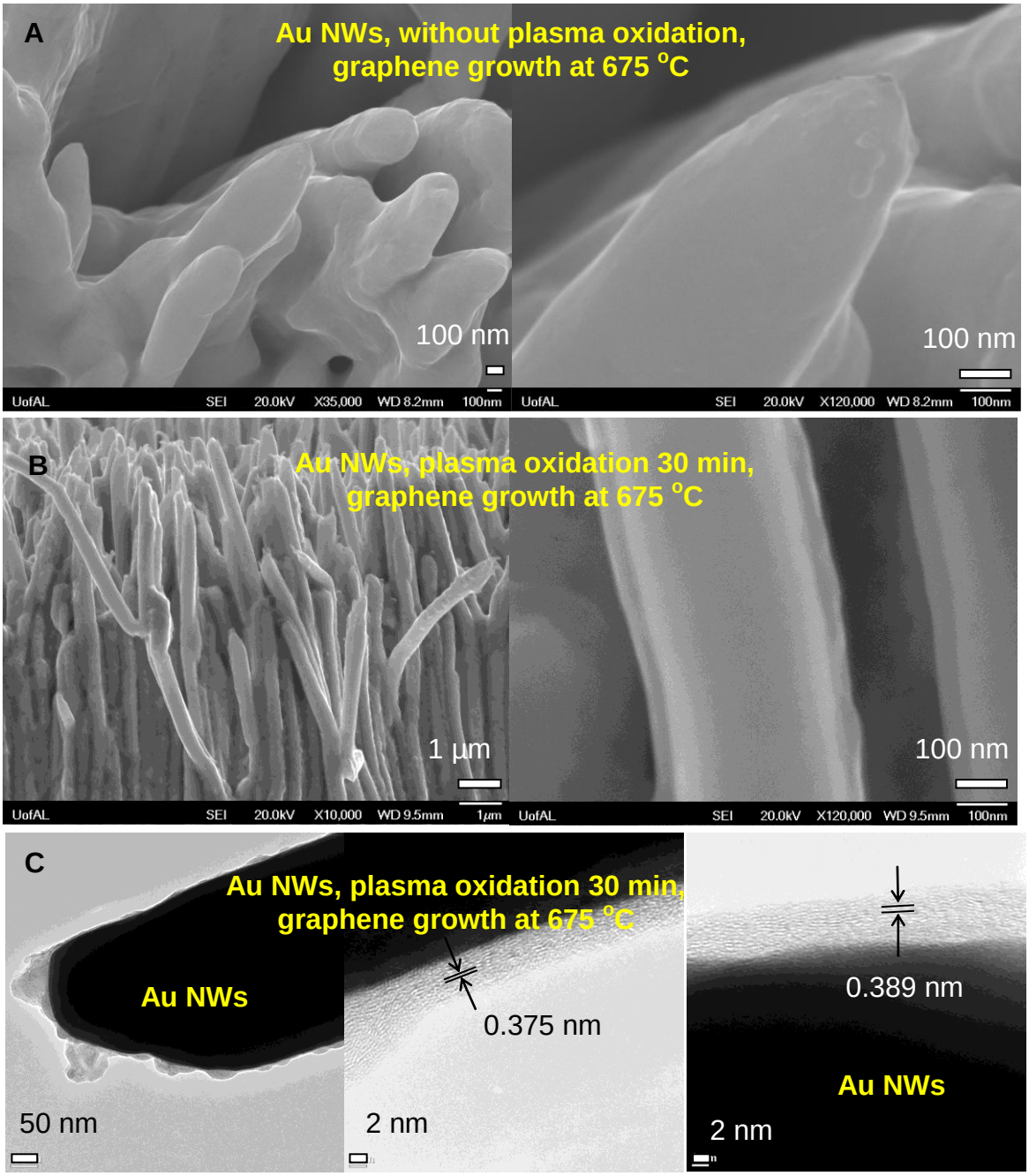

Figure 6.10 SEM images show Au NWs underwent CVD process at 675 ^{o}C (A) without plasma oxidation before graphene shells growth; (B) plasma oxidized for 30 min; (C) TEM images for Au NWs after plasma oxidation 30 min and graphene shells growth at 675 ^{o}C

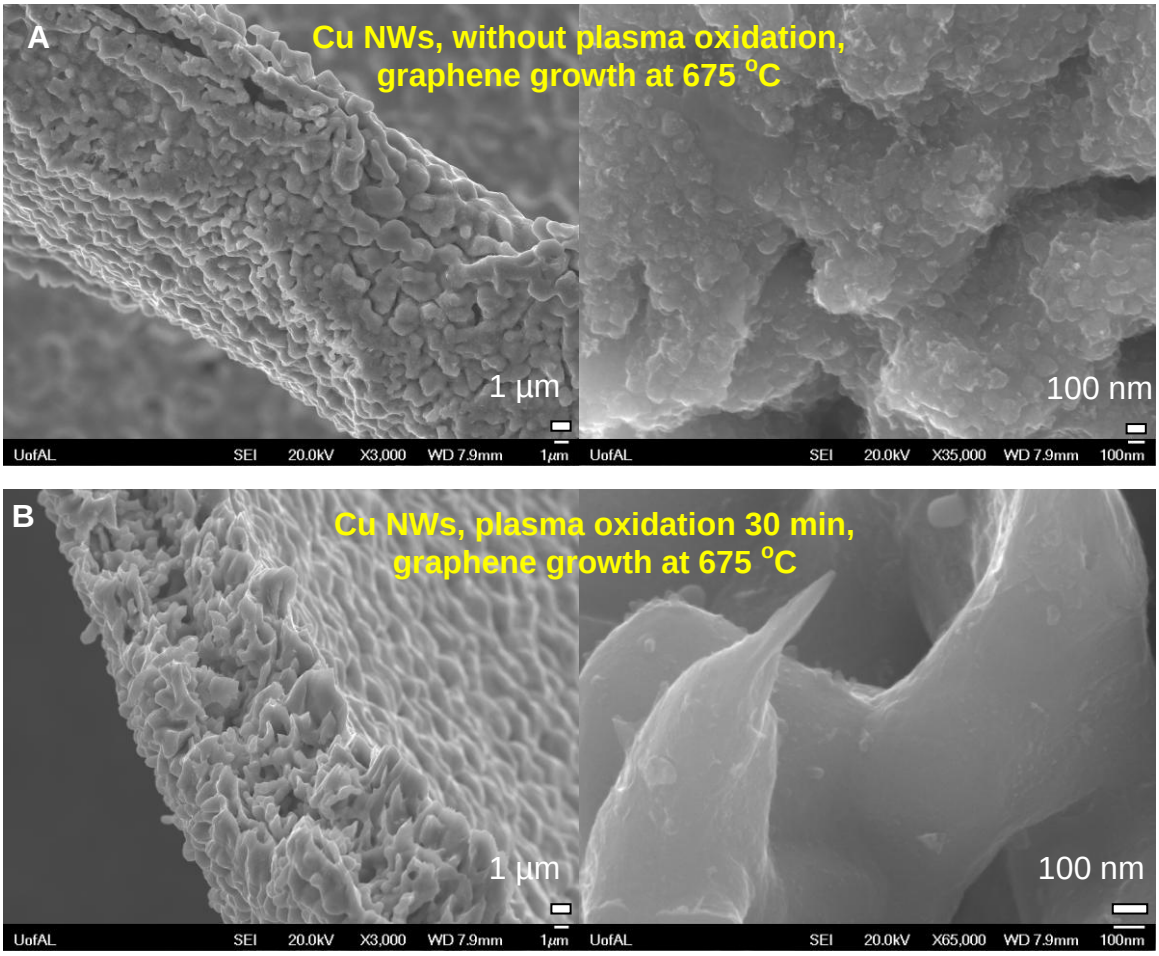

Figure 6.11SEM images show Cu NWs underwent CVD process at 675 ^{o}C (A) without plasma oxidation before graphene shells growth; (B) plasma oxidized for 30 min before graphene shells growth

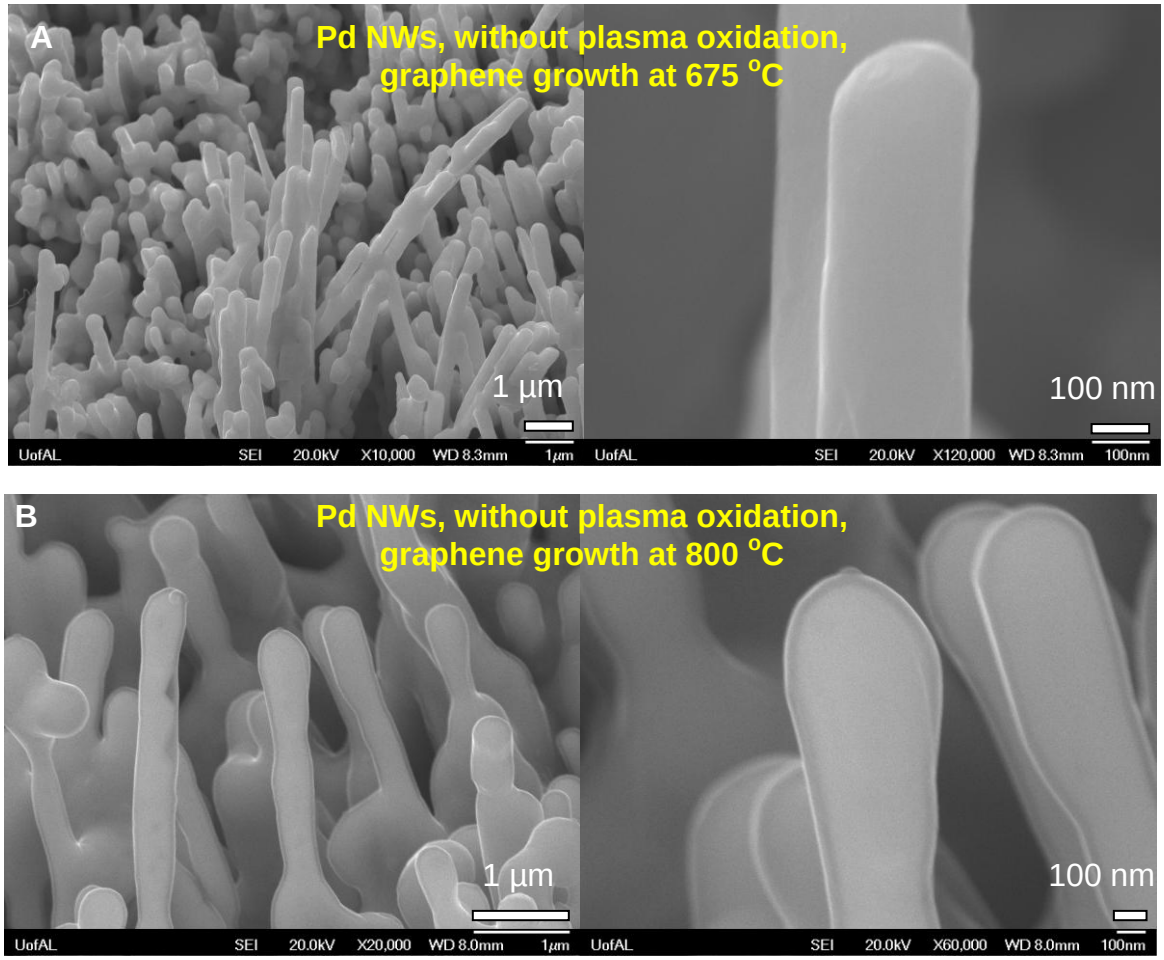

Figure 6.12 SEM images show Pd NWs without plasma oxidation underwent CVD process at different temperatures: (A) 675 ^{o}C, (B) 800 ^{o}C

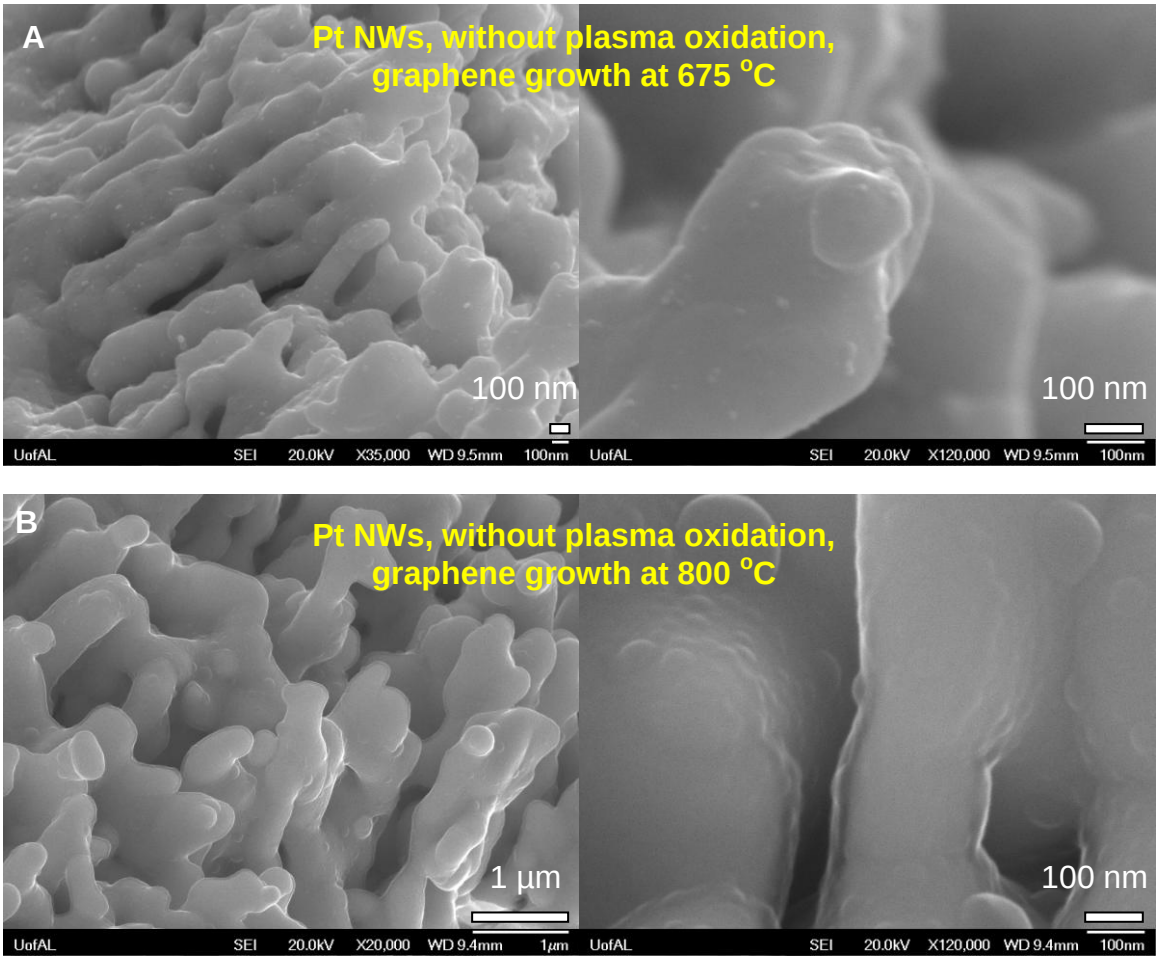

Figure 6.13 SEM images show Pd NWs without plasma oxidation underwent CVD process at different temperatures: (A) 675 ^{o}C, (B) 800 ^{o}C

6.5 Synthesis of Nanowire-CNT Heterostructures, decoration with Ni Nanoparticles, and Electrochemical Characterization

Another approach to synthesize metal-graphite heterostructure is to fabricate one-dimensional hybrid nanowires consisting of multiple segments with CNT on one end and metal nanowires on the other (named as NWs-CNT). This architecture was built by combination of electrodeposition and chemical vapor deposition in AAO template for the growth of Au-Ni NWs and CNTs, respectively (Figure 6.14). We are interested in using this NWs-CNT hybrid to fabricate materials in energy storage. Electrochemical capacitors (ECs) are energy storage devices that attracted much attention due to their high power capability and long cycle life.[183]Electrochemical double layer capacitors (EDLCs) are the most common devices at present, use carbon-based active materials that have high surface area. Another group of ECs use fast and reversible surface or near-surface reactions for charge storage, are called as pseudo-capacitors or redox supercapacitors. Hybrid capacitors, combining a capacitive or pseudo-capacitive electrode with a battery electrode, are the latest kind of EC.

Nickel oxide is known as a good pseudo-capacitor material.[184]Meanwhile, CNTs have been proved to be a good material to construct super-capacitor electrodes due to the high conductivity, electrochemical stability and open porosity.[185] So the construction of Au-Ni NWs-CNTs hybrid holds potential to have good capacitance activity. In this case, Au NWs section was applied as current collector.[88] Furthermore, nickel nanoparticles were decorated on NWs-CNT hybrid in a single wet-chemistry and resulted in Au-Ni NWs-CNT-Ni NPs heterostructure named as NWs-CNC (Figure 6.14).

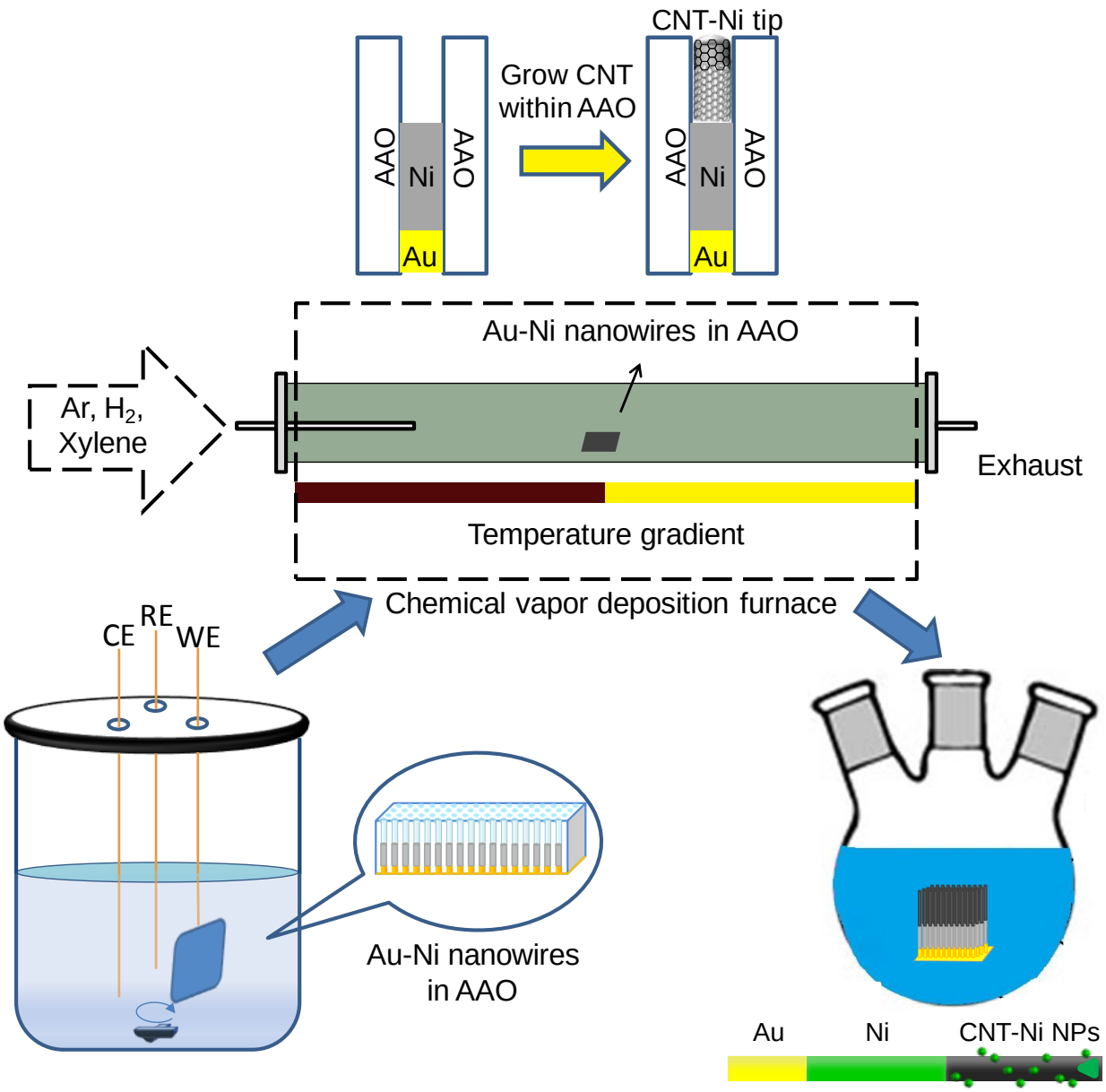

Figure 6.14 Schematic show process of 1) Electrodeposition Au-Ni NWs; 2) Growth CNT on tip of nanowires using AAO as template; 3) Attachment of Ni nanoparticles on NWs-CNT to form NWs-CNC heterostructure

Figure 6.15 shows XRD patterns for Au-Ni NWs, NWs-CNT and NWs-CNC heterostructures. The as-synthesized Au-Ni NWs exhibit gold peak and strong peaks of nickel with (220) as dominant plane due to the high overpotential during electrodeposition (Figure 6.15A). CNT (002) peak was observed after chemical vapor deposition, Ni_3C (006) and x(009) peaks were also observed (Figure 6.15B). After decoration of Ni NPs on NWs-CNT heterostructure, the Ni (111) intensity became strong and dominant because of the formation of Ni NPs.

SEM images show well aligned Au-Ni NWs (Figure 6.16, the AAO template was removed in the purpose of SEM characterization). In HR-SEM, it shows the inter-junction between Au segment and Ni segment were well contacted. A uniform sheet of NWs-CNT was obtained after CVD process and removing of AAO template (Figure 6.17A). Each segment of NWs-CNT was characterized by SEM and EDS (Figure 6.17B-G). Ni NWs segment acted as catalysts for CNT growth, and part of Ni NWs remained inside of CNTs' tip, lifting-off with the growth of CNT. The process is documented as tip-growth model of CNTs:[186] During CVD growth, diffusion of carbon atoms decomposed at the Ni segment surface into the Ni nanowire segregated and precipitated. As graphite layer was formed, a Ni tip was liftoff from the Ni nanowire; then carbon nanotubes were formed and preferentially grew along the channels of AAO template. NWs and CNTs were well connected after CVD growth (Figure 6.17F). However, It should be noticed some Au NWs and Ni NWs were disconnected after CVD process (Figure 6.17G). This may attributed to recrystallization of some coarse Au NWs during high temperature CVD process, this may lead to a problem of current collection when use this nanostructure as capacitor materials. HR-TEM and EDS were used to characterize NWs-CNT inter-junction and CNTs' tip (Figure 6.18). The lattice fringe distance of CNT is ~0.34 nm, suggesting a good graphite

structure. The EDS line-profiling of NW-CNT inter-junction shows that not only the tips of CNTs contain nickel, there are also some nickel diffused through other parts of CNTs. The NWs-CNT heterostructures were also characterized by Raman spectroscopy. Figure 6.19 shows a typical Raman spectrum of NWs-CNT and a chemical mapping for G-band of graphene. The peaks for graphite structure including D-, G-, and 2D-band were well presented in Raman spectrum.

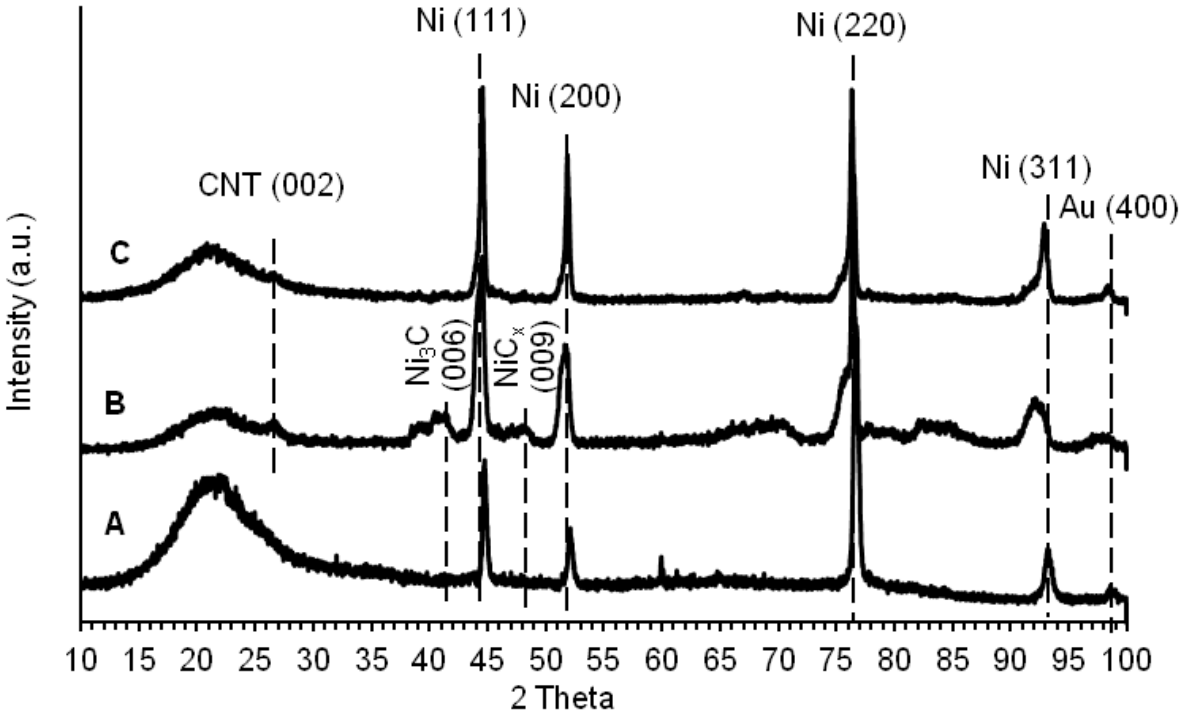

Figure 6.15 XRD of (A) Au-Ni NWs, (B) NWs-CNT heterostructures, and (C) NWs-CNC heterostructures

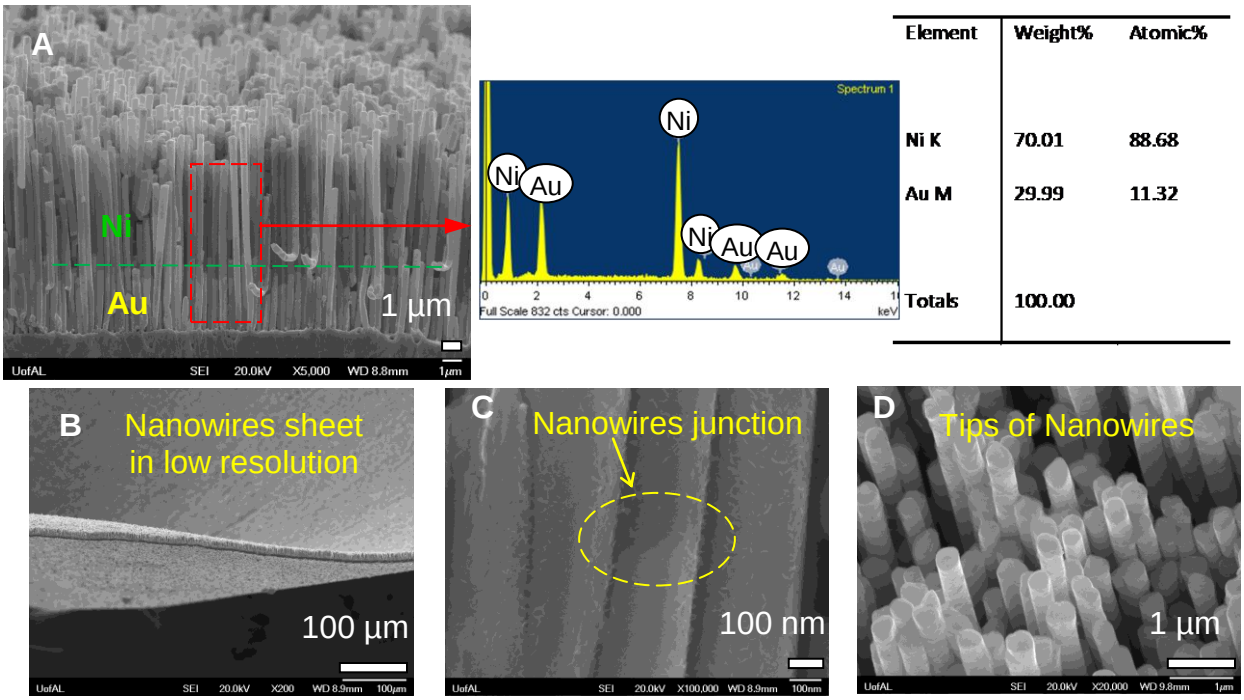

Element	Weight%	Atomic%
Ni K	70.01	88.68
Au M	29.99	11.32
Totals	100.00	

Figure 6.16 SEM images and EDS show Au-Ni NWs

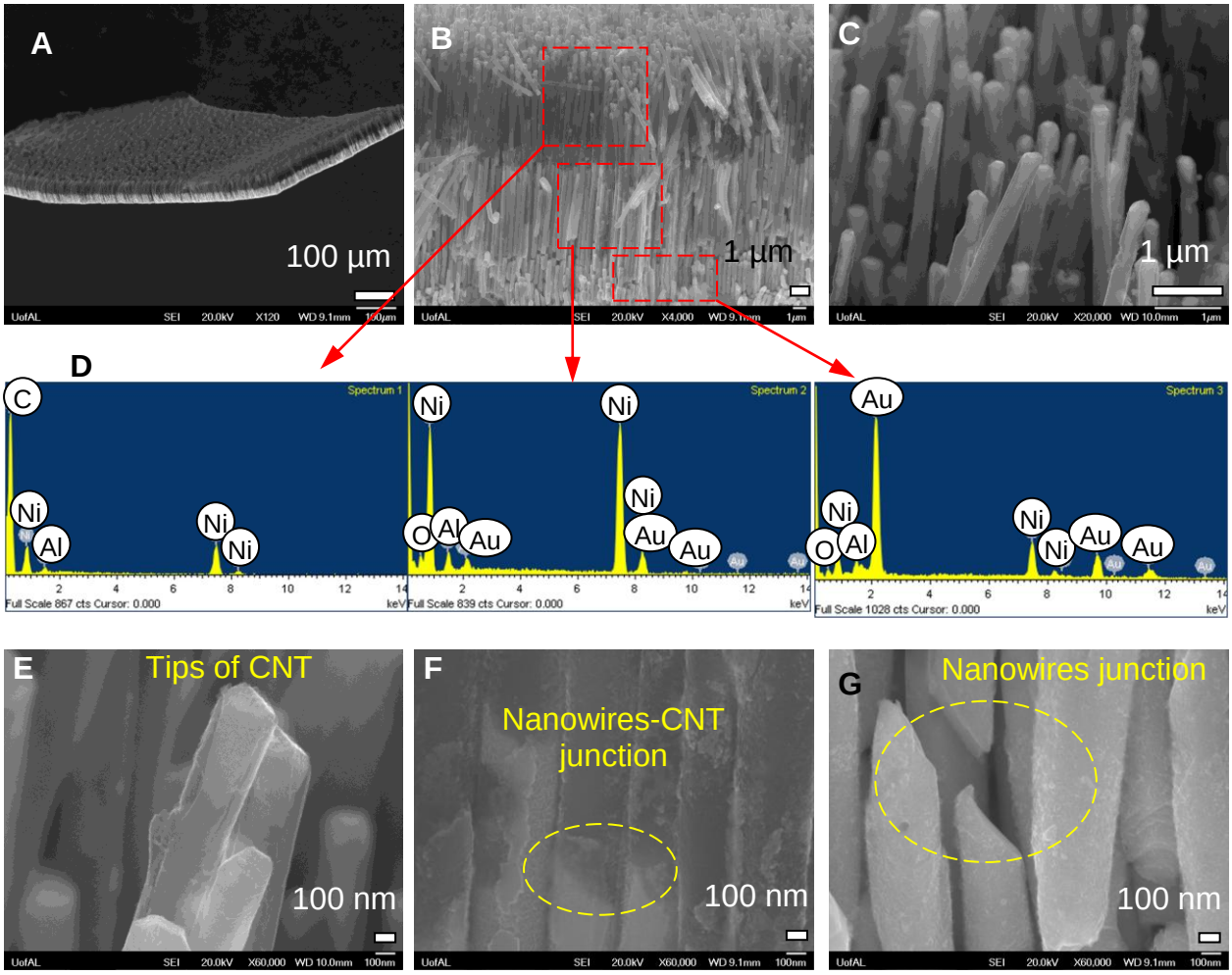

Figure 6.17 (A-C) SEM images, (D) EDS for Au-Ni NWs-CNT heterostructures, and HR-SEM for (E) CNT tips, (F) NWs-CNT junction, and (G) Au-Ni NWs junctions.

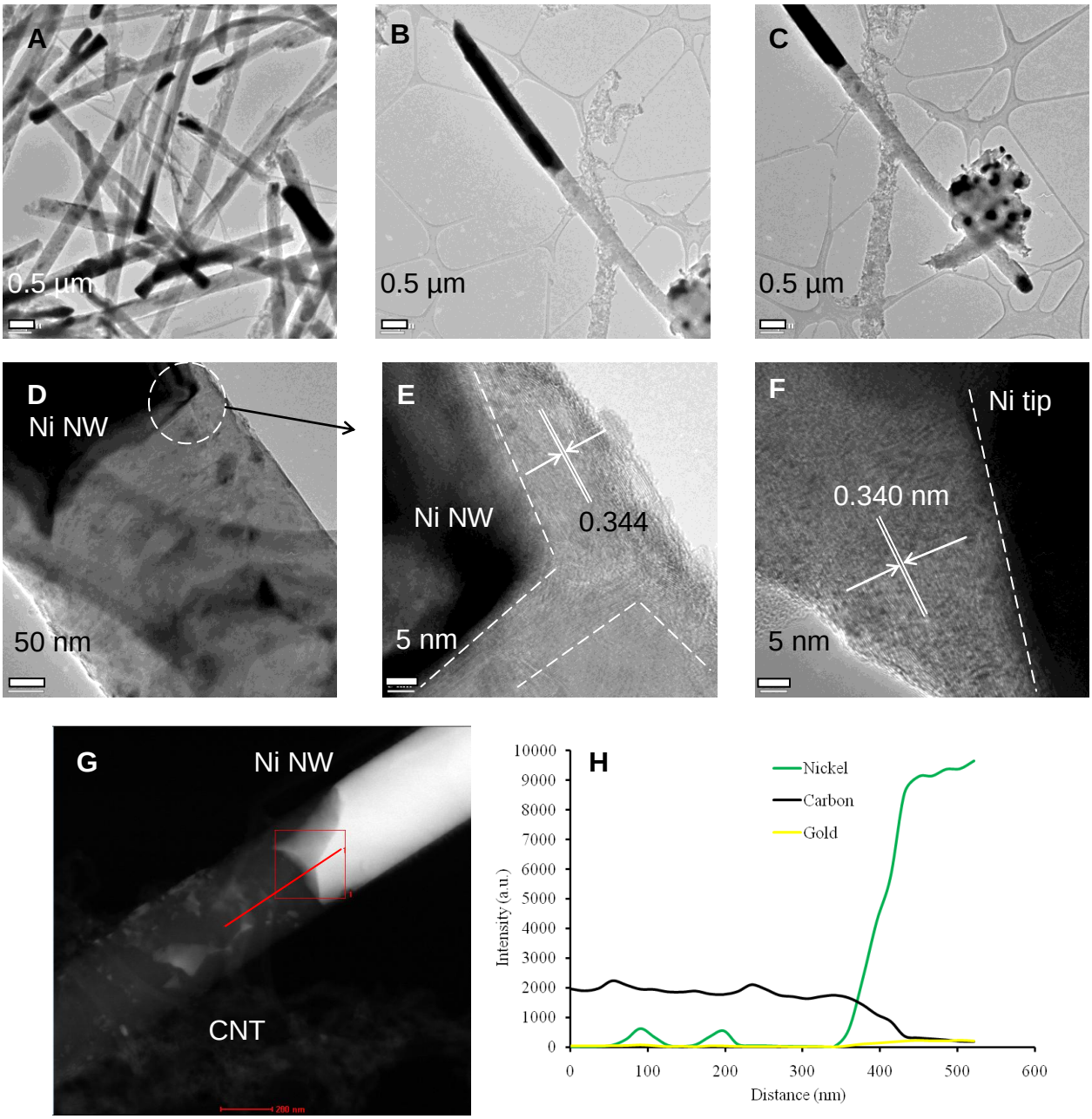

Figure 6.18 (A-F) TEM images, (G) STEM image show NWs-CNT heterostructure; (H) Line-profile for Nanowires-CNT junction

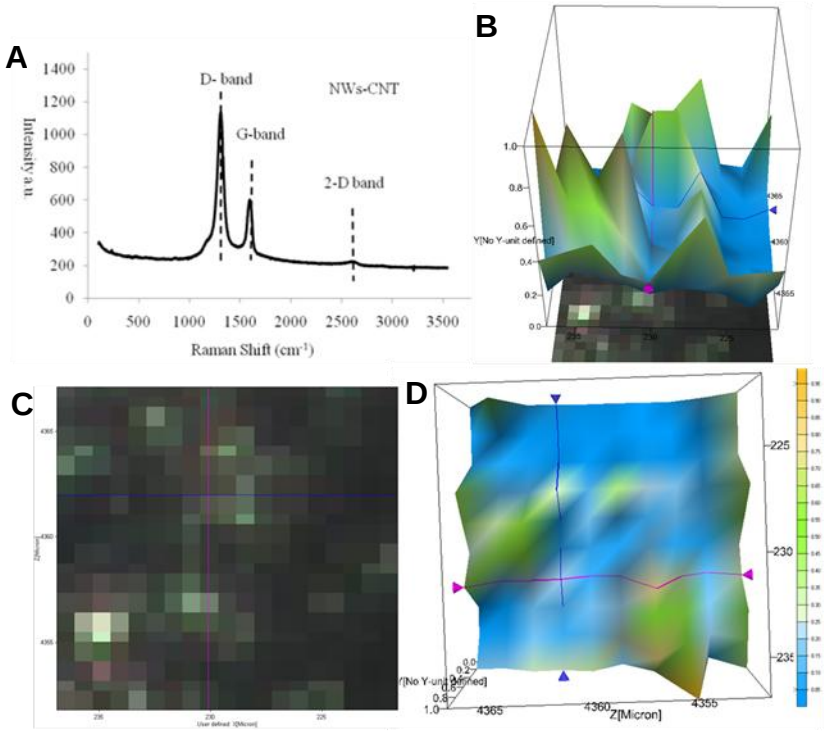

Figure 6.19 (A) Raman spectrum of NWs-CNT, (B) 3D mapping for G-band, (C) optical image of sample surface, and (D) vertical view of 3D mapping

Figure 6.20 represents SEM images and EDS for NWs-CNC heterostructure. Ni NPs with diameter ~20 nm were decorated on NWs-CNT, majorly on the surface of CNT because good wettability of hydrophobic CNT segment in oil phase solution for Ni NPs nucleation (Figure 6.20F, G). TEM and EDS line-profiling were shown in Figure 6.21. HR-TEM of decorated Ni NPs (Figure 6.21C) indicates that single-crystal Ni NPs were encapsulated in thin NiO shells, which is important for their pseudo-capacitor performance. The formation of NiO was also confirmed by showing peak of Longitudinal optical phonon modes (~546 cm^{-1}) in NWs-CNC Raman spectrum (Figure 6.22A).[187] By knowing the density of nanowires (8.3×10^{8} cm^{-2}), the length and diameter of nanowires and CNTs, and the diameter of Ni NPs, we can calculate the specific area of Au-Ni NWs, NWs-CNT, and NWs-CNC heterostructures (Table 6.1). In case of NWs-CNC hybrid, we assuming hemisphere Ni NPs were only attached on CNT segment. It suggested the sheet sample of NWs-CNT and NWs-CNC exhibit ~150 times real surface area comparing to the sheet area, the enhancement of surface area is important for the fabrication of supercapacitor electrode.

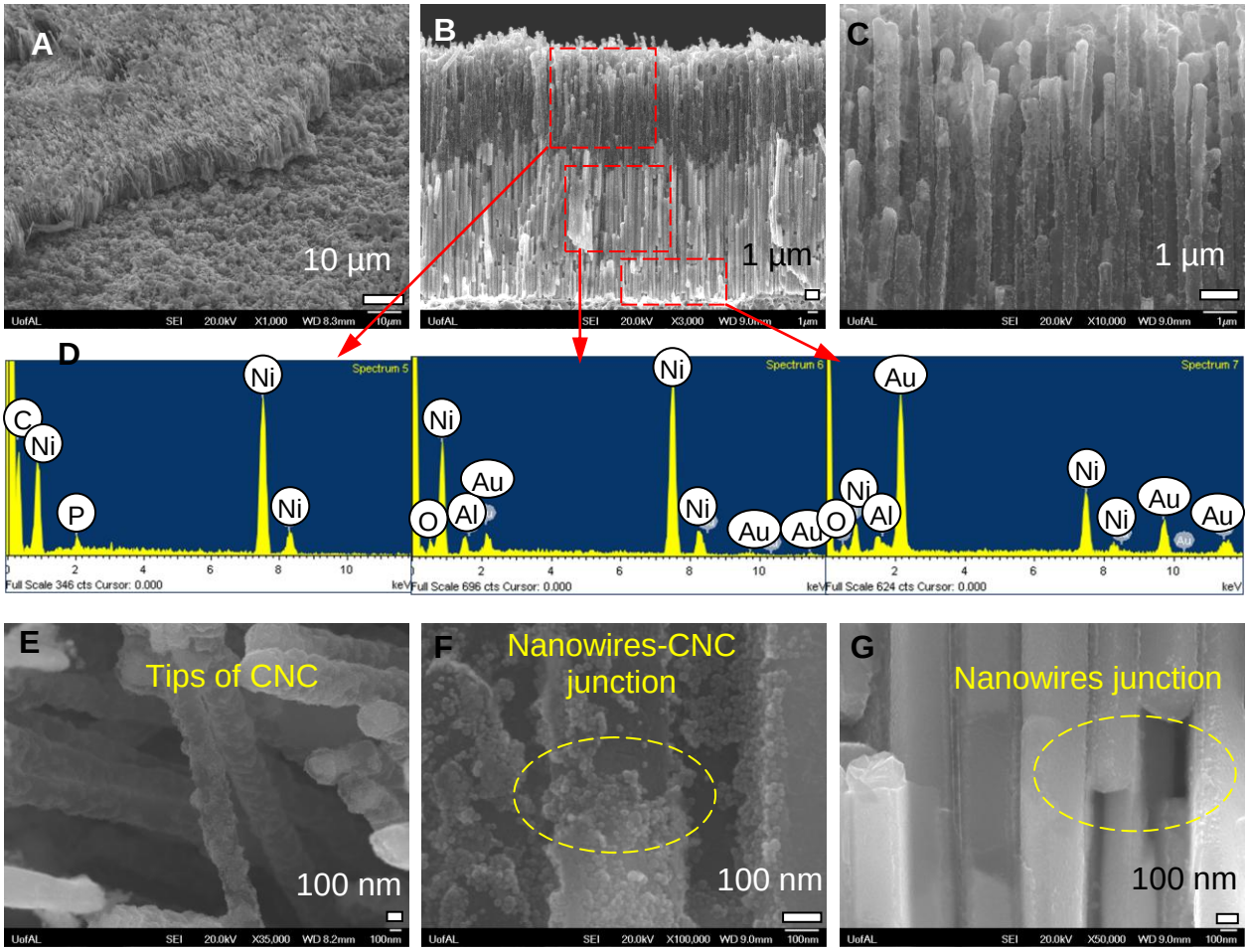

Figure 6.20 (A-C) SEM images, (D) EDS for Au-Ni NWs-CNT-NiNPs heterostructures (NWs-CNC), and HR-SEM images for (E) CNT tips, (F) NWs-CNC junction, and (G) Au-Ni NWs junctions.

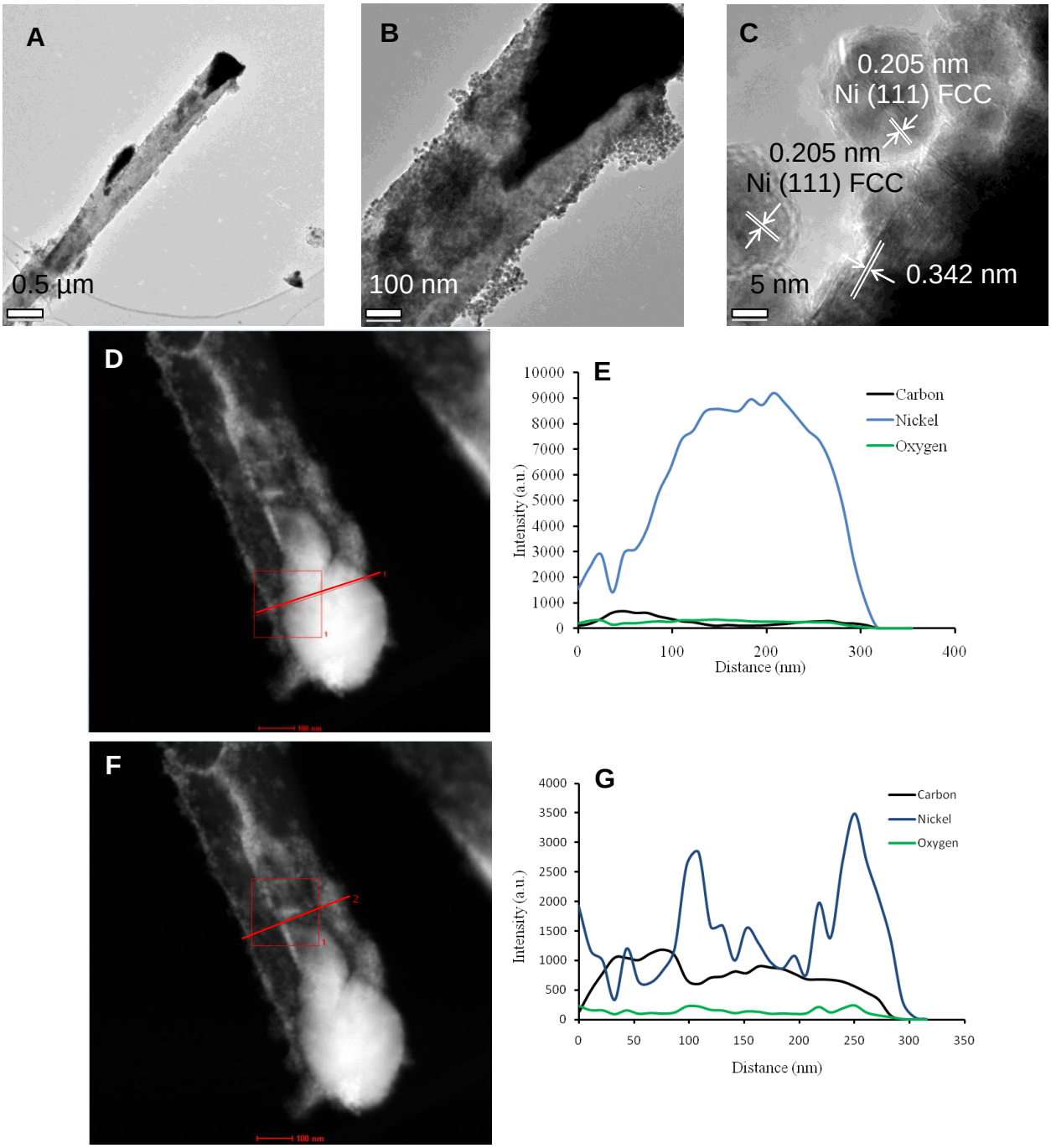

Figure 6.21 (A-C) TEM images show NWs-CNC heterostructure, (D-G) STEM images and line-profiling show the tip of NWs-CNT.

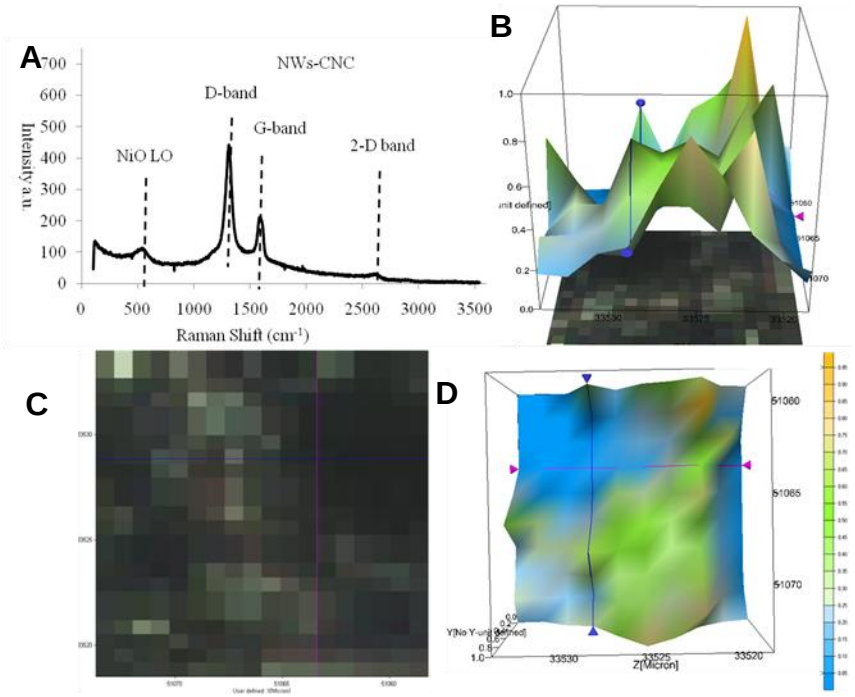

Figure 6.22 (A) Raman spectrum of NWs-CNC, (B) 3D mapping for G-band, (C) optical image of sample surface, and (D) vertical view of 3D mapping

Table 6.1 Surface area calculation for NWs, NWs-CNT, and NWs-CNC heterostructures

	NWs	NWs-CNT	NWs-CNC
Piece area (cm^2)	0.24	0.2	0.21
Surface area (cm^2)	19.60	29.92	31.49
Surface area per unit sample area	82	150	150
Surface area per mass (cm^2/g)	3062.5	4825.8	2624.2

The capacitive behavior of an electrode material is generally characterized by cyclic voltammogram (CV). In an ideal electrical double-layer capacitor containing smooth electrodes, its CV current response shows a rectangular mirror image with respect to the zero-current line.[188] When faradic reaction and Ohmic resistance (resulting from electrolyte diffusion within porous electrode) are involved, the rectangular mirror image is no longer maintained.[189]

$$C = \frac{q}{V_f - V_{io}} \tag{6.1}$$

$$q = \frac{\int I(V)dV}{v_{scan}} \tag{6.2}$$

where C is capacitance (F), q is quantity of electric charge (C), V_f is final potential, V_{io} is starting potential, $\int I(V)dV$ is the area of CV curve and represents the average, v_{scan} is the potential scan-rate for CV test. The faradaic capacitance is coming from the Ni^{2+} to Ni^{3+} redox reaction given as[190],[191]

$$NiO + OH^- \leftrightarrow NiOOH + e^- \tag{6.3}$$

Nickel hydroxides also exist in the Ni^{2+} to Ni^{3+} redox couple in alkaline solution as:[190,191]

$$Ni(OH)_2 + OH^- \leftrightarrow NiOOH + H_2O + e^- \tag{6.4}$$

A typical CV measurement for NWs, NWs-CNT, and NWs-CNC is shown in Figure 6.23. Capacitance for each sample at different conditions were calculated and listed in Table 6.2. It was found that after adding CNT and Ni NPs on the architecture, the capacitance not increased, but decreased than pre-treated sample. This may attribute to two reasons: 1) After CVD growth

of CNT and Ni NPs nucleation, some inter-sections of Au-Ni NWs were disconnected as observed in Figure 6.17G and Figure 6.20G. The disconnection of nanowires would interrupt the current collection step when those materials were measured with CV. 2) The surface of CNT grown from AAO template deposition is hydrophobic. Also, the Ni NPs nucleation step were conducted in oil-phase solution, which may resulted in a more hydrophobic surface of NWs-CNC. The hydrophobic surface would inhibit the redox reaction since the KOH solution cannot properly wet the nanostructures.

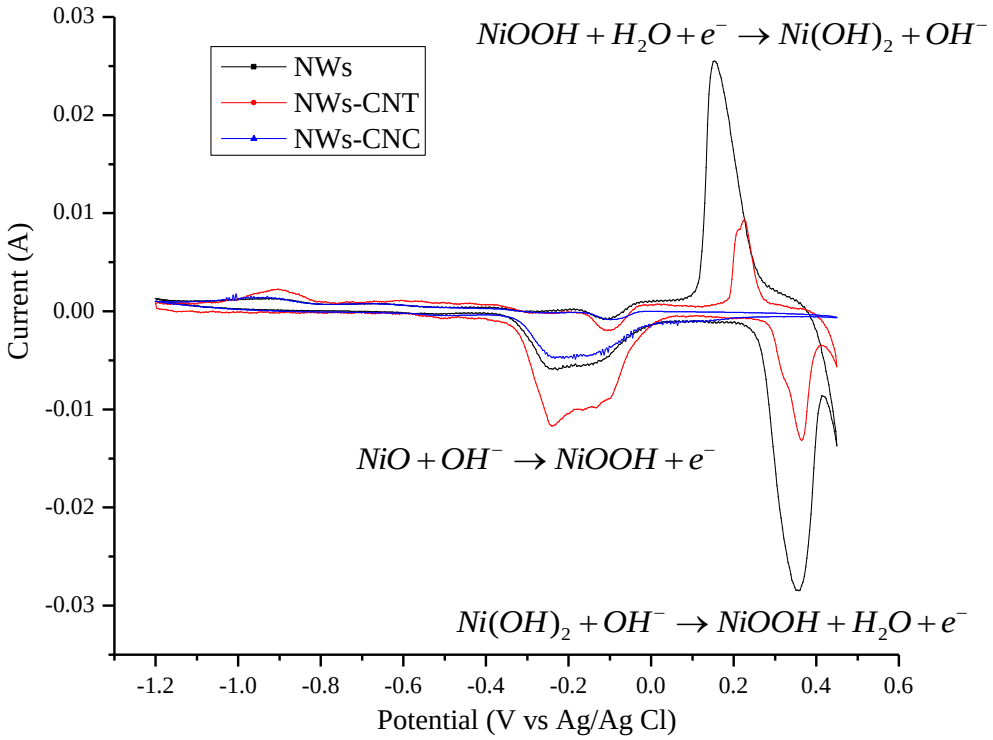

Figure 6.23 Cyclic Voltammetric (CV) measurements for NWs, NWs-CNT, and NWs-CNC heterostructures, reactions were reference[190],[191].

Table 6.2 Capacitances in different concentration of KOH, scan range, and scan rate

Sample	Mass (g)	Concentration of KOH (M)	Scan range (V vs. Ag/AgCl)	Scan Rate (mV/s)	C(F)	C/m (F/g)	C/A (F/cm^2)
NWs	0.0064	9M	-1.2-0.45	100	0.099394	15.53	0.00507
			-1.2-0.45	50	0.132121	20.64	0.00647
			-1.2-0.45	30	0.155556	24.30	0.00793
			-0.3~0.45	30	0.275556	43.06	0.01406
			0~0.45	30	0.437037	68.29	0.02229
			-1.2-0.45	15	0.197980	30.93	0.01010
			-1.2-0.45	5	0.303030	47.34	0.01546
		6M	-1.2-0.45	30	0.139390	21.78	0.00711
		3M	-1.2-0.45	30	0.094949	14.84	0.00484
		1M	-1.1-0.45	30	0.043011	6.72	0.00219
		0.05M	-1.1-0.45	30	0.013937	2.17	0.00071
NWs-CNT	0.0062	9M	-1.2-0.45	100	0.06424	10.36	0.00215
			-1.2-0.45	50	0.08121	13.10	0.00271
			-1.2-0.45	30	0.10707	17.27	0.00358
			-0.3~0.45	30	0.08444	13.62	0.00282
			0~0.45	30	0.11852	19.12	0.00396
			-1.2-0.45	15	0.15757	25.41	0.00527
			-1.2-0.45	5	0.25454	41.05	0.00852
		6M	-1.2-0.45	30	0.09899	15.97	0.00331
		3M	-1.2-0.45	30	0.66667	10.75	0.00231
		1M	-1.1-0.45	30	0.03010	4.86	0.00100
		0.05M	-1.1-0.45	30	0.00105	0.17	0.00003
CNC	0.0125	9M	-1.2-0.45	100	0.02000	1.60	0.00063
			-1.2-0.45	50	0.02545	2.03	0.00081
			-1.2-0.45	30	0.04040	3.23	0.00128
			-0.3~0.45	30	0.00145	0.12	0.00005
			0~0.45	30	0.00405	0.32	0.00013
			-1.2-0.45	15	0.06868	5.49	0.00219
			-1.2-0.45	5	0.12121	9.70	0.00387
		6M	-1.2-0.45	30	0.04848	3.88	0.00152
		3M	-1.2-0.45	30	0.02020	1.61	0.00064
		1M	-1.1-0.45	30	0.01295	1.04	0.00004
		0.05M	-1.1-0.45	30	0.00713	0.57	0.00002

6.6 Conclusions

Vertically aligned metal nanowires comprised of single-, or multi-segment with uniform diameters and micron-scale lengths were fabricated inside anodized aluminum oxide template (AAO) by electrodeposition from their metal salt electrolytes. Two kinds of nanowire-graphite structures were fabricated: graphene shell encapsulated nanowires, and nanowire-carbon nanotube heterostructures.

In case of synthesizing graphene shell on nanowires, the thermal stability of Cu-Au-Cu NWs were studied first by annealing nanowires at different temperature (from 100 ^{o}C to 800 ^{o}C), as well as annealing nanowires at 675 ^{o}C for different duration (from 15 s to 60 min), with the purpose to understand the melting kinetics of metal nanowires. Without protection, the metal nanowires were easily to be sintered or melted when temperature higher than 300 ^{o}C, or been heated at 675 ^{o}C for more than 1 min. This became the biggest challenge for the fabrication of graphene shells encapsulated nanowires. However, since the formation of carbon shell can prevent further melting of nanowires, we were able to produce some graphene shell encapsulated single-segment wire-like hybrid using (Au NWs, Cu NWs, Pd NWs, and Pt NWs). Plasma oxidation and high temperature were identified as key factors for the growth of graphene shell.

The nanowire-carbon nanotube heterostructure was fabricated by chemical vapor deposition within AAO template using Au-Ni nanowires as catalysts, denoted as NWs-CNT heterostructure. The length of nanowires and CNT could be controlled by varying the duration of electrodeposition and CVD growth. After removing AAO template, nickel nanoparticles (diameter ~20 nm) were attached on NWs-CNT heterostructure, mainly on CNT surface, denoted as NWs-CNC heterostructure. The capacitive behavior of NWs, NWs-CNT and NWs-CNC were investigated in 9 M KOH solution using cyclic voltammetry (CV). However, the NWs-CNT and

NWs-CNC heterostructures did not gain better capacitance activity as we expected, due to the disconnection of some Au-Ni nanowires and the hydrophobic property of CNT/CNC.

CHAPTER 7: NANOWIRE-BASED STIMULI-RESPONSIVE POLYMER NANOCOMPOSITES

7.1 Introduction

Here we fabricate vertically aligned and axially heterostructured metal nanowires with uniform diameters and micron-scale lengths inside AAO template in a wet-chemical deposition process. In order to prepare a smart and multi-functional material utilizing these nanowires, they were incorporated into PVA hydrogel that could swell or shrink in presence or absence of water. Those encapsulated materials, whichever has Ni nanowire segment, can be driven by varying magnetic field. Some important parameters of PVA-hydrogel were characterized such as the polymer volume fraction in a swollen/relaxed state ($v_{2,s}$, $v_{2,r}$), the molecular weight of polymer chain between two neighboring crosslinking points ($\overline{M_C}$), and the corresponding mesh size (ξ). A diffusion test was conducted in a U-tube using PVA-hydrogel membrane. The NWs-hydrogel hybrid was utilized for releasing chemical species. Also, the hybrid materials were pyrolysis under high temperature and reserved a carbon shell on the metals' surface.

7.2 Experimental Methods

7.2.1 Materials and Methods

Cupric sulfate pentahydrate ($CuSO_4 \cdot 5H_2O$) and Sodium hydroxide (NaOH), sodium chloride (NaCl) were purchased from Fisher Scientific (New Jersey), Niceklous sulfate 6-hydrate ($NiSO_4 \cdot 6H_2O$) were bought from Mallinckrodt Baker, Inc. (New Jersey). Gold (I) potassium cyanide ($KAu(CN)_2$), Sodium hydrogen carbonate ($NaHCO_3$, 99.7~100.3%), Methyl Orange (MO), Polyethylene glycol 600 (PEG) were purchased from Alfa Aesar (Ward Hill, MA). 3-

mercaptopropyltrimethoxysilane (MPTMS) was bought from TCI America (Portland). L-Histidine (non-animal source), Poly (vinyl alcohol) (PVA, 99+% hydrolyzed, Mw: 89,000-98,000) were purchased from Sigma-Aldrich (St. Louis). Potassium hydroxide (KOH) was bought from Acros Organics (New Jersey). All chemicals were used without further purification. DI water (18.1 MΩ-cm) was obtained using a Barnstead International DI water system (E-pure D4641). Labnet centrifuge (Edison, NJ) was used to wash and separate nanoparticles. Wet samples were dried and stored in a VWR vacuum oven (West Chester, PA).

7.2.2 Synthesis of PVA Hydrogel, and PVA Hydrogel Encapsulated Nanowires

PVA hydrogel was synthesized by the following process: 0.8g Poly (vinyl alcohol) (PVA) was added into 1mL Polyethylene glycol (PEG) + 9ml DI water, then the mixture was heated in 95~100℃ for 1h formed hydrogel solution. Then the solution was poured into Teflon mode and stored in -20℃ fridge for 24 hours. Then hydrogel was immersed in copious DI water for another 24 hours (for releasing experiments samples, escape the water washing step). To make hydrogel encapsulated nanowires, we add nanowires into Teflon mold when hydrogel still was liquid. And the heterostructure materials were obtained after frozen-washing part.

7.2.3 Measurement of Equilibrium Water Content of PVA Hydrogel

The sorption behavior of the PVA hydrogel was analyzed by measurement of equilibrium water content (EWC). Before analysis, hydrogel samples were totally dried in a desiccator at room temperature for a day. The dried hydrogel or hydrogel encapsulated nanowires were weighted, followed by immersing in DI water and measure weight periodically until the hydrated weight remained constant.

7.2.4 Measurement of Polymer volume Fraction

To calculate the polymer volume fractions in the relaxed and in the swollen state, hydrogel was prepared by freezing- thawing process, and immediately weighed in air and n-heptane after 4 h thawing. Then it was placed in copious DI water allowing swollen for 24 h. Once the hydrogel had swelled to equilibrium it was weighed in air and n-heptane again. Finally, the sample was dried at room temperature and re-weighed in air and n-heptane. The volumes of relaxed, swollen and dried polymers can be calculated as given:

$$V_{pol} = (W_{air} - W_{n-heptane}) / \rho_{n-heptane} \qquad (7.1)$$

where W_{air} is the weight of the corresponding polymer in air, $W_{n\text{-}heptane}$ is the weight of the corresponding polymer in n-heptane, and $\rho_{n\text{-}heptane}$ is 0.684 g/mL.

7.2.5 Chemical Releasing

Au-Ni-Cu three segment nanowires were first functionalized with MPTMS (by immersing in 12.4mM MPTMS with reagent alcohol for 24 hours). Then 1µL saturated histidine solution and 45 µL 2.5mM MO solution was added to A) Au-Ni-Cu three segment nanowires; B) Blank PVA hydrogel; and C) Au-Ni-Cu three segment nanowires encapsulated in PVA hydrogel. The nanowires part and PVA hydrogel part were kept the same amount (1 mL in liquid state) for each sample. Each sample was immersed in 10mL DI water for 15min, then add stable magnetic field for 15min. After that, add/remove magnetic field for every 10 seconds. Pick up 2.5mL solution and do UV-vis for every 5 minutes.

7.2.6 Pyrolysis of Nanowire-Hydrogel Hybrid

Pyrolysis of nanowire-hydrogel hybrid was processed in Thermogravimetric Analyzer TGA 7 (Perkin Elmer). Samples were annealed in N_2 atmosphere from room temperature (~25 ^oC) to 700 ^oC at 25 ^oC/min, and then held at 700 ^oC for 3 h. N_2 flow was on in the entire process.

7.2.7 Characterization

Scanning Electron Microscopy (SEM) images were obtained using FE-SEM JEOL-7000 at 20 kV. Tecnai F-20 was used to collect Transmission Electron Microscopy (TEM) images at 200 kV. TEM samples were prepared by dispersing samples on lacey carbon TEM copper grids purchased from Ted Pella Inc. (Redding, CA). X-ray diffraction (XRD) data of samples were recorded with a Philips diffractometer (XRG 3100, Cu Ka radiation, 35mA and 40 kV). Raman data were acquired using a Bruker Senterra Raman microscope (Bruker Optics Inc. Woodlands, TX) with 785nm excitation, a 1200 rulings/mm holographic grating and a CCD detector, with the power at the sample ranging from 10 to 100 mW.

7.3 Measurement of PVA Hydrogel

7.3.1 Equilibrium Water Content of PVA hydrogel

The PVA hydrogel, and hydrogel encapsulated nanowires were totally dried, and then immersed in copious DI water for the sorption behavior study. The weight of each sample was measured until it maintained consistent. The equilibrium water content (EWC) is given by:[192]

$$EWC = \frac{W_t - W_d}{W_t} \times 100\% \qquad (7.2)$$

where W_t is the weight of sample at time t=t during swollen, W_d is weight of dry sample.

All of the samples swelled rapidly at initial 2 h, and reached equilibrium within 8 h (as shown in Figure 7.1A). The swelling data were analyzed with the following equation:[193]

$$M_t / M_\infty = kt^n \tag{7.3}$$

where M_t and M_∞ represent amount of water uptake at times t and ∞, respectively; k is a characteristic constant of the hydrogel, and n is a characteristic exponent of the mode of transport of the penetrating molecule. The constant n was calculated from the slopes of $\ln(M_t/M_\infty)$ against $\ln(t)$. For a polymer film, a value of n=0.5 indicates Fickian diffusion, a value $0.5 < n < 1$ indicates non-Fickian or anomalous transport and n=1 implies relaxation-controlled transport.[97] Figure 7.1B shows fitting lines of $\ln(M_t/M_\infty)$ against $\ln(t)$. The constant n for blank PVA hydrogel, hydrogel encapsulated Ni NWs, Au NWs, Ni-Cu NWs, and Au-Ni-Cu nanowires are 0.53, 0.50, 0.49, 0.54, and 0.56, indicating the rate of diffusion of the penetrant is rate liming step.

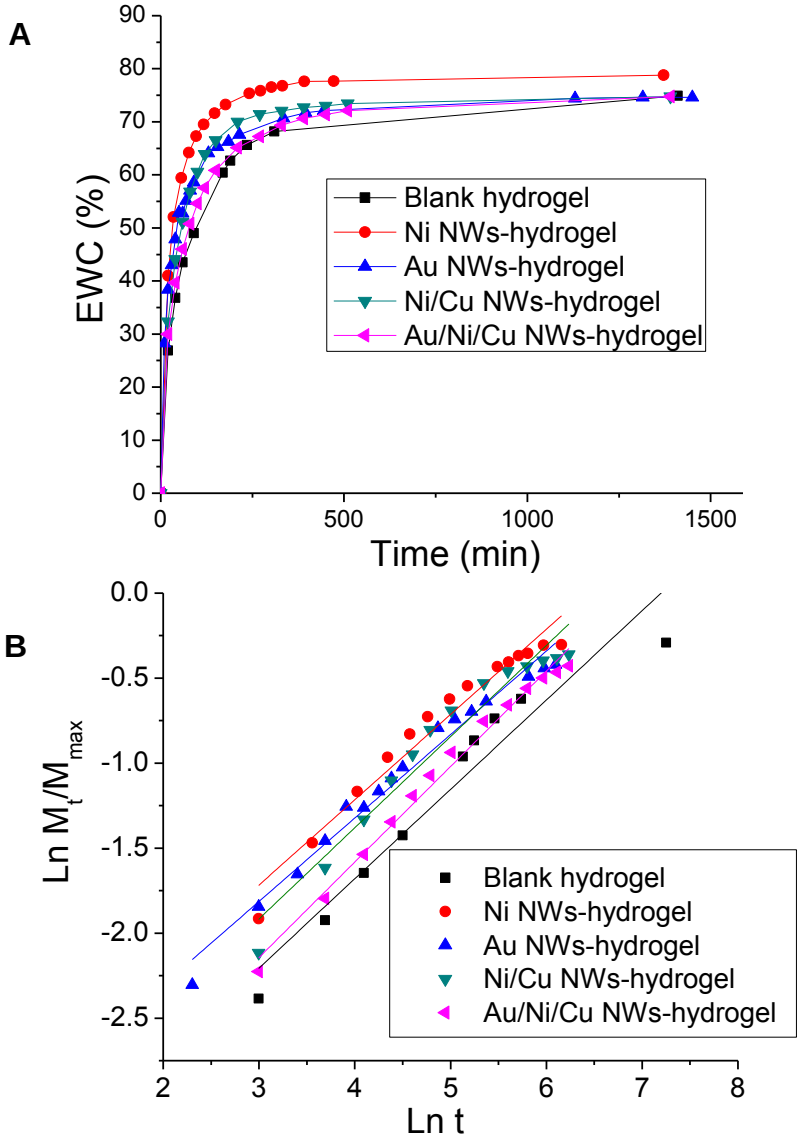

Figure 7.1 (A) EWC for PVA hydrogel and NW-hydrogel hybrid, (B) *Ln t* vs. *Ln* (M_t/M_{max})

7.3.2 Polymer Volume Fraction and Mesh Size measurement

As introduced in the first chapter (Chapter 1.6.3), the polymer volume fraction in a swollen state ($v_{2,s}$), the molecular weight of the polymer chain between two neighboring crosslinking points ($\overline{M_C}$), and the corresponding mesh size (ξ) are the most important parameters for the hydrogel structure characterization. The polymer volume of PVA hydrogel in relaxed-state, swollen-state and dried-state were measured and calculated by Equation 7.1, thus

$$v_{2,s} = V_{pol(dried)} / V_{pol(swollen)} \tag{7.4}$$

$$v_{2,r} = V_{pol(dried)} / V_{pol(relaxed)} \tag{7.5}$$

As calculated $v_{2,s}$=0.1222, $v_{2,r}$=0.1038. The molecular weight between crosslinks ($\overline{M_C}$) was calculated from the swelling data by Equation 1.22, as suggested by Peppas and Merrill.[96] This equation can be applied to systems such as ours that have solvent present during the crosslinking process of the macromolecular chains. We recall Equation 1.22:

$$\frac{1}{\overline{M_C}} = \frac{2}{\overline{M_n}} - \frac{(\frac{\bar{v}}{V_1})[\ln(1-v_{2,s}) + v_{2,s} + \chi_1 v_{2,s}^2]}{v_{2,r}[(\frac{v_{2,s}}{v_{2,r}})^{1/3} - (\frac{v_{2,s}}{2v_{2,r}})]} \tag{1.22}$$

Here $\overline{M_n}$ is the number-average molecular weight of PVA before crosslinking (ca. 50000), $\bar{v}$ is the specific volume of PVA (0.788 cm^3/g), [194] V_1 is the molar volume of water (18.1 cm^3/mol), χ_1 is the PVA-water interaction parameter (0.494).[195] The calculated molecular weight between two adjacent crosslinks $\overline{M_C}$ is ~1385. We then recall Equation 1.27:

$$\xi = v_{2,s}^{-1/3}\left(\frac{2C_n\overline{M_C}}{M_r}\right)^{1/2} l \tag{1.27}$$

Here $\overline{M_C}$ is 1385, $v_{2,s}$ is 0.1222, C_n is the Flory characteristic ratio (8.3) for PVA, M_r is the average of the molecular weights on the repeating units of PVA (44), and l is the carbon-carbon bond length (1.54 Å). The mesh size (ξ), which is also be called pore-size of our PVA hydrogel is ~71Å. It was reported that PVA hydrogel prepared in a similar procedure exhibit a much larger mesh size (6-7 μm), this is attributed to the different PVA we used. The small mesh size of PVA hydrogel may be used for the filtration of large molecules from diffusion.

7.4 Nanowire-PVA Hydrogel Hybrid

7.4.1 Encapsulation of nanowires in PVA hydrogel

Nanowires were encapsulated in PVA hydrogel and form "sandwich" structure NWs-hydrogel hybrid. First of all, some liquid hydrogel solution was casted into Teflon mold and been frozen for 30 min to form jelly-like gel on the bottom of the mold. Then nanowires were placed on top of the jelly-like gel, and more liquid hydrogel was poured on both nanowires and jelly-like gel. The NWs-hydrogel were formed through freezing-thawing process same as blank hydrogel. After been washed in copious DI water to remove excess PEG, the hybrid was dried in air and stored in desiccator. The digital images of swollen-state blank hydrogel and NWs-hydrogel hybrid were shown in Figure 7.2A, and the dried-state NWs-hydrogel were shown in Figure 7.2B. The hydrogel part shrink into a much smaller volume compared to its swollen-state. SEM images of dry-state NWs-hydrogel were shown in Figure 7.2C-F. The SEM samples were prepared by splitting the sandwiched structure. It indicated that nanowires encapsulated in hydrogel can maintain alignment after hydrogel preparation.

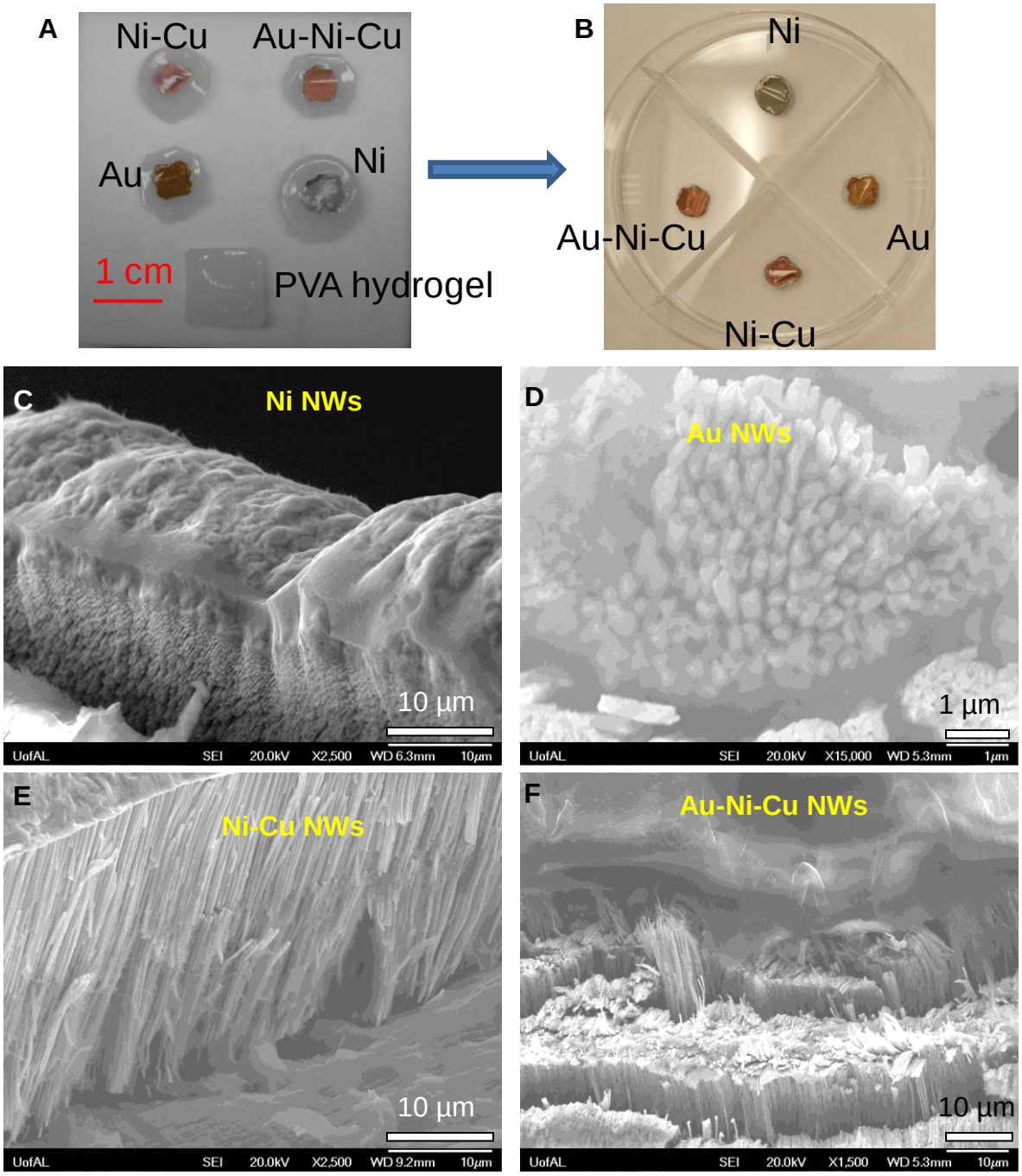

Figure 7.2 Digital image of Nanowires were encapsulated in (A) swollen-state PVA-hydrogel, (B) Dry-state PVA-hydrogel. SEM images show PVA hydrogel encapsulated (C) Ni NWs, (D) Au NWs, (E) Ni-Cu NWs, and (F) Au-Ni-Cu NWs.

7.4.2 Chemical Releasing

A chemical releasing process was demonstrated using PVA hydrogel encapsulated Au-Ni-Cu nanowires. L-histidine (99.67mM, 1μL) and Methyl Orange (MO, 2.5mM, 45 μL) solutions were dropped on nanowires before they were encapsulated with liquid PVA hydrogel. NWs-hydrogel hybrid was fabricated through freezing-throwing process without washing in DI water. After been dried in air, NWs-hydrogel hybrid was immersed in 10 mL DI water. Three chemical releasing samples (A, B, and C) were prepared: A. NWs-hydrogel loaded with L-histidine; B. NW-hydrogel loaded with Methyl Orange; C. NWs-hydrogel loaded with both L-histidine and Methyl Orange. As the hydrogel swollen in water, L-histidine and Methyl Orange would diffuse out (Figure 7.3). If we set $C_{0(histidine)}$ and $C_{0(MO)}$ are the concentration of 1μL 99.67mM L-histidine, 45 μL 2.5mM MO in 10 mL DI water, respectively. Thus,

$$C_{0(histidine)} = \frac{1\mu L}{10mL} \cdot 99.67mM \approx 0.01mM \tag{7.6}$$

$$C_{0(MO)} = \frac{45\mu L}{10mL} \cdot 2.5mM = 0.01125mM \tag{7.7}$$

The chemical releasing was characterized through UV-Vis absorbance using standard lines for L-histidine and Methyl Orange (Figure 7.4). It shows that both L-histidine and Methyl Orange can be released during the swollen process of hydrogel encapsulated nanowires, and the releasing amount would be slightly increased by adding two chemicals (L-histidine and Methyl Red) compared with just loading one chemical (L-histidine or Methyl Red) However, the signal of L-histidine after releasing showed unexpected high, even higher than adding 1 μL, 99.67 mM into 10 mL DI water. We instinctively assumed it is because hydrogel absorbed a large amount of water and make the concentration of L-histidine very high, while the absolute amount of L-histidine still smaller than the loading amount. To verify this assumption, we calculate the

amount of water hydrogel need to absorb. The dried NWs-hydrogel mass is about 0.08g. Within 3 hours releasing test, EWC for PVA hydrogel should be about 60%, which can be represented as:

$$\frac{m_{3h} - 0.08}{m_{3h}} = 0.6 \tag{7.8}$$

Solve Equation 7.8 we have m_{3h}=0.2g, so the amount of water the hydrogel can maximum absorbs within 3 h is:

$$m_{H_2O} = 0.2 - 0.08 = 0.12g \tag{7.9}$$

As we can calculate from the UV-vis result, at the end of releasing, the final concentration of histidine for hydrogel heterostructure with and without anchored MO was 0.018mM and 0.019mM, respectively. Assuming all the histidine we physically anchored in the materials came out into the solution, thus the volume of solution should be 5.56mL and 5.26mL, respectively, corresponding to the hydrogel absorbed water 4.44mL and 4.74mL. Apparently, these calculated absorbed water amounts are much higher than practical value. Considering the hydrogel did not been washed in DI water after frozen process, the excessive polymers (PVA or PEG) left in the hydrogel may released during the experiment, interacted with histidine and increased the signal of histidine.

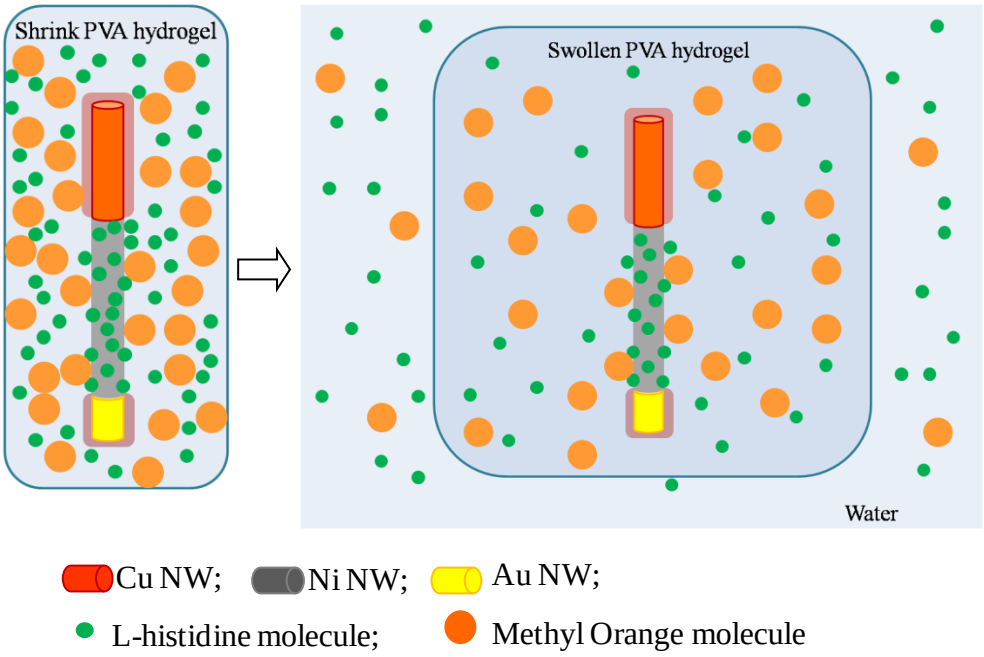

Figure 7.3 Schematic shows chemical releasing process.

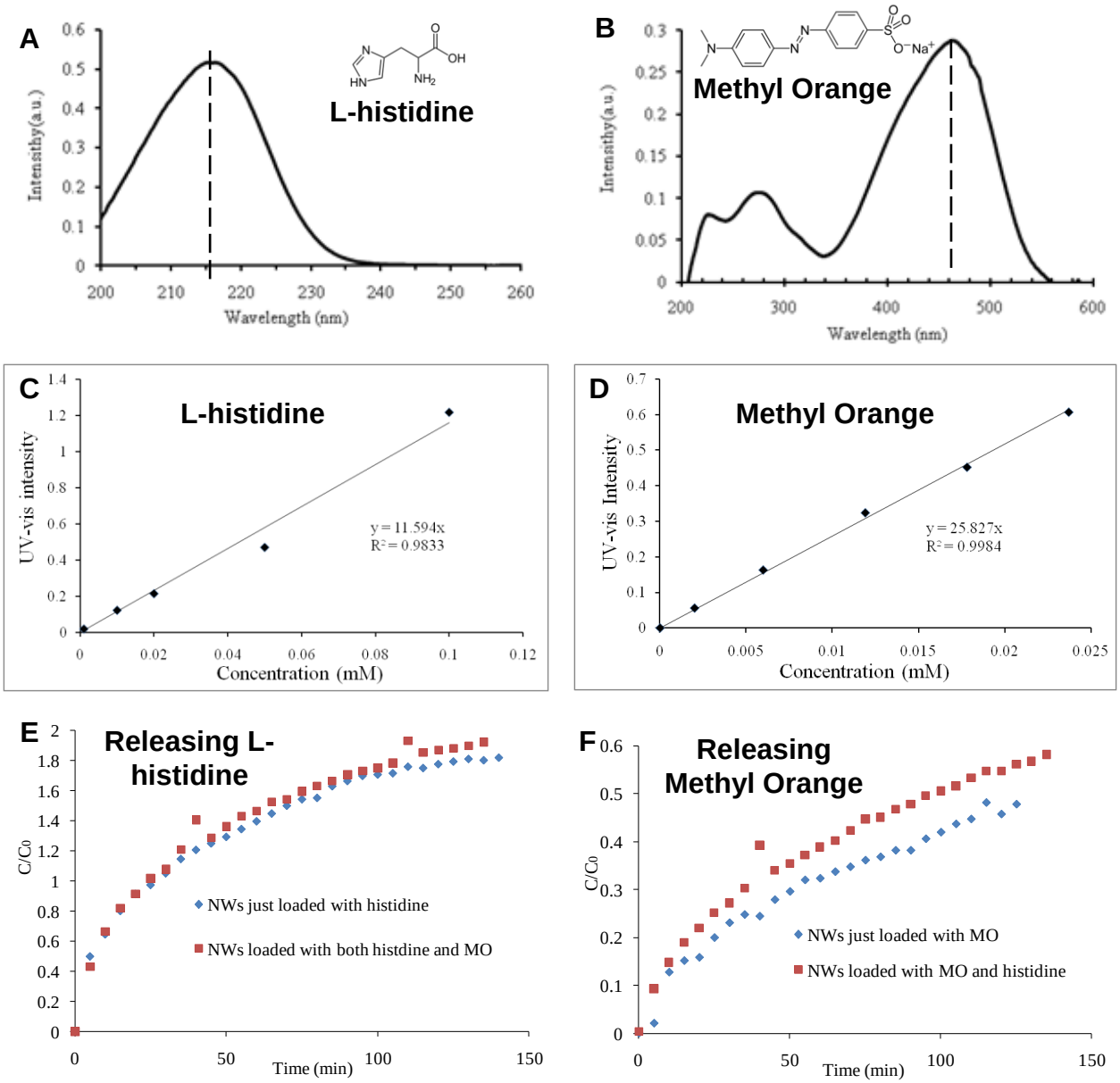

Figure 7.4 Typical UV-Vis spectra show (A) L-histidine and (B) Methyl Orange; Standard line for (C) L-histidine; and (D) Methyl Orange; Releasing kinetics for (E) L-histidine, (F) Methyl Orange.

7.4.3 Carbon shell formation by pyrolysis of NWs-hydrogel hybrid

It has been demonstrate that polymer encapsulated metal, by undergoing a thermal heating process, can transform into graphitic structure (graphene shell) surround the metal.[19,196] In this regard, we are interested to study the pyrolysis behavior of PVA-hydrogel encapsulated nanowires, and expected to produce carbon/graphene shells using this NWs-hydrogel hybrid through the pyrolysis process.

PVA-hydrogel encapsulated Ni NWs, Au NWs, Ni-Cu NWs, and Au-Ni-Cu NWs were synthesized and dried in air for 24 h. Their pyrolysis was done by a TGA instrument in N_2 atmosphere. The temperature was increased from room temperature to 50 ^{o}C and hold for 1 min, followed by increasing temperature to 700 ^{o}C with ramping rate 25 ^{o}C/min. Samples were hold at 700 ^{o}C for 3 h, and then cooled down to room temperature with the protection of N_2. TGA was recorded, and the residual of pyrolysis was collected, characterized by SEM (Figure 7.5). It was shown that, with the protection of hydrogel, nanowires were able to maintain their morphology even undergo 700 ^{o}C for 3 h. The surrounding hydrogel, on the other hand, carbonized into carbon shell and acted as protecting barrier to prevent serious melting of the nanowires. TGA showed the change of samples' weight during pyrolysis process. A small hump at temperature lower than 200 ^{o}C was corresponding to the evaporation of water inside NWs-hydrogel hybrid. The PVA hydrogel decomposed region was shown in temperature range from 250-500 ^{o}C. After pyrolysis, the weight of blank hydrogel was reduced ~95%, while the NWs-hydrogel hybrid reduced less due to the incorporation of nanowires. The pyrolysis samples, especially with Au NWs and Ni NWs presented strong D-, G-band (Figure 7.7), proved the formation of carbon shells around nanowires.

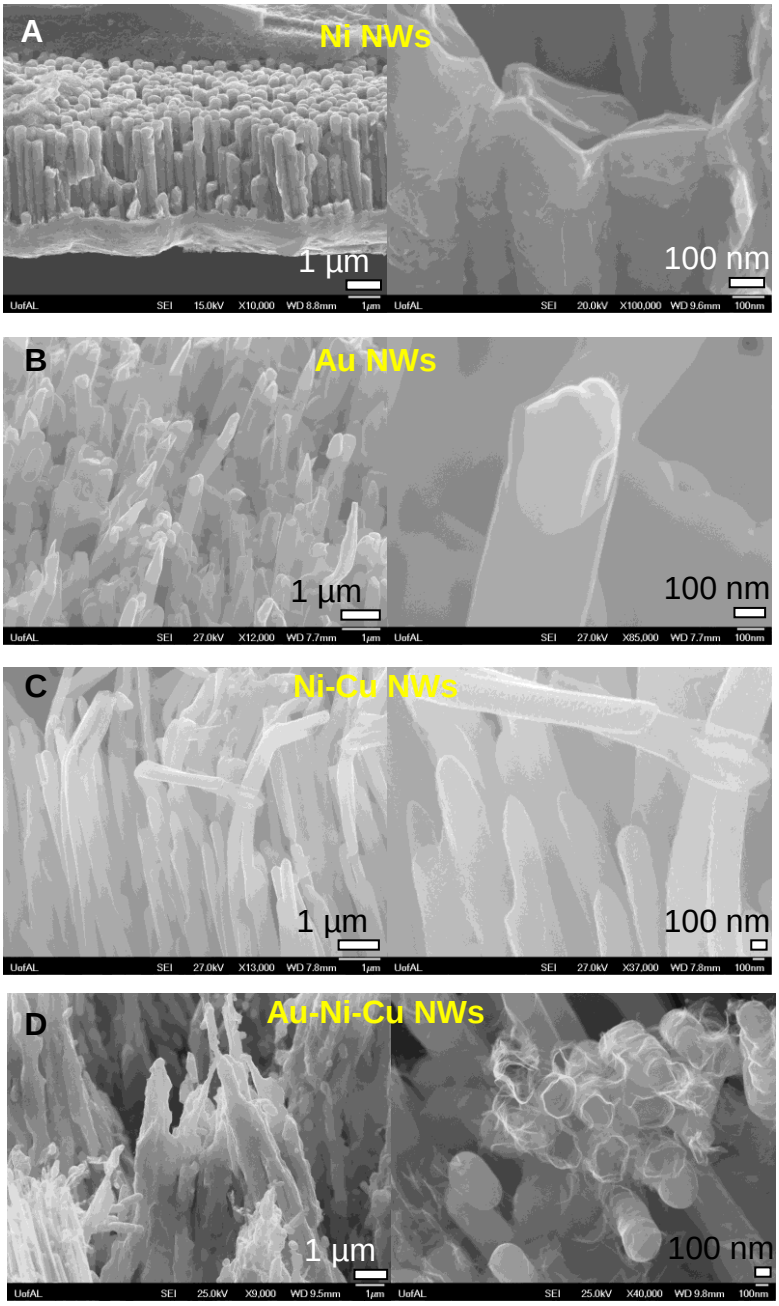

Figure 7.5 SEM images show PVA-hydrogel encapsulated nanowires after pyrolysis at 700 ^{o}C for 3 h, in N_2 atmosphere.

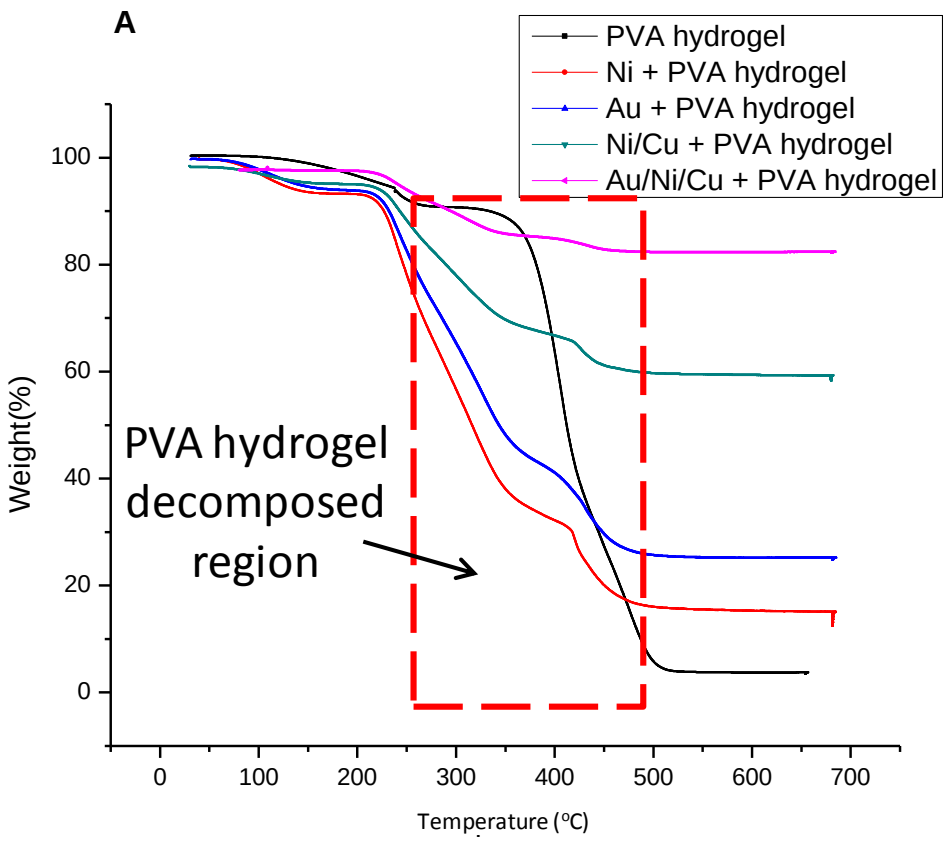

Figure 7.6 TGA showing nanowires-hydrogel hybrid decomposed at high temperature

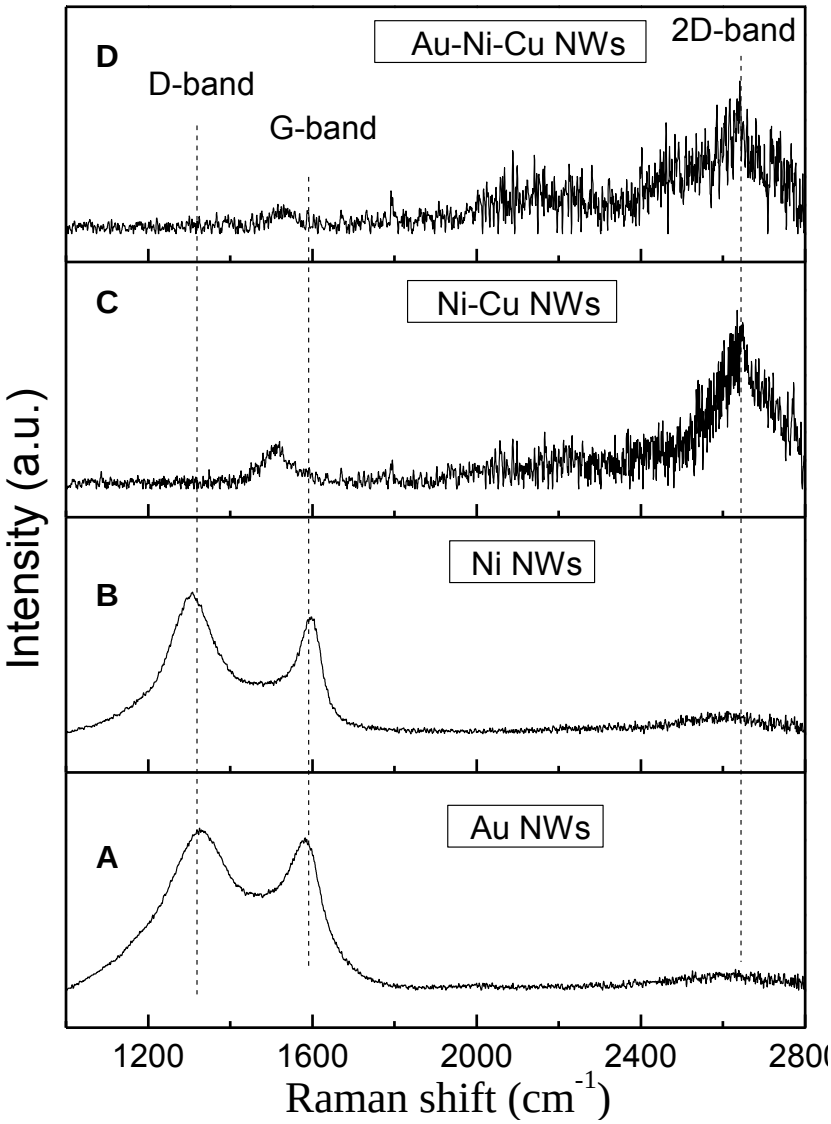

Figure 7.7 Raman spectra show nanowires-hydrogel hybrid after pyrolysis at 700 ^{o}C for 3 h, in N_2 atmosphere.

7.5 Conclusions

PVA hydrogel was fabricated through freezing-thawing process. Three important structural parameters: the polymer volume fraction in a swollen state ($v_{2,s}$), the molecular weight of the polymer chain between two neighboring crosslinking points ($\overline{M_C}$), and the corresponding mesh size (ξ) were measured. The mesh size ξ of synthesized PVA hydrogel was calculated ~ 7 nm, which is relatively small and important in the applications such as chemical releasing and separation. NWs-hydrogel hybrids were prepared in a "sandwiched" architecture. Their EWC indicated water absorbance is a Fickian diffusion process. A chemical releasing process was demonstrated using PVA hydrogel encapsulated Au-Ni-Cu NWs. Finally, the pyrolysis of NWs-hydrogel hybrid was investigated. The hydrogel around nanowires was proved to be able to help nanowires maintain their morphology at high temperature, and carbonized into carbon shell during the pyrolysis process.

CHAPTER 8: CONCLUSIONS AND FUTURE WORK

This dissertation represents a detailed study towards a comprehensive understanding of the mechanism of formation graphene shell encapsulating noble metal nanoparticles and metal nanowires. Various architectures have been built such as graphene shells encapsulated nanoparticles on planar substrate (GNPs for Au, Pd, and C-PtNPs), one-dimensional nanohybrids (multisegment nanowires, NWs-CNTs), nanoparticles decorated 1-D structures (AuNPs formed on CNT by dewetting, NiNPs nucleation on NWs-CNT and form NWs-CNC heterostructure), and NWs-PVA hydrogel heterostructures. However, a number of gaps still exist in our current knowledge. In particular, future work should be directed in the following specific areas:

- In Chapter 2, we observed defects such as twin boundaries, grain boundaries, and vacancies can be induced to AuNPs by a quenching process. A detailed oxidation kinetic study suggested the oxidation process of AuNPs follows Cabrera-Mott model. The influence of defects in AuNPs on graphene shell growth was also been studied. Amorphous carbon shell and relaxed carbon shells were found on defect-induced AuNPs due to ineffective surface oxidation.
- In Chapter 3, we demonstrated the formation of AuNPs-CNT and graphene shells encapsulated AuNPs-CNT, proved their potential in Optical sensing through both DDA modeling and Raman spectra. To maximize their plasmon resonance, a high density dispersion of AuNPs on CNT with small inter-spacing is highly expected. The next step toward application would be further increase the AuNPs dispersion density and stabilize CNT-Au-graphene structure on substrate.

- In Chapter 4, oxidation kinetics of PdNPs was studied by XPS and found to obey Valensi-Carter model, which is applied to diffusion control step and can be used for cracked oxide film. Discrete dipole approximation was performed for PdNPs with different sizes and shapes, as well as graphene shells encapsulated PdNPs with different core-size and shell-thickness. A red-shift of plasmon resonance peak was observed by increasing particle size, which revealed the potential of using PdNPs in optical sensing.
- In Chapter 5, C-PtNPs exhibited excellent stability at high temperature comparing PtNPs without any protection. We proved that C-PtNPs have a better catalytic activity than PtNPs after high temperature annealing. C-PtNPs also showed good recycling ability. To further increase their catalytic performance, a critical step would be reducing their aggregation during graphene shells growth step.
- In Chapter 6, we demonstrate that with appropriate oxidation and temperature, graphene shells can form on nanowires through chemical vapor deposition process. However, in order to utilize the graphene shells encapsulated nanowires as multifunctional sensor (as demonstrated in Figure 8.1), we need to maintain the morphology of nanowires. The possible approach would be utilizing plasma-CVD to reduce graphene shells growth temperature, protection of nanowires using thin layer polymers, or reduce sample heating duration.
- In Chapter 7, PVA hydrogel encapsulated nanowires were fabricated, and a chemical releasing was demonstrated. This heterostructure has the potential to be fabricated into a chemical valve depending on the shrink/swollen state of hydrogel (Figure 8.2). The inter-spacing between encapsulated nanowires can be tuned by the shrink/swollen state of hydrogel. Moreover, the surface of nanowires can be functionalized and results in ionized

groups interact with the environment. A critical step is to remove the back-film of metal-nanowire-arrays formed with nanowires during electrodeposition.

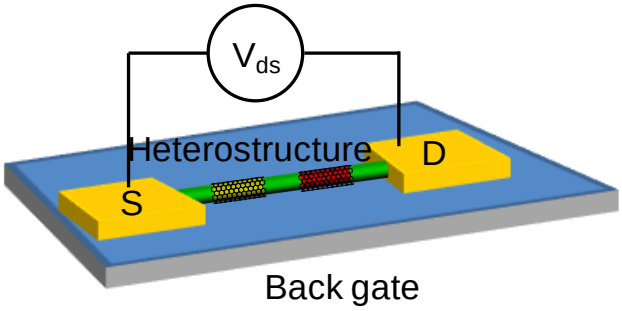

Figure 8.1 Construction of FET using graphene shells encapsulated nanowires

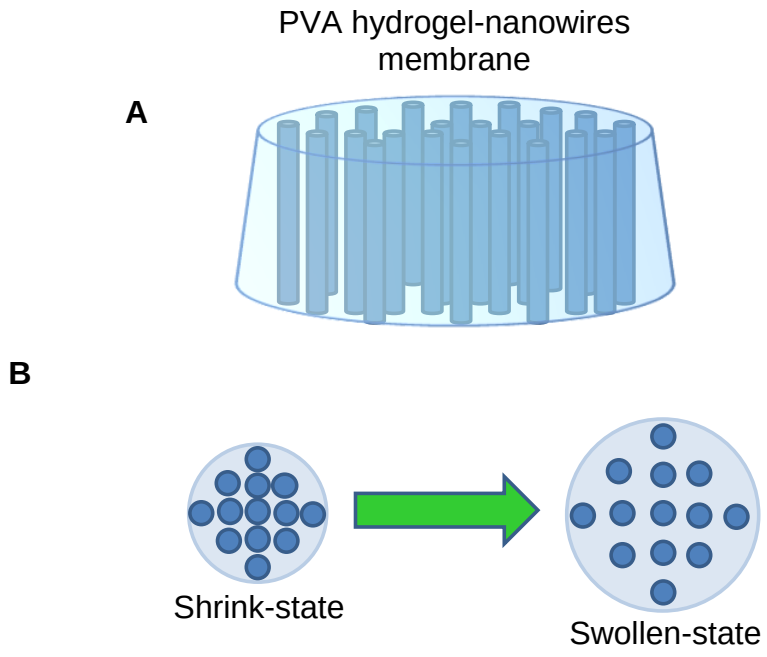

Figure 8.2 (A) A membrane of PVA hydrogel encapsulated vertically aligned nanowires. (B) Schematic shows the switch of inter-spacing of nanowires from close to open by changing the shrink/swollen state of PVA hydrogel.

REFERENCES

[1] Chopra, N.; Bachas, L. G.; Knecht, M. R., Fabrication and Biofunctionalization of Carbon-Encapsulated Au Nanoparticles. *Chemistry of Materials* **2009,** *21*, 1176-1178.

[2] Daniel, M. C.; Astruc, D., Gold nanoparticles: Assembly, supramolecular chemistry, quantum-size-related properties, and applications toward biology, catalysis, and nanotechnology. *Chemical Reviews* **2004,** *104* (1), 293-346.

[3] Lyon, J. L.; Fleming, D. A.; Stone, M. B.; Schiffer, P.; Williams, M. E., Synthesis of Fe Oxide Core/Au shell Nanoparticles by Iterative Hydroxylamine Seeding. *Nano Letters* **2004,** *4*, 719-723.

[4] Kanemitsu, Y.; Ogawa, T.; Shiraishi, K.; Takeda, K., Visible Photoluminescene from Oxidized Si Nanometer-Sized Spheres: Exciton Confinement on a Spherical-Shell. *Physical Review B* **1993,** *48*, 4883-4886.

[5] Cortie, M. B.; McDonagh, A. M. Synthesis and Optical Properties of Hybrid and Alloy Plasmonic Nanoparticles. *Chem. Rev*. **2011**, *111*, 3713-3735.

[6] Newman, J. D. S.; Blanchard, G. J. Formation and Encapsulation of Gold Nanoparticles Using a Polymeric Amine Reducing Agent. *J. Nanopart. Res*. **2007**, *9*, 861–868.

[7] Wang, S. N.; Zhang, M. C.; Zhang, W. Q. Yolk-Shell Catalyst of Single Au Nanoparticle Encapsulated within Hollow Mesoporous Silica Microspheres. *ACS Catal*. **2011**, *1*, 207-211.

[8] Jain, P. K.; Huang, X. H.; El-Sayed, I. H.; El-Sayed, M. A., Noble Metals on the Nanoscale: Optical and Photothermal Properties and Some Applications in Imaging, Sensing, Biology, and Medicine. *Accounts of Chemical Research* **2008,** *41* (12), 1578-1586.

[9] Grunwaldt, J. D.; Kiener, C.; Wogerbauer, C.; Baiker, A., Preparation of supported gold catalysts for low-temperature CO oxidation via "size-controlled" gold colloids. *Journal of Catalysis* **1999,** *181* (2), 223-232.

[10] Karakouz, T.; Holder, D.; Goomanovsky, M.; Vaskevich, A.; Rubinstein, I., Morphology and Refractive Index Sensitivity of Gold Island Films. *Chemistry of Materials* **2009,** *21* (24), 5875-5885.

[11] Doron-Mor, I.; Cohen, H.; Barkay, Z.; Shanzer, A.; Vaskevich, A.; Rubinstein, I., Sensitivity of transmission surface plasmon resonance (T-SPR) spectroscopy: Self-assembled multilayers on evaporated gold island films. *Chemistry-a European Journal* **2005,** *11* (19), 5555-5562.

[12] Tesler, A. B.; Chuntonov, L.; Karakouz, T.; Bendikov, T. A.; Haran, G.; Vaskevich, A.; Rubinstein, I., Tunable Localized Plasmon Transducers Prepared by Thermal Dewetting of Percolated Evaporated Gold Films. *Journal of Physical Chemistry C* **2011,** *115* (50), 24642-24652.

[13] Jia, J.; Seraphin, S. Carbon Encapsulated Nanoparticles of Ni, Co, Cu, and Ti. *J. Appl. Phys.* **1998**, 83, 2442−2448.

[14] Nagatsu, M.; Yoshida, T.; Mesko, M.; Ogino, A.; Matsuda, T.; Tanaka, T.; Tatsuoka, H.; Murakami, K. Narrow Multi-Walled Carbon Nanotubes Produced by Chemical Vapor Deposition Using Graphene Layer Encapsulated Catalytic Metal Particles. *Carbon* **2006,** 44, 3336−3341.

[15] Takagi, D.; Kobayashi, Y.; Hibino, H.; Suzuki, S.; Homma, Y. Mechanism of Gold-Catalyzed Carbon Material Growth. *Nano Lett*. **2008,** 8, 832−835.

[16] Sutter, E.; Sutter, P.; Zhu, Y. Assembly and Interaction of Au/C Core-Shell Nanostructures: In Situ Observation in the Transmission Electron Microscope. *Nano Lett*. **2005,** 5, 2092−2096.

[17] Ugarte, D. How To Fill and Empty a Graphitic Onion. *Chem. Phys. Lett*. **1993,** 209, 99−103.

[18] Banhart, F.; Redlich, P.; Ajayan, P. M. The Migration of Metal Atoms Through Carbon Onions. *Chem. Phys. Lett*. **1998,** 292, 554−560.

[19] Hore, S.; Kaiser, G.; Hu, Y.-S.; Schulz, A.; Konuma, M.; Gotz, G.; Sigle, W.; Verhoeven, A.; Maier, J. Carbonization of Polyethylene on Gold Oxide. *J. Mater. Chem*. **2008,** 18, 5589−5591.

[20] Saito, Y.; Nishikubo, K.; Kawabata, K.; Matsumoto, T., Carbon nanocapsules and single-layered nanotubes produced with platinum-group metals (Ru, Rh, Pd, Os, Ir, Pt) by arc discharge. *Journal of Applied Physics* **1996,** *80* (5), 3062-3067.

[21] Wang, Y., Encapsulation of palladium crystallites in carbon and the formation of wormlike nanostructures. *Journal of the American Chemical Society* **1994,** *116* (1), 397-398.

[22] Kang, W.; Li, H.; Yan, Y.; Xiao, P.; Zhu, L.; Tang, K.; Zhu, Y.; Qian, Y., Worm-Like Palladium/Carbon Core-Shell Nanocomposites: One-Step Hydrothermal Reduction-Carbonization Synthesis and Electrocatalytic Activity. *Journal of Physical Chemistry C* **2011,** *115* (14), 6250-6256.

[23] Harada, T.; Ikeda, S.; Hashimoto, F.; Sakata, T.; Ikeue, K.; Torimoto, T.; Matsumura, M., Catalytic Activity and Regeneration Property of a Pd Nanoparticle Encapsulated in a Hollow Porous Carbon Sphere for Aerobic Alcohol Oxidation. *Langmuir* **2010,** *26* (22), 17720-17725.

[24] Ge, X.; Peng, B.; Ying, X.; Wang, R.; Liu, X.; Xiao, F.; Qiu, S.; Li, J., In-situ transmission electron microscopy observation of particle size effect of nanoscale platinum catalysts on the formation of fullerenelike carbon shells. *Carbon* **2008,** *46* (11), 1411-1416.

[25] Ikeda, S.; Ishino, S.; Harada, T.; Okamoto, N.; Sakata, T.; Mori, H.; Kuwabata, S.; Torimoto, T.; Matsumura, M., Ligand-free platinum nanoparticles encapsulated in a hollow porous carbon shell as a highly active heterogeneous hydrogenation catalyst. *Angewandte Chemie-International Edition* **2006,** *45* (42), 7063-7066.

[26] Wu, Z.; Lv, Y.; Xia, Y.; Webley, P. A.; Zhao, D., Ordered Mesoporous Platinum@Graphitic Carbon Embedded Nanophase as a Highly Active, Stable, and Methanol-Tolerant Oxygen Reduction Electrocatalyst. *Journal of the American Chemical Society* **2012,** *134* (4), 2236-2245.

[27] Ng, Y. H.; Ikeda, S.; Harada, T.; Higashida, S.; Sakata, T.; Mori, H.; Matsumura, M., Fabrication of hollow carbon nanospheres encapsulating platinum nanoparticles using a photocatalytic reaction. *Advanced Materials* **2007,** *19* (4), 597-601.

[28] Wu, J.; Chopra, N. Graphene Encapsulated Gold Nanoparticles and Their Characterization. *Processing of Nanoparticle Materials and Nanostructured Films*. **2010**, 223, 1−7.

[29] Wu, J.; Shi, W.; Chopra, N., Plasma Oxidation Kinetics of Gold Nanoparticles and Their Encapsulation in Graphene Shells by Chemical Vapor Deposition Growth. *Journal of Physical Chemistry C* **2012,** *116* (23), 12861-12874.

[30] Bhaviripudi, S.; Mile, E.; Steiner, S. A., III; Zare, A. T.; Dresselhaus, M. S.; Belcher, A. M.; Kong, J. CVD Synthesis of Single-Walled Carbon Nanotubes from Gold Nanoparticle Catalysts. *J. Am. Chem. Soc*. **2007**, 129, 1516−1517.

[31] Zhdanov, V. P.; Kasemo, B., Cabrera-Mott kinetics of oxidation of nm-sized metal particles. *Chemical Physics Letters* **2008,** *452* (4-6), 285-288.

[32] Fromhold, A. T., Growth-Rate of Low-Space-Charge Oxides on Spherical Metal Particles. *Journal of Physics and Chemistry of Solids* **1988,** *49* (10), 1159-1166.

[33] Carter, R. E.; Kinetic Model for Solid-State Reactions. *Journal of Chemical Physics* **1961**, *34* (6), 2010-2015.

[34] Shimada, E.; Yamashita, H.; Matsumoto, S.; Ikuma, Y.; Ichimura, H., The oxidation kinetics of spherically shaped palladium powder. *Journal of Materials Science* **1999,** *34* (16), 4011-4015.

[35] Hao, E.; Schatz, G. C., Electromagnetic fields around silver nanoparticles and dimers. *Journal of Chemical Physics* **2004,** *120* (1), 357-366.

[36] Gonzalez-Diaz, J. B.; Garcia-Martin, A.; Garcia-Martin, J. M.; Cebollada, A.; Armelles, G.; Sepulveda, B.; Alaverdyan, Y.; Kall, M., Plasmonic Au/Co/Au nanosandwiches with enhanced magneto-optical activity. *Small* **2008,** *4* (2), 202-205.

[37] Draine, B. T.; Flatau P. J., Discrete-Dipole Approximation for Periodic Targets: Theory and Tests. *Journal of the Optical Society of America A* **2008**, *25* (11), 2693-2703.

[38] Draine, B. T.; Flatau P. J., Discrete-Dipole Approximation for scattering calculations. *Journal of the Optical Society of America A* **1994**, *4* (11), 1491-1499.

[39] Kolmakov, A.; Moskovits, M., Chemical sensing and catalysis by one-dimensional metal-oxide nanostructures. *Annual Review of Materials Research* **2004,** *34*, 151-180.

[40] Sailor, M. J.; Link, J. R., "Smart dust": nanostructured devices in a grain of sand. *Chemical Communications* **2005,** (11), 1375-1383.

[41] Lu, Y.; Chen, S. C., Micro and nano-fabrication of biodegradable polymers for drug delivery. *Advanced Drug Delivery Reviews* **2004,** *56* (11), 1621-1633.

[42] Hannon, J. B.; Kodambaka, S.; Ross, F. M.; Tromp, R. M., The influence of the surface migration of gold on the growth of silicon nanowires. *Nature* **2006,** *440* (7080), 69-71.

[43] Gao, J. X.; Bender, C. M.; Murphy, C. J., Dependence of the gold nanorod aspect ratio on the nature of the directing surfactant in aqueous solution. *Langmuir* **2003,** *19* (21), 9065-9070.

[44] Martin, C. R., Membrane-based synthesis of nanomaterials. *Chemistry of Materials* **1996,** *8* (8), 1739-1746.

[45] Rogers, J. A.; Paul, K. E.; Jackman, R. J.; Whitesides, G. M., Using an elastomeric phase mask for sub-100 nm photolithography in the optical near field. *Applied Physics Letters* **1997,** *70* (20), 2658-2660.

[46] Chik, H.; Xu, J. M., Nanometric superlattices: non-lithographic fabrication, materials, and prospects. *Materials Science & Engineering R-Reports* **2004,** *43* (4), 103-138.

[47] Martin, C. R., Nanometarials- A Memberane-Based Synthetic Approach. *Science* **1994,** *266* (5193), 1961-1966.

[48] Skinner, K.; Dwyer, C.; Washburn, S., Selective functionalization of arbitrary nanowires. *Nano Letters* **2006,** *6* (12), 2758-2762.

[49] Chopra, N., Multifunctional and multicomponent heterostructured one-dimensional nanostructures: advances in growth, characterisation, and applications. *Materials Technology* **2010,** *25* (3-4), 212-230.

[50] Bellino, M. G.; Calvo, E. J.; Gordillo, G. J., Nanowire manipulation on surfaces through electrostatic self-assembly and magnetic interactions. *Physica Status Solidi-Rapid Research Letters* **2009,** *3* (1), 1-3.

[51] Guo, Y. G.; Wan, L. J.; Zhu, C. F.; Yang, D. L.; Chen, D. M.; Bai, C. L., Ordered Ni-Cu nanowire array with enhanced coercivity. *Chemistry of Materials* **2003,** *15* (3), 664-667.

[52] Tresback, J. S.; Vasiliev, A. L.; Padture, N. P.; Park, S. Y.; Berger, P. R., Characterization and electrical properties of individual Au-NiO-Au heterojunction nanowires. *Ieee Transactions on Nanotechnology* **2007,** *6* (6), 676-681.

[53] Wang, J. G.; Tian, M. L.; Kumar, N.; Mallouk, T. E., Controllable template synthesis of superconducting Zn nanowires with different microstructures by electrochemical deposition. *Nano Letters* **2005,** *5* (7), 1247-1253.

[54] Schonenberger, C.; vanderZande, B. M. I.; Fokkink, L. G. J.; Henny, M.; Schmid, C.; Kruger, M.; Bachtold, A.; Huber, R.; Birk, H.; Staufer, U., Template synthesis of nanowires in porous polycarbonate membranes: Electrochemistry and morphology. *Journal of Physical Chemistry B* **1997,** *101* (28), 5497-5505.

[55] Wang, X.; Ozkan, C. S., Multisegment Nanowire Sensors for the Detection of DNA Molecules. *Nano Letters* **2008,** *8*, 398-404.

[56] Wang, D.; Qian, F.; Yang, C.; Zhong, Z. H.; Lieber, C. M., Rational Growth of Branched and Hyperbranched Nanowire Structures. *Nano Letters* **2004,** *4*, 871-874.

[57] Wang, D. L.; Lieber, C. M., Inorganic Materials - Nanocrystals Branch out. *Nature Materials* **2003,** *2*, 355-356.

[58] Wang, H.; Wang, X.; Zhang, X.; Qin, X.; Zhao, Z.; Miao, Z.; Huang, N.; Chen, Q., A Novel Glucose Biosensor Based on the Immobilization of Glucose Oxidase onto Gold Nanoparticles-Modified Pb Nanowires. *Biosensors & Bioelectronics* **2009,** *25*, 142-146.

[59] Nirmal, M.; Brus, L., Luminescence Photophysics in Semiconductor Nanocrystals. *Accounts of Chemical Research* **1999,** *32*, 407-414.

[60] Lauhon, L. J.; Gudiksen, M. S.; Wang, C. L.; Lieber, C. M., Epitaxial Core-Shell and Core-Multishell Nanowire Heterostructures. *Nature* **2002,** *420*, 57-61.

[61] Geim, A. K.; Novoselov, K. S., The rise of graphene. *Nature Materials* **2007,** *6* (3), 183-191.

[62] Eda, G.; Fanchini, G.; Chhowalla, M., Large-area ultrathin films of reduced graphene oxide as a transparent and flexible electronic material. *Nature Nanotechnology* **2008,** *3* (5), 270-274.

[63] Balandin, A. A.; Ghosh, S.; Bao, W.; Calizo, I.; Teweldebrhan, D.; Miao, F.; Lau, C. N., Superior thermal conductivity of single-layer graphene. *Nano Letters* **2008,** *8* (3), 902-907.

[64] Vickery, J. L.; Patil, A. J.; Mann, S., Fabrication of Graphene-Polymer Nanocomposites With Higher-Order Three-Dimensional Architectures. *Advanced Materials* **2009,** *21* (21), 2180-2184.

[65] Novoselov, K. S.; Geim, A. K.; Morozov, S. V.; Jiang, D.; Zhang, Y.; Dubonos, S. V.; Grigorieva, I. V.; Firsov, A. A., Electric field effect in atomically thin carbon films. *Science* **2004,** *306* (5696), 666-669.

[66] Kosynkin, D. V.; Higginbotham, A. L.; Sinitskii, A.; Lomeda, J. R.; Dimiev, A.; Price, B. K.; Tour, J. M., Longitudinal unzipping of carbon nanotubes to form graphene nanoribbons. *Nature* **2009,** *458* (7240), 872- 876.

[67] Gao, W.; Alemany, L. B.; Ci, L. J.; Ajayan, P. M., New insights into the structure and reduction of graphite oxide. *Nature Chemistry* **2009,** *1* (5), 403-408.

[68] Bae, S.; Kim, H.; Lee, Y.; Xu, X. F.; Park, J. S.; Zheng, Y.; Balakrishnan, J.; Lei, T.; Kim, H. R.; Song, Y. I.; Kim, Y. J.; Kim, K. S.; Ozyilmaz, B.; Ahn, J. H.; Hong, B. H.; Iijima, S., Roll-to-roll production of 30-inch graphene films for transparent electrodes. *Nature Nanotechnology* **2010,** *5* (8), 574-578.

[69] Han, T. H.; Lee, W. J.; Lee, D. H.; Kim, J. E.; Choi, E.-Y.; Kim, S. O., Peptide/Graphene Hybrid Assembly into Core/Shell Nanowires. *Advanced Materials* **2010,** *22* (18), 2060-2064.

[70] Reches, M.; Gazit, E., Casting metal nanowires within discrete self-assembled peptide nanotubes. *Science* **2003,** *300* (5619), 625-627.

[71] Han, T. H.; Kim, J.; Park, J. S.; Park, C. B.; Ihee, H.; Kim, S. O., Liquid crystalline peptide nanowires. *Advanced Materials* **2007,** *19* (22), 3924-3927.

[72] Kim, S.-W.; Han, T. H.; Kim, J.; Gwon, H.; Moon, H.-S.; Kang, S.-W.; Kim, S. O.; Kang, K., Fabrication and Electrochemical Characterization of TiO2 Three-Dimensional Nanonetwork Based on Peptide Assembly. *Acs Nano* **2009,** *3* (5), 1085-1090.

[73] Yang, Z. H.; Li, Z. F.; Wu, H. Q.; Simard, B., Effects of doped copper on electrochemical performance of the raw carbon nanotubes anode. *Materials Letters* **2003,** *57* (21), 3160-3166.

[74] Kitaura, R.; Nakanishi, R.; Saito, T.; Yoshikawa, H.; Awaga, K.; Shinohara, H., High-Yield Synthesis of Ultrathin Metal Nanowires in Carbon Nanotubes. *Angewandte Chemie-International Edition* **2009,** *48* (44), 8298-8302.

[75] Chang, Y.; Lye, M. L.; Zeng, H. C., Large-scale synthesis of high-quality ultralong copper nanowires. *Langmuir* **2005,** *21* (9), 3746-3748.

[76] Deng, B.; Xu, A.-W.; Chen, G.-Y.; Song, R.-Q.; Chen, L., Synthesis of copper-core/carbon-sheath nanocables by a surfactant-assisted hydrothermal reduction/carbonization process. *Journal of Physical Chemistry B* **2006,** *110* (24), 11711-11716.

[77] Zhang, G. Y.; Wang, E. G., Cu-filled carbon nanotubes by simultaneous plasma-assisted copper incorporation. *Applied Physics Letters* **2003,** *82* (12), 1926-1928.

[78] Zhao, Y.; Zhang, Y.; Li, Y.; Yan, Z., A flexible chemical vapor deposition method to synthesize copper@carbon core-shell structured nanowires and the study of their structural electrical properties. *New Journal of Chemistry* **2012,** *36* (5), 1161-1169.

[79] Wang, R.; Hao, Y.; Wang, Z.; Gong, H.; Thong, J. T. L., Large-Diameter Graphene Nanotubes Synthesized Using Ni Nanowire Templates. *Nano Letters* **2010,** *10* (12), 4844-4850.

[80] Hinds, B. J.; Chopra, N.; Rantell, T.; Andrews, R.; Gavalas, V.; Bachas, L. G., Aligned multiwalled carbon nanotube membranes. *Science* **2004,** *303* (5654), 62-65.

[81] Andrews, R.; Jacques, D.; Rao, A. M.; Derbyshire, F.; Qian, D.; Fan, X.; Dickey, E. C.; Chen, J., Continuous production of aligned carbon nanotubes: a step closer to commercial realization. *Chemical Physics Letters* **1999,** *303* (5-6), 467-474.

[82] Fan, S. S.; Chapline, M. G.; Franklin, N. R.; Tombler, T. W.; Cassell, A. M.; Dai, H. J., Self-oriented regular arrays of carbon nanotubes and their field emission properties. *Science* **1999,** *283* (5401), 512-514.

[83] Hu, J. T.; Ouyang, M.; Yang, P. D.; Lieber, C. M., Controlled growth and electrical properties of heterojunctions of carbon nanotubes and silicon nanowires. *Nature* **1999,** *399* (6731), 48-51.

[84] Luo, J.; Zhu, J.; Huang, Z.; Zhang, L., Arrays of Ni nanowire/multiwalled carbon nanotube/amorphous carbon nanotube heterojunctions containing Schottky contacts. *Applied Physics Letters* **2007,** *90* (3), 033114/1-033114/3.

[85] Che, G. L.; Lakshmi, B. B.; Fisher, E. R.; Martin, C. R., Carbon nanotubule membranes for electrochemical energy storage and production. *Nature* **1998,** *393* (6683), 346-349.

[86] An, K. H.; Kim, W. S.; Park, Y. S.; Moon, J. M.; Bae, D. J.; Lim, S. C.; Lee, Y. S.; Lee, Y. H., Electrochemical properties of high-power supercapacitors using single-walled carbon nanotube electrodes. *Advanced Functional Materials* **2001,** *11* (5), 387-392.

[87] Burke, A., Ultracapacitors: why, how, and where is the technology. *Journal of Power Sources* **2000,** *91* (1), 37-50.

[88] Shaijumon, M. M.; Ou, F. S.; Ci, L. J.; Ajayan, P. M., Synthesis of hybrid nanowire arrays and their application as high power supercapacitor electrodes. *Chemical Communications* **2008,** (20), 2373-2375.

[89] Ou, F. S.; Shaijumon, M. M.; Ajayan, P. M., Controlled manipulation of giant hybrid inorganic nanowire assemblies. *Nano Letters* **2008,** *8* (7), 1853-1857.

[90] Slaughter, B. V.; Khurshid, S. S.; Fisher, O. Z.; Khademhosseini, A.; Peppas, N. A., Hydrogels in Regenerative Medicine. *Advanced Materials* **2009,** *21* (32-33), 3307-3329.

[91] Nel, A.; Xia, T.; Madler, L.; Li, N., Toxic Potential of Materials at the Nanolevel. *Science* **2006,** *311*, 622-627.

[92] Qiu, Y.; Park, K., Environment-Sensitive Hydrogels for Drug Delivery. *Advanced Drug Delivery Reviews* **2001,** *53*, 321-339.

[93] Hribar, K. C.; Lee, M. H.; Lee, D.; Burdick, J. A., Enhanced Release of Small Molecules from Near-Infrared Light Responsive Polymer-Nanorod Composites. *Acs Nano* **2011,** *5*, 2948-2956.

[94] Ogoshi, T.; Takashima, Y.; Yamaguchi, H.; Harada, A., Chemically-Responsive Sol-Gel Transition of Supramolecular Single-Walled Carbon Nanotubes (SWNTs) Hydrogel Made by Hybrids of SWNTs and Cyclodextrins. *Journal of the American Chemical Society* **2007,** *129*, 4878-4879.

[95] Hishiya, T.; Asanuma, H.; Komiyama, M., Spectroscopic Anatomy of Molecular-Imprinting of Cyclodextrin. Evidence for Preferential Formation of Ordered Cyclodextrin Assemblies. *Journal of the American Chemical Society* **2002,** *124*, 570-575.

[96] Peppas, N. A.; Hilt, J. Z.; Khademhosseini, A.; Langer, R., Hydrogels in biology and medicine: From molecular principles to bionanotechnology. *Advanced Materials* **2006,** *18* (11), 1345-1360.

[97] Ruiz, J.; Mantecon, A.; Cadiz, V., Synthesis and properties of hydrogels from poly (vinyl alcohol) and ethylenediaminetetraacetic dianhydride. *Polymer* **2001,** *42* (15), 6347-6354.

[98] Gudiksen, M. S.; Lauhon, L. J.; Wang, J.; Smith, D. C.; Lieber, C. M. Growth of Nanowire Superlattice Structures for Nanoscale Photonics and Electronics. *Nature*. **2002**, *415*, 617-620.

[99] Grier, D. G., A Revolution in Optical Manipulation. *Nature* **2003,** *424*, 810-816.

[100] Moos, R., A Brief Overview on Automotive Exhaust Gas Sensors Based on Electroceramics. *International Journal of Applied Ceramic Technology* **2005,** *2*, 401-413.

[101] Christofides, C.; Mandelis, A., Solid-State Sensors for Trace Hydrogen Gas-Detection. *Journal of Applied Physics* **1990,** *68*, R1-R30.

[102] Zhou, Y.; Wang, S.; Ding, B.; Yang, Z. Preparation of Onion-Like Pd–Bi–Au/C Trimetallic Catalyst and their Application. *J. Sol-Gel. Sci. Techn.* **2008**, *47*, 182-186.

[103] Tang, S.; Zhu, S.; Lu, H.; Meng, X. Shape Evolution and Thermal Stability of Ag Nanoparticles on Spherical SiO2 Substrates. *J. Solid State Chem.* **2008**, *181*, 587–592.

[104] Aharoni, A.; Mokari, T.; Popov, I.; Banin, U. Synthesis of InAs/CdSe/ZnSe Core/Shell1/Shell2 Structures with Bright and Stable Near-Infrared Fluorescence. *J. Am. Chem. Soc.* **2006**, *128*, 257–264.

[105] Chopra, N.; Claypoole, L.; Bachas, L. G. Morphological Control of Ni/NiO Core/Shell Nanoparticles and Production of Hollow NiO Nanostructures. *J. Nanopart. Res.* **2010**, *12*, 2883-2893.

[106] Cornell, B. A.; BraachMaksvytis, V. L. B.; King, L. G.; Osman, P. D. J.; Raguse, B.; Wieczorek, L.; Pace, R. J., A Biosensor that Uses Ion-Channel Switches. *Nature* **1997,** *387*, 580-583.

[107] Wong, Y. M.; Kang, W. P.; Davidson, J. L.; Wisitsora-at, A.; Soh, K. L., A Novel Microelectronic Gas Sensor Utilizing Carbon Nanotubes for Hydrogen Gas Detection. *Sensors and Actuators B-Chemical* **2003,** *93*, 327-332.

[108] Kong, J.; Chapline, M. G.; Dai, H. J., Functionalized Carbon Nanotubes for Molecular Hydrogen Sensors. *Advanced Materials* **2001,** *13*, 1384-1386.

[109] Caruso, F., Nanoengineering of Particle Surfaces. *Advanced Materials* **2001,** *13*, 11-22.

[110] Powell, C. J.; Jablonski, A.; Tilinin, I. S.; Tanuma, S.; Penn, D. R., Surface Sensitivity of Auger-Electron Spectroscopy and X-ray Photoelectron Spectroscopy. *J. Electron Spectrosc.* **1999,** *99*, 1-15.

[111] Shi, H.; Asahi, R.; Stampfl, C. Properties of the Gold Oxides Au_2O_3 and Au_2O: First-Principles Investigation. *Phys. Rev. B* **2007**, *75*, 205125/1-205125/8.

[112] Jones, P. G.; Rumpel, H.; Schwarzmann, E.; Sheldrick, G. M.; Paulus, H., Gold (III) Oxide. *Acta. Crystallogr. B* **1979,** *35*, 1435-1437.

[113] Harris, J. W.; Stocker, H. Spherical Segment (Spherical Cap) in *Handbook of Mathematics and Computational Science.* Springer-Verlag: New York, 1998; pp 107.

[114] Niklasson, G. A.; Karmhag, R. Oxidation Kinetics of Metallic Nanoparticles. *Surf. Sci*. **2003**, *532*-535, 324-327.

[115] Tsai, H. C.; Hu, E.; Perng, K.; Chen, M. K.; Wu, J. C.; Chang, Y. S. Instability of Gold Oxide Au_2O_3. *Surf. Sci.* **2003**, *537*, L447-L450.

[116] Dieter G.; *Mechanical Metallurgy*. McGraw-Hill: Columbus, OH, 1986

[117] Rico, I.; Lattes, A., Formide, a Water Substitute. 12. Krafft Temperature and Micelle Formation of Ionic Surfactants in Formamide. *J. Phys. Chem.* **1986,** *90*, 5870-5872.

[118] Modaressi, A.; Sifaoui, H.; Grzesiak, B.; Solimando, R.; Domanska, U.; Rogalski, M. CTAB Aggregation in Aqueous Solutions of Ammonium Based Ionic Liquids; Conductimetric Studies. *Colloids and Surfaces A: Physcochem. Eng. Aspects* **2007**, *296*, 104-108.

[119] Park, H. J.; Ah, C. S.; Kim, W.-J.; Choi, I. S.; Lee, K. P.; Yun, W. S. Temperature-Induced Control of Aspect Ratio of Gold Nanorods. *J. Vac. Sci. Technol. A.* **2006**, *24*, 1323-1326.

[120] Cao, G. *Nanostructure and Nanomaterials*; Imperial College Press: London, UK, 2004.

[121] Cvelbar, U.; Chen, Z.; Sunkara, M. K.; Mozetic, M. Spontaneous Growth of Superstructure α-Fe2O3 Nanowire and Nanobelt Arrays in Reactive Oxygen Plasma, *Small*, **2008**, *4*, 1610-1614.

[122] Barth, S.; Boland, J. J.; Holmes, J. D. Defect transfer from nanoparticles to nanowires, *Nano Lett.* **2011**, *11*, 1550-1555.

[123] Datsyuk, V.; Kalyva, M.; Papagelis, K.; Parthenios, J.; Tasis, D.; Siokou, A.; Kallitsis, I.; Galiotis, C. Chemical Oxidation of Multiwalled Carbon Nanotubes. *Carbon* **2008**, *46*, 833-840.

[124] Koga, K.; Ikeshoji, T.; Sugawara, K. Size- and Temperature-Dependent Structural Transitions in Gold Nanoparticles, *Phys. Rev. Lett.* **2004**, *92*, 115507/1-115507/4.

[125] Zhang, M. N.; Su, L.; Mao, L. Q., Surfactant functionalization of carbon nanotubes (CNTs) for layer-by-layer assembling of CNT multi-layer films and fabrication of gold nanoparticle/CNT nanohybrid. *Carbon* **2006,** *44* (2), 276-283.

[126] Ulman, A. Formation and Structure of Self-Assembled Monolayers. *Chemical Reviews* **1996,** *96*, 1533-1554.

[127] Li, W. Z.; Liang, C. H.; Zhou, W. J.; Qiu, J. S.; Zhou, Z. H.; Sun, G. Q.; Xin, Q. Preparation and Characterization of Multiwalled Carbon Nanotube-Supported Platinum

for Cathode Catalysts of Direct Methanol Fuel Cells. *The Journal of Physical Chemistry B* **2003,** *107*, 6292-6299.

[128] Liu, J.; Rinzler, A. G.; Dai, H. J.; Hafner, J. H.; Bradley, R. K.; Boul, P. J.; Lu, A.; Iverson, T.; Shelimov, K.; Huffman, C. B.; Rodriguez-Macias, F.; Shon, Y. S.; Lee, T. R.; Colbert, D. T.; Smalley, R. E., Fullerene pipes. *Science* **1998,** *280* (5367), 1253-1256.

[129] Li, W. Z.; Liang, C. H.; Zhou, W. J.; Qiu, J. S.; Zhou, Z. H.; Sun, G. Q.; Xin, Q., Preparation and characterization of multiwalled carbon nanotube-supported platinum for cathode catalysts of direct methanol fuel cells. *Journal of Physical Chemistry B* **2003,** *107* (26), 6292-6299.

[130] Xue, B.; Chen, P.; Hong, Q.; Lin, J. Y.; Tan, K. L., Growth of Pd, Pt, Ag and Au nanoparticles on carbon nanotubes. *Journal of Materials Chemistry* **2001,** *11* (9), 2378-2381.

[131] Li, J.; Moskovits, M.; Haslett, T. L., Nanoscale electroless metal deposition in aligned carbon nanotubes. *Chemistry of Materials* **1998,** *10* (7), 1963-1967.

[132] Draine, B.T.; Flatau, P.J., User Guide to the Discrete Dipole Approximation Code DDSCAT 7.2, 2012

[133] Chopra, N.; Shi, W. W.; Bansal, A., Structural evolution and stability studies of heterostructures comprised of carbon nanotubes decorated with nickel/nickel oxide core/shell nanoparticles. *Carbon* **2011,** *49* (11), 3645-3662.

[134] Mizsei, J.; Lantto, V., In situ AFM, XRD and resistivity studies of the agglomeration of sputtered silver nanolayers. *Journal of Nanoparticle Research* **2001,** *3* (4), 271-278.

[135] Logothetidis, S.; Stergioudis, G., Studies of density and surface roughness of ultrathin amorphous carbon films with regards to thickness with x-ray reflectometry and spectroscopic ellipsometry. *Applied Physics Letters* **1997,** *71* (17), 2463-2465.

[136] Buffat, Ph.; Borel J-P., Size Effect on the Melting Temperature of Gold Particles. *Physical Review A* **1976,** *13* (6), 2287-2298.

[137] Sambles, J.R., An Electron Microscope Study of Evaporating Gold Particles: The Kelvin Equation for Liquid Gold and the Lowering of the Melting Point of solid Gold Particles. *Proceedings of the Royal Society of London. Series A* **1971**, *324* (1558), 339-351.

[138] Ni, Z. H.; Yu, T.; Lu, Y. H.; Wang, Y. Y.; Feng, Y. P.; Shen, Z. X. Uniaxial Strain on Graphene: Raman Spectroscopy Study and Band-Gap Opening. *Acs Nano* **2008,** *2*, 2301-2305.

[139] Lordi, V.; Yao, N.; Wei, J., Method for supporting platinum on single-walled carbon nanotubes for a selective hydrogenation catalyst. *Chemistry of Materials* **2001,** *13* (3), 733-737.

[140] Parthasarathy, R.; Lin, X. M.; Jaeger, H. M., Electronic transport in metal nanocrystal arrays: The effect of structural disorder on scaling behavior. *Physical Review Letters* **2001,** *87* (18), 186807/1-186807/4.

[141] Li, Y. H.; Xu, C. L.; Wei, B. Q.; Zhang, X. F.; Zheng, M. X.; Wu, D. H.; Ajayan, P. M., Self-organized ribbons of aligned carbon nanotubes. *Chemistry of Materials* **2002,** *14* (2), 483-485.

[142] Chopra, N.; Xu, W. T.; De Long, L. E.; Hinds, B. J., Incident angle dependence of nanogap size in suspended carbon nanotube shadow lithography. *Nanotechnology* **2005,** *16* (1), 133-136.

[143] Pietrzak, L.; Jeszka, J. K., Gold nanoparticles grown on multiwall carbon nanotubes. *Materials Science-Poland* **2009,** *27* (3), 693-698.

[144] Mieszawska, A. J.; Jalilian, R.; Sumanasekera, G. U.; Zamborini, F. P., Synthesis of gold nanorod/single-wall carbon nanotube heterojunctions directly on surfaces. *Journal of the American Chemical Society* **2005,** *127* (31), 10822-10823.

[145] Miller, M. M.; Lazarides, A. A., Sensitivity of metal nanoparticle surface plasmon resonance to the dielectric environment. *Journal of Physical Chemistry B* **2005,** *109* (46), 21556-21565.

[146] Chen, H.; Kou, X.; Yang, Z.; Ni, W.; Wang, J., Shape- and size-dependent refractive index sensitivity of gold nanoparticles. *Langmuir* **2008,** *24* (10), 5233-5237.

[147] Yu, K.; Kelly, K. L.; Sakai, N.; Tatsuma, T., Morphologies and surface plasmon resonance properties of monodisperse bumpy gold nanoparticles. *Langmuir* **2008,** *24* (11), 5849-5854.

[148] Langhammer, C.; Kasemo, B.; Zoric, I., Absorption and scattering of light by Pt, Pd, Ag, and Au nanodisks: Absolute cross sections and branching ratios. *Journal of Chemical Physics* **2007,** *126* (19), 194702/1-194702/11.

[149] Bohren, C.F.; Huffman, D.R. *Absorption and Scattering of Light by Small Particles*; John Wiley & Sons, Inc.: New York, **1983**.

[150] Flatau, P.J.; Draine, B.T.; Fast near-field calculations in the discrete dipole approximation for regular rectilinear grids, *Optics Express*, **2012**, 20, 1247-1252.

[151] Zhang, C. J.; Hu, P., CO oxidation on Pd(100) and Pd(111): A comparative study of reaction pathways and reactivity at low and medium coverages. *Journal of the American Chemical Society* **2001**, *123* (6), 1166-1172.

[152] Yong, K. T.; Sahoo, Y.; Choudhury, K. R.; Swihart, M. T.; Minter, J. R.; Prasad, P. N., Shape control of PbSe nanocrystals using noble metal seed particles. *Nano Letters* **2006**, *6* (4), 709-714.

[153] Jin, M. S.; Liu, H. Y.; Zhang, H.; Xie, Z. X.; Liu, J. Y.; Xia, Y. N., Synthesis of Pd Nanocrystals Enclosed by {100} Facets and with Sizes < 10 nm for Application in CO Oxidation. *Nano Research* **2011**, *4* (1), 83-91.

[154] Xiong, Y. J.; Chen, J. Y.; Wiley, B.; Xia, Y. N.; Yin, Y. D.; Li, Z. Y., Size-dependence of surface plasmon resonance and oxidation for pd nanocubes synthesized via a seed etching process. *Nano Letters* **2005,** *5* (7), 1237-1242.

[155] Wagner, C. D. Handbook of X-ray Photoelectron Spectroscopy; Physical Electronics, Inc.: Eden Prairie, MN, 1979.

[156] Kim, K.; Gossmann, A.; Winograd N., X-ray Photoelectron Spectroscopic Studies of Palladium Oxides and the Palladium-Oxygen Electrode, *Anal. Chem.*, **1974**, *46* (2), 197-200.

[157] Chaim, R.; Marder, R.; Estournes, C., Optically transparent ceramics by spark plasma sintering of oxide nanoparticles. *Scripta Materialia* **2010,** *63* (2), 211-214.

[158] Reinhold, I.; Hendriks, C. E.; Eckardt, R.; Kranenburg, J. M.; Perelaer, J.; Baumann, R. R.; Schubert, U. S., Argon plasma sintering of inkjet printed silver tracks on polymer substrates. *Journal of Materials Chemistry* **2009,** *19* (21), 3384.3388.

[159] Sun, X.; Kiang, C. H.; Endo, M.; Takeuchi, K.; Furuta, T.; Dresselhaus, M. S., Stacking characteristics of graphene shells in carbon nanotubes. *Physical Review B* 1996, *54* (18), 12629-12632.

[160] Nguyen Viet, L.; Nguyen Duc, C.; Hayakawa, T.; Hirata, H.; Lakshminarayana, G.; Nogami, M., The synthesis and characterization of platinum nanoparticles: a method of controlling the size and morphology. *Nanotechnology* **2010,** *21* (3), 1-16.

[161] Song, H.; Kim, F.; Connor, S.; Somorjai, G. A.; Yang, P. D., Pt nanocrystals: Shape control and Langmuir-Blodgett monolayer formation. *Journal of Physical Chemistry B* **2005,** *109* (1), 188-193.

[162] Chen, J.; Lim, B.; Lee, E. P.; Xia, Y., Shape-controlled synthesis of platinum nanocrystals for catalytic and electrocatalytic applications. *Nano Today* **2009,** *4* (1), 81-95.

[163] Lim, B.; Jiang, M.; Camargo, P. H. C.; Cho, E. C.; Tao, J.; Lu, X.; Zhu, Y.; Xia, Y., Pd-Pt Bimetallic Nanodendrites with High Activity for Oxygen Reduction. *Science* **2009,** *324* (5932), 1302-1305.

[164] Lim, B.; Lu, X.; Jiang, M.; Camargo, P. H. C.; Cho, E. C.; Lee, E. P.; Xia, Y., Facile Synthesis of Highly Faceted Multioctahedral Pt Nanocrystals through Controlled Overgrowth. *Nano Letters* **2008,** *8* (11), 4043-4047.

[165] Bartholomew, C. H., Mechanisms of catalyst deactivation. *Applied Catalysis a-General* **2001,** *212* (1-2), 17-60.

[166] Ng, Y. H.; Ikeda, S.; Harada, T.; Morita, Y.; Matsumura, M., An efficient and reusable carbon-supported platinum catalyst for aerobic oxidation of alcohols in water. *Chemical Communications* **2008,** (27), 3181-3183.

[167] Boudou, J. P.; Paredes, J. I.; Cuesta, A.; Martinez-Alonso, A.; Tascon, J. M. D., Oxygen plasma modification of pitch-based isotropic carbon fibres. *Carbon* **2003,** *41* (1), 41-56.

[168] Leon, C.; Radovic, L. R., Interfacial Chemistry and Electrochemistry of Carbon Surfaces. *Chemistry and Physics of Carbon,* **1994,** *24*, 213-310.

[169] Lopez-Ramon, M. V.; Stoeckli, F.; Moreno-Castilla, C.; Carrasco-Marin, F., On the characterization of acidic and basic surface sites on carbons by various techniques. *Carbon* **1999,** *37* (8), 1215-1221.

[170] Bismarck, A.; Kumru, M. E.; Springer, J., Influence of oxygen plasma treatment of PAN-based carbon fibers on their electrokinetic and wetting properties. *Journal of Colloid and Interface Science* **1999,** *210* (1), 60-72.

[171] Bismarck, A.; Righter, D.; Wuertz, C.; Kumru, M. E.; Song, B.; Springer, J., Adhesion: Comparison between physico-chemical expected and measured adhesion of oxygen-plasma-treated carbon fibers and polycarbonate. *Journal of Adhesion* **2000,** *73* (1), 19-42.

[172] Chen, M. S.; Cal, Y.; Yan, Z.; Gath, K. K.; Axnanda, S.; Goodman, D. W., Highly active surfaces for CO oxidation on rh, pd, and pt. *Surface Science* **2007,** *601* (23), 5326-5331.

[173] Zaera, F., The surface chemistry of hydrocarbon partial oxidation catalysis. *Catalysis Today* **2003,** *81* (2), 149-157.

[174] Huber, G. W.; Corma, A., Synergies between bio- and oil refineries for the production of fuels from biomass. *Angewandte Chemie-International Edition* **2007,** *46* (38), 7184-7201.

[175] Ciuparu, D.; Lyubovsky, M. R.; Altman, E.; Pfefferle, L. D.; Datye, A., Catalytic combustion of methane over palladium-based catalysts. *Catalysis Reviews-Science and Engineering* **2002,** *44* (4), 593-649.

[176] Jiang, Z. M.; Jiang, X. M.; Liu, W. H.; Wu, Z. Q., Thermal-Stability of Multilayer Films Pt/Si, W/Si, Mo/Si, and W/C. *Journal of Applied Physics* **1989,** *65* (1), 196-200.

[177] Pan, H.; Sun, H.; Poh, C.; Feng, Y. P.; Lin, J. Y., Single-crystal growth of metallic nanowires with preferred orientation. *Nanotechnology* **2005,** *16* (9), 1559-1564.

[178] Cao, H.; Wang, L.; Qiu, Y.; Wu, Q.; Wang, G.; Zhang, L.; Liu, X., Generation and growth mechanism of metal (Fe, Co, Ni) nanotube arrays. *Chemphyschem* **2006,** *7* (7), 1500-1504.

[179] Karim, S.; Toimil-Molares, M. E.; Balogh, A. G.; Ensinger, W.; Cornelius, T. W.; Khan, E. U.; Neumann, R., Morphological evolution of Au nanowires controlled by Rayleigh instability. *Nanotechnology* **2006,** *17* (24), 5954-5959.

[180] Toimil-Molares, M. E.; Balogh, A. G.; Cornelius, T. W.; Neumann, R.; Trautmann, C., Fragmentation of nanowires driven by Rayleigh instability. *Applied Physics Letters* **2004,** *85* (22), 5337-5339.

[181] Yang, Q. H.; Bai, S.; Sauvajol, J. L.; Bai, J. B., Large-diameter single-walled carbon nanotubes synthesized by chemical vapor deposition. *Advanced Materials* **2003,** *15* (10), 792-795.

[182] Coleman, J. N.; Khan, U.; Blau, W. J.; Gun'ko, Y. K., Small but strong: A review of the mechanical properties of carbon nanotube-polymer composites. *Carbon* **2006,** *44* (9), 1624-1652.

[183] Conway, B. E., Transition from Supercapacitor to Battery Behavior in Electrochemical Energy-Storage. *Journal of the Electrochemical Society* **1991,** *138* (6), 1539-1548.

[184] Yuan, G. H.; Jiang, Z. H.; Aramata, A.; Gao, Y. Z., Electrochemical behavior of activated-carbon capacitor material loaded with nickel oxide. *Carbon* **2005,** *43* (14), 2913-2917.

[185] Futaba, D. N.; Hata, K.; Yamada, T.; Hiraoka, T.; Hayamizu, Y.; Kakudate, Y.; Tanaike, O.; Hatori, H.; Yumura, M.; Iijima, S., Shape-engineerable and highly densely packed single-walled carbon nanotubes and their application as super-capacitor electrodes. *Nature Materials* **2006,** *5* (12), 987-994.

[186] Han, J. H.; Yoo, J. B.; Park, C. Y.; Kim, H. J.; Park, G. S.; Yang, M.; Han, I. T.; Lee, N.; Yi, W. K.; Yu, S. G.; Kim, J. M., Tip growth model of carbon tubules grown on the glass substrate by plasma enhanced chemical vapor deposition. *Journal of Applied Physics* **2002,** *91* (1), 483-486.

[187] Wang, W. Z.; Liu, Y. K.; Xu, C. K.; Zheng, C. L.; Wang, G. H., Synthesis of NiO nanorods by a novel simple precursor thermal decomposition approach. *Chemical Physics Letters* **2002,** *362* (1-2), 119-122.

[188] Yoon, S.; Lee, J. W.; Hyeon, T.; Oh, S. M., Electric double-layer capacitor performance of a new mesoporous carbon. *Journal of the Electrochemical Society* **2000,** *147* (7), 2507-2512.

[189] Wu, M.-S.; Hsieh, H.-H., Nickel oxide/hydroxide nanoplatelets synthesized by chemical precipitation for electrochemical capacitors. *Electrochimica Acta* **2008,** *53* (8), 3427-3435.

[190] Hsieh, C.-T.; Chou, Y.-W.; Chen, W.-Y., Synthesis and electrochemical characterization of carbon nanotubes decorated with nickel nanoparticles for use as an electrochemical capacitor. *Journal of Solid State Electrochemistry* **2008,** *12* (6), 663-669.

[191] Srinivasan, V.; Weidner, J. W., An electrochemical route for making porous nickel oxide electrochemical capacitors. *Journal of the Electrochemical Society* **1997,** *144* (8), L210-L213.

[192] Ishihara, K.; Ueda, T.; Nakabayashi, N., Preparation of Phospholipid Polymers and their Properties as Polymer Hydrogel Membranes. *Polymer Journal* **1990,** *22* (5), 355-360.

[193] Kim, S. J.; Park, S. J.; An, K. H.; Kim, N. G.; Kim, S. I., Water behavior of poly(vinyl alcohol)/poly(vinylpyrrolidone) interpenetrating polymer network hydrogels. *Journal of Applied Polymer Science* **2003,** *89* (1), 24-27.

[194] Crystallinity determination. Encyclopaedia of Polymer Science Engineering, vol. 4. 2nd ed. New York: Wiley, 1987. P. 487.

[195] Peppas, N. A.; Wright, S. L., Solute diffusion in poly(vinyl alcohol) poly(acrylic acid) interpenetrating networks. *Macromolecules* **1996,** *29* (27), 8798-8804.

[196] Liu, Z.; Zhan, Y.; Shi, G.; Moldovan, S.; Gharbi, M.; Song, L.; Ma, L.; Gao, W.; Huang, J.; Vajtai, R.; Banhart, F.; Sharma, P.; Lou, J.; Ajayan, P. M., Anomalous high capacitance in a coaxial single nanowire capacitor. *Nature Communications* **2012,** *3*, 1-7.